ANTI SWING UP CONTROL OF A SINGLE, DOUBLE AND TRIPLE LINK ROTARY INVERTED PENDULUM WITH NONLINEAR FRICTION MODELS

A THESIS SUBMITTED TO
GRADUATE SCHOOL OF NATURAL AND APPLIED SCIENCES
OF
KOCAELİ UNIVERSITY

BY

ZIED BEN HAZEM

IN PARTIAL FULFILLMENT OF THE REQUIREMENTS
FOR
THE DEGREE OF DOCTOR OF PHILOSOPHY
IN
MECHATRONICS ENGINEERING

KOCAELİ 2021

ANTI SWING UP CONTROL OF A SINGLE, DOUBLE AND TRIPLE LINK ROTARY INVERTED PENDULUM WITH NONLINEAR FRICTION MODELS

A THESIS SUBMITTED TO
GRADUATE SCHOOL OF NATURAL AND APPLIED SCIENCES
OF
KOCAELI UNIVERSITY

BY

ZIED BEN HAZEM

IN PARTIAL FULFILLMENT OF THE REQUIREMENTS
FOR
THE DEGREE OF DOCTOR OF PHILOSOPHY
IN
MECHATRONICS ENGINEERING

Prof.Dr. Zafer BİNGÜL		
Supervisor,	**Kocaeli University**	**.....**
Prof.Dr. Serdar KÜÇÜK		
Jury member,	**Kocaeli University**	**.....**
Assist.Prof.Dr. Oğuzhan KARAHAN		
Jury member,	**Kocaeli University**	**.....**
Prof.Dr. Duygun EROL BARKANA		
Jury member,	**Yeditepe University**	**.....**
Prof.Dr. Osman PARLAKTUNA		
Jury member,	**Eskişehir Osmangazi University**	**.....**

Thesis Defense Date: 25.01.2021

ACKNOWLEDGEMENTS

I would like to thank my supervisor Prof. Dr. ZAFER BİNGÜL, for his support and encouragement throughout my PhD and express deep gratitude for having provided me with an excellent search environment. At many stages in this research project, I benefited from his advice, particularly so when exploring new ideas. His positive outlook and confidence in my research inspired me and gave me confidence. His careful editing contributed enormously to the production of this thesis. Also, for his essential corrections while I was writing the scientific papers.

I would like to thank the Mechatronics Engineering Department at Kocaeli University. I would like to express my gratitude and deep respect for all my professors for their high educational qualities and teaching competence. Moreover, I would like to thank the Automation and Robotics Research Laboratory (ARRL) research assistants in the Mechatronics Engineering Department at Kocaeli University for their help and encouragement during my PhD.

I would like to thank The Presidency for Turks Abroad and Related Communities, Turkey for the PhD scholarship.

I would like to thank the Scientific Research Projects Coordination Unit (SRPCU) of Kocaeli University for the experimental setup support.

I would like to thank my laboratory partner, the Iranian friend Dr. Mohammad Javad Fotuhi for his theoretical and experimental support. Also, many thanks for his wife Ms. Nasim Fotuhi, for their social support during the PhD.

Finally, I would like to say a big thank to my family, who supported me from afar, but they always felt near in my heart. Thank you very much for your kind support, love and patience. I would especially like to thank my father and my mother, Mohamed Ben Hazem and Awatef Bellaj, who always supported me and they made me feel much healthier after talking to them. Many thanks to my parents for teaching us that hard work and love for what we do are the ingredients for success. Also thank you both for your encouragement to try always for better things. I would like to thank my lovely sister Ahlem Ben Hazem. She is a good biologist, and I hope she visits Turkey. Finally, I would like to thank my brother, Hamza Ben Hazem, for his gentle encouragement that made me believe that everything is possible with hard work and patience.

January – 2021 ZIED BEN HAZEM

TABLE OF CONTENTS

LIST OF FIGURES

LIST OF TABLES

LIST OF SYMBOLS AND ABBREVIATIONS

θ_i	:	The angle of the i-th link, (rad, °)
$\dot{\theta}_i$	:	The angular velocity of the i-th link, (rad/s, °/s)
$\ddot{\theta}_i$	:	The angular acceleration of the i-th link, (rad/s^2, °/s^2)
τ_i	:	Torque of the i-th link, (Nm)
I_i	:	Inertia tensor of i-th link, (Kg m^2)
I_{zzi}	:	Z-component of the inertia tensor of i-th link, (Kg m^2)
m_i	:	Mass of the i-th link, (Kg)
m_B	:	Mass of balance mass, (Kg)
L_i	:	Length of the i-th link, (m)
b_i	:	Viscous damping coefficient of i-th link, (N-m-s/rad)
g	:	Gravity, (N kg^{-1})
C_p	:	Viscous friction coefficient of the NCFM, (N-m-s/rad)
B_i	:	Viscous friction coefficient of the LFM, (N-m-s/rad)
C_i	:	Coulomb friction coefficient of the LFM, (Nm)
f_o	:	Zero-drift error of friction torque of the NLFM, (Nm)
f_c	:	Coulomb friction coefficient of the NLFM, (Nm)
f_v	:	Viscous friction coefficient of the NLFM, (N-m-s/rad)
f_a	:	Experimental friction coefficient of the NLFM, (Nm)
f_b	:	Experimental friction coefficient of the NLFM, (Nm)
U	:	Control signal, (V)
T_s	:	Settling time, (s)
PO	:	Peak overshoot, (°)
MP	:	Maximum peak, (°)
E_{ss}	:	Steady-state error, (°)
Δ_{h_i}	:	Center of gravity vectors of the i-th link
h_i	:	The coordinate vector in the mass center of the i-th link
${}^{i}_{i+1}R$	:	Rotation matrix from a coordinate i-th link to a coordinate *i+1-th* link
J_i	:	Jacobian matrix of the i-th link
$D(\theta)$	:	Mass matrix
$C(\theta, \dot{\theta})$	:	Coriolis and Centripetal force vector
$G(\theta)$	:	Gravity vector
$\tau_f\ (\theta, \dot{\theta})$	:	Friction torque vector
$J(\theta)$	:	Jacobian matrix
$J_v(\theta)$	:	Jacobian matrix obtained from the linear velocities
$J_w(\theta)$	:	Jacobian matrix obtained from the angular velocities
${}^{i-1}_{i}T$	:	Homogeneous transformation matrix from a coordinate attached to an $i\ th$ link to a coordinate attached to *i-1-th*.

Abbreviations

ACE	:	Automation and Control Engineering
AFEMs	:	Adaptive Friction Estimation Models
AFLC	:	Adaptive Fuzzy Logic Controller
ALFM	:	Adaptive Linear Friction Model
ANCFM	:	Adaptive Non-Conservative Friction Model
ANFIS	:	Adaptive Neuro-Fuzzy Inference System
ANLFM	:	Adaptive Non-Linear Friction Model
ANN	:	Artificial Neural Network
ARRL	:	Automation and Robotics Research Laboratory
BR	:	Bayesian Regularization
DH	:	Denavit Hartenberg
DLLIP	:	Double Link Linear Inverted Pendulum
DLRIP	:	Double Link Rotary Inverted Pendulum
DOF	:	Degree of Freedom
EKF	:	Extended Kalman Filter
FLC	:	Fuzzy Logic Controller
FLQG	:	Fuzzy based Linear Quadratic Gaussian
FLQR	:	Fuzzy based Linear Quadratic Regulator
IPS	:	Inverted Pendulum System
IRR	:	Infinite Impulse Response
LQR	:	Linear Quadratic Regulator
LQG	:	Linear Quadratic Gaussian
LFM	:	Linear Friction Model
LFIP	:	Linear Flexible Inverted Pendulum
LLPIP	:	Linear-Linear Planar Inverted Pendulum
MSE	:	Means Squared Error
NCFM	:	Non-Conservative Friction Model
NF	:	Neuro-Fuzzy
NFFEMs	:	Neuro-Fuzzy Friction Estimation Models
NFLFM	:	Neuro-Fuzzy Linear Friction Model
NFNCFM	:	Neuro-Fuzzy Non-Conservative Friction Model
NFNLFM	:	Neuro-Fuzzy Nonlinear Friction Model
NLCT	:	Non-Linear Control Theory
NLFM	:	Non-Linear Friction Model
PIP	:	Planar Inverted Pendulum
PID	:	Proportional Integral Derivative
PS	:	Pendulum System
QDIP	:	Quadrotor Driven Inverted Pendulum
RBNFLQR	:	Radial Basis Neuro-Fuzzy based LQR
RBNN	:	Radial Basis Neural Network
RIPS	:	Rotary Inverted Pendulum System
RLPIP	:	Rotary-Linear Planar Inverted Pendulum
RMSEs	:	Root Mean Squared Errors
RRPIP	:	Rotary-Rotary Planar Inverted Pendulum
RTIP	:	Rotary Twin Inverted Pendulum
RTLIP	:	Rotary Triple Link Inverted Pendulum
RTLIP	:	Rotary Triple Link Inverted Pendulum

RWP	:	Reaction Wheel Pendulum
SFC	:	State Feedback Control
SLIP	:	Spring-Loaded Inverted Pendulum
SLLIP	:	Single Link Linear Inverted Pendulum
SLRIP	:	Single Link Rotary Inverted Pendulum
SMC	:	Sliding Mode Control
TLLIP	:	Triple Link Linear Inverted Pendulum
TLRIP	:	Triple Link Rotary Inverted Pendulum
TWIPMR	:	Two-Wheeled Inverted Pendulum Mobile Robot
VLIP	:	Variable Length Inverted Pendulum
WIPMR	:	Wheeled Inverted Pendulum Mobile Robot

ANTI SWING CONTROL OF A SINGLE, DOUBLE AND TRIPLE LINK ROTARY INVERTED PENDULUM WITH NONLINEAR FRICTION MODELS

ABSTRACT

RIPS is one of the fundamental problems in the control theory field. To verify the modern control theory, RIPS may be considered as a better example in control engineering. It is the best model for the attitude control such as space booster, rocket, satellite, aircraft stabilization in the turbulent air-flow, humanoid robots, etc…. The RIPS is a highly non-linear and open-loop unstable system that makes the control more challenging. It is an intriguing subject from the control point of view due to its intrinsic nonlinearity. The RIPS include a nonlinearity due to the frictions in the joints. Common control approaches require a good knowledge of the frictions in the joints of the system and accurate friction estimation to obtain the desired performances of feedback controllers. However, the frictions have high non-linear values, which result in steady-state errors, limit cycles, and poor performance of the system. It has an influence on the system's response, and it should be considered seriously. Therefore, friction estimation has the potential to ameliorate the quality and dynamic behavior of the system.

One of the aims of this thesis is to estimate the nonlinear frictions in the triple link rotary inverted pendulum. In this research, novel NFFEMs are developed to estimate the joint friction coefficients of three link rotary pendulum and compared with AFEMs. The different versions of AFEMs and NFFEMs are generated based on each of the following friction estimation models: NCFM, LFM, and NLFM. The aim of this friction study is to obtain joint friction models which depend on both velocity and acceleration in a large range of motion trajectory that involves difficult and sudden large changes. In the proposed NFFEMs, joint velocities and accelerations of the TLRIP are used as the input variables of the NF system trained by using a RBNN. Several experiments are conducted on the TLRIP system to verify the NFFEMs. In order to determine the estimation performance of the friction models, total RMSEs between position simulation results obtained from each joint friction model and encoders in the experimental setup are computed. Based on the position RMSEs, the NFFEMs produce better estimation results than the AFEMs. Among the novel NFFEMs, the NFNLM gives the best results.

Another aim of this thesis is to develop non-linear controllers for the stabilization and anti-swing control problems. PID, LQR and swing-up based LQR controllers are developed for the stability control of the SLRIP. Moreover, FLQR and FLQG controllers are developed for the stability control of DLRIP and TLRIP. The aim of the stability control is to study the dynamic performance of both FLQR and FLQG controllers and to compare them with the classical LQR and LQG controllers, respectively. To determine the control performance of the controllers, Ts, PO, Ess, MP and the total RMSEs of the joint positions are computed. Furthermore, the dynamic responses of the controllers were compared based on robustness analysis under internal

and external disturbances. To show the control performance of the controllers, several simulations were conducted. Based on the comparative results, the dynamic responses of both FLQR and FLQG controllers produce better results than the dynamic responses of the classical LQR and LQG controllers, respectively. Moreover, the robustness results indicate that the FLQR and FLQG controllers under the internal and external disturbances were effective. Furthermore, an anti-swing control of the SLRIP, DLRIP and TLRIP is developed. To determine the control performance of the anti-swing controllers, different control parameters are computed, such as Ts, MP, Ess, and RMSEs of the joint positions. Based on the comparative results, the LQR controller produces better results than the classical PID for the SLRIP. Moreover, a novel RBNF-LQR controller is developed for an anti-swing control of the DLRIP and TLRIP. The objective of this research is to study the RBNF-LQR controller and to compare it with the FLQR and the LQR controllers. In the proposed RBNF-LQR controllers, the positions and velocities of state variables multiplied by their LQR gains are trained by using RBNNs architecture. The outputs of the two RBNNs are used as the input variables of the fuzzy controller. The novel architecture of the RBNF controller is developed in order to obtain better control performance than the classical ANFIS. To show the control performance of the anti-swing controllers, simulation and experiments results are given and compared. According to the comparative results, the RBNF-LQR anti-swing controller produces better results than FLQR and LQR. Furthermore, the performance of the three controllers developed was compared based on robustness analysis under external disturbance. The results obtained here indicate that the RBNF-LQR anti-swing controller produces better performance than others in term of vibration suppression capability.

Keywords: Anti-swing Control, Fuzzy Based LQR and LQG Control, Nonlinear Friction Joint Estimation Model, Radial Basis Function Neural Network Control, Single Double Triple Link Rotary Pendulums.

DOĞRUSAL OLMAYAN SÜRTÜNME MODELLERİYLE TEK, ÇİFT VE ÜÇ BAĞLI DÖNEL TERS SARKACIN SALINIM ÖNLEYİCİ KONTROLÜ

ÖZET

Dönel ters sarkaç sistemi, kontrol teorisi alanındaki temel problemlerden biridir. Dönel ters sarkaç sistemleri, kontrol mühendisliğinde modern kontrol teorisinin uygulanması için bir örnek deneysel düzenek olarak kullanılmaktadır. Roketlerin, uyduların ve uçakların türbülanslı hava akışı içerisindeki konumlarının kontrolü, insansı robotların benzetimi esnasında model olarak sarkaç sistemleri kullanılmaktadır. Döner ters sarkaç sistemi, kontrolü daha zor hale getiren son derece doğrusal olmayan ve açık döngülü kararsız bir sistemdir. Doğrusal olmaması nedeniyle kontrol açısından ilgi çekici bir konudur. Döner ters sarkaç sistemi, eklemlerdeki sürtünmelerden kaynaklanan bir doğrusal olmayan davranışlar sergiler. Yaygın kontrol yaklaşımları, geri besleme denetleyicileri ile sistemin kontrolünde istenen performansları elde edilebilmesi için sistemin eklemlerindeki sürtünmeler hakkında net bir bilgi ve doğru sürtünme tahmini modeller gerektirir. Bununla birlikte, sürtünmelerin yüksek doğrusal olmayan ifadeleri içermesi, kararlı durum hatalarına, sınır döngülerine ve sistemin kötü performansı göstermesine neden olmaktadır. Sistemin tepkisi üzerinde doğrudan etkisi vardır ve dikkate alınmalıdır. Bu nedenle, sürtünme tahmini, sistemin kontrol performansını ve dinamik davranışını iyileştirme potansiyeline sahiptir.

Bu tezin amaçlarından biri, üç bağlı ters dönel sarkaçtaki doğrusal olmayan sürtünmeleri tahmin etmektir. Bu araştırmada, üç bağlı döner sarkacın eklem sürtünme katsayılarını tahmin etmek ve uyarlamalı sürtünme modelleriyle karşılaştırmak için yeni nöro-bulanık sürtünme tahmin modelleri geliştirilmiştir. Uyarlanabilir sürtünme modellerinin ve nöro-bulanık sürtünme tahmin modellerinin farklı versiyonları, aşağıdaki sürtünme tahmin modellerinin her birine dayalı olarak oluşturulmaktadır: Konservatif olmayan sürtünme modeli, doğrusal sürtünme modeli ve doğrusal olmayan sürtünme modeli. Bu sürtünme çalışmasının amacı, zor ve ani büyük değişiklikleri içeren geniş bir hareket yörüngesinde hem hıza hem de ivmeye bağlı olan eklem sürtünme modellerini elde etmektir. Önerilen nöro-bulanık sürtünme tahmin modellerinde, üç bağlı döner ters sarkacın eklem hızları ve ivmeleri, radyal tabanlı bir sinir ağı kullanılarak eğitilen nöro-bulanık systemin, girdi değişkenleri olarak kullanılmıştır. Nöro-bulanık sürtünme tahmin modellerini doğrulamak için üç bağlı dönel ters sarkaç sistemi üzerinde bazı deneyler yapılmıştır. Sürtünme modellerinin tahmin performansının belirlenmesi için her bir eklem sürtünme modelinden elde edilen konum simülasyon sonuçları ile deney düzeneğindeki kodlayıcılar arasındaki toplam kök ortalama kare hataları hesaplanmıştır. Konum kökü ortalama kare hatalarına dayalı olarak, nöro-bulanık sürtünme tahmin modelleri, nöro-bulanık sürtünme tahmin modellerinden daha iyi tahmin sonuçları üretmiştir. Yeni nöro-bulanık sürtünme tahmin modelleri arasında, nöro-bulanık doğrusal olmayan sürtünme tahmin modeli en iyi sonuçları vermektedir.

Bu tezin bir diğer amacı, stabilizasyon ve salınım önleyici kontrol problemleri için doğrusal olmayan kontrolörler geliştirmektir. Orantılı integral türev, doğrusal

kuadratik regülatör ve salınım tabanlı doğrusal kuadratik regülatör denetleyicileri, tek bağlı dönel ters sarkacın stabilizasyon kontrolü için geliştirilmiştir. Ayrıca, çift ve üç bağlı dönel ters sarkacın stabilizasyon kontrolü için bulanık tabanlı doğrusal kuadratik regülatör ve bulanık tabanlı doğrusal ikinci dereceden gauss kontrolörleri geliştirilmiştir. Stabilite kontrolünün amacı, hem bulanık tabanlı doğrusal kuadratik regülatör hem de bulanık tabanlı doğrusal ikinci dereceden gauss kontrolörlerinin dinamik performansını incelemek ve bunları sırasıyla klasik doğrusal kuadratik regülatör ve doğrusal ikinci dereceden gauss kontrolörleriyle karşılaştırmaktır. Kontrolörlerin kontrol performansını belirlemek için, yerleşme süresi, pik aşımı, sabit durum hatası, maksimum piki ve eklem konumlarının toplam kök ortalama kare hataları hesaplanır. Ayrıca, kontrolörlerin dinamik tepkileri, iç ve dış bozucu etkiler altında sağlamlık (gürbüzlük) analizine dayalı olarak karşılaştırılmıştır. Kontrolörlerin kontrol performansını göstermek için bazı simülasyonlar gerçekleştirilmiştir. Karşılaştırmalı sonuçlara dayanarak, hem bulanık tabanlı doğrusal kuadratik regülatör hem de bulanık tabanlı doğrusal ikinci dereceden gauss kontrolörlerinin dinamik yanıtları, sırasıyla klasik doğrusal kuadratik regülatör ve doğrusal ikinci dereceden gauss kontrolörlerinin dinamik yanıtlarından daha iyi sonuçlar üretmektedir. Dahası, sağlamlık sonuçları, iç ve dış bozucu etkiler altındaki bulanık tabanlı doğrusal kuadratik regülatör ve bulanık tabanlı doğrusal ikinci dereceden gauss kontrolörlerinin etkili olduğunu göstermektedir. Ayrıca, tek bağlı ters dönel sarkaç, çift bağlı ters dönel sarkaç, ve üç bağlı dönel ters sarkaç için bir salınım önleyici kontrolü geliştirilmiştir. Salınım önleyici kontrolörlerin kontrol performansını belirlemek için, eklem konumlarının yerleşme süresi, sabit durum hatası, maksimum piki ve eklem konumlarının toplam kök ortalama kare hataları gibi farklı kontrol parametreleri hesaplanmaktadır. Karşılaştırmalı sonuçlara göre, doğrusal kuadratik regülatör kontrolörü tek bağlı ters dönel sarkaç için klasik orantılı integral türev kontrolöründen daha iyi sonuçlar vermiştir. Dahası, çift bağlı döner ters sarkaç ve üç bağlı döner ters sarkacın anti-salınım kontrolü için yeni bir radyal temel nöro-bulanık tabanlı doğrusal karesel regülatör denetleyici geliştirilmiştir. Bu araştırmanın amacı, radyal temel nöro-bulanık tabanlı doğrusal kuadratik düzenleyici denetleyiciyi incelemek ve onu bulanık tabanlı doğrusal karesel düzenleyici ve doğrusal karesel düzenleyici denetleyicileri ile karşılaştırmaktır. Önerilen radyal temel nöro-bulanık tabanlı doğrusal kuadratik düzenleyici denetleyicilerde, doğrusal karesel düzenleyici kazanımlarıyla çarpılan durum değişkenlerinin konumları ve hızları, radyal temel yapay sinir ağları mimarisi kullanılarak eğitilmektedir. İki radyal temelli sinir ağının çıktıları, bulanık denetleyicinin giriş değişkenleri olarak kullanılmıştır. Radyal temel neuro-fuzzy denetleyicinin yeni mimarisi, klasik uyarlanabilir nöro-bulanık çıkarım sisteminden daha iyi kontrol performansı elde etmek için geliştirilmiştir. Salınım önleyici kontrolörlerin kontrol performansını göstermek için simülasyon ve deney sonuçları verilmiş ve karşılaştırılmıştır. Karşılaştırmalı sonuçlara göre, radyal temel nöro-bulanık tabanlı doğrusal kuadratik düzenleyici salınım önleyici denetleyicisi, bulanık tabanlı doğrusal kuadratik düzenleyici ve doğrusal kuadtarik düzenleyiciden daha iyi sonuçlar vermektedir. Ayrıca, geliştirilen üç denetleyicinin performansı, harici bozucu etkiler altındaki sağlamlık analizine dayalı olarak karşılaştırılmıştır. Burada elde edilen sonuçlar, radyal temel nöro-bulanık tabanlı doğrusal karesel regülatör anti-salınım denetleyicisinin titreşim bastırma özelliği açısından diğerlerinden daha iyi performans ürettiğini göstermektedir.

Anahtar Kelimeler: Salınım Önleyici Kontrolü, Bulanık Tabanlı Doğrusal Kuadratik Regülatör ve Doğrusal İkinci Dereceden Gauss Kontrolü, Doğrusal Olmayan Sürtünme Eklem Tahmin Modeli, Radyal Temel Fonksiyonlu Yapay Sinir Ağı Kontrolü, Tek Çift Üç Bağlı Döner Sarkaçlar.

INTRODUCTION

PS is the most well-known equipment in the field of ACE. PS is an open-loop and unstable system used in different application such as Segway human transporter, missile launcher or humanoid robot, etc.... Therefore, it has been a benchmark control problem in the field of ACE which verifies a modern control theory. It is an expensive system, can be designed and installed in a research laboratory for control education. RIPS is one of the most interesting and popular mechatronic systems in the ACE field, and it can exist in many different forms. RIPS is a challenging problem in the area of control engineering applications in linear and nonlinear control. RIPS can be called "Furuta Pendulum". Furuta pendulum is a SLRIP. It consists of a driven arm which rotates in the horizontal plane and a pendulum attached to the extremity of the base arm which rotate in the vertical plane. Furuta pendulum was developed by K. Furuta at Tokyo Institute of Technology and was called the "TITECH pendulum". Due to the gravitational forces and the coupling arising from the Coriolis and centripetal forces, RIPS is underactuated, unstable and extremely nonlinear.

RIPS include nonlinearity due to the frictions in the joints. RIPS is the most convenient example to understand the influence of the joint frictions on the performance of feedback controllers, which aim to stabilise the pendulum in the upward unstable position and the downward stable position. Furthermore, frictions can have high nonlinear values which result in steady-state errors, limit cycles, and poor performance of the system. It influences the system's control response that should be considered seriously. Therefore, friction estimation has the potential to ameliorate the quality and dynamic behavior of the system. In this thesis, joint frictions of the TLRIP are examined based on its experimental and simulation dynamic responses. TLRIP might be considered as the most appropriate mechanical setup to investigate friction phenomena and understand the frictions' influence in the dynamics of any mechanical system.

In this work, three different friction estimation models such as Non-Conservative, Linear and Nonlinear friction models are compared to estimate the joint frictions of the TLRIP developed in our laboratory. NCFM considers only viscous frictions. LFM is dependent on Coulomb and viscous frictions. The NLFM is the sum of five types of frictions: the zero drift error of friction, the Coulomb friction, the viscous friction, and two experimental frictions. Based on comparative experimental friction analysis, the joint frictions of the TLRIP are estimated more effectively using an NLFM. Moreover, AFEMs were developed to estimate the frictions in three pendulums' joints of the TLRIP and compared with existing friction estimation models NCFM, LFM, and NLFM. Joint accelerations were classified into three groups such as low, medium and high. The adaptive friction coefficients were optimised based on this classification of acceleration. Based on the position RMSEs obtained from each joint friction model, the AFEMs were better than the existing friction estimation models (NCFM, LFM, and NLFM). Among the friction estimation models, the best results were produced by ANLFM. Besides, NFFEMs are developed to estimate the joint friction coefficients in a TLRIP system and compared with the AFEMs. The different versions of AFEMs and NFFEMs are generated based on each of the following friction estimation models: NCFM, LFM, and NLFM. The aim of this study is to obtain joint friction models which depend on both velocity and acceleration in a large range of motion trajectory that involves difficult and sudden large changes. In the proposed NFFEMs, joint velocities and accelerations of the TLRIP are used as the input variables of the NF system trained by using a Radial RBNN. Several experiments are conducted on TLRIP system to verify the NFFEMs. In order to determine the estimation performance of the friction models, RMSEs between position simulation results obtained from each joint friction model and encoders in the experimental setup are computed. Based on the RMSEs' position, the NFFEMs produce better estimation results than the AFEMs. Among NFFEMs, the NFNLM gives the best results.

The friction study has three important contributions to the literature. Firstly, all friction models in the literature depend only on velocity. However, the friction model developed here depends on both velocity and acceleration. This approach has enabled us to obtain a two-dimensional friction model. Secondly, the coefficients of all friction models in the literature were constant when the physical quantities change. On the

other hand, the coefficients of the friction models in this work vary depending on the state of the velocity and acceleration. Hence, this friction model allows for better estimation of the effects of friction in different velocity and acceleration conditions. Thirdly, much of existing researches in the literature have studied only the frictions of the linear motion which depends on linear velocity and force. This work examines frictions on the joints which have hard rotational motions.

In this work, the stability control problem is studied for the SLRIP, DLRIP and TLRIP systems, respectively. For the stability control problem of the SLRIP, a PID, LQR and swing-up based LQR controllers are developed and compared under external disturbance. The robustness results indicate that the LQR controller under external disturbances was effective. Moreover, for stability control of the DLRIP and TLRIP systems, FLQR and FLQG controllers are developed. The aim is to study dynamic performance analysis of both FLQR and FLQG controllers and to compare them with the classical LQR and LQG controllers, respectively. A dynamic mechanical simulation model of the system was obtained using both the numerically SimMechanics toolbox in MATLAB and the analytically dynamic nonlinear equations. To determine the control performance of the controllers, T_s, PO, E_{ss}, and the RMSEs of the joint positions are computed. Furthermore, the dynamic responses of the controllers were compared based on robustness analysis under internal and external disturbances. To show the control performance of the controllers, several simulations were conducted. Based on the comparative results, the dynamic responses of both FLQR and FLQG controllers produce better results than the dynamic responses of the classical LQR and LQG controllers, respectively. Moreover, the robustness results indicate that the FLQR and FLQG controllers under the internal and external disturbances were effective.

In this work, anti-swing control of the SLRIP, DLRIP and TLRIP is developed. To determine the control performance of the anti-swing controllers, different control parameters are computed such as T_s, MP, E_{ss}, and the RMSEs of the joint positions. Based on the robustness comparative results, the LQR controller produces better results than classical PID under external disturbance for the SLRIP. Moreover, RBNF-LQR controller is developed for an anti-swing control of the DLRIP and TLRIP. The objective of this work is to study the RBNF-LQR controller and to compare it with a

FLQR and the LQR controllers. In the proposed RBNF-LQR controllers, the positions and velocities of state variables multiplied by their LQR gains are trained by using RBNNs architecture. The output of the two RBNNs are used as the input variables of the fuzzy controller. The novel architecture of RBNF controller is developed in order to obtain better control performance than the classical ANFIS. According to the comparative results, the RBNF-LQR anti-swing controller produces better results than FLQR and LQR. Furthermore, the performance of three controllers developed was compared based on robustness analysis under external disturbance. Moreover, to show the control performance of the anti-swing controllers, simulation and experiments results are given and compared.The results obtained here indicate that the RBNF-LQR anti-swing controller has better performance than others in term of the vibration suppression capability. This thesis is organized as follows:

The first chapter deals with the overview of the PS: working principles, types, classification and application of the IPS are described. A detailed literature survey of IPS is provided, and the structure of the RIPS is investigated. Definition and contributions of the thesis are presented.

The second chapter investigates kinematic model, nonlinear dynamic model, Jacobian and dynamic simulation of the SLRIP, DLRIP and TLRIP systems. The kinematic model of each system is derived based on the DH convention. Rotation and homogeneous transformation matrices between coordinates are calculated. The nonlinear dynamic equations of each system are obtained by the Newton-Euler method and explained in details. The nonlinear dynamic equations are obtained based on the calculated rotation and homogeneous transformation matrices. The Jacobian matrix of the system is calculated and used to estimate the best length of each link. Dynamic comparison between the obtained results from both nonlinear mathematical and the Matlab/SimMechanics models is described. Finally, inertia analysis of the vertical arms of the TLRIP is given.

In the third chapter, novel approaches to estimate the joint friction coefficients of three link rotary pendulum are explained in detailed. Firstly, three NCFM, LFM, NLFM are compared to estimate the joint frictions of the TLRIP developed in our laboratory. Secondly, AFEMs were developed to estimate the frictions in three pendulums' joints

of the TLRIP and compared with NCFM, LFM, NLFM. Finally, NFFEMs were developed to estimate the joint friction coefficients in TLRIP and compared with an AFEMs. NFFEMs are developed in order to obtain joint friction models which, depend on both velocity and acceleration in a large range of motion trajectory that involves difficult and sudden large changes. In the proposed NFFEMs, joint velocities and accelerations of the TLRIP are used as the input variables of the NF system trained by using an RBNN.

In the fourth chapter, stability and anti-swing control problems of the SLRIP, DLRIP and TLRIP systems are explained. PID, LQR and swing-up based LQR controllers are developed for stabilisation control problem of the SLRIP. Furthermore, FLQR and FLQG controllers are developed for stability control of DLRIP and TLRIP. FLQR and FLQG controllers are compared with the LQR and LQG controllers, respectively. The dynamic responses of the controllers were compared based on robustness analysis such as under noises, internal and external disturbances. For the anti-swing control problem, PID and LQR controllers are applied to the SLRIP. Furthermore, a novel RBNF-LQR controller is developed for an anti-swing control of the DLRIP and TLRIP. The RBNF-LQR controller was compared with the FLQR and the LQR controllers. The novel architecture RBNF controller is developed in order to obtain better control performance than ANFIS. The dynamic responses of the anti-swing controllers were compared based on robustness analysis under external disturbances.

The last chapter focuses on experimental studies. The anti-swing control of a SLRIP DLRIP and TLRIP with NLFMs are verified in real experimental setups. The results obtained experimentally are compared with simulation results.

1. INVERTED PENDULUM SYSTEM

1.1. Introduction

The reviews existing in literature are undertaken as a part of the TLRIP project. It is focused to understand: the background and the principal application of the IPS, the nonlinear analytic mathematical model, numerical mechanical simulation model, mechanical design aspects, friction models, control algorithms, and other successful projects of the similar nature. The IPS is a classic model of the nonlinear control topic. It is used frequently to study the design, implementation and control development for nonlinear systems. The IPS appears in the undergraduate control textbooks, for example, it is used as an example to describe the physical systems mathematically by Dorf and Bishop [1]. The physical analysis of the IPS has been an important consideration in the modern control theory studies [2]. The control of the IPS, for which different configurations exist, is a very complicated task. it has provided the best demonstration of the capabilities of the scientific and engineering area [3]. The control of this type of systems is based on to maintain the hinged pendulum in a predetermined stable position by adding a driving force. In the most ordinary case, the objective is to keep the pendulum on the upward position [4-5]. The pendulum must be stable against the gravitational force, which would make it in an upward position to a more resting-state stable. Different mechanical configurations have been studied in the field of IPS [6]. Furthermore, many controllers have been used to maintain the inverted pendulum to a stable position. The control problem of the IPS has been complicated by adding the pendulums link together. The IPS configuration depends on the actuation method and the number of DOF. The simple model of the controllable IPS given in [1], is consist of a pendulum link directly attached to the shaft of the motor. This model of the IPS is controlled open-loop using a stepper motor, this model is deemed too simple for further consideration. Figure 1.1. shows the simple model of the IPS.

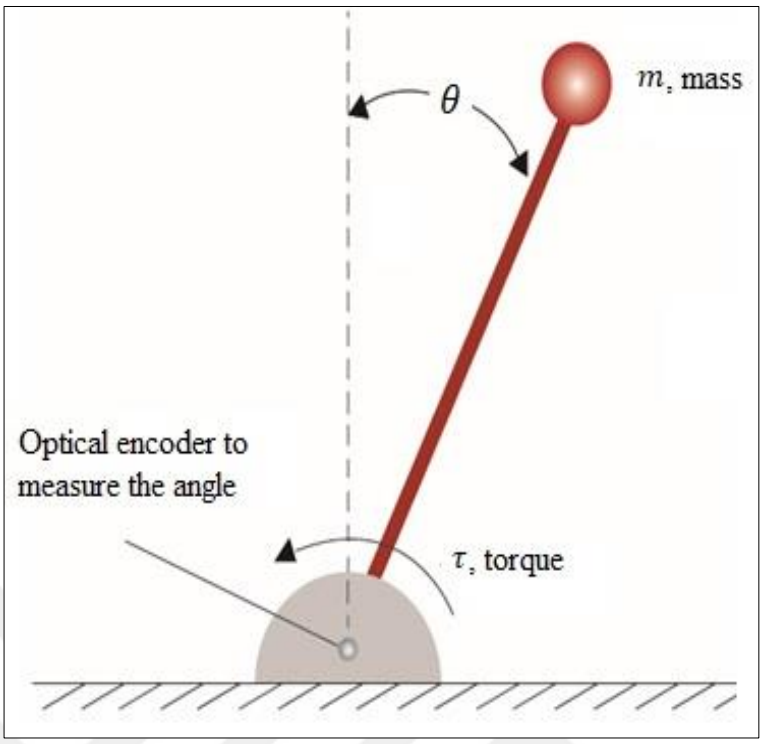

Figure 1.1. A simple model of the IPS

In Figure 1.1, τ is the input torque motor, and an optical encoder is used to measure the angular shaft position of the motor. θ is the angular position of the pendulum link, and m is mass attached to the pendulum link. Therefore, to have a simple controllable IPS, the system must have at least two DOF. For the two DOF system, the pendulum base is limited to move in one linear or rotary dimension, and the pendulum angle is varied only in the vertical dimension [7]. A classification of the IPS based on the number actuators in the system is given in Figure 1.2. In the next section, different configurations of the IPS will be discussed.

1.2. Single Actuator Linear Serial IPS

1.2.1. Single link linear inverted pendulum

Figure 1.3 shows examples of physical models and a real experimental implementation of the SLLIP. In the SLLIP, a motor is used to move a cart linearly along a straight track, to modify the pendulum angle, as shown in Figure 1.3 (c). The pendulum link of the SLLIP is attached to the cart joint. The rotational axis of the pendulum about the cart joint is horizontal and perpendicular to the direction of the cart's movement. The input of the SLLIP is a force applied to the cart, via the motor [8].

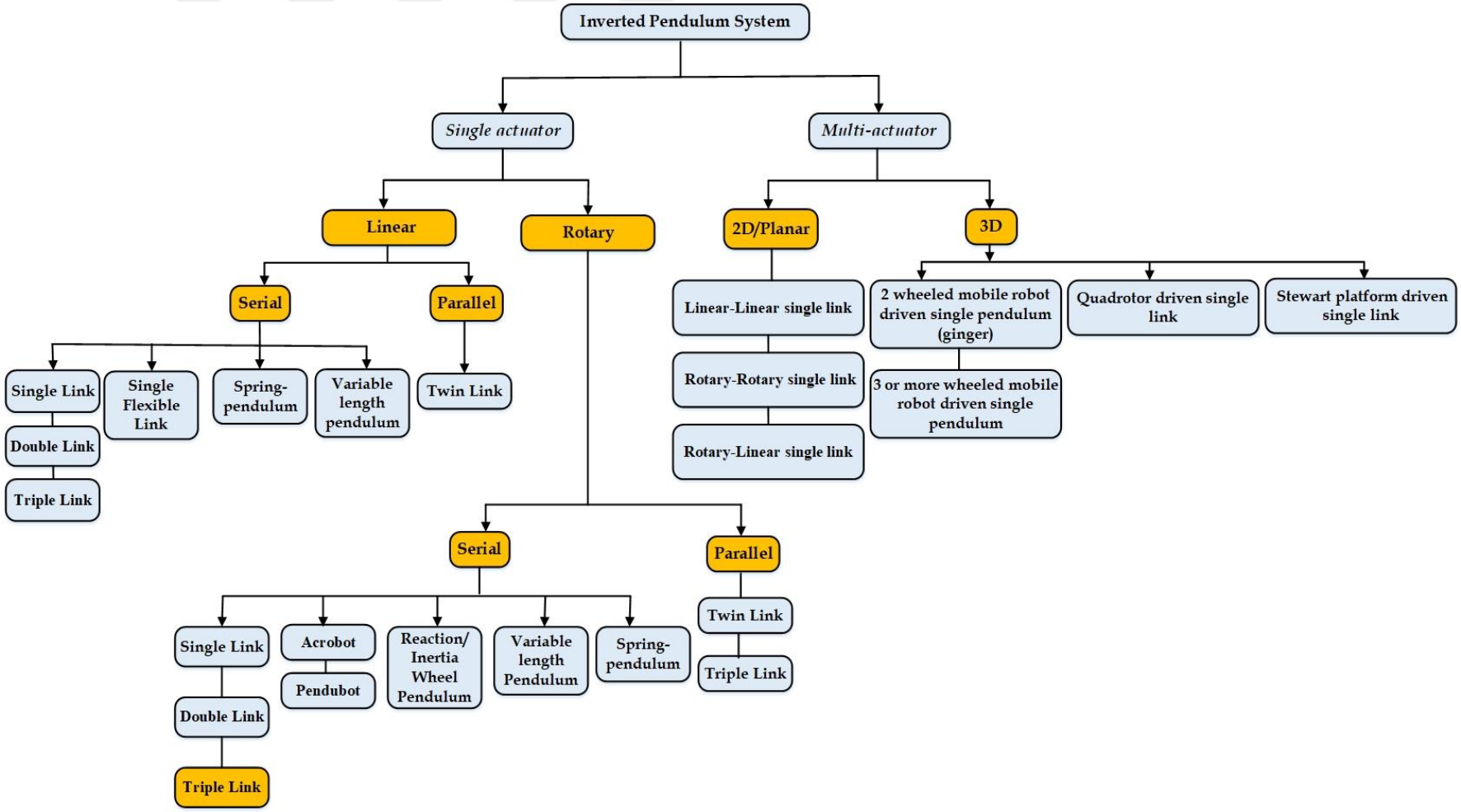

Figure 1.2. Classification of the IPS according to the actuator configuration

The SLLIP has two equilibrium points [9-10], Figure 1.3 (a) shows one of them; the objective is to maintain the pendulum in the upward vertical position above the cart. Allowing for small changes in its angle and preventing it from falling. The pendulum position above the cart is an unstable equilibrium state of the system. Figure 1.3 (b) shows the other equilibrium state is somewhat similar to the known problem of the gantry crane system control. The aim is to keep the pendulum link in the downward vertical position below the cart. The cart moves and prevents the pendulum from oscillating.

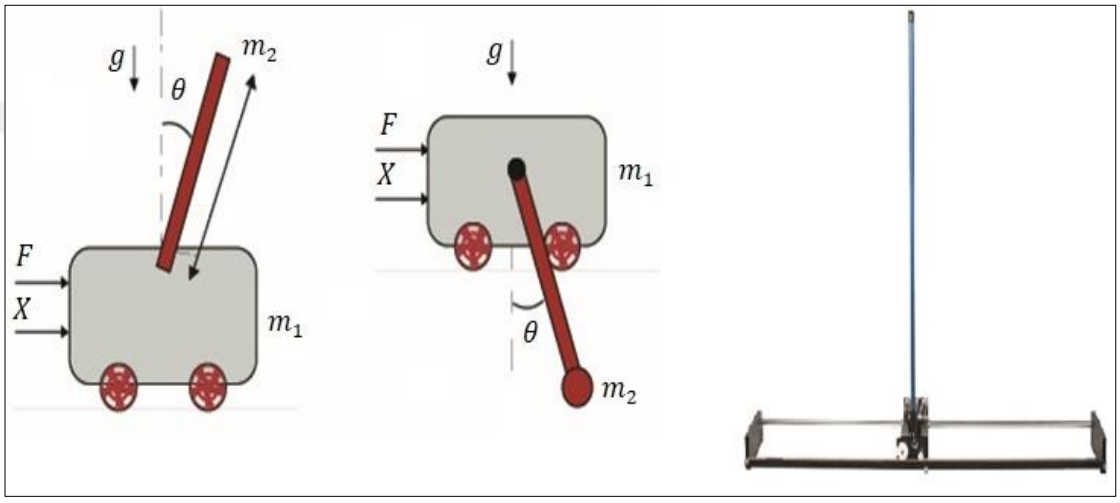

(a) (b) (c)

Figure 1.3. SLLIP: (a) physical model of a cart-pole system, (b) physical model of a crane system and (c) real experimental implementation [11]

A reproduction of the diagram is shown in Figure 1.3 (a) and (b). F is the input force, X is the linear displacement of the cart, θ is the angular position of the pendulum, m_1 is the mass of the cart and m_2 is the mass of the pendulum link.

1.2.2. Double link linear inverted pendulum

Figure 1.4 shows a physical model and real experimental implementation example of a DLLIP. The mechanical configuration of the DLLIP have a cart with linear motion, and two series pendulum links mounted to the cart. The system aims to maintain the two pendulum links in the upward vertical position [12-14]. DLLIP is an under-actuated system, and it is highly unstable. The number of DOFs surpasses the actuation number. The dynamic complexity and the nonlinearity of the system increase; for this reason, the system controllability will be more complex. In Figure 1.4, F is the input

force, X is the cart position, θ_1 is the angular position of the first pendulum link and θ_2 is the angular position of the second pendulum link. L_1, L_2 are the lengths of the first and second links, respectively. Moreover, m_0, m_1 and m_2 are the mass of the cart, first link and second links respectively.

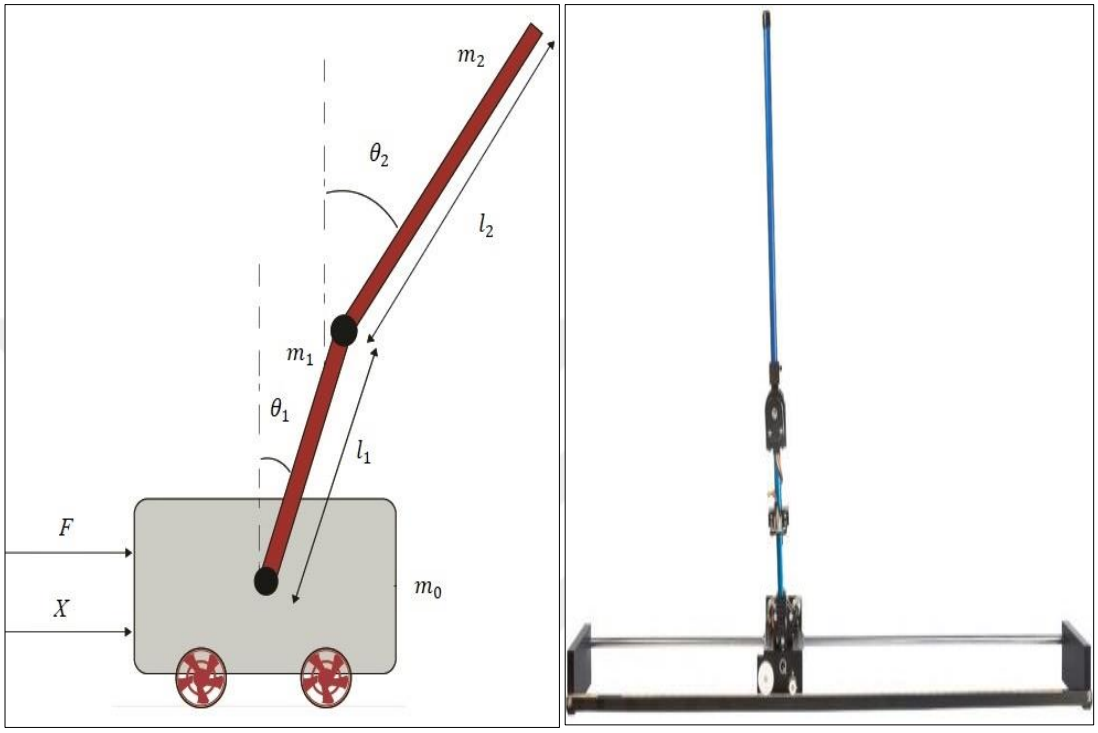

(a) (b)

Figure 1.4. DLRIP: (a) physical model and (b) real experimental implementation [15]

1.2.3. Triple link linear inverted pendulum

A physical model and real experimental example of the TLLIP system are shown in Figure 1.5. The TLLIP consists of three pendulum links of various lengths mounted on the cart. The cart is driven on a rail track by a servo motor. Each pendulum link rotates in the vertical plane about the axis of a position. The system aims to maintain the three pendulum links in the up-ward vertical position [16-17]. TLLIP is an under-actuated system and highly unstable. TLLIP is 4 DOFs with complex dynamic behaviour. The dynamic of the system is highly nonlinear. For this reason, the control of the three links is very complex [18-19]. In Figure 1.5, F is the input force, X is the cart position, θ_1 is the angular position of the first pendulum link, θ_2 is the angular position of the second pendulum link and θ_3 is the angular position of the third pendulum link. L_1, L_2, L_3 are the lengths of the first, second and third links,

respectively. Furthermore, m_0, m_1, m_2 and m_3 are the mass of the cart, first, second and third links, respectively.

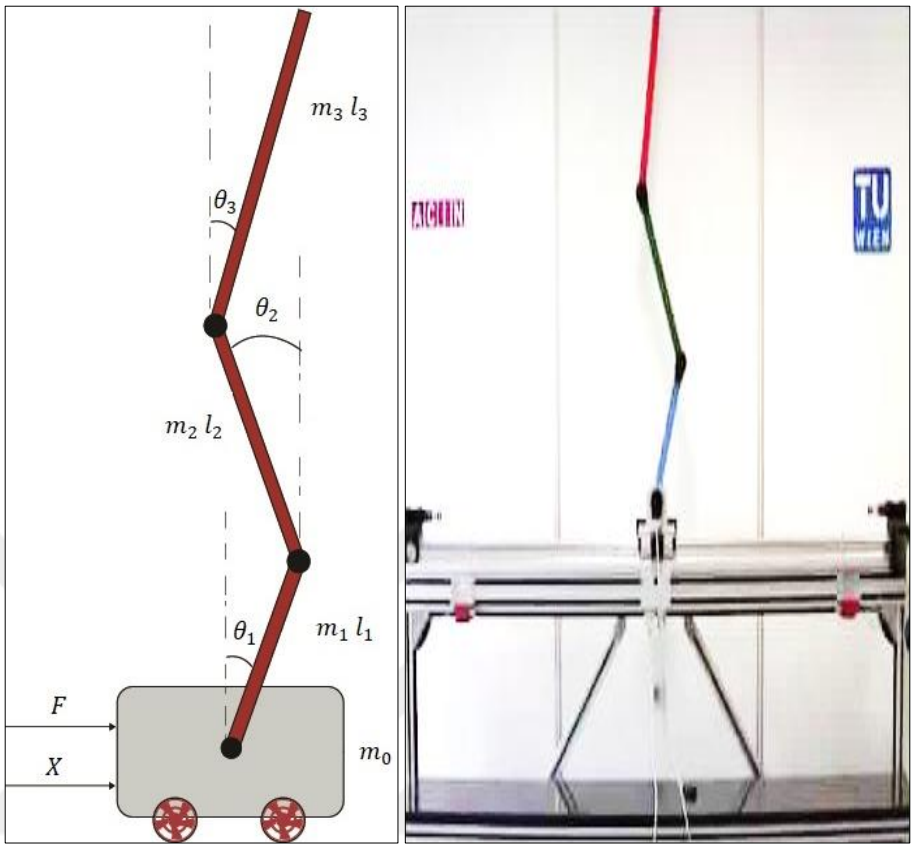

(a) (b)

Figure 1.5. TLLIP: (a) physical model and (b) real experimental implementation [20]

1.2.4. Linear flexible inverted pendulum

Figure 1.6 shows a physical model and real experimental implementation example of a LFIP. LFIP is composed of a flexible pendulum link which moves horizontally by the cart in the X −direction, and a load is attached at the end of the pendulum link. The cart can be driven by a torque servo motor on a rail. The control of the cart motion and inverted flexible pendulum link is assumed by controlling the motor rotation [21]. The main feature of this IPS model, which distinguishes it from other IPS, is that to take into account the large deformations of the pendulum link its length is assumed constant giving rise to a holonomic constraint. The system aims to maintain the flexible pendulum link in the up-ward vertical position [22]. In Figure 1.6 (a), τ is the input torque provided by the servo motor, z is the motion axis of the cart, $\alpha(\theta, X_e)$ is the

deflection of the flexible pendulum link (θ) is the deflection angle and X_e is the deflection length and m is the load mass.

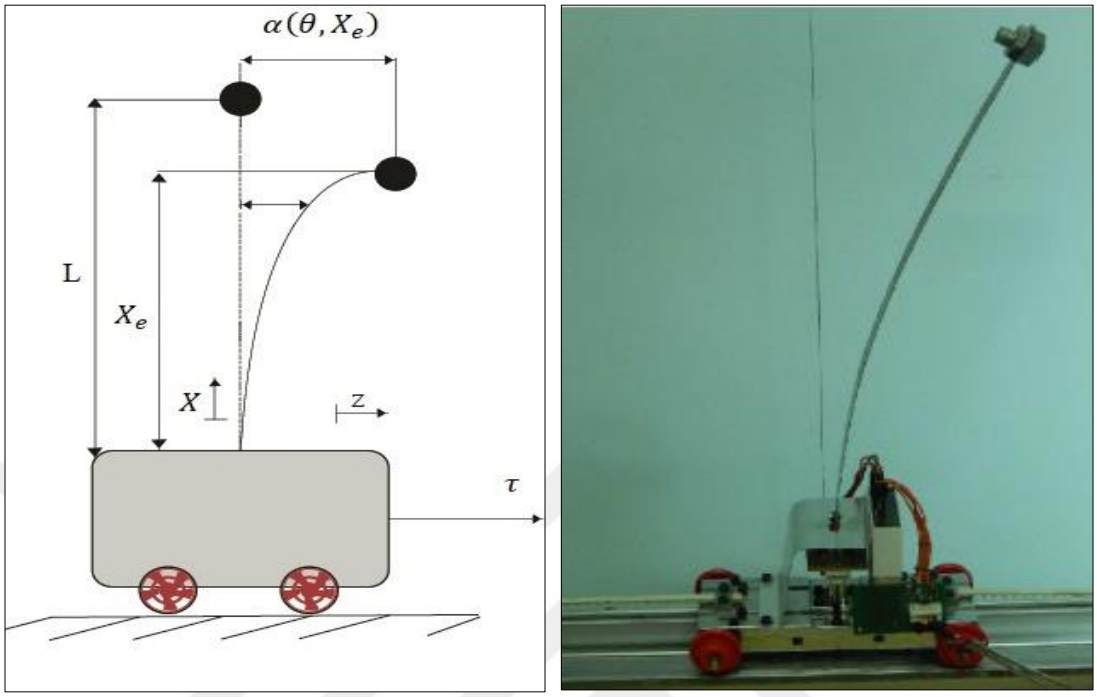

(a) (b)

Figure 1.6. LFIP: (a) physical model and (b) real experimental implementation [22]

1.2.5. Spring-loaded inverted pendulum

The physical model of the SLIP system is shown in Figure 1.7. The SLIP model consists of a point mass attached to a massless leg with a linear spring. SLIP is usually used for analysing running and hopping for a wide range of species. It consists of two phases, the flight and the stance phase. In the flight phase, the point mass follows a ballistic trajectory until the foot touches the ground with a fixed angle. This is known as touchdown and signals the start of the stance phase. At this point, the foot position remains fixed, the spring starts to compress, and the point mass remains moving. When the spring length is equal to the resting spring length, the spring lifts off and enters the flight phase again. The angle makes by the spring with the ground is reset to the original attack angle, that is, the spring is rotated [23-24]. The SLIP was introduced by Blickhan and used as modeling of legged locomotion [25]. In Figure 1.7, m is the mass of the load, k is the stiffness of the spring, L_0 is the length of the spring, and α is the attack angle (control parameter).

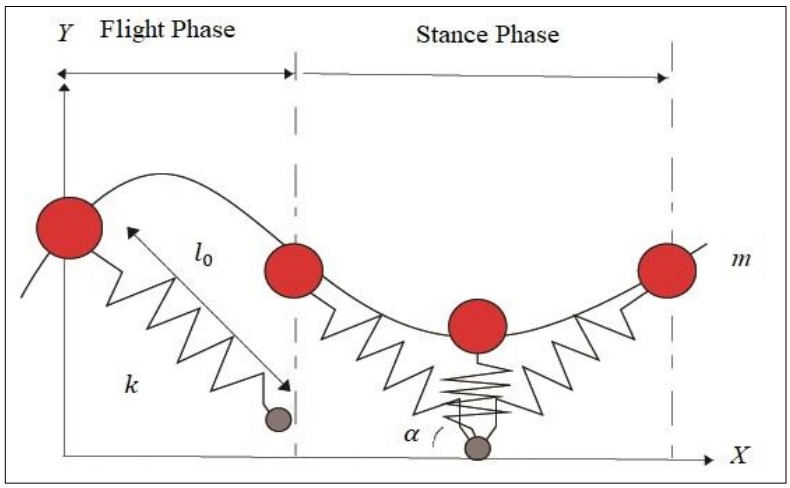

Figure 1.7. Physical model of the standard SLIP system

1.2.6. Variable length inverted pendulum

The VLIP is an underactuated mechanical system with 2DOF with a single input to adjust the length of the pendulum link. VLIP can also be viewed as a model of the child's swing motion. The VLIP is composed of a torque servo-motor used to move the pendulum link in the vertical upward position and a sliding mass mounted to the pendulum link. The aim is to maintain the pendulum link in the upward vertical position on changing the sliding mass position [26-28]. Figure 1.8 shows a physical model of the VLIP.

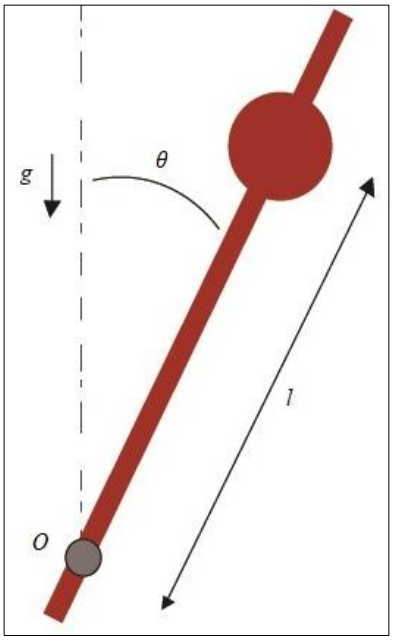

Figure 1.8. Physical model of the VLIP

In Figure 1.8, l is the distance from the center of the sliding mass to the origin of coordinates around which the pendulum link rotates. θ is the angle of the pendulum deviation from the vertical position.

1.3. Single Actuator Linear Parallel IPS

1.3.1. Linear twin inverted pendulum

A physical model and real experimental example of a LTIP are shown in Figure 1.9. The LTIP consists of a straight line rail, a cart moving on the rail, a longer first pendulum link attached to the cart in the right side. Furthermore, a shorter second pendulum link attached to the cart in the left side, and a driving unit. The two pendulum links can rotate freely around their pivots. The aim is to maintain the two pendulum links in the up-ward vertical position [29-31]. In Figure 1.9 (a) the force F applied to cart in objective to balance the two pendulum links on the cart and to maintain θ_1 and θ_2 in a stable position. θ_1, θ_2 are the angle of the first pendulum and second pendulum links, respectively. X refers to the cart position, m_0, m_1, m_2 are the cart mass, the mass of the first pendulum and second pendulum links, respectively. L_1, L_2 are the distance between the joint and the centre of mass of the two pendulum links, respectively.

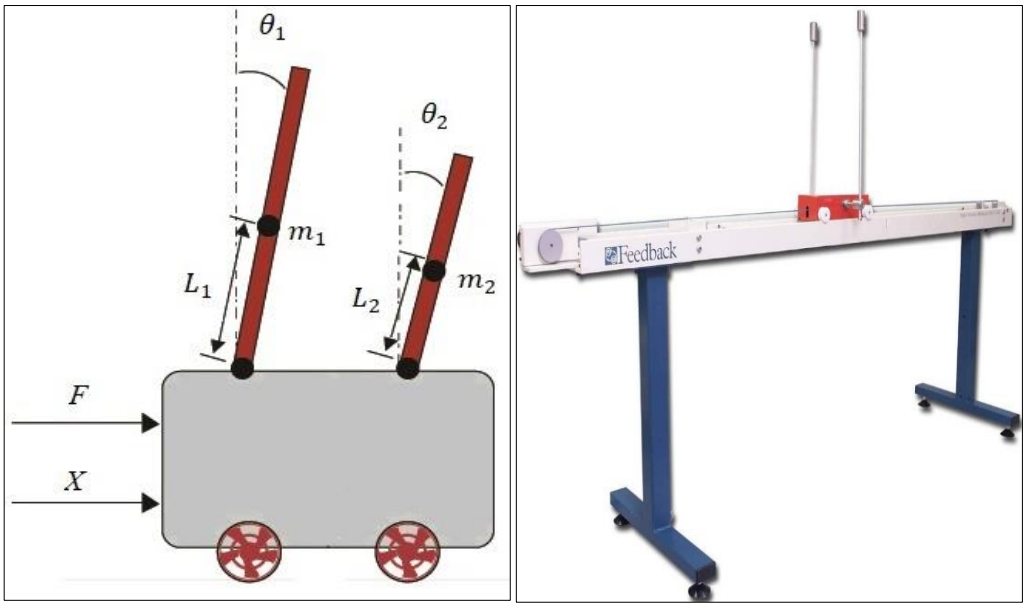

(a) (b)

Figure 1.9. LTIP: (a) physical model and (b) real experimental implementation [32]

1.4. Single Actuator Rotary Serial IPS

1.4.1. Single link rotary inverted pendulum

According to the works existing in the literature, there is another single link pendulum with different mechanical configuration. In this configuration, the motion of the pendulum link is limited to rotate on the vertical plane. Figure 1.10 shows a physical model and real experimental implementation examples of a SLRIP. The pendulum base link is attached to the horizontal arm link via a joint. The rotation axis of the pendulum link is collinear with the axis of the horizontal arm link. The angle of the pendulum link is θ_2. The horizontal arm link is coupled directly to the motor shaft giving it rotary motion. The angular position of the rotary link (horizontal arm) is θ_1. The system input is the torque τ, applied using the motor. The driving force to control the pendulum angle θ_2 come from the rotational arm [33-34]. m_1 and m_2 are the mass of the horizontal arm and the pendulum link, respectively. The first SLRIP system is called "Furuta Pendulum" [35]. The Furuta pendulum system was developed by "Katsuhisa Furuta" at Tokyo Institute of Technology". The Furuta Pendulum is used to experiment with the nonlinear controllers.

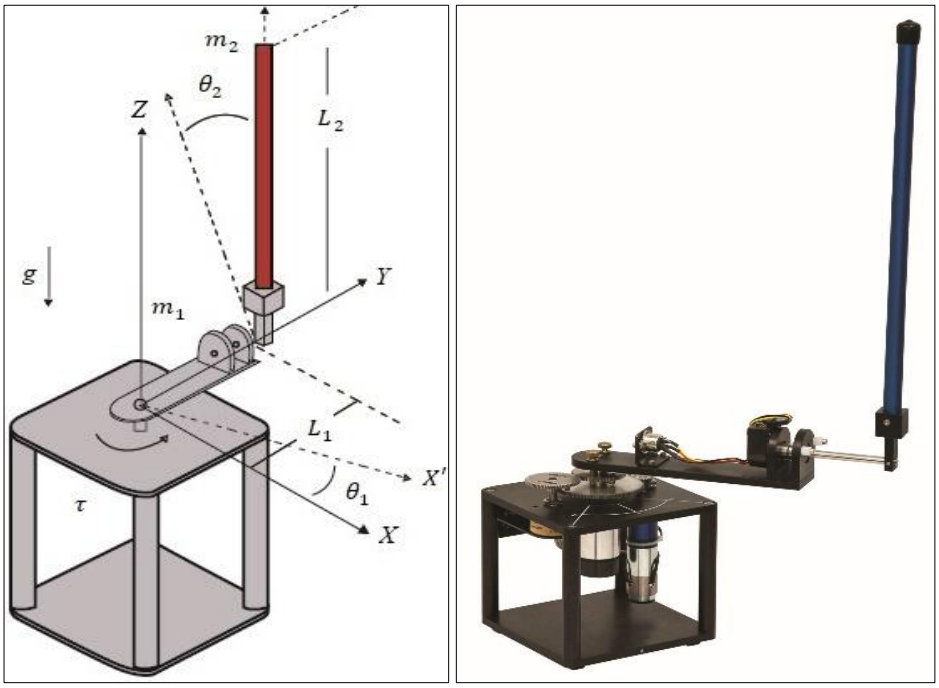

(a) (b)

Figure 1.10. SLRIP: (a) physical model and (b) real experimental implementation [36]

Moreover, based on the works existing in the literature, any number of links may be mounted on the cart or the horizontal rotor arm. Double and three-link systems are observed and demonstrated. For these type of configuration, each link, including the rotary horizontal arm link or cart, has only one DOF.

1.4.2. Double link rotary inverted pendulum

A physical model and real experimental implementation example of a DLRIP are shown in Figure 1.11. DLRIP comprises a horizontal rotary link and two pendulum links. A direct drive brushless DC torque motor servo system is necessary to provide torque to the horizontal arm link to control the system. The rotary arm link rotates in the horizontal plane. The first pendulum link is connected to the extremity of the rotary link and the second pendulum link is connected to the extremity of first pendulum link. The two pendulum links move like an inverted pendulum in a plane perpendicular to the rotary link [37-39]. In Figure 1.11 (a), τ is the input torque motor, θ_0 is the angular position of the horizontal arm, θ_1 is the angular position of the first pendulum link and θ_2 is the angular position of the second pendulum link. L_0, L_1, L_2 are the lengths of the horizontal arm, the first pendulum link and second pendulum link, respectively. Moreover, m_0, m_1 and m_2 are the mass of the horizontal arm, the first pendulum link and second pendulum link, respectively.

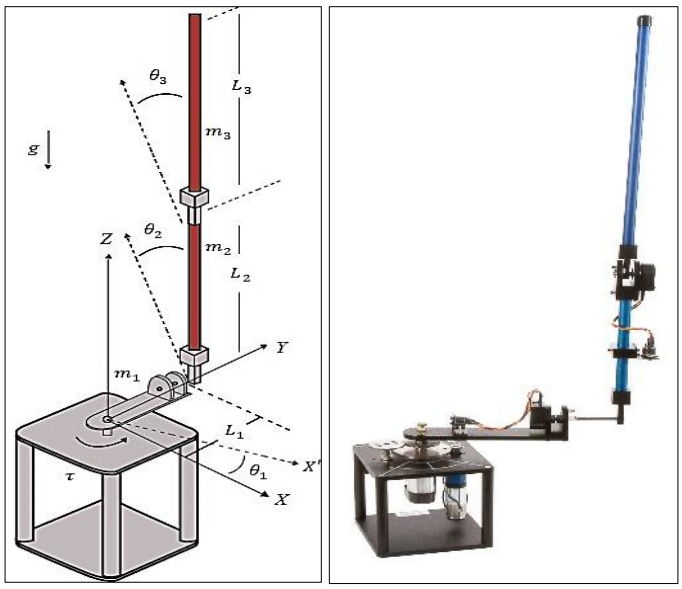

(a) (b)

Figure 1.11. DLRIP: (a) physical model and (b) real experimental implementation [40]

1.4.3. Triple link rotary inverted pendulum

The case studied in this thesis is as the one depicted in Figure 1.12. Figure 1.12 shows examples of a CAD model and real experimental implementation of TLRIP developed in our Laboratory (ARRL) in the Department of Mechatronics Engineering at Kocaeli University. Three hinged links connected in series will be mounted over a horizontal arm which gives the system a rotary motion. The apparatus is commonly named either TLRIP. The TLRIP is composed of a horizontal arm which is controlled by a torque servo motor, attached to the three vertical pendulum links. A balance mass can be mounted on the horizontal arm to maintain the balance inertia of the system. The angle of the horizontal arm link is θ_1 and the angles of three vertical pendulum links are θ_2, θ_3 and θ_4. L_1 is the length from the centre of horizontal arm to the first pendulum link. L_2, L_3, L_4 are the lengths of the first, second and third pendulum links respectively. m_1, m_2, m_3 and m_4 are the mass of the horizontal, first, second and third links, respectively. The three rotary pendulum links have two equilibrium points in the upward and downward positions.

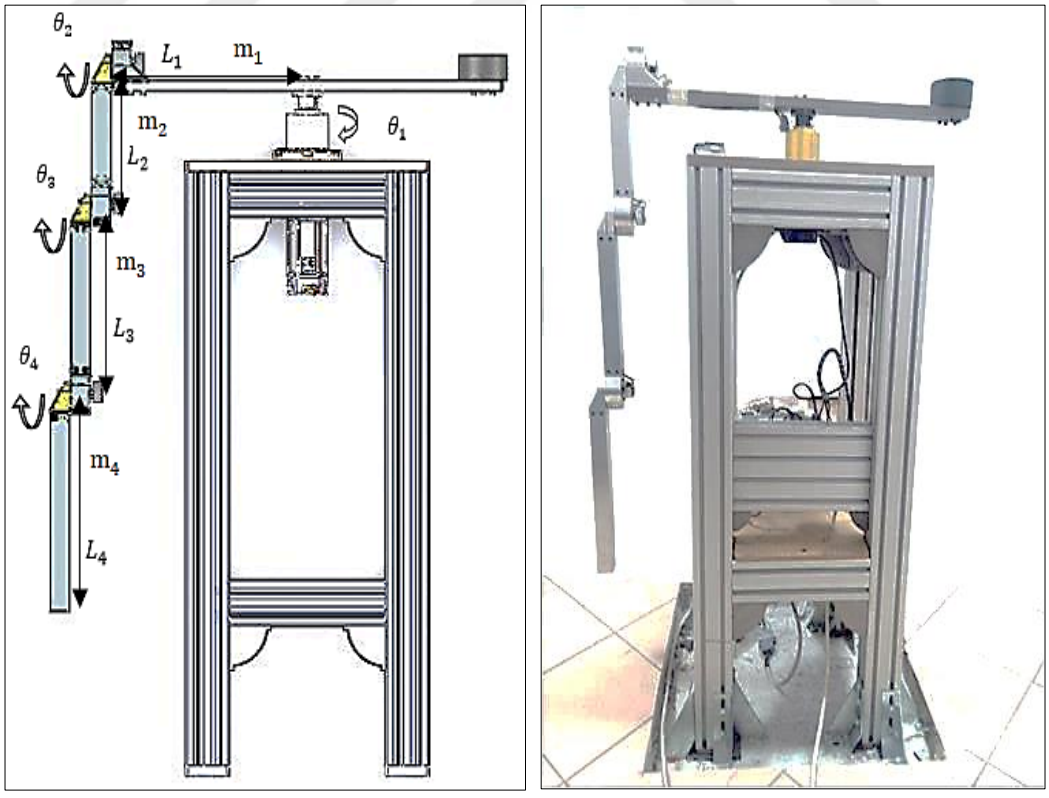

(a) (b)

Figure 1.12. TLRIP: (a) CAD model and (b) real experimental implementation

It is clear from the mechanical construction of the TLRIP that by rotating the horizontal arm from side to side, the angles of the links will be affected. The controller implementation is based on manipulating those angles to make them equal to predetermined angles values. More physical variables parameters should be measured to obtain appropriate information about the system's dynamic behaviour.

1.4.4. Pendubot

In contrast to the TLRIP, the mechanical configuration of the IPS can be rotational with a radial pendulum. This system can be called "Pendubot". A physical model and real experimental implementation example of a Pendubot are shown in Figure 1.13. The angle of the first pendulum link (θ_1) is controlled by a torque motor directly, and the angle of the second pendulum (θ_2) is freely hinged. The second pendulum link moves freely around the first link, and the control objective is to bring the system to the stable equilibrium points [41-43]. Pendubot is used for nonlinear control research, for education in various concepts as nonlinear dynamics, robotics and control system design.

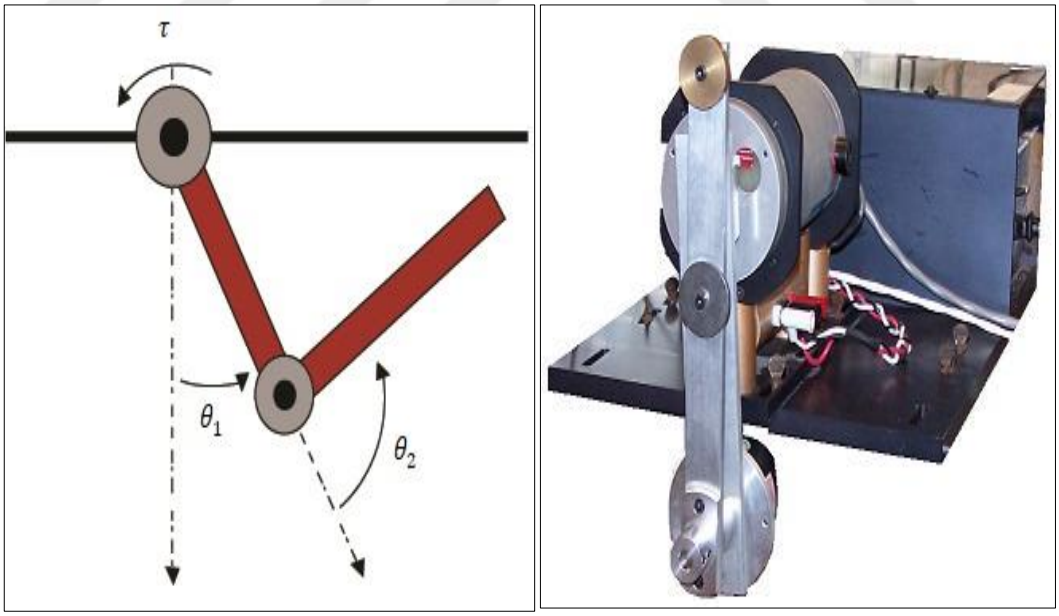

(a) (b)

Figure 1.13. Pendubot: (a) physical model and (b) real experimental implementation [44]

In Figure 1.13, τ is the input torque motor in the first pendulum link. θ_1 and θ_2 are the angular position of the first and second pendulum links, respectively.

1.4.5. Acrobot

Figure 1.14 shows examples of a physical model and real experimental implementation of an Acrobot system. It is a planar two-links robotic arm in the vertical plane. Acrobot has an actuator at the elbow (active joint) but doesn't have actuator at the shoulder (passive joint), and it is working against gravity. The Acrobot system resembles a gymnast on a parallel bar, which controls his motion predominantly by an effort at the waist [45]. The most important control task studied by the Acrobot system is the swing-up control, in which the system must use the elbow torque to move the system into a vertical configuration then balance [46].

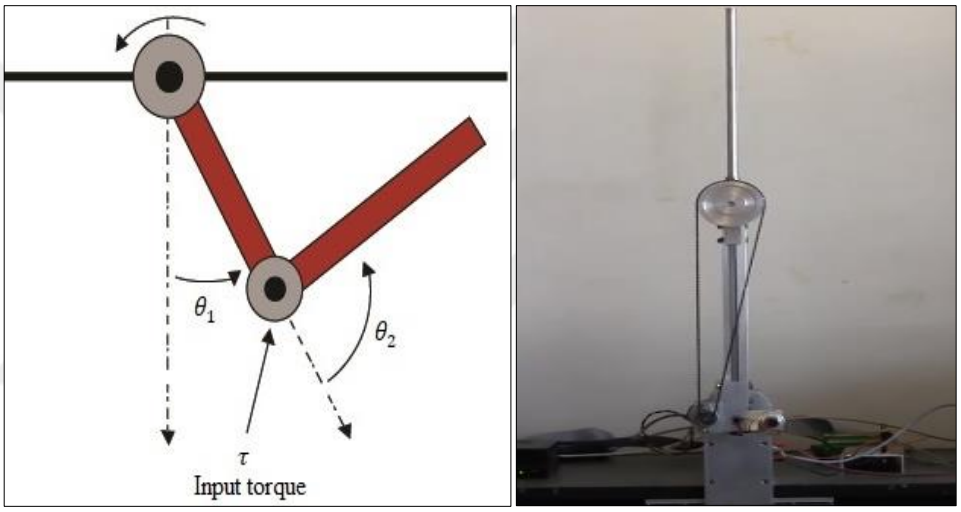

(a) (b)

Figure 1.14. Acrobot: (a) schematic model and (b) real experimental implementation [47]

τ is the input torque motor in the second pendulum joint (active joint). θ_1 and θ_2 are the angular position of the first and second pendulum links, respectively.

1.4.6. Reaction wheel pendulum

RWP is a variant of IPS, was first introduced by Spong [48]. It has a pendulum link which can spin freely around the support point at one of its ends. The RWP have a torque servo motor attached to the extremity of the pivot, acting on a wheel of inertia with which the oscillations of the wheel are controlled, due to the reaction torque τ. The physical model of the RWP system is depicted in Figure 1.15. φ is the angle of the pendulum link in the vertical position. α is the angle between the pendulum and

the wheel. θ is the angle between the vertical axis and the wheel axis. The RWP presents two control problems: the first is to maintain the local stability of the system around the equilibrium position. The second control problem is to swing up the pendulum link from the rest position to the upright vertical position. [49]

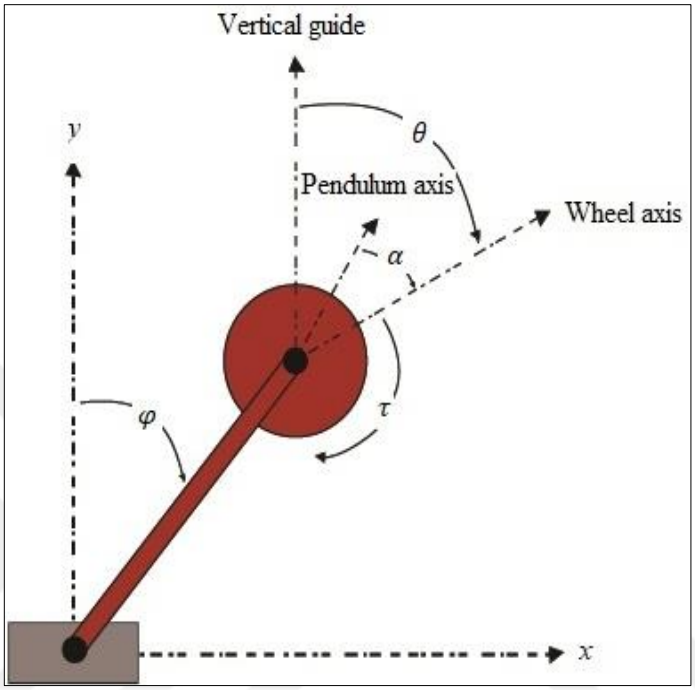

Figure 1.15. Physical model of the RWP

1.5. Single Actuator Rotary Parallel IPS

1.5.1. Rotary twin inverted pendulum

A physical model and example of a real experimental implementation of a RTIP are shown in Figure 1.16. Similar to SLRIP, the RTIP has three parts: rotary horizontal arm, first pendulum link (the long one) and second pendulum link (more short than the first pendulum link). Among them, the rotary horizontal arm is driven by a torque servo motor. The first and second pendulum links are attached to the horizontal arm. The two pendulum links do 2 DOF oscillation in the vertical plane, perpendicular to the horizontal arm, only when they are driven by the horizontal arm. The aim is to stabilise the two pendulum links in the upward position [50-51]. τ is the input torque of applied by the servo motor to the horizontal arm. θ_1 stands for rotation angle of the rotary arm, θ_2 , θ_3 represent the angle of the first and second pendulum deviation from the vertical position, respectively.

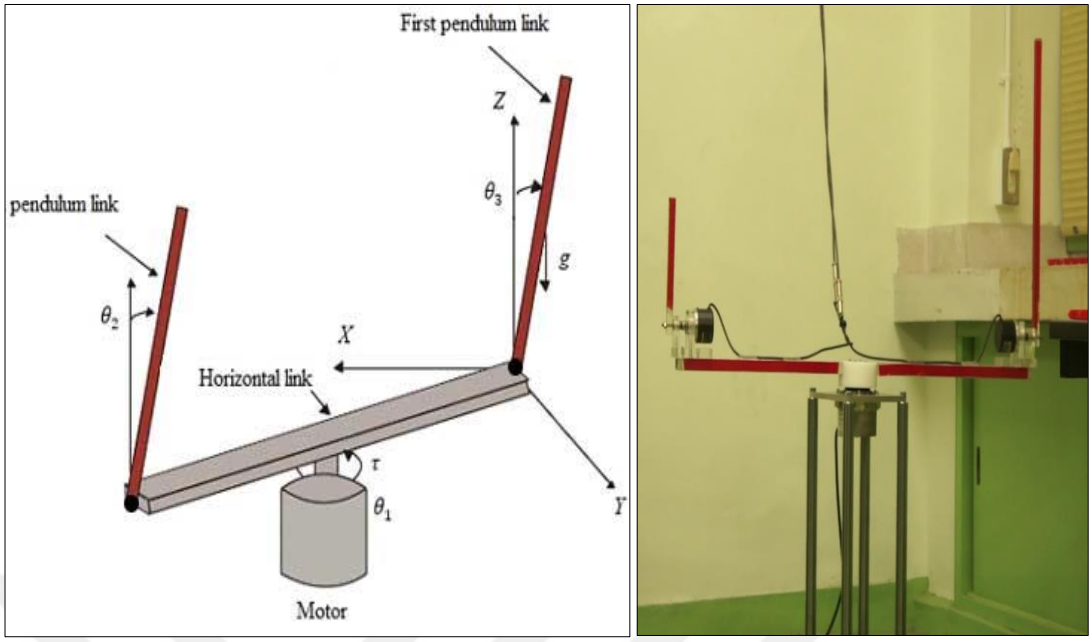

(a) (b)

Figure 1.16. RTIP: (a) physical model and (b) real experimental implementation [52]

1.5.2. Rotary triple link inverted pendulum

The physical model of a RTLIP is depicted in Figure 1.17. The RTLIP has six parts: three rotary horizontal arms, first pendulum link (the long one), second pendulum link (average length), and third pendulum link (the short one). The three rotary horizontal arms are attached to the shaft of the servo motor [51]. The first, second and third pendulum links are attached in the extremity of the three horizontal arms, respectively. The three pendulum links do 3 DOF oscillation in the vertical plane, perpendicular to the horizontal arm, only when they are driven by the horizontal arm [53]. The aim is to stabilise the three pendulum links in the upward position. τ is the input torque applied by the servo motor to the horizontal arm. θ_0 is the rotation angle of the rotary arm. θ_1, θ_2 and θ_3 are the angles of the first, second and third pendulum links, respectively.

1.6. Multi-Actuator Planar IPS

1.6.1. Linear-linear planar inverted pendulum

In some mechanical configuration, the pendulum link can be moved about two axes instead of one axis. The base point of the pendulum link is actuated in 2 DOF, which

form a horizontal plane. These types of configuration are called the Planar Inverted Pendulum (PIP). The PIP referred to as a spatial inverted pendulum, and it is a more complex system compared to the linear and rotary inverted pendulum [54]. A physical model and example of a real experimental implementation of the LLPIP are shown in Figure 1.18. The LLPIP comprises two rails with $X-$axis and $Y-$axis, the cart is driven with two servo-motor in each axis, and a pendulum link. The aim of this system is to stabilise the pendulum link in the upward vertical position [55].

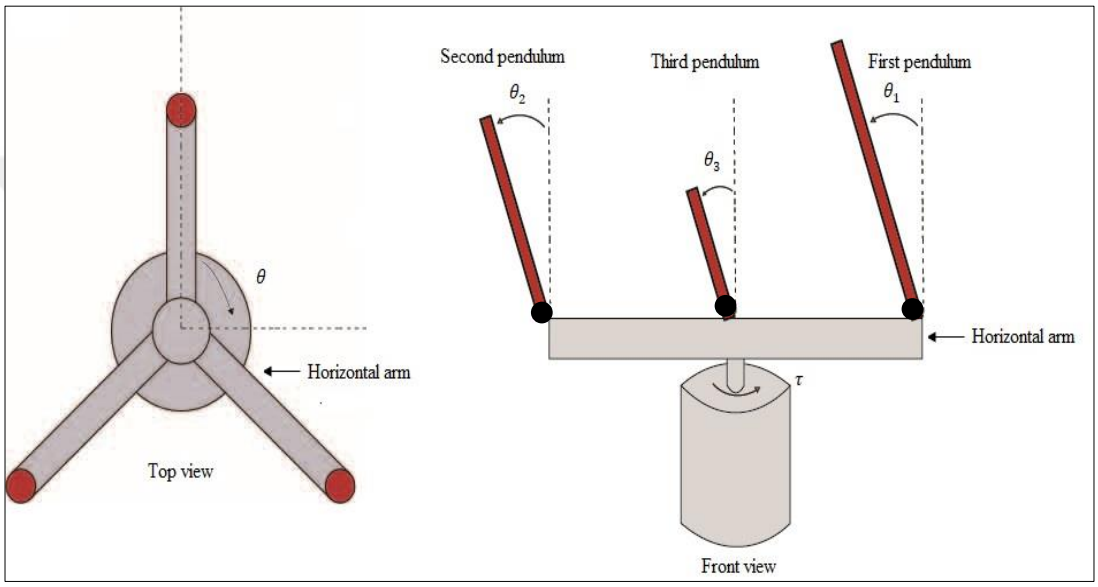

Figure 1.17. A physical model of the RTLIP

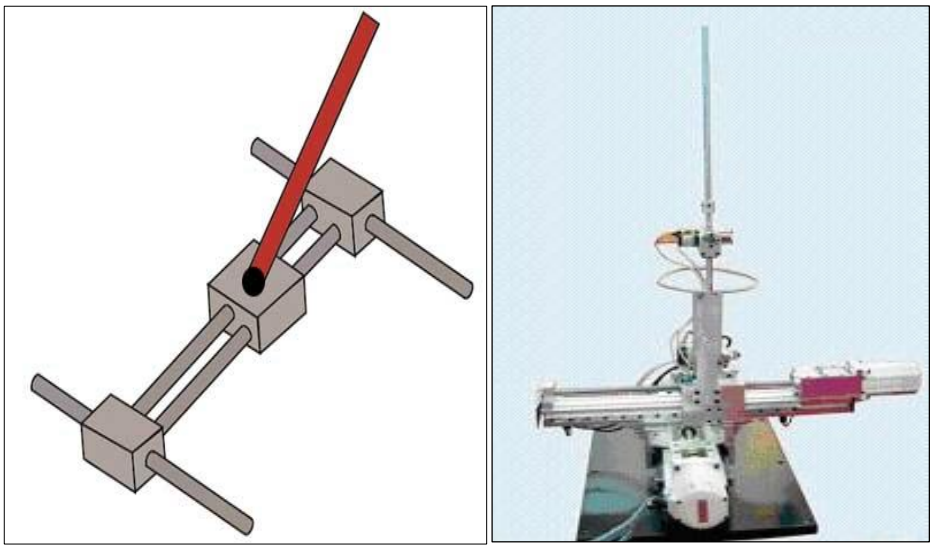

(a) (b)

Figure 1.18. LLPIP: (a) physical model and (b) real experimental implementation [56]

1.6.2. Rotary-rotary planar inverted pendulum

A physical model and 3D example of a RRPIP are shown in Figure 1.19. The RRPIP consists of three main part: two horizontal arms and a pendulum link. The first horizontal arm is connected to the shaft of the servo-motor and allowed to revolute in the horizontal plane. The two horizontal arms are attached with a revolute joint in the extremity, and a servo motor is attached to the joint to provide a torque to rotate it in the horizontal plane. The pendulum link is attached link in joint at the other extremity of the second horizontal arm. [57]

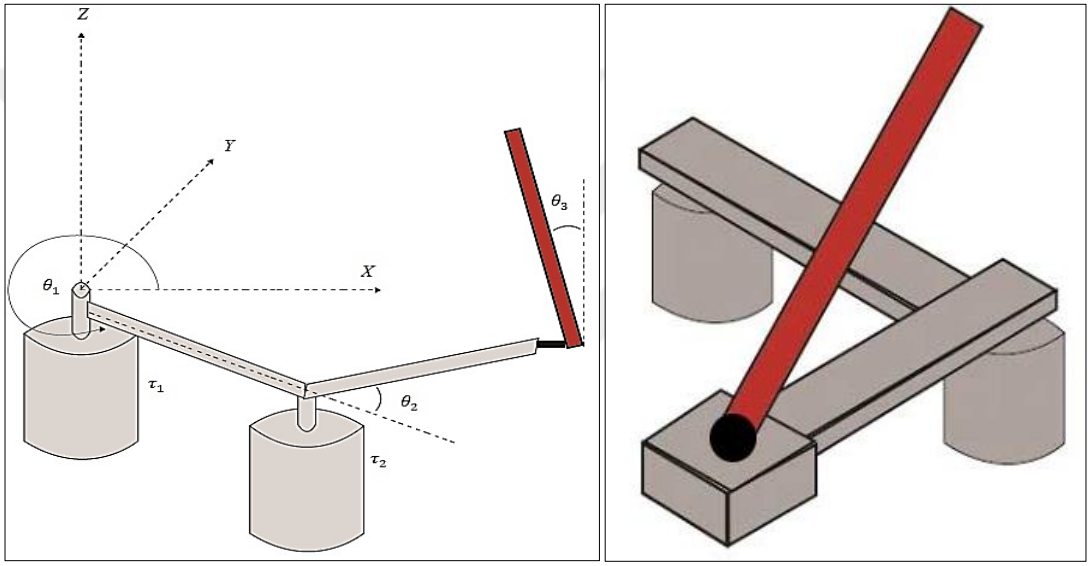

(a) (b)

Figure 1.19. RRPIP: (a) physical model and (b) 3D model

θ_1 is the angular position of the first horizontal arm. θ_2 is the angular position of the second horizontal arm. θ_3 is the angular position of the pendulum link measured with respect to the vertical upright position. τ_1, τ_2 are the input torques in the joints of the first and second horizontal arms, respectively.

1.6.3. Rotary-linear planar inverted pendulum

A 3D model example of a RLPIP is shown in Figure 1.20. The RRPIP is composed of a horizontal arm, and a pendulum link module mounted to the horizontal arm. The mechanism of RRPIP has two different motion inputs (rotational and linear). The horizontal arm is connected with the shaft of the servo-motor and allowed to revolute

in the horizontal plane. Furthermore, the pendulum link moves linearly all along the horizontal arm.

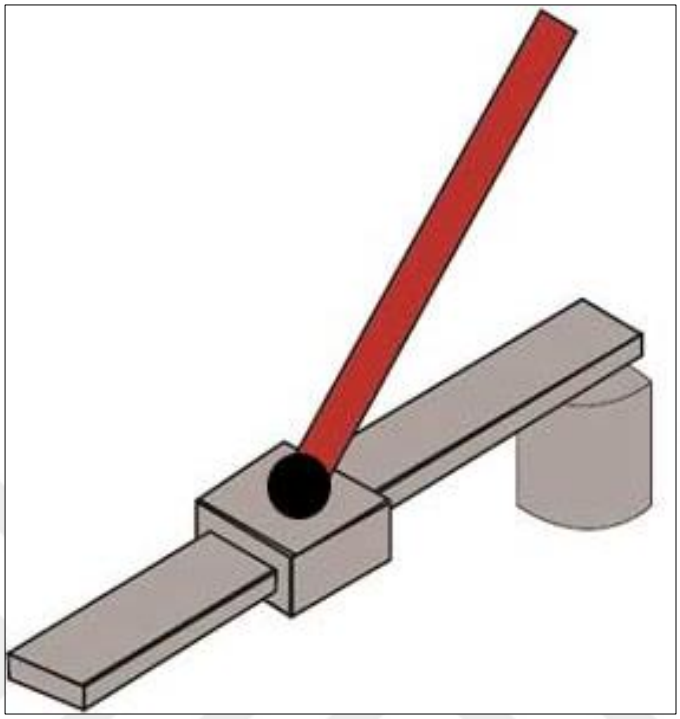

Figure 1.20. A 3D model example of a RLPIP

1.7. Multi-Actuator 3D IPS

1.7.1. Two-wheeled inverted pendulum mobile robot

TWIPMRs are underactuated mechanical systems. They are used in the autonomous robotics, intelligent vehicles, etc…. Mobility and dexterity are the two principal advantages of this type of robots. TWIPMRs are based on the concept of IPS are also known as self-balancing robots, and they are useful used like service robots, human transportation and baggage transportation... etc. TWIPMR has the capability to stand firm with its two wheels (balancing) and make a sharp U-turn (rotation). The research on the TWIPMR is known as the self-balancing robot [58]. The system is inherently unstable and without external control would roll around the wheels' rotation axis and eventually fall. By driving the motors in the right direction returns the system to a stable upward position [59]. The two wheels of the robot are only two points of contact with the ground. TWIPMRs are classified into two class: without input coupling where the actuator is mounted on the wheel, and with input coupling where the actuator is

mounted on the pendulum [60-61]. The first class is more complex in order of mechanical construction, but it is easier in controller design owing to the absence of input coupling between the wheel and pendulum. The second class is easier in order of mechanical construction, but it is more challenging in controller design due to the input coupling between the wheel and the pendulum. A physical model and example of a real experimental implementation of a TWIPMR are shown in Figure 1.21. It is required to balance the pendulum at a zero degrees ($\theta = 0°$) .

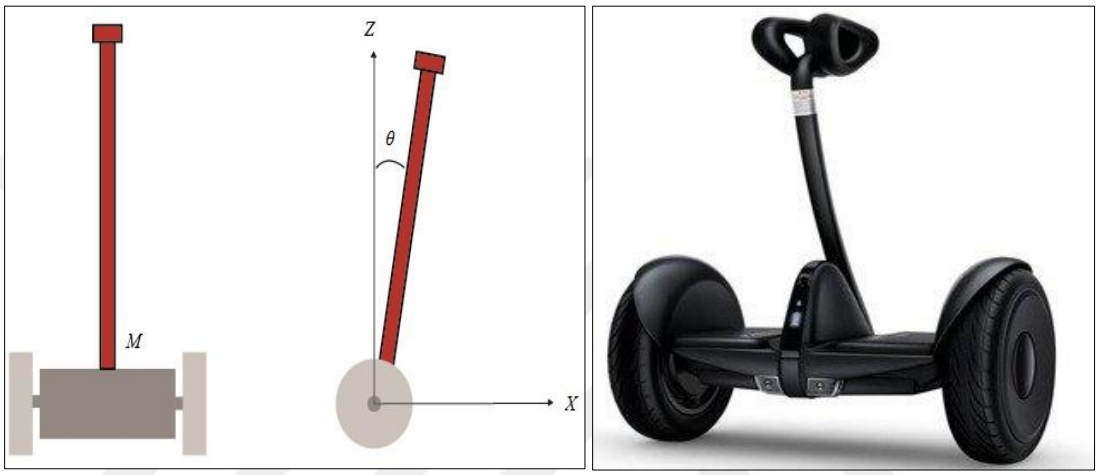

(a) (b)

Figure 1.21. TWIPMR: (a) physical model and (b) real experimental implementation [62]

Furthermore, this type of system can be driven with multi-wheel, called Multi-Wheeled Inverted Pendulum Mobile Robot (MWIPMR)

1.7.2. Quadrotor driven inverted pendulum

Recently, QDIP has attracted much attention in the field of ACE. QDIP is a nonlinear underactuated mechanical system. The system is composed of Quadrotor and an inverted pendulum link mounted on the top of the Quadrotor. The aim is to stabilise the pendulum link in the upward vertical position in the space. QDIP is an 8-DOFs system (Quadrotor have 6-DOFs and the inverted pendulum have 2-DOFs). Linear and nonlinear controllers can be designed to stabilise the whole system. A physical model and example of a real experimental implementation of a QDIP are shown in Figure 1.22. [63]

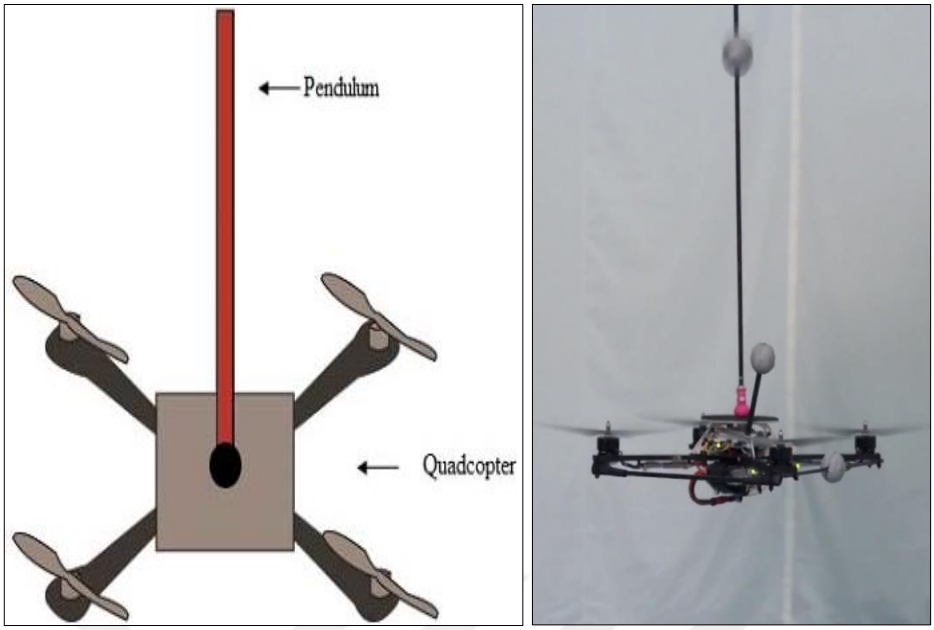

Figure 1.22. QDIP: (a) physical model and (b) real experimental implementation [64]

1.8. Control Methods Used for the IPS

According to the literature reviews, there are two balance points for the IPS. The first balance point is when the pendulums are in the downward position and stable. The second equilibrium point is when the pendulums are in the upward and unstable. Figure 1.23 shows an example of the stable and unstable equilibrium points of a DLLIP.

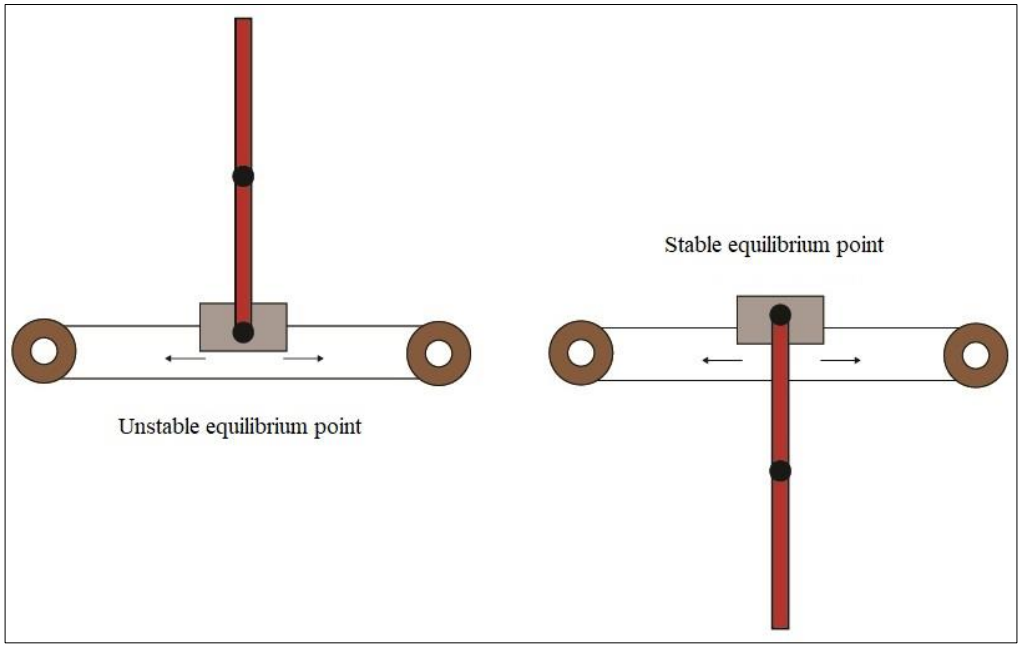

Figure 1.23. Example of the stable and unstable equilibrium points of a DLLIP

Each equilibrium point creates a different control problem. The swing-up control problem consists of swinging of the pendulums from the downward position (stable equilibrium point) to the upward position (unstable equilibrium point) using the input torque provided by a motor. A Linear or nonlinear controller need to be applied to maintain the stability control of pendulums in the upward vertical position. The stability control problem considers the control of the system once it is already in the upward position (unstable equilibrium point). The pendulum links are held in the upward position and stationary by the experimenters while the controller is initialised. Furthermore, the anti-swing control problem exists. Its consists to control the pendulums from the upward position (determined angle position of the pendulum) to the downward position using the torque motor in order to minimise the oscillation and vibration of the pendulum links The anti-swing control method is usefully used for the crane systems. There are three basic control problems in IPS. Moreover, the applied control methods can be different for each model of IPS.

1.8.1. Stabilisation control problem

According to the works existing in the literature, it can be seen that the control methods used for the stabilisation problem are: PID, optimal control, Fuzzy logic and Sliding mode control methods…etc. These methods are the basic methods used to stabilisation control problem of the IPS.

In 1995, D.J. Block et al. [65], are mounted two pendulum links in a fixed place, and only the first pendulum link was driven by a torque motor. It is a concept of a two links underactuated planar revolute robot (Pendubot). The system is used for research and instruction in the field of ACE. The stabilisation problem for the Pendubot is solved by linearising the equations of motion about equilibrium point, and a linear state feedback controller is developed. Furthermore, the partial feedback linearization method is applied to swing up the Pendubot.

In 1996, Li-Xin Wang [66], has developed a stable adaptive fuzzy controller for the tracking application of SLLIP. This technique is used in order to keep the inverted pendulum in an upward position (The unstable equilibrium point). The adaptive fuzzy controller is constructed from a set of fuzzy rules. The fuzzy parameters are adjusted on-line according to some adaptation law for the purpose of controlling the plant to

track a given trajectory. The adaptive fuzzy controllers are used to control the SLLIP to track the trajectory. The simulation results indicate that adaptive fuzzy controllers can perform successful tracking.

In 1996, F. Cheng et al. [67], have developed a high accuracy FLC to stabilise a DLLIP in the upright position. The composition coefficient is gained by combining the fuzzy control theory with the optimal control theory. Thus a high-resolution fuzzy controller is obtained. This controller has verified under a real experimental setup of a DLLIP.

In 1998, K.G. Eltohamy et al. [16], have developed a single-input feedback controller for a TLLIP by using a nonlinear optimisation technique. This technique is necessary because the traditional linear design method cannot incorporate the nonlinear dynamics of the system and its physical limitations. The TLLIP has been successfully stabilised about the vertical upward position through a good understanding of the factors influencing to the control effort. According to obtained results, the linear controller which doesn't look robust enough to achieve stability.

In 2002, J. Aracil, F. Gordillo and J.A. Acosta [68], have developed a technique for obtaining stable and robust oscillations around the upright position in a SLRIP (Furuta pendulum). A control law has been introduced that drives the system to a stable limit cycle. This control law belongs to the family of energy shaping methods. The results have been verified in both simulation and experiment.

In 2010, Nasir et al. [69], have developed a conventional controller PID controller and modern controller Sliding Mode Control (SMC) for a SLLIP. Both control methods are succeeded to control the system for the stabilisation control problem. Moreover, the two controllers are compared according to the time specification performance. The performance of controllers is given based on the simulation results. The result indicates that SMC produced better response compared to the PID control strategy.

In 2010, S. Kizir and Z. Bingül [70], are focused on both stabilisation and swing-up problems for a real experimental setup of a SLLIP. Different controllers are tested using the experimental setup. The FLC is used to swing-up the pendulum. PID controller is used to stabilising the pendulum in the unstable equilibrium point. Furthermore, full status feedback and fuzzy logic methods are successfully applied to

control the pendulum link in the upward position. The robustness of each controller method is verified in both simulation and experimental environment.

In 2012, J. Zhang and W. Zhang [71], have developed an LQR self-adjusting controller to stabilise a planar double inverted pendulum system. LQR self-adjusting controller is based on an optimise factor. Furthermore, the LQR output is refined through the optimise factor. By using this method, the control action exerted on the pendulum is improved. The obtained results indicate that the controller ensured a fast response, good stability and robustness in the different operating conditions applied to the system.

In 2013, B.Li [72], has worked on the stabilisation control problem of a DLRIP in his master thesis. An LQR controller is designed for the system, and its stability analysis is presented in the Lyapunov method. To improve the performance of the LQR controller, a direct adaptive fuzzy control is developed. According to the simulation results of the two control algorithms, the Adaptive Fuzzy Logic Controller (AFLC) can increase the LQR Performance and the robustness of the DLRIP. The simulation results of the two controllers obtained by their comparative analysis indicate that the AFLC is able to enhance the LQR by increasing its robustness in the DLRIP.

In 2013, Glück et al. [20], are focused on both stabilisation and swing-up problems control problems for a real experimental setup of a TLLIP. Nonlinear feedforward controller and optimal feedback controllers are applied for the swing-up problem. A time-variant Riccati controller was developed in order to stabilise the system along the nominal trajectory, and an Extended Kalman Filter (EKF) was used to estimate the no measurable states.

1.8.2. Swing-up control problem

According to the works existing in the literature, it can be seen that the control methods used for the swing-up control problem are generally divided into, feedforward and feedback control, energy shaping, nonlinear model predictive control, and optimum trajectory approaches...etc.

In 1992, K. Furuta et al. [73], have proposed a new bang-bang type state feedback control algorithm which can swing up the pendulum to the vertical upward position.

In the control system, a conventional LQ control method is employed to maintain the pendulum in the unstable equilibrium point. Experimental results have shown that the proposed method is robust for parameter uncertainties of the controlled system computing with feedforward control.

In 1993, M. Yamakita, K. Nonaka and K. Furuta [74], have proposed a method to transfer a state of a double pendulum from a stable equilibrium point to an unstable equilibrium point. The proposed method is applied to real experimental implementation DLRIP. The proposed method is effective for the swing-up control problem. A learning control method is used to modify feedforward control. The proposed method is a combination of feedforward and feedback controls. The control is not robust when feedforward control is used, and the learning process should be repeated if the system parameters are changed.

In 1995, M. Yamakita, M. Iwashiro, Y. Sugahara and K. Furuta [75], have proposed robust methods to swing up a double pendulum links from one equilibrium to the others. Two types of control methods are developed for the swing-up control. One is a control method based on the energy function, and the other is a method based on the control, which makes a limit cycle in the system stable. The proposed methods are effective for a real experimental implementation DLRIP.

In 1997, S. Yasunobu and M. Mori [76], have proposed a fuzzy controller based on formulated human's control strategy. It was applied to a SLLIP. This controller is applied to an inverted pendulum link which has unknown parameters. The swing-up control and the stabilisation control are modelled using FLC. The effectiveness of the fuzzy control method by human control strategy was verified in both simulation and experimental environments.

In 2000, K.J Aström and K. Furuta [77-78], have studied the swing-up strategy based on the energy control method applied to a SLRIP. Simulation results of different situations are explained.

In 2002, J. Rubi, A. Rubio and A. Avello [79], are studied the swing-up problems for a DLLIP. A technique to design controlled trajectories for nonlinear underactuated mechanisms is developed. The reference trajectory is obtained as a result of the

optimisation of an initial trajectory defined through interpolation by splines. This reference is tracked using a gain scheduling linear-quadratic optimal controller specifically designed for the reference trajectory. Simulation and the experimental results confirm the validity of this approach.

In 2007, Graichen et al. [80], are studied the swing-up and the stability problems for DLLIP. A nonlinear feedforward is used for the swing-up problem. Further, a linear feedback controller is used for the stabilisation control problem. The two controllers are verified in a real implementation of a DLLIP.

In 2014, P. Jaiwat and T. Ohtsuka [81]**,** have studied the swing-up strategies based on the nonlinear model predictive control for DLLIP. The nonlinear model predictive controller is verified in both simulation and real experimental environments.

1.8.3. Anti-swing control problem

According to the works existing in the literature, the control methods used for the anti-swing control problem are generally nonlinear controllers.

In 1998, Ho-Hoon Lee [82], propose a new dynamic model of a 3-D crane system, it is derived based on a newly defined 2DOF swing angle. For the anti-swing control problem, a decoupled control scheme based on the dynamic model linearised around the stable equilibrium point is developed. The theoretical and experimental results show that the proposed control scheme guarantees both rapid damping of load swing and accurate control of crane position and rope length with excellent transient responses for the practical case of simultaneous travelling, traversing, and slow hoisting motions.

In 2000, B. Vikramaditya and R. Rajamani [83], have proposed a nonlinear trajectory tracking controller for a crane system. The state equations of the system are highly nonlinear and closely coupled with more DOFs than the number of independent actuators available. A modified sliding-surface formulation was developed to design the controller. Theoretical bounds were established for tracking the performance of the controller. Stability of the control system has been demonstrated both to random initial conditions and parameter variations while meeting the desired trajectory tracking performance specifications.

In 2006, Cheng-Yuan Chang et al. [84], have proposed an enhanced adaptive sliding mode fuzzy approach witch applied to control the position and load swing of a 3-D overhead crane system. This method includes the robustness and model-free properties of the sliding mode and fuzzy logic controllers, respectively. An adaptable slope of the sliding surface is given, and the chattering phenomenon of the sliding mode controller is discussed to enhance the control performance. Moreover, this work provides a compensating algorithm to the control dead zone of an overhead crane system. The simulation results demonstrate the effectiveness of this method.

In 2010, MI. Solihin et al. [85], have developed a Fuzzy-tuned PID controller for a robust anti-swing controller applied to a crane system. The proposed Fuzzy-tuned PID utilises fuzzy system as PID gain tuners to achieve robust performance to parameters' variations in the gantry crane. The experimental results show that the proposed anti-swing controller has a satisfactory performance. Besides, the proposed method is straightforward in the design.

In 2017, Zhongcai Zhang et al. [86], have proposed flatness-based regulation controllers for the anti-swing of crane system. The anti-swing and high-speed positioning problems are considered for constant cable length crane and varying cable length crane, respectively. Furthermore, nonlinear feedback control and a combined application of finite-time control and Lyapunov-based control are used to facilitate the development of the proposed control laws, which, unlike the traditional energy-based control law, is designed in a much simpler manner.

1.9. Application Fields of the IPS

IPSs have a wide range of applications. The design and development of these systems are increasing each day. The pendulum systems were started to be used in the 1650s, witch the first pendulum structure was integrated into the clock structure. Figure 1.24 shows an example of pendulum clocks. The movement mechanism of the system depends on the oscillation of the pendulum processing, and it is used as a simple time counting tool.

Figure 1.24. Example of a pendulum clock

Furthermore, balance problems are similar to a simplified IPS problem. Balancing systems are used in the robotic field, and they have been developed according to the IPS. Additionally, the control problem in the industrial robot arms is similar to the control problem of an IPS, such as the control problem of crane systems which used to carry loads with minimal oscillation. The oscillation that occurs on the crane decreases transport efficiency. Therefore, it is important to solve the swing control problem. The solution to this problem is considered as the solution to the pendulum problem. Hence, the control principle of the IPS has a wide place in the crane system. An example of a gantry crane system is shown in Figure 1.25.

Finally, one of the most famous applications of the IPS that is commercially available is the Segway system, as shown in Figure 1.26. Segway system is a mobile IPS. It has been paid attention due to mobility whose structure is a combination of an IPS and a wheeled mobile robot. Segway is a typical mobile pendulum a transportation system that has been commercialised to carry a human.

Figure 1.25. Example of a gantry crane system

According to the above applications with many more render the IPS of great importance for engineers. This is the main reason why IPS is chosen frequently for testing new developed control methods. Furthermore, the construction of IPS in a university laboratory is relatively easy. Many universities afford the necessary equipment for testing the developed control methods in real-time, making it easier for students to engage in the problem. Overall, it can be seen that IPSs are a problem that is highly applicable in everyday applications.

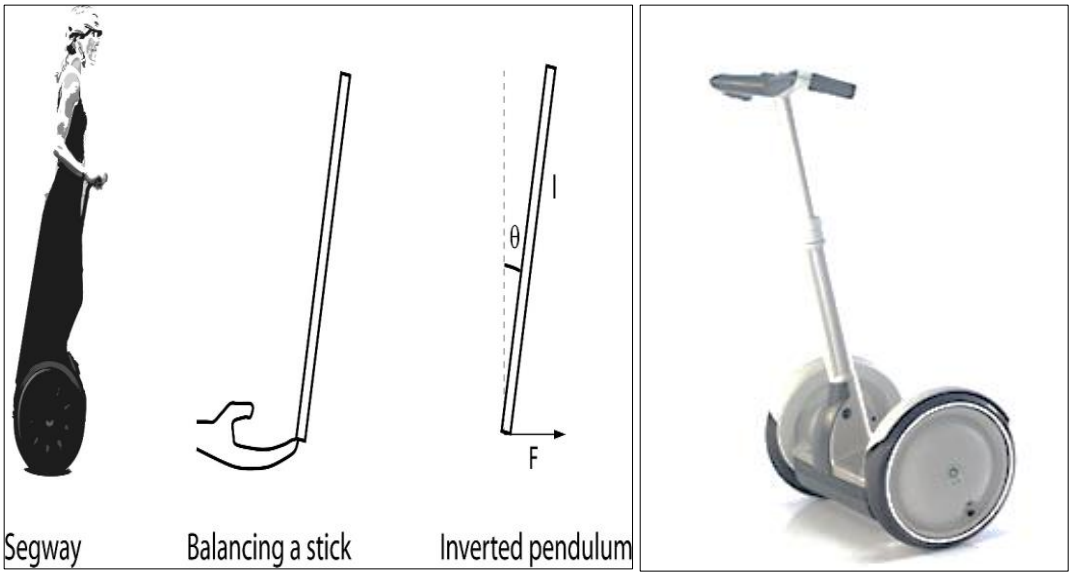

Figure 1.26. Segway system [150]

1.10. Objectives and Contributions of the Thesis

The main objective of this research is to develop an anti- swing up control of a single, double and triple link rotary inverted pendulum with nonlinear friction models. TLRIP system has been developed in the ARRL, in the Mechatronics Engineering Department part of the Faculty of Engineering at Kocaeli University. In reality, the control of three pendulum links attached to a rotary horizontal link seems to be impossible. But nowadays, according to computer control power, can give the ability to balance three or more pendulum links. The system can be used in classrooms demonstration and departmental exhibits. Physically, the system must be robust enough to permit people to attempt balancing the pendulum manually to give them a better idea about the degree of difficulty applied in the control method phase. The system is a highly nonlinear and open-loop unstable system that makes control more challenging. It is an intriguing subject from the control point of view due to its intrinsic nonlinearity. On the other hand, the system includes a nonlinearity caused by the existing frictions in the joints. Common control approaches require a good knowledge of the frictions in the system's joints and accurate friction estimation to obtain desired performances of feedback controllers. However, the frictions have high nonlinear values resulting in steady-state errors, limit cycles, and poor performance of the system [93]. It has an influence on the system's response that must be taken seriously. Moreover, friction estimation ameliorates the system's quality and dynamic. In this project, NFFEMs are developed to estimate the joint friction coefficients in our system and compared with AFEMs. The different versions of AFEMs and NFFEMs are generated based on each of the following friction estimation models: NCFM, LFM, and NLFM. This study aims to obtain joint friction models that depend on both velocity and acceleration in a large range of motion trajectory that involves difficult and sudden large changes. Additionally, two different control problems are studied for this system, stability and anti-swing control problems. For the stabilisation control problem of the system, nonlinear controllers such as FLQR and FLQG are developed. The FLQR and FLQG controllers were compared to the LQR and LQG based on the response parameters of controllers and robustness analysis under internal, external and noise disturbances. For the anti-swing control problem of the system, a nonlinear RBNF-LQR controller is developed. The RBNF-LQR is compared with FLQR and the LQR controllers.

Moreover, the anti-swing controllers' performances were compared based on robustness analysis under external disturbance. The anti-swing control of system with NLFMs are verified in real experimental setup. The contributions of this thesis can be summarized as follows:

- A detailed review of the IPSs based on their actuator configuration and motions type.
- The complex nonlinear dynamics models of the SLRIP, DLRIP and TLRIP are derived using the Euler-Lagrange formulation, explained in detail in chapter 2.
- All friction models existing in the literature depend only on velocity. However, the friction model developed here depends on both velocity and acceleration. This approach has enabled us to obtain a two-dimensional friction model.
- The coefficients of all friction models in the literature were constant when the physical quantities change. On the other hand, the coefficients of the friction models in this thesis vary depending on the state of the velocity and acceleration. Hence, this friction model allows for better estimation of the effects of friction in different velocity and acceleration conditions.
- Much of existing papers in the literature have studied only the frictions of the linear motion which depends on linear velocity and force. This thesis examines frictions on the joints which have hard rotational motions.
- In this thesis, a nonlinear FLQR and FLQG controllers are developed to stabilise the pendulum links of the system in the upward vertical position. In order to obtain the desired angular position of pendulums with a better dynamic response, compared to the classical LQR and LQG controllers, the fuzzy controllers were combined with the LQR and LQG in objective to adjust the closed-loop controller feedback gains, respectively.
- Nonlinear RBNF-LQR controllers are developed for an anti-swing control of the system. In the proposed RBNF-LQR controllers, the positions and velocities of state variables multiplied by their LQR gains are trained by using two RBNNs architecture. The output of the two RBNNs are used as the input variables of the fuzzy controller. The novel architecture of the RBNF controller is developed in order to obtain better control performance than the classical ANFIS.

2. SYSTEM MODELING AND DYNAMIC SIMULATION

In this chapter, kinematic, nonlinear dynamic models and Jacobian matrix of each model (SLRIP, DLRIP and TLRIP) are explained in details. The kinematic parameters of each model are described corresponding to its design. The kinematics model was derived using an adaptation of the DH convention. The nonlinear dynamics model was derived based on the Euler-Lagrange formulation. Furthermore, rotation and transformation matrices of the kinematics model are used to determine the dynamic model. Additionally, the Jacobian matrix of each system is calculated, which used to estimate the parameters of the system. To verify the mathematical model of each system, a numeric model is developed using the Matlab/SimMechanics toolbox. A comparison of the pendulum joint positions obtained from the mathematical and Matlab/SimMechanics model of each system are explained. Finally, in order to examine the effects of the inertia of the three pendulum links, the dynamic equations of the TLRIP were solved and simulated in three different inertia cases.

2.1. Modeling of the SLRIP

2.1.1. Kinematic model of the SLRIP

Solid 3D model and kinematics parameters of the SLRIP are shown in the Figure. 2.1. The SLRIP comprises a horizontal rotary link and one pendulum link. A direct drive brushless DC torque motor servo system is mounted to provide torque to the horizontal arm link to control the system. The rotary arm rotates in the horizontal plane. The pendulum link is connected to the extremity of the rotary link. The pendulum link moves as an inverted pendulum in a plane perpendicular to the rotary link. A balance mass is attached to the other extremity of the horizontal arm to maintain the balance inertia of the system. The angle of the rotary link (θ_1) and the angles of the pendulum links (θ_2) of the SLRIP are illustrated in Figure 2.1. The SLRIP is assumed to be a serial kinematic chain. The kinematic model of the system is derived based on the DH convention [87]. Rotation and homogeneous transformation matrices between coordinates the SLRIP are calculated. The parameters and variables of the model are

given in Table 2.1. The physical parameters of the SLRIP are given in Table 2.2. DH Parameters of the SLRIP are given in Table 2.3.

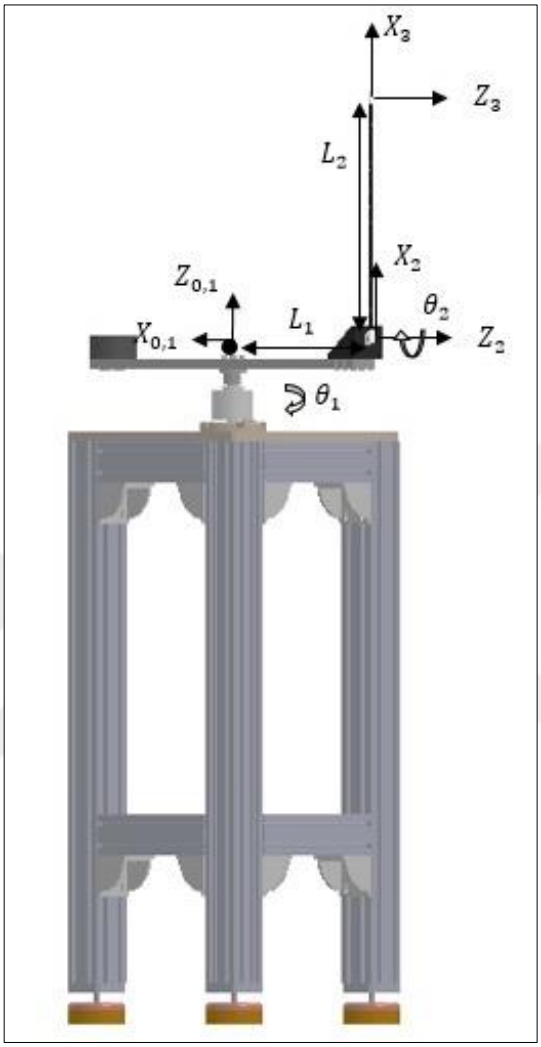

Figure 2.1. Solid 3D model and kinematic parameters of the SLRIP

Table 2.1. Parameters and physical variables of the system

Symbol	Description	Unit
θ_i	The angle of the i-th link.	[rad]
τ_i	Torque for the i-th link.	[Nm]
I_1	Inertia tensor of i-th link.	$[kg \cdot m^2]$
I_{zzi}	Z-component of the inertia tensor of i-th link.	$[kg \cdot m^2]$
m_i	Mass of i-th link.	[kg]
m_B	Mass of balance mass.	[kg]
L_i	Length of i-th link.	[m]
b_i	Viscous damping coefficient of i-th link.	[N-m-s/rad]
g	Gravity	$[N \cdot kg^{-1}]$

${}^{i-1}_{i}T$ denotes a homogeneous transformation matrix from a coordinate attached to an *i*-th link to a coordinate attached to i-1-th link, $i = 1,2,3,4$. ${}^{i-1}_{i}T$ is given in equation (2.1). [88]

Table 2.2. Physical parameters of the SLRIP

Parameters	Values	Parameters	Values	Parameters	Values
m_1	3.1129 [kg]	L_1	0.44 [m]	I_{zz2}	0.0025 [kg · m^2]
m_2	0.08 [kg]	L_2	0.526 [m]	$b_{1,2}$	0.0024 [N-m-s/Rad]
m_B	3.1469 [kg]	I_{zz1}	0.4398 [kg · m^2]	g	9.81 [N kg^{-1}]

Table 2.3. DH-Parameters of the SLRIP

Coordinate	α_{i-1}	a_{i-1}	d_i	θ_i
1	0	0	0	θ_1
2	$-\frac{\pi}{2}$	0	L_1	$\theta_2 - \frac{\pi}{2}$
3	0	L_2	0	0

$$ {}^{i-1}_{i}T = \begin{bmatrix} \cos\theta_i & -\sin\theta_i & 0 & a_{i-1} \\ \sin\theta_i \cos a_{i-1} & \cos\theta_i \cos a_{i-1} & -\sin a_{i-1} & -\sin a_{i-1}\, d_i \\ \sin\theta_i \sin a_{i-1} & \cos\theta_i \sin a_{i-1} & \cos a_{i-1} & \cos a_{i-1}\, d_i \\ 0 & 0 & 0 & 1 \end{bmatrix} \tag{2.1} $$

The homogeneous transformation matrix of the SLRIP is derived in equation (2.2) using the DH-parameters in Table 2.3.

$$ {}^{0}_{3}T = {}^{0}_{1}T\,{}^{1}_{2}T\,{}^{2}_{3}T \tag{2.2} $$

Where

$$ {}^{0}_{1}T = \begin{bmatrix} \cos\theta_1 & -\sin\theta_1 & 0 & 0 \\ \sin\theta_1 & \cos\theta_1 & 0 & 0 \\ 0 & 0 & 1 & 0 \\ 0 & 0 & 0 & 1 \end{bmatrix} {}^{1}_{2}T = \begin{bmatrix} \sin\theta_2 & \cos\theta_2 & 0 & 0 \\ 0 & 0 & 1 & L_1 \\ \cos\theta_2 & -\sin\theta_2 & 0 & 0 \\ 0 & 0 & 0 & 1 \end{bmatrix} \tag{2.3} $$

$$ {}^{2}_{3}T = \begin{bmatrix} 1 & 0 & 0 & L_2 \\ 0 & 1 & 0 & 0 \\ 0 & 0 & 1 & 0 \\ 0 & 0 & 0 & 1 \end{bmatrix} \tag{2.4} $$

$$ {}^{0}_{3}T = \begin{bmatrix} \sin\theta_2 \cos\theta_1 & \cos\theta_2 \cos\theta_1 & -\sin\theta_1 & L_2 \cos\theta_1 \sin\theta_2 - L_1 \sin\theta_1 \\ \sin\theta_2 \sin\theta_1 & \cos\theta_2 \sin\theta_1 & \cos\theta_1 & L_1 \cos\theta_1 + L_2 \sin\theta_1 \sin\theta_2 \\ \cos\theta_2 & -\sin\theta_2 & 0 & L_2 \cos\theta_2 \\ 0 & 0 & 0 & 1 \end{bmatrix} \tag{2.5} $$

The position vector is given from the calculated homogeneous transformation matrix ${}^{0}_{3}T$, as follows:

$$ \begin{bmatrix} P_x \\ P_y \\ P_z \end{bmatrix} = \begin{bmatrix} L_2 \cos\theta_1 \sin\theta_2 - L_1 \sin\theta_1 \\ L_1 \cos\theta_1 + L_2 \sin\theta_1 \sin\theta_2 \\ L_2 \cos\theta_2 \end{bmatrix} \tag{2.6} $$

2.1.2. Dynamic model of the SLRIP

The nonlinear motion equations of this system are derived based on the DH convention. The nonlinear equations of the RIPS may be given in a matrix form, given in equation (2.7): [89]

$$ D(\theta)\ddot{\theta} + C(\theta, \dot{\theta}) + G(\theta) = \begin{bmatrix} \tau_1 \\ 0 \\ 0 \end{bmatrix} \tag{2.7} $$

Where the vector of joint positions is θ, the vectors of angular velocities is $\dot{\theta}$, and the vector of angular accelerations is $\ddot{\theta}$. $D(\theta)$ is the mass matrix, $C(\theta, \dot{\theta})$ is Coriolis and Centripetal force vector, $G(\theta)$ is the gravity vector and τ_1 is the torque input in the horizontal link. The dynamic equations of RIPS are derived using the "Euler-Lagrangian" method [90]. The terms of the mass matrix are calculated using equation (2.8)

$$ D(\theta) = \sum_{i=1}^{n} [(A_i)^T m_i A_i + (B_i)^T I_i B_i] \tag{2.8} $$

m_i is the mass of i-th link; $I_i \in R\,3 \times 3$ is the link inertia tensor with respect to the frame attached at the link centroid and parallel to the corresponding attached frame.

A_i and $B_i \in R\ 3\times n$ are Jacobian matrices. The terms of Coriolis and Centripetal vector are calculated using the equations as follows:

$$C(\theta,\dot{\theta}) = \sum_{k=1}^{n}\sum_{j=1}^{n}\left[c_{kj}^{i}(\theta)\dot{\theta}_k\dot{\theta}_j\right] \tag{2.9}$$

$$c_{kj}^{i}(\theta) = \frac{\partial}{\partial\theta_k} D_{ij}(\theta) - \frac{1}{2}\frac{\partial}{\partial\theta_i} D_{kj}, 1 \le i,j,k \le n \tag{2.10}$$

The gravity vectors can be calculated using equation (2.11)

$$G(\theta) = -\sum_{k=1}^{n}\sum_{j=1}^{n}\left[g_k\, m_j\, A_{ki}^{j}(\theta)\right] \tag{2.11}$$

The elements of each matrix calculated are calculated as follows. Δ_{h_1} and Δ_{h_2} are center of gravity vectors of the first and the second link, respectively. They are given in equations (2.12) and (2.13). The two vectors are given according to the coordinate system of each link.

$$\Delta_{h_1} = \begin{bmatrix} 0 & \frac{L_1}{2} & 0 & 1 \end{bmatrix}^T \tag{2.12}$$

$$\Delta_{h_2} = \begin{bmatrix} \frac{L_2}{2} & 0 & 0 & 1 \end{bmatrix}^T \tag{2.13}$$

I_{m1} and I_{m2} are the inertia tensors of the first and the second link respectively.

$$I_{m1} = \begin{bmatrix} 0 & 0 & 0 \\ 0 & 0 & 0 \\ 0 & 0 & I_{zz_1} \end{bmatrix}, I_{m2} = \begin{bmatrix} 0 & 0 & 0 \\ 0 & 0 & 0 \\ 0 & 0 & I_{zz_2} \end{bmatrix} \tag{2.14}$$

According to the main coordinate system, the coordinates of the mass center of each link are given in equations (2.15) and (2.16).

$$h_1 = {}_1^0T\,\Delta_{h_1} = \begin{bmatrix} \cos\theta_1 & -\sin\theta_1 & 0 & 0 \\ \sin\theta_1 & \cos\theta_1 & 0 & 0 \\ 0 & 0 & 1 & 0 \\ 0 & 0 & 0 & 1 \end{bmatrix}\begin{bmatrix} 0 \\ \frac{L_1}{2} \\ 0 \\ 1 \end{bmatrix} = \begin{bmatrix} -\frac{L_1\sin\theta_1}{2} \\ \frac{L_1\cos\theta_1}{2} \\ 0 \\ 1 \end{bmatrix} \tag{2.15}$$

$$h_2 = {}^{0}_{2}T\,\Delta_{h_2} = \begin{bmatrix} \frac{L_2 \cos\theta_1 \sin\theta_2}{2} - L_1 \sin\theta_1 \\ \frac{L_2 \sin\theta_1 \sin\theta_2}{2} + L_1 \cos\theta_1 \\ \frac{L_2 \cos\theta_2}{2} \\ 1 \end{bmatrix} \tag{2.16}$$

Where

$${}^{0}_{2}T = \begin{bmatrix} \sin\theta_2 \cos\theta_1 & \cos\theta_2 \cos\theta_1 & -\sin\theta_1 & -L_1 \sin\theta_1 \\ \sin\theta_2 \sin\theta_1 & \cos\theta_2 \sin\theta_1 & \cos\theta_1 & L_1 \cos\theta_1 \\ \cos\theta_2 & -\sin\theta_2 & 0 & 0 \\ 0 & 0 & 0 & 1 \end{bmatrix} \tag{2.17}$$

To obtain the Jacobian matrix of the first link, the derivative of the vector h_1 is calculated according to θ_1 and θ_2. ξ_i indicates the joint type variable (ξ_i=1 for rotary joint). i present the unit vector of the third column of the coordinate system.

$$z^1 = {}^{0}_{1}R\, i^2 = \begin{bmatrix} \cos\theta_1 & -\sin\theta_1 & 0 \\ \sin\theta_1 & \cos\theta_1 & 0 \\ 0 & 0 & 1 \end{bmatrix} \begin{bmatrix} 0 \\ 0 \\ 1 \end{bmatrix} = \begin{bmatrix} 0 \\ 0 \\ 1 \end{bmatrix} \tag{2.18}$$

Furthermore, the variables z^1 and ξ_1 are used. The first link is a rotational link $\xi_1 = 1$ and $b_1 = \xi_1 z^1 = [0 \quad 0 \quad 1]^T$. The Jacobian matrix of the first link is given as follows:

$$J_1 = \begin{bmatrix} \frac{\partial}{\partial\theta_1}\left(-\frac{L_1 \sin\theta_1}{2}\right) & \frac{\partial}{\partial\theta_2}\left(-\frac{L_1 \sin\theta_1}{2}\right) \\ \frac{\partial}{\partial\theta_1}\left(\frac{L_1 \cos\theta_1}{2}\right) & \frac{\partial}{\partial\theta_2}\left(\frac{L_1 \cos\theta_1}{2}\right) \\ 0 & 0 \\ 0 & 0 \\ 0 & 0 \\ 1 & 0 \end{bmatrix} = \begin{bmatrix} -\frac{L_1 \cos\theta_1}{2} & 0 \\ -\frac{L_1 \sin\theta_1}{2} & 0 \\ 0 & 0 \\ 0 & 0 \\ 0 & 0 \\ 1 & 0 \end{bmatrix} \tag{2.19}$$

The Jacobian matrix of the first link can be written in two matrices A_1 and B_1.

$$A_1 = \begin{bmatrix} -\frac{L_1 \cos\theta_1}{2} & 0 \\ -\frac{L_1 \sin\theta_1}{2} & 0 \\ 0 & 0 \end{bmatrix} \text{ and } B_1 = \begin{bmatrix} 0 & 0 \\ 0 & 0 \\ 1 & 0 \end{bmatrix} \tag{2.20}$$

Furthermore, to obtain the Jacobian matrix of the second link, the derivative of the vector h_2 is calculated according to θ_1 and θ_2.

$$z^2 = {}^0_2R\, i^2 = \begin{bmatrix} \cos\theta_1 \sin\theta_2 & \cos\theta_1 \cos\theta_2 & -\sin\theta_1 \\ \sin\theta_1 \sin\theta_2 & \cos\theta_2 \sin\theta_1 & \cos\theta_1 \\ \cos\theta_2 & -\sin\theta_2 & 0 \end{bmatrix} \begin{bmatrix} 0 \\ 0 \\ 1 \end{bmatrix} = \begin{bmatrix} -\sin\theta_1 \\ \cos\theta_1 \\ 0 \end{bmatrix} \quad (2.21)$$

The second link is a rotational link, $\xi_2 = 1$ and $b_2 = \xi_2 z^2 = [0 \quad 0 \quad 1]^T$. The Jacobian matrix of the second link is given as follows:

$J_2 =$

$$\begin{bmatrix} \frac{\partial}{\partial\theta_1}\left(\frac{L_2 \cos\theta_1 \sin\theta_2}{2} - L_1 \sin\theta_1\right) & \frac{\partial}{\partial\theta_2}\left(\frac{L_2 \cos\theta_1 \sin\theta_2}{2} - L_1 \sin\theta_1\right) \\ \frac{\partial}{\partial\theta_1}\left(\frac{L_2 \sin\theta_1 \sin\theta_2}{2} + L_1 \cos\theta_1\right) & \frac{\partial}{\partial\theta_2}\left(\frac{L_2 \sin\theta_1 \sin\theta_2}{2} + L_1 \cos\theta_1\right) \\ \frac{\partial}{\partial\theta_1}\left(\frac{L_2 \cos\theta_2}{2}\right) & \frac{\partial}{\partial\theta_2}\left(\frac{L_2 \cos\theta_2}{2}\right) \\ 0 & -\sin\theta_1 \\ 0 & \cos\theta_1 \\ 1 & 0 \end{bmatrix} \quad (2.22)$$

The Jacobian matrix of the second link can be written in two matrices A_2 and B_2.

$$A_2 = \begin{bmatrix} -\frac{L_2 \sin\theta_1 \sin\theta_2}{2} - L_1 \cos\theta_1 & \frac{L_2 \cos\theta_1 \cos\theta_2}{2} \\ \frac{L_2 \cos\theta_1 \sin\theta_2}{2} - L_1 \sin\theta_1 & \frac{L_2 \cos\theta_2 \cos\theta_1}{2} \\ 0 & \frac{-L_2 \sin\theta_2}{2} \end{bmatrix} \quad (2.23)$$

$$B_2 = \begin{bmatrix} 0 & -\sin\theta_1 \\ 0 & \cos\theta_1 \\ 1 & 0 \end{bmatrix} \quad (2.24)$$

The mass matrix of first and second links are given in equations (2.25) and (2.26), respectively.

$$D(\theta_1) = m_1 {A_1}^T A_1 + {B_1}^T I_1 B_1 = \begin{bmatrix} \frac{m_1 {L_1}^2}{4} + I_{zz_1} & 0 \\ 0 & 0 \end{bmatrix} \quad (2.26)$$

$$D(\theta_2) = m_2 {A_2}^T A_2 + {B_2}^T I_2 B_2$$

$$= \begin{bmatrix} m_2\left(\frac{{L_2}^2 \sin^2\theta_2}{4} + {L_1}^2\right) & -\left(\frac{L_1\, L_2\, m_2 \cos\theta_2}{2}\right) \\ -\left(\frac{L_1\, L_2\, m_2 \cos\theta_2}{2}\right) & \left(\frac{{L_2}^2 m_2}{4} + I_{zz_2}\right) \end{bmatrix} \quad (2.27)$$

The inertial tensor of each link is calculated according to the main coordinate system, given in the following equations :

$$I_1 = {}^0_1R\, I_{m1}\, {}^0_1R^T \ , \ I_2 = {}^0_2R\, I_{m2}\, {}^0_2R^T \quad (2.28)$$

The mass matrix of the SLRIP system is given in equation (2.29)

$$D(\theta) = D(\theta_1) + D(\theta_2)$$

$$= \begin{bmatrix} \frac{m_1 {L_1}^2}{4} + I_{zz_1} + m_2\left(\frac{{L_2}^2 \sin^2\theta_2}{4} + {L_1}^2\right) & -\left(\frac{L_1\, L_2\, m_2 \cos\theta_2}{2}\right) \\ -\left(\frac{L_1\, L_2\, m_2 \cos\theta_2}{2}\right) & \left(\frac{{L_2}^2 m_2}{4} + I_{zz_2}\right) \end{bmatrix} \quad (2.29)$$

The elements of the velocity coupling matrix of the first link, are calculated as follows:

$${C^2}_{11} = \frac{\partial}{\partial\theta_1} D_{21}(\theta) - \frac{1}{2}\frac{\partial}{\partial\theta_2} D_{11}(\theta) = -\frac{1}{8}\left({L_2}^2 m_2 \sin(2\theta_2)\right) \quad (2.30)$$

$${C^2}_{12} = \frac{\partial}{\partial\theta_1} D_{22}(\theta) - \frac{1}{2}\frac{\partial}{\partial\theta_2} D_{12}(\theta) = -\frac{1}{4}(L_1 L_2 m_2 \sin(\theta_2)) \quad (2.31)$$

$${C^2}_{21} = \frac{1}{2}\frac{\partial}{\partial\theta_2} D_{21}(\theta) = \frac{1}{4}(L_1 L_2 m_2 \sin(\theta_2)) \quad (2.32)$$

$${C^2}_{22} = \frac{1}{2}\frac{\partial}{\partial\theta_2} D_{22}(\theta) = \frac{1}{2}(L_1 L_2 m_2 \sin(\theta_2)) \quad (2.33)$$

The velocity coupling matrix of the first link is given in equation (2.34)

$$C_2 = \begin{bmatrix} -\frac{1}{8}\left({L_2}^2 m_2 \sin(2\theta_2)\right) & -\frac{1}{4}(L_1 L_2 m_2 \sin(\theta_2)) \\ \frac{1}{4}(L_1 L_2 m_2 \sin(\theta_2)) & 0 \end{bmatrix} \quad (2.34)$$

In order to find the Coriolis and Centripetal force vector of the SLRIP, each element of the velocity coupling matrices (C_1 and C_2) need to verify the equality of the elements of the following matrices.

$$\begin{bmatrix} 0 & 0 \\ \frac{1}{4}\left(L_2{}^2 m_2 \sin(2\theta_2)\right) & \frac{1}{2}(L_1 L_2 m_2 \sin(\theta_2)) \end{bmatrix} = \begin{bmatrix} \dot{\theta_1}^2 & \dot{\theta_1}\dot{\theta_2} \\ \dot{\theta_1}\dot{\theta_2} & \dot{\theta_2}^2 \end{bmatrix} \tag{2.35}$$

$$\begin{bmatrix} -\frac{1}{8}\left(L_2{}^2 m_2 \sin(2\theta_2)\right) & -\frac{1}{4}(L_1 L_2 m_2 \sin(\theta_2)) \\ \frac{1}{4}(L_1 L_2 m_2 \sin(\theta_2)) & 0 \end{bmatrix} = \begin{bmatrix} \dot{\theta_1}^2 & \dot{\theta_1}\dot{\theta_2} \\ \dot{\theta_1}\dot{\theta_2} & \dot{\theta_2}^2 \end{bmatrix} \tag{2.36}$$

Coriolis and Centripetal force vector of the SLRIP is given in equation (2.37)

$$C(\theta, \dot{\theta}) = \begin{bmatrix} \frac{1}{2}\left(L_1 L_2 m_2 \dot{\theta_2}^2 \sin(\theta_2)\right) + \frac{1}{4}\left(L_2{}^2 m_2 \dot{\theta_1}\dot{\theta_2} \sin(2\theta_2)\right) \\ -\frac{1}{8}\left(L_2{}^2\, \dot{\theta_1}^2\, m_2 \sin(2\theta_2)\right) \end{bmatrix} \tag{2.37}$$

The gravity vector of the SLRIP is given in equation (2.38)

$$G = \begin{bmatrix} 0 \\ -\frac{1}{2}(L_2 g\, m_2 \sin(\theta_2)) \end{bmatrix} \tag{2.38}$$

Based on equation (2.7), the nonlinear equations of the SLRIP system is given in a matrix form, as follows:

$$\begin{bmatrix} \frac{m_1 L_1{}^2}{4} + I_{zz_1} + m_2\left(\frac{L_2{}^2 \sin^2\theta_2}{4} + L_1{}^2\right) & -\left(\frac{L_1\, L_2\, m_2 \cos\theta_2}{2}\right) \\ -\left(\frac{L_1\, L_2\, m_2 \cos\theta_2}{2}\right) & \left(\frac{L_2{}^2 m_2}{4} + I_{zz_2}\right) \end{bmatrix} \begin{bmatrix} \ddot{\theta_1} \\ \ddot{\theta_2} \end{bmatrix}$$

$$+ \begin{bmatrix} \frac{1}{2}\left(L_1 L_2 m_2 \dot{\theta_2}^2 \sin(\theta_2)\right) + \frac{1}{4}\left(L_2{}^2 m_2 \dot{\theta_1}\dot{\theta_2} \sin(2\theta_2)\right) \\ -\frac{1}{8}\left(L_2{}^2\, \dot{\theta_1}^2\, m_2 \sin(2\theta_2)\right) \end{bmatrix}$$

$$+ \begin{bmatrix} 0 \\ -\frac{1}{2}(L_2 g\, m_2 \sin(\theta_2)) \end{bmatrix} = \begin{bmatrix} \tau_1 \\ 0 \end{bmatrix} \tag{2.39}$$

2.1.3. Jacobian matrix of the SLRIP

The linear and angular velocities of the links of the SLRIP are used to determine the Jacobian matrix. A formula to compute the Jacobian matrix of the SLRIP is given in equation (2.40). J_v and J_w represents the Jacobian matrices obtained from the linear and angular velocities in the end-link, respectively. [91]

$$J(\theta) = \begin{bmatrix} J_v(\theta) \\ J_w(\theta) \end{bmatrix} \tag{2.40}$$

The linear velocities matrix of the system is given in equation (2.41).

$$\begin{aligned} {}^0_3V &= {}^0_3R\,{}^3_3V \\ &= \begin{bmatrix} \cos\theta_1 \sin\theta_2 & \cos\theta_1 \cos\theta_2 & \sin\theta_1 \\ \sin\theta_1 \sin\theta_2 & \cos\theta_2 \sin\theta_1 & -\cos\theta_1 \\ \cos\theta_2 & -\sin\theta_2 & 0 \end{bmatrix} \begin{bmatrix} -L_1 \sin\theta_2 \dot{\theta_1} \\ L_2\dot{\theta_2} - L_1 \cos\theta_2 \dot{\theta_1} \\ \sin\theta_2 L_2 \dot{\theta_1} \end{bmatrix} \end{aligned} \tag{2.41}$$

The linear velocities matrix of the system can be written as follows:

$${}^0_3V = \begin{bmatrix} -L_1 \cos\theta_1 - \sin\theta_2 & L_2 \sin\theta_1 & L_2 \cos\theta_1 \cos\theta_2 \\ -L_1 \sin\theta_1 + \sin\theta_2 & L_2 \cos\theta_1 & L_2 \cos\theta_2 \sin\theta_1 \\ 0 & & -L_2 \sin\theta_2 \end{bmatrix} \begin{bmatrix} \dot{\theta_1} \\ \dot{\theta_2} \end{bmatrix} \tag{2.43}$$

The Jacobian matrix taken from the linear velocities is given as follows:

$$J_{v_0}^{3}(\theta) = \begin{bmatrix} -L_1 \cos\theta_1 - \sin\theta_2 & L_2 \sin\theta_1 & L_2 \cos\theta_1 \cos\theta_2 \\ -L_1 \sin\theta_1 + \sin\theta_2 & L_2 \cos\theta_1 & L_2 \cos\theta_2 \sin\theta_1 \\ 0 & & -L_2 \sin\theta_2 \end{bmatrix} \tag{2.44}$$

The angular velocities matrix of the system is given in equation (2.45)

$$\begin{aligned} {}^0_3w &= {}^0_3R\,{}^3_3w = \begin{bmatrix} \cos\theta_1 \sin\theta_2 & \cos\theta_1 \cos\theta_2 & \sin\theta_1 \\ \sin\theta_1 \sin\theta_2 & \cos\theta_2 \sin\theta_1 & -\cos\theta_1 \\ \cos\theta_2 & -\sin\theta_2 & 0 \end{bmatrix} \begin{bmatrix} \dot{\theta}_1 \cos\theta_2 \\ -\dot{\theta}_1 \sin\theta_2 \\ \dot{\theta}_2 \end{bmatrix} \\ &= \begin{bmatrix} -\dot{\theta}_2 \sin\theta_1 \\ \dot{\theta}_2 \cos\theta_1 \\ \dot{\theta}_1 \end{bmatrix} \end{aligned} \tag{2.45}$$

The angular velocities matrix of the system can be written as follows:

$$ {}^{0}_{3}w = {}^{0}_{3}R\,{}^{3}_{3}w = \begin{bmatrix} -\dot{\theta}_2 \sin\theta_1 \\ \dot{\theta}_2 \cos\theta_1 \\ \dot{\theta}_1 \end{bmatrix} = \begin{bmatrix} 0 & -\sin\theta_1 \\ 0 & \cos\theta_1 \\ 1 & 0 \end{bmatrix} \begin{bmatrix} \dot{\theta}_1 \\ \dot{\theta}_2 \end{bmatrix} \tag{2.46} $$

The Jacobian matrix taken from the angular velocities is given as follows.

$$ J_{w_0^3}(\theta) = \begin{bmatrix} 0 & -\sin\theta_1 \\ 0 & \cos\theta_1 \\ 1 & 0 \end{bmatrix} \tag{2.47} $$

The Jacobian matrix taken from the linear and angular velocities is given in equation (2.46).

$$ J_0^3(\theta) = \begin{bmatrix} -L_1\cos\theta_1 - \sin\theta_2 & L_2\sin\theta_1 & L_2\cos\theta_1\cos\theta_2 \\ -L_1\sin\theta_1 + \sin\theta_2 & L_2\cos\theta_1 & L_2\cos\theta_2\sin\theta_1 \\ 0 & & -L_2\sin\theta_2 \\ 0 & & -\sin\theta_1 \\ 0 & & \cos\theta_1 \\ 1 & & 0 \end{bmatrix} \tag{2.48} $$

Furthermore, using the determinant of the Jacobian matrix, $w = \left|\det\left(J_0^3(\theta) \times J_0^3(\theta)^T\right)\right|$, the optimal length of each link of the SLRIP is estimated using the PSO optimization algorithm. The optimal lengths are given in Table 2.2.

2.1.4. Dynamic simulation of the SLRIP

According to the equation (2.39), the expression for the angular acceleration vector ($\ddot{\theta}$) can be given in equation (2.49).

The two equations of $\ddot{\theta}_1$ and $\ddot{\theta}_2$ are derived and simulated in Matlab/Simulink. The Matlab code of the mathematical expression of both equations is given in the appendix.

$$ \begin{bmatrix} \ddot{\theta}_1 \\ \ddot{\theta}_2 \end{bmatrix} = M^{-1}\left[\tau - C\left(\theta, \dot{\theta}\right) - G(\theta)\right] \tag{2.49} $$

Figure 2.2 shows the non-linear mathematical model of the SLRIP in Matlab/Simulink. In order to verify the mathematical model, a mechanical dynamic model of the SLRIP was developed by using the MATLAB/SimMechanics toolbox.

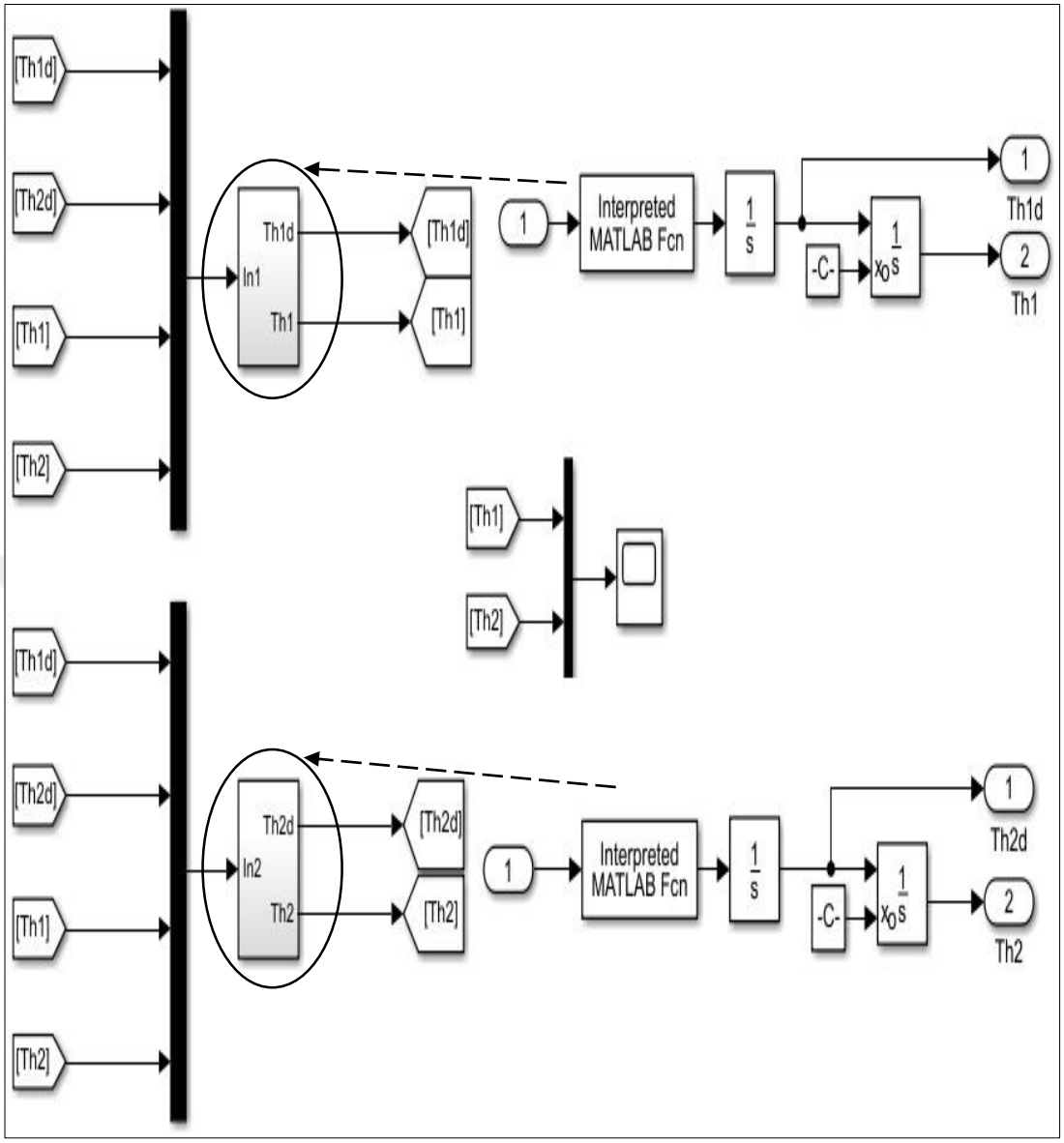

Figure 2.2. Mathematical model of the SLRIP in Matlab/Simulink

MATLAB/SimMechanics model of the SLRIP is shown in Figure 2.3 (a). Different views from virtual reality model of the SLRIP in Matlab Simulink is shown in Figure 2.3 (b). Furthermore, for both model, the initial conditions of pendulums' joint positions are chosen as follows $\theta_1 = 0\,°$, and $\theta_2 = 20\,°$. The obtained results from both MATLAB/SimMechanics and the mathematical models match exactly. Figure 2.4 illustrates a comparison of the two joint positions obtained from simulation mathematical and the SimMechanics models without frictions. The simulations are performed by the sampling time 1ms and 10s simulation time. A numerical method Bogacki-Shampine solver is selected with fixed-step.

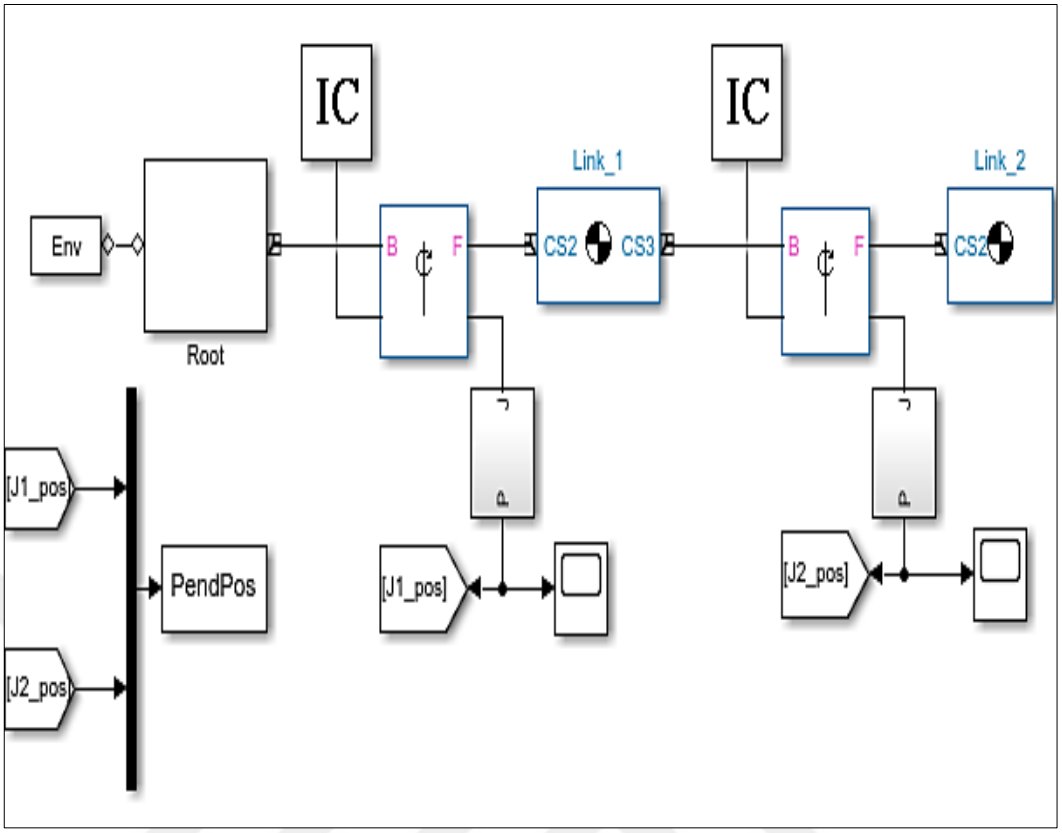

(a)

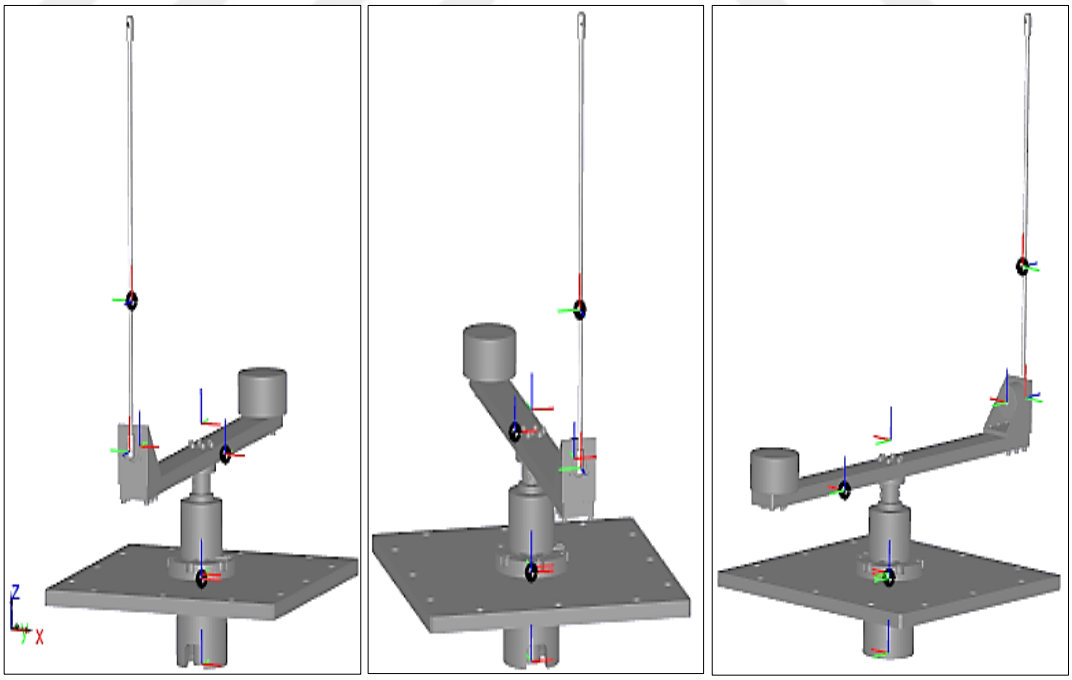

(b)

Figure 2.3. (a) MATLAB/SimMechanics model of SLRIP, (b) Different views from virtual reality model of SLRIP in Matlab Simulink

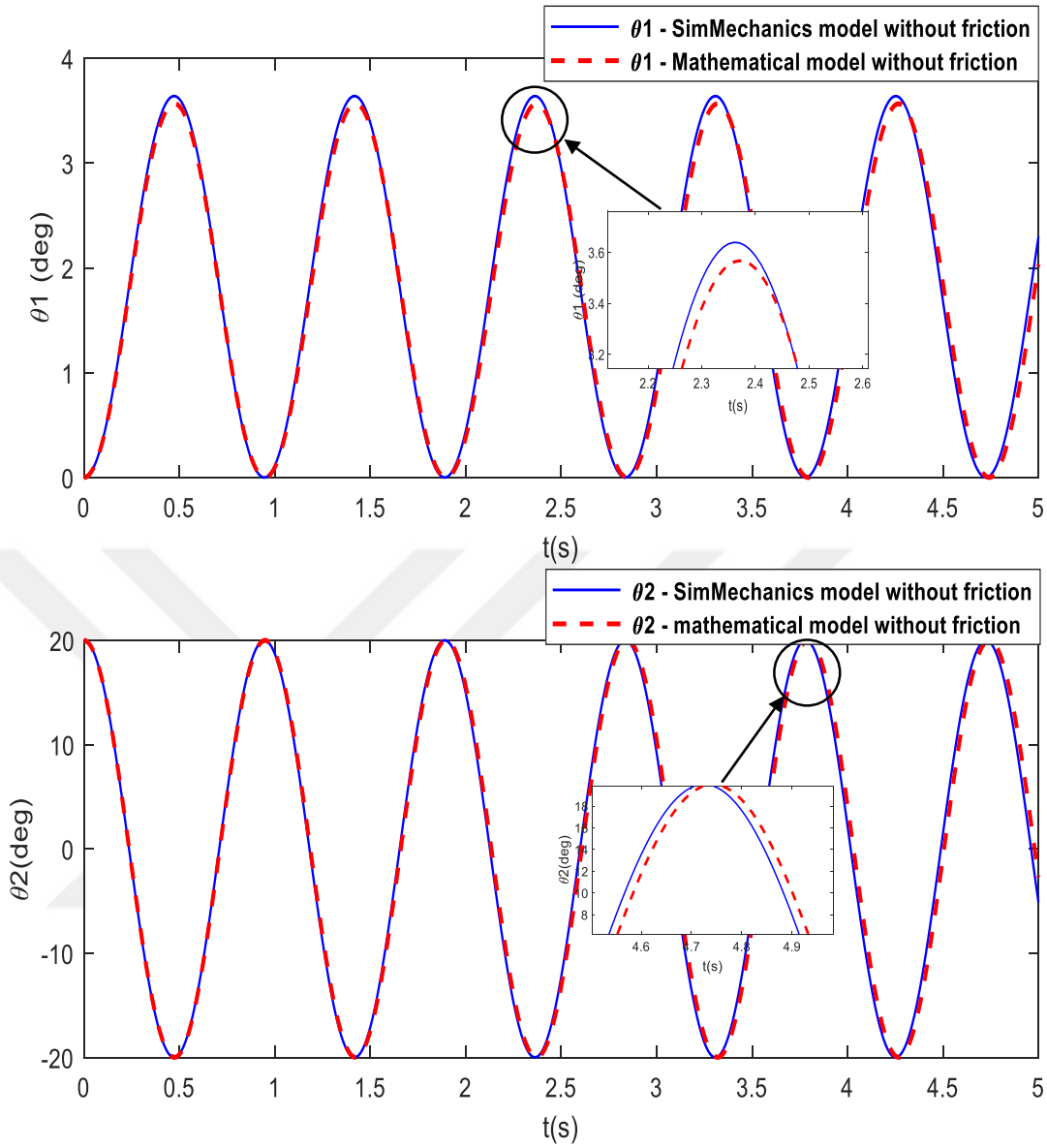

Figure 2.4. Comparison of the pendulum joint positions obtained from the analytic mathematical model and SimMechanics numerical model of the SLRIP

2.2. Modeling of the DLRIP

2.2.1. Kinematic model of the DLRIP

Solid 3D model and kinematics parameters of the DLRIP are shown in the Figure. 2.5. DLRIP comprises a horizontal rotary link and two pendulum links. A direct drive brushless DC torque motor servo system is mounted to provide torque to the horizontal arm to control the system. The rotary arm rotates in the horizontal plane. The first pendulum link is connected to the extremity of the rotary link and the second pendulum link is connected to the extremity of first pendulum link. The two pendulum links move

as an inverted pendulum in a plane perpendicular to the rotary link. A balance mass can be attached to the other extremity of the horizontal arm to maintain the balance inertia of the system. The angle of the rotary link (θ_1) and the angles of the two pendulum links (θ_2 and θ_3) of the DLRIP are illustrated in Figure 2.5. The kinematic model of the system is derived based on the DH convention. Rotation and homogeneous transformation matrices between coordinates the DLRIP are calculated. The parameters and variables of the model are given in Table 2.1 (section 2.1.1). The physical parameters of the DLRIP are given in Table 2.4. DH Parameters of the DLRIP are given in Table 2.5.

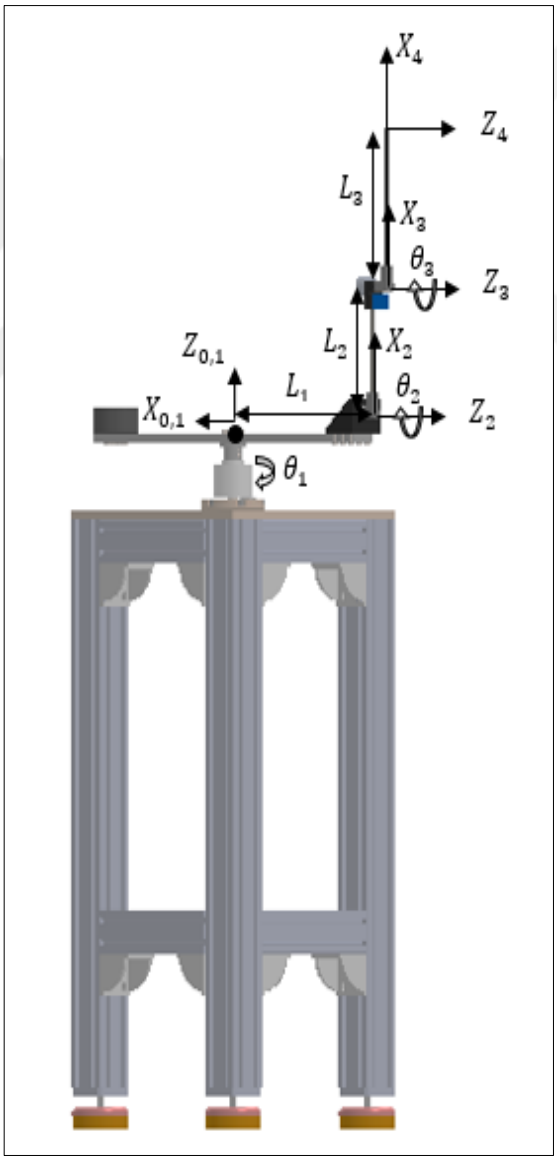

Figure 2.5. Solid 3D model and kinematic parameters of the DLRIP

Table 2.4. Physical parameters of the DLRIP

Parameters	Values	Parameters	Values	Parameters	Values
m_1	3.1129 [kg]	L_1	0.44 [m]	I_{zz2}	0.0020 [kg · m^2]
m_2	0.1908 [kg]	L_2	0.278 [m]	I_{zz1}	0.0015 [kg · m^2]
m_3	0.0832 [kg]	L_3	0.430 [m]	$b_{1,2,3}$	0.0024 [N-m-s/Rad]
m_B	3.1469 [kg]	I_{zz1}	0.4398 [kg · m^2]	g	9.82 [N kg^{-1}]

Table 2.5. DH-Parameters of the DLRIP

Coordinate	α_{i-1}	a_{i-1}	d_i	θ_i
1	0	0	0	θ_1
2	$-\frac{\pi}{2}$	0	L_1	$\theta_2 - \frac{\pi}{2}$
3	0	L_2	0	0
4	0	L_3	0	0

The expression of the homogeneous transformation matrix from a coordinate attached to an *i*-th link to a coordinate attached to *i*-1-th link, $i = 1,2,3,4$. The expression of ${}^{i-1}_{i}T$ is given in equation (2.1). The homogeneous transformation matrix of the DLRIP is derived in equation (2.50) using the DH-parameters in Table 2.5.

$$ {}^{0}_{4}T = {}^{0}_{1}T\,{}^{1}_{2}T\,{}^{2}_{3}T\,{}^{3}_{4}T \tag{2.50} $$

Where

$$ {}^{0}_{1}T = \begin{bmatrix} \cos\theta_1 & -\sin\theta_1 & 0 & 0 \\ \sin\theta_1 & \cos\theta_1 & 0 & 0 \\ 0 & 0 & 1 & 0 \\ 0 & 0 & 0 & 1 \end{bmatrix} {}^{1}_{2}T = \begin{bmatrix} \sin\theta_2 & \cos\theta_2 & 0 & 0 \\ 0 & 0 & 1 & L_1 \\ \cos\theta_2 & -\sin\theta_2 & 0 & 0 \\ 0 & 0 & 0 & 1 \end{bmatrix} \tag{2.51} $$

$$ {}^{2}_{3}T = \begin{bmatrix} \cos\theta_3 & -\sin\theta_3 & 0 & L_2 \\ \sin\theta_3 & \cos\theta_3 & 0 & 0 \\ 0 & 0 & 1 & 0 \\ 0 & 0 & 0 & 1 \end{bmatrix} {}^{3}_{4}T = \begin{bmatrix} 1 & 0 & 0 & L_3 \\ 0 & 1 & 0 & 0 \\ 0 & 0 & 1 & 0 \\ 0 & 0 & 0 & 1 \end{bmatrix} \tag{2.52} $$

$$
{}^{0}_{4}\mathrm{T} = \begin{bmatrix} \sin\theta_{23}\cos\theta_1 & \cos\theta_{23}\cos\theta_1 & -\sin\theta_1 & \cos\theta_1(\mathrm{L}_2\sin\theta_2 + \mathrm{L}_3\sin\theta_{23}) - \mathrm{L}_1\sin\theta_1 \\ \sin\theta_{23}\sin\theta_1 & \cos\theta_{23}\sin\theta_1 & \cos\theta_1 & \mathrm{L}_1\cos\theta_1 + \sin\theta_1(\mathrm{L}_3\sin\theta_{23} + \mathrm{L}_2\sin\theta_2) \\ \cos\theta_{23} & -\sin\theta_{23} & 0 & \mathrm{L}_3\cos\theta_{23} + \mathrm{L}_2\cos\theta_2 \\ 0 & 0 & 0 & 1 \end{bmatrix} \quad (2.53)
$$

Where $\theta_{23} = (\theta_2 + \theta_3)$.

The position vector is given from the calculated homogeneous transformation matrix ${}^{0}_{4}\mathrm{T}$ as follows:

$$
\begin{bmatrix} \mathrm{P_x} \\ \mathrm{P_y} \\ \mathrm{P_z} \end{bmatrix} = \begin{bmatrix} \cos\theta_1(\mathrm{L}_2\sin\theta_2 + \mathrm{L}_3\sin\theta_{23}) - \mathrm{L}_1\sin\theta_1 \\ \mathrm{L}_1\cos\theta_1 + \sin\theta_1(\mathrm{L}_3\sin\theta_{23} + \mathrm{L}_2\sin\theta_2) \\ \mathrm{L}_3\cos\theta_{23} + \mathrm{L}_2\cos\theta_2 \end{bmatrix} \quad (2.54)
$$

2.2.2. Dynamic model of the DLRIP

The non-linear motion equations of this DLRIP are derived based on the DH convention and can be given in a matrix form, given in equation (2.7). The dynamic equations of DLRIP system are derived using the "Euler-Lagrangian" method. The terms of each matrix of equation (2.7) are calculated using the equations (2.8-2.11). The elements of each matrix calculated are calculated as follows:

Δ_{h_1}, Δ_{h_2} and Δ_{h_3} are center of gravity vectors of the first, second and third links respectively. The three vectors are given according to the coordinate system of each link.

$$
\Delta_{h_1} = \begin{bmatrix} 0 & \frac{\mathrm{L}_1}{2} & 0 & 1 \end{bmatrix}^{\mathrm{T}}, \Delta_{h_2} = \begin{bmatrix} \frac{\mathrm{L}_2}{2} & 0 & 0 & 1 \end{bmatrix}^{\mathrm{T}} \text{ and } \Delta_{h_3} = \begin{bmatrix} \frac{\mathrm{L}_3}{2} & 0 & 0 & 1 \end{bmatrix}^{\mathrm{T}} \quad (2.55)
$$

I_1, I_2 and I_3 are the inertia tensors of the first, second and the third links, respectively.

$$
\mathrm{I}_1 = \begin{bmatrix} 0 & 0 & 0 \\ 0 & 0 & 0 \\ 0 & 0 & \mathrm{I}_{zz_1} \end{bmatrix}, \mathrm{I}_2 = \begin{bmatrix} 0 & 0 & 0 \\ 0 & 0 & 0 \\ 0 & 0 & \mathrm{I}_{zz_2} \end{bmatrix} \text{ and } \mathrm{I}_3 = \begin{bmatrix} 0 & 0 & 0 \\ 0 & 0 & 0 \\ 0 & 0 & \mathrm{I}_{zz_3} \end{bmatrix} \quad (2.56)
$$

The coordinate of the mass center of each link according to the main coordinate of the system, are given in equations $(2.57 - 2.59)$.

$$h_1 = {}^{0}_{1}T\,\Delta_{h_1} = \begin{bmatrix} \cos\theta_1 & -\sin\theta_1 & 0 & 0 \\ \sin\theta_1 & \cos\theta_1 & 0 & 0 \\ 0 & 0 & 1 & 0 \\ 0 & 0 & 0 & 1 \end{bmatrix} \begin{bmatrix} 0 \\ \frac{L_1}{2} \\ 0 \\ 1 \end{bmatrix} = \begin{bmatrix} -\frac{L_1 \sin\theta_1}{2} \\ \frac{L_1 \cos\theta_1}{2} \\ 0 \\ 1 \end{bmatrix} \tag{2.57}$$

$$h_2 = {}^{0}_{2}T\,\Delta_{h_2} = \begin{bmatrix} \frac{L_2 \cos\theta_1 \sin\theta_2}{2} - L_1 \sin\theta_1 \\ \frac{L_2 \sin\theta_1 \sin\theta_2}{2} + L_1 \cos\theta_1 \\ \frac{L_2 \cos\theta_2}{2} \\ 1 \end{bmatrix} \tag{2.58}$$

$$h_3 = {}^{0}_{3}T\,\Delta_{h_3}$$

$$= \begin{bmatrix} \frac{L_3 \cos\theta_1 \cos\theta_2 \sin\theta_3}{2} + \frac{L_3 \cos\theta_1 \cos\theta_3 \sin\theta_2}{2} + L_2 \cos\theta_1 \sin\theta_2 - L_1 \sin\theta_1 \\ \frac{L_3 \cos\theta_2 \sin\theta_1 \sin\theta_3}{2} + \frac{L_3 \cos\theta_3 \sin\theta_1 \sin\theta_2}{2} + L_2 \sin\theta_1 \sin\theta_2 + L_1 \cos\theta_1 \\ \frac{L_3 \cos(\theta_2 + \theta_3)}{2} + L_2 \cos\theta_2 \\ 1 \end{bmatrix} \tag{2.59}$$

To obtain the Jacobian matrix of the first link, the derivative of the vector h_1 is calculated according to θ_1, θ_2 and θ_3. ξ_i indicates the joint type variable (ξ_i=1 for rotary joint). i present the unit vector of the third column of the coordinate system.

$$z^1 = {}^{0}_{1}R\,i^3 = \begin{bmatrix} \cos\theta_1 & -\sin\theta_1 & 0 \\ \sin\theta_1 & \cos\theta_1 & 0 \\ 0 & 0 & 1 \end{bmatrix} \begin{bmatrix} 0 \\ 0 \\ 1 \end{bmatrix} = \begin{bmatrix} 0 \\ 0 \\ 1 \end{bmatrix} \tag{2.60}$$

Furthermore, the first link is a rotational link $\xi_1 = 1$ and $b_1 = \xi_1 z^1 = [0 \quad 0 \quad 1]^T$. The Jacobian matrix of the first link is given as follows:

$$J_1 = \begin{bmatrix} \frac{\partial}{\partial\theta_1}\left(-\frac{L_1 \sin\theta_1}{2}\right) & \frac{\partial}{\partial\theta_2}\left(-\frac{L_1 \sin\theta_1}{2}\right) & \frac{\partial}{\partial\theta_3}\left(-\frac{L_1 \sin\theta_1}{2}\right) \\ \frac{\partial}{\partial\theta_1}\left(\frac{L_1 \cos\theta_1}{2}\right) & \frac{\partial}{\partial\theta_2}\left(\frac{L_1 \cos\theta_1}{2}\right) & \frac{\partial}{\partial\theta_3}\left(\frac{L_1 \cos\theta_1}{2}\right) \\ 0 & 0 & 0 \\ 0 & 0 & 0 \\ 0 & 0 & 0 \\ 1 & 0 & 0 \end{bmatrix}$$

$$= \begin{bmatrix} -\frac{L_1 \cos\theta_1}{2} & 0 & 0 \\ -\frac{L_1 \sin\theta_1}{2} & 0 & 0 \\ 0 & 0 & 0 \\ 0 & 0 & 0 \\ 1 & 0 & 0 \end{bmatrix} \tag{2.61}$$

The Jacobian matrix of the first link can be written in two matrices A_1 and B_1.

$$A_1 = \begin{bmatrix} -\frac{L_1 \cos\theta_1}{2} & 0 & 0 \\ -\frac{L_1 \sin\theta_1}{2} & 0 & 0 \\ 0 & 0 & 0 \end{bmatrix} \text{ and } B_1 = \begin{bmatrix} 0 & 0 & 0 \\ 0 & 0 & 0 \\ 1 & 0 & 0 \end{bmatrix} \tag{2.62}$$

To obtain the Jacobian matrix of the second link, the derivative of the vector h_2 is calculated according to θ_1, θ_2 and θ_3.

$$z^2 = {}^0_2R\, i^3 = \begin{bmatrix} \cos\theta_1 \sin\theta_2 & \cos\theta_1 \cos\theta_2 & -\sin\theta_1 \\ \sin\theta_1 \sin\theta_2 & \cos\theta_2 \sin\theta_1 & \cos\theta_1 \\ \cos\theta_2 & -\sin\theta_2 & 0 \end{bmatrix} \begin{bmatrix} 0 \\ 0 \\ 1 \end{bmatrix}$$

$$z^2 = \begin{bmatrix} -\sin\theta_1 \\ \cos\theta_1 \\ 0 \end{bmatrix} \tag{2.63}$$

The second link is a rotational link which $\xi_2 = 1$ and $b_2 = \xi_2 z^2 = [0 \quad 0 \quad 1]^T$. The Jacobian matrix of the second link is given as follows:

$$J_2 = \begin{bmatrix} \frac{\partial}{\partial\theta_1}\left(\frac{L_2 \cos\theta_1 \sin\theta_2}{2} - L_1 \sin\theta_1\right) & \frac{\partial}{\partial\theta_2}\left(\frac{L_2 \cos\theta_1 \sin\theta_2}{2} - L_1 \sin\theta_1\right) & \frac{\partial}{\partial\theta_3}\left(\frac{L_2 \cos\theta_1 \sin\theta_2}{2} - L_1 \sin\theta_1\right) \\ \frac{\partial}{\partial\theta_1}\left(\frac{L_2 \sin\theta_1 \sin\theta_2}{2} + L_1 \cos\theta_1\right) & \frac{\partial}{\partial\theta_2}\left(\frac{L_2 \sin\theta_1 \sin\theta_2}{2} + L_1 \cos\theta_1\right) & \frac{\partial}{\partial\theta_3}\left(\frac{L_2 \cos\theta_1 \sin\theta_2}{2} - L_1 \sin\theta_1\right) \\ \frac{\partial}{\partial\theta_1}\left(\frac{L_2 \cos\theta_2}{2}\right) & \frac{\partial}{\partial\theta_2}\left(\frac{L_2 \cos\theta_2}{2}\right) & \frac{\partial}{\partial\theta_3}\left(\frac{L_2 \cos\theta_2}{2}\right) \\ 0 & -\sin\theta_1 & 0 \\ 0 & \cos\theta_1 & 0 \\ 1 & 0 & 0 \end{bmatrix}$$

(2.64)

$$J_2 = \begin{bmatrix} -\frac{L_2 \sin\theta_1 \sin\theta_2}{2} - L_1 \cos\theta_1 & \frac{L_2 \cos\theta_1 \cos\theta_2}{2} & 0 \\ \frac{L_2 \cos\theta_1 \sin\theta_2}{2} - L_1 \sin\theta_1 & \frac{L_2 \cos\theta_2 \cos\theta_1}{2} & 0 \\ 0 & \frac{-L_2 \sin\theta_2}{2} & 0 \\ 0 & -\sin\theta_1 & 0 \\ 0 & \cos\theta_1 & 0 \\ 1 & 0 & 0 \end{bmatrix} \quad (2.65)$$

The Jacobian matrix of the second link may be written in two matrices A_2 and B_2.

$$A_2 = \begin{bmatrix} -\frac{L_2 \sin\theta_1 \sin\theta_2}{2} - L_1 \cos\theta_1 & \frac{L_2 \cos\theta_1 \cos\theta_2}{2} & 0 \\ \frac{L_2 \cos\theta_1 \sin\theta_2}{2} - L_1 \sin\theta_1 & \frac{L_2 \cos\theta_2 \cos\theta_1}{2} & 0 \\ 0 & \frac{-L_2 \sin\theta_2}{2} & 0 \end{bmatrix} \quad (2.66)$$

$$B_2 = \begin{bmatrix} 0 & -\sin\theta_1 & 0 \\ 0 & \cos\theta_1 & 0 \\ 1 & 0 & 0 \end{bmatrix} \quad (2.67)$$

To obtain the Jacobian matrix of the third link, the derivative of the vector h_3 is calculated according to θ_1, θ_2 and θ_3.

$$z^3 = {}^0_3R\, i^3 = \begin{bmatrix} \sin(\theta_2+\theta_3) + \cos\theta_1 & \cos(\theta_2+\theta_3)\cos\theta_1 & -\sin\theta_1 \\ \sin(\theta_2+\theta_3)\sin\theta_1 & \cos(\theta_2+\theta_3)\sin\theta_1 & \cos\theta_1 \\ \cos(\theta_2+\theta_3) & -\sin(\theta_2+\theta_3) & 0 \end{bmatrix} \begin{bmatrix} 0 \\ 0 \\ 1 \end{bmatrix}$$

$$= \begin{bmatrix} -\sin\theta_1 \\ \cos\theta_1 \\ 0 \end{bmatrix} \quad (2.68)$$

The third link is a rotational link which $\xi_3 = 1$ and $b_3 = \xi_3 z^3 = [0 \quad 0 \quad 1]^T$. The Jacobian matrix of the third link is given as follows:

$$J_3 = \begin{bmatrix} \frac{\partial}{\partial\theta_1}\left(\frac{L_3 \cos\theta_1 \cos\theta_2 \sin\theta_3}{2} + \frac{L_3 \cos\theta_1 \cos\theta_3 \sin\theta_2}{2} + L_2 \cos\theta_1 \sin\theta_2 - L_1 \sin\theta_1\right) \dots \\ \frac{\partial}{\partial\theta_1}\left(\frac{L_3 \cos\theta_2 \sin\theta_1 \sin\theta_3}{2} + \frac{L_3 \cos\theta_3 \sin\theta_1 \sin\theta_2}{2} + L_2 \sin\theta_1 \sin\theta_2 + L_1 \cos\theta_1\right) \dots \\ \frac{\partial}{\partial\theta_1}\left(\frac{L_3 \cos(\theta_2+\theta_3)}{2} + L_2 \cos\theta_2\right) \dots \\ 0 \\ 0 \\ 1 \end{bmatrix}$$

$$\begin{bmatrix} \frac{\partial}{\partial\theta_2}\left(\frac{L_3\cos\theta_1\cos\theta_2\sin\theta_3}{2}+\frac{L_3\cos\theta_1\cos\theta_3\sin\theta_2}{2}+L_2\cos\theta_1\ \sin\theta_2-L_1\sin\theta_1\right)\ldots \\ \frac{\partial}{\partial\theta_2}\left(\frac{L_3\cos\theta_2\sin\theta_1\sin\theta_3}{2}+\frac{L_3\cos\theta_3\sin\theta_1\sin\theta_2}{2}+L_2\sin\theta_1\ \sin\theta_2+L_1\cos\theta_1\right)\ldots \\ \frac{\partial}{\partial\theta_2}\left(\frac{L_3\cos(\theta_2+\theta_3)}{2}+L_2\cos\theta_2\right)\ldots \\ -\sin\theta_1 \\ \cos\theta_1 \\ 0 \end{bmatrix}$$

$$\begin{bmatrix} \frac{\partial}{\partial\theta_2}\left(\frac{L_3\cos\theta_1\cos\theta_2\sin\theta_3}{2}+\frac{L_3\cos\theta_1\cos\theta_3\sin\theta_2}{2}+L_2\cos\theta_1\ \sin\theta_2-L_1\sin\theta_1\right) \\ \frac{\partial}{\partial\theta_2}\left(\frac{L_3\cos\theta_2\sin\theta_1\sin\theta_3}{2}+\frac{L_3\cos\theta_3\sin\theta_1\sin\theta_2}{2}+L_2\sin\theta_1\ \sin\theta_2+L_1\cos\theta_1\right) \\ \frac{\partial}{\partial\theta_2}\left(\frac{L_3\cos(\theta_2+\theta_3)}{2}+L_2\cos\theta_2\right) \\ -\sin\theta_1 \\ \cos\theta_1 \\ 0 \end{bmatrix} \tag{2.69}$$

The Jacobian matrix of the third link can be written in two matrices $A_3$and B_3.

$$A_3 = \begin{bmatrix} \frac{L_3\cos\theta_3\sin\theta_1\sin 2}{2}-\frac{L_3\cos\theta_2\sin\theta_1\sin\theta_3}{2}-L_2\sin\theta_1\ \sin\theta_2-L_1\cos\theta_1\ldots \\ \frac{L_3\cos\theta_1\cos\theta_2\sin\theta_3}{2}+\frac{L_3\cos\theta_1\cos\theta_3\sin\theta_2}{2}+L_2\cos\theta_1\ \sin\theta_2-L_1\sin\theta_1\ldots \\ 0 \end{bmatrix}$$

$$\begin{bmatrix} \frac{\cos\theta_1\,(L_3\cos(\theta_2+\theta_3)+2L_2\cos\theta_2)}{2} & \frac{\cos\theta_1\,(L_3\cos(\theta_2+\theta_3))}{2} \\ \frac{\sin\theta_1\,(L_3\cos(\theta_2+\theta_3)+2L_2\cos\theta_2)}{2} & \frac{\sin\theta_1\,(L_3\cos(\theta_2+\theta_3))}{2} \\ \frac{-L_3\sin(\theta_2+\theta_3)}{2}-L_2\sin\theta_2 & -\frac{L_3\sin(\theta_2+\theta_3)}{2} \end{bmatrix} \tag{2.70}$$

$$B_3 = \begin{bmatrix} 0 & -\sin\theta_1 & -\sin\theta_1 \\ 0 & \cos\theta_1 & \cos\theta_1 \\ 1 & 0 & 0 \end{bmatrix} \tag{2.71}$$

The mass matrix of first, second and third links are given in equations (2.72-2.74), respectively.

$$D(\theta_1) = m_1\,{A_1}^{T}A_1 + {B_1}^{T}\,I_1B_1 = \begin{bmatrix} \frac{m_1{L_1}^2}{4}+I_{zz_1} & 0 & 0 \\ 0 & 0 & 0 \\ 0 & 0 & 0 \end{bmatrix} \tag{2.72}$$

$$D(\theta_2) = m_2\,{A_2}^{T}A_2 + {B_2}^{T}\,I_2B_2$$

$$= \begin{bmatrix} m_2\left(\frac{{L_2}^2 \sin^2\theta_2}{4} + {L_1}^2\right) & -\left(\frac{L_1 L_2 m_2 \cos\theta_2}{2}\right) & 0 \\ -\left(\frac{L_1 L_2 m_2 \cos\theta_2}{2}\right) & \left(\frac{{L_2}^2 m_2}{4} + I_{zz_2}\right) & 0 \\ 0 & 0 & 0 \end{bmatrix} \quad (2.73)$$

$$D(\theta_3) = m_3 {A_3}^T A_3 + {B_3}^T I_3 B_3 \quad (2.74)$$

To simplify the equations of DLRIP, Table 2.6 gives the employed parameters used in this section.

Table 2.6. Simplified parameters description of the DLRIP

Parameters	Description	Parameters	Description
a_1	${L_3}^2 m_3$	a_8	$L_2 L_3 m_3$
a_2	${L_2}^2 m_2$	a_9	$L_1 L_2 m_2$
a_3	${L_1}^2 m_1$	a_{10}	$L_1 L_2 m_3$
a_4	${L_2}^2 m_3$	a_{11}	$L_1 L_3 m_3$
a_5	${L_1}^2 m_2$	a_{12}	$L_2 g m_2$
a_6	${L_1}^2 m_3$	a_{13}	$L_2 g m_3$
a_7	${L_3}^2 m_3$	a_{14}	$L_3 g m_3$

$$D^3{}_{11} = \frac{I_{zz3}}{2} + a_6 + \frac{a_4}{2} + \frac{a_7}{8} - \frac{I_{zz3}\cos(2\theta_2 + 2\theta_3)}{2} - \frac{a_4 \cos(2\theta_2)}{2} - \frac{a_7 \cos(2\theta_2 + 2\theta_3)}{8} - \frac{a_8 \cos(\theta_3)}{2} - \frac{a_8 \cos(2\theta_2 + \theta_3)}{2} \quad (2.75)$$

$$D^3{}_{12} = -\frac{a_{11}\cos(\theta_2 + \theta_3) + 2\, a_{10} \cos\theta_2}{2} \quad (2.76)$$

$$D^3{}_{13} = -\frac{a_{11}\cos(\theta_2 + \theta_3)}{2} \quad (2.77)$$

$$D^3{}_{22} = a_4 + a_8 \cos\theta_3 + \frac{a_1}{4} + I_{zz3} \quad (2.78)$$

$$D^3{}_{23} = \frac{a_1}{4} + \frac{a_8 \cos\theta_3}{2} + I_{zz3} \quad (2.79)$$

$$D^3{}_{33} = \frac{a_7}{4} + I_{zz3} \tag{2.80}$$

$$D^3{}_{21} = D^3{}_{12}\,, D^3{}_{31} = D^3{}_{13} \tag{2.81}$$

The expression of $D(\theta_3)$ matrix is given in equation (2.82)

$$D(\theta_3) = \begin{bmatrix} D^3{}_{11} & D^3{}_{12} & D^3{}_{13} \\ D^3{}_{21} & D^3{}_{22} & D^3{}_{23} \\ D^3{}_{31} & D^3{}_{32} & D^3{}_{33} \end{bmatrix} \tag{2.82}$$

The expression of the mass matrix of the DLRIP system is given as follows :

$$D(\theta) = D(\theta_1) + D(\theta_2) + D(\theta_3) \tag{2.83}$$

$$D_{11} = I_{zz_1} + \frac{I_{zz3}}{2} + a_6 + \frac{a_4}{2} + \frac{a_7}{8} - \frac{I_{zz3}\cos(2\theta_2 + 2\theta_3)}{2} - \frac{a_4\cos(2\theta_2)}{2} + \frac{a_3}{4}$$
$$- \frac{a_7\cos(2\theta_2 + 2\theta_3)}{8}\frac{a_8\cos(\theta_3)}{2} - \frac{a_8\cos(2\theta_2 + \theta_3)}{2} + \left(\frac{a_2\sin^2\theta_2}{4} + a_5\right) \tag{2.84}$$

$$D_{12} = -\frac{a_{11}\cos(\theta_2 + \theta_3) + 2\,a_{10}\cos\theta_2}{2} + -\left(\frac{a_9\cos\theta_2}{2}\right) \tag{2.85}$$

$$D_{13} = -\frac{a_{11}\cos(\theta_2 + \theta_3)}{2} \tag{2.86}$$

$$D_{22} = a_4 + a_8\cos\theta_3 + \frac{a_1}{4} + I_{zz3} + \left(\frac{a_2}{4} + I_{zz_2}\right) \tag{2.87}$$

$$D_{23} = \frac{a_1}{4} + \frac{a_8\cos\theta_3}{2} + I_{zz3} \tag{2.89}$$

$$D_{33} = \frac{a_7}{4} + I_{zz3} \tag{2.90}$$

$$D_{21} = D_{12}\,, D_{31} = D_{13} \tag{2.91}$$

$$D(\theta) = \begin{bmatrix} D_{11} & D_{12} & D_{13} \\ D_{21} & D_{22} & D_{23} \\ D_{31} & D_{32} & D_{33} \end{bmatrix} \tag{2.92}$$

The elements of the velocity coupling matrix of the first link, are calculated as follows:

$$C^1{}_{11} = \frac{1}{2}\frac{\partial}{\partial\theta_1} D_{11}(\theta) = 0 \tag{2.93}$$

$$C^1{}_{12} = \frac{1}{2}\frac{\partial}{\partial\theta_1} D_{12}(\theta) = 0 \tag{2.94}$$

$$C^1{}_{13} = \frac{1}{2}\frac{\partial}{\partial\theta_1} D_{13}(\theta) = 0 \tag{2.95}$$

$$C^1{}_{21} = \frac{\partial}{\partial\theta_2} D_{11}(\theta) - \frac{1}{2}\frac{\partial}{\partial\theta_1} D_{21}(\theta) = L_2 \sin(2\theta_2) + L_3 \sin(2\theta_2 + 2\theta_3)$$
$$+\frac{a_2 \sin 2\theta_2}{4} + a_4 \sin 2\theta_2 + \frac{a_2 \sin(2\theta_2 + 2\theta_3)}{4} + a_8 \sin\sin(2\theta_2 + 2\theta_3) \tag{2.96}$$

$$C^1{}_{22} = \frac{\partial}{\partial\theta_2} D_{12}(\theta) - \frac{1}{2}\frac{\partial}{\partial\theta_1} D_{22}(\theta)$$
$$= \frac{a_{11}\sin(\theta_2 + \theta_3) + a_9 \sin\theta_2 + 2\,a_{10}\sin\theta_2}{2} \tag{2.97}$$

$$C^1{}_{23} = \frac{\partial}{\partial\theta_2} D_{13}(\theta) - \frac{1}{2}\frac{\partial}{\partial\theta_1} D_{23}(\theta) = \frac{a_{11}\sin(\theta_2 + \theta_3)}{2} \tag{2.98}$$

$$C^1{}_{31} = \frac{\partial}{\partial\theta_3} D_{11}(\theta) - \frac{1}{2}\frac{\partial}{\partial\theta_1} D_{31}(\theta)$$
$$= I_{zz3}\sin(2\theta_2 + 2\theta_3) + \frac{a_1 \sin(2\theta_2 + 2\theta_3)}{4} + \frac{a_8 \sin\theta_3}{2} + \frac{a_8 \sin(2\theta_2 + \theta_3)}{2} \tag{2.99}$$

$$C^1{}_{32} = \frac{\partial}{\partial\theta_3} D_{12}(\theta) - \frac{1}{2}\frac{\partial}{\partial\theta_1} D_{32}(\theta) = \frac{a_{11}\sin(\theta_2 + \theta_3)}{2} \tag{2.100}$$

$$C^1{}_{33} = \frac{\partial}{\partial\theta_3} D_{13}(\theta) - \frac{1}{2}\frac{\partial}{\partial\theta_1} D_{33}(\theta) = \frac{a_{11}\sin(\theta_2 + \theta_3)}{2} \tag{2.101}$$

The velocity coupling matrix of the first link may be given in equation (2.102).

$$C_1 = \begin{bmatrix} C^1{}_{11} & C^1{}_{12} & C^1{}_{13} \\ C^1{}_{21} & C^1{}_{22} & C^1{}_{23} \\ C^1{}_{31} & C^1{}_{32} & C^1{}_{33} \end{bmatrix} \tag{2.102}$$

The elements of the velocity coupling matrix of the second link, are calculated as follows:

$$C^2{}_{11} = \frac{\partial}{\partial\theta_1} D_{21}(\theta) - \frac{1}{2}\frac{\partial}{\partial\theta_2} D_{11}(\theta)$$

$$= -\frac{I_{zz2}\sin(2\theta_2)}{2} - \frac{I_{zz3}\sin(2\theta_2 + 2\theta_3)}{2} - \frac{a_2\sin(2\theta_2)}{8}$$
$$-\frac{a_4\sin(2\theta_2)}{2} - \frac{a_1\sin(2\theta_2 + 2\theta_3)}{8} - \frac{a_8\sin(2\theta_2 + \theta_3)}{2} \quad (2.103)$$

$$C^2{}_{12} = \frac{\partial}{\partial\theta_1} D_{22}(\theta) - \frac{1}{2}\frac{\partial}{\partial\theta_2} D_{12}(\theta)$$
$$= \frac{-a_{11}\sin(\theta_2 + \theta_3) - a_9\sin\theta_2 - 2a_{10}\sin\theta_2}{4} \quad (2.104)$$

$$C^2{}_{13} = \frac{\partial}{\partial\theta_1} D_{22}(\theta) - \frac{1}{2}\frac{\partial}{\partial\theta_2} D_{12}(\theta) = \frac{-a_{11}\sin(\theta_2 + \theta_3)}{4} \quad (2.105)$$

$$C^2{}_{21} = \frac{1}{2}\frac{\partial}{\partial\theta_2} D_{21}(\theta) = \frac{1}{4}(a_{11}\sin(\theta_2 + \theta_3) + a_9\sin\theta_2 + 2\,a_{10}\sin\theta_2) \quad (2.106)$$

$$C^2{}_{22} = \frac{1}{2}\frac{\partial}{\partial\theta_2} D_{22}(\theta) = 0 \quad (2.107)$$

$$C^2{}_{23} = \frac{1}{2}\frac{\partial}{\partial\theta_2} D_{23}(\theta) = 0 \quad (2.108)$$

$$C^2{}_{31} = \frac{\partial}{\partial\theta_3} D_{21}(\theta) - \frac{1}{2}\frac{\partial}{\partial\theta_2} D_{31}(\theta) = \frac{a_{11}\sin(\theta_2 + \theta_3)}{4} \quad (2.109)$$

$$C^2{}_{32} = \frac{\partial}{\partial\theta_3} D_{22}(\theta) - \frac{1}{2}\frac{\partial}{\partial\theta_2} D_{32}(\theta) = -a_8\sin\theta_3 \quad (2.110)$$

$$C^2{}_{33} = \frac{\partial}{\partial\theta_3} D_{23}(\theta) - \frac{1}{2}\frac{\partial}{\partial\theta_2} D_{33}(\theta) = \frac{-a_8\sin\theta_3}{2} \quad (2.111)$$

The velocity coupling matrix of the second link can be given in equation (2.112)

$$C_2 = \begin{bmatrix} C^2{}_{11} & C^2{}_{12} & C^2{}_{13} \\ C^2{}_{21} & C^2{}_{22} & C^2{}_{23} \\ C^2{}_{31} & C^2{}_{32} & C^2{}_{33} \end{bmatrix} \tag{2.112}$$

The elements of the velocity coupling matrix of the third link are calculated as follows:

$$C^3{}_{11} = \frac{\partial}{\partial\theta_1} D_{31}(\theta) - \frac{1}{2}\frac{\partial}{\partial\theta_3} D_{11}(\theta) = \frac{a_{15}\sin\theta_3}{4} - \frac{a_1 \sin(2\theta_2 + 2\theta_3)}{8}$$
$$- \frac{I_{zz3}\sin(2\theta_2 + 2\theta_3)}{2} - \frac{a_8 \sin(2\theta_2 + \theta_3)}{4} \tag{2.113}$$

$$C^3{}_{12} = \frac{\partial}{\partial\theta_1} D_{32}(\theta) - \frac{1}{2}\frac{\partial}{\partial\theta_3} D_{12}(\theta) = -\frac{a_{11}\sin(\theta_2 + \theta_3)}{4} \tag{2.114}$$

$$C^3{}_{13} = \frac{\partial}{\partial\theta_1} D_{33}(\theta) - \frac{1}{2}\frac{\partial}{\partial\theta_3} D_{13}(\theta) = \frac{-a_{11}\sin(\theta_2 + \theta_3)}{4} \tag{2.115}$$

$$C^3{}_{21} = \frac{\partial}{\partial\theta_2} D_{31}(\theta) - \frac{1}{2}\frac{\partial}{\partial\theta_3} D_{21}(\theta) = \frac{a_{11}\sin(\theta_2 + \theta_3)}{4} \tag{2.116}$$

$$C^3{}_{22} = \frac{\partial}{\partial\theta_2} D_{32}(\theta) - \frac{1}{2}\frac{\partial}{\partial\theta_3} D_{22}(\theta) = \frac{a_8 \sin\theta_3}{2} \tag{2.117}$$

$$C^3{}_{23} = \frac{\partial}{\partial\theta_2} D_{33}(\theta) - \frac{1}{2}\frac{\partial}{\partial\theta_3} D_{23}(\theta) = \frac{a_8 \sin\theta_3}{2} \tag{2.118}$$

$$C^3{}_{31} = \frac{1}{2}\frac{\partial}{\partial\theta_3} D_{31}(\theta) = \frac{a_{11}\sin(\theta_2 + \theta_3)}{4} \tag{2.119}$$

$$C^3{}_{32} = \frac{1}{2}\frac{\partial}{\partial\theta_3} D_{32}(\theta) = \frac{-a_8 \sin\theta_3}{4} \tag{2.120}$$

$$C^3{}_{33} = \frac{1}{2}\frac{\partial}{\partial\theta_3} D_{33}(\theta) = 0 \tag{2.121}$$

The velocity coupling matrix of the third link may be given in equation (2.122)

$$C_3 = \begin{bmatrix} C^3{}_{11} & C^3{}_{12} & C^3{}_{13} \\ C^3{}_{21} & C^3{}_{22} & C^3{}_{23} \\ C^3{}_{31} & C^3{}_{32} & C^3{}_{33} \end{bmatrix} \tag{2.122}$$

In order to find the Coriolis and Centripetal force vector of the DLRIP, each element of the velocity coupling matrices (C_1, C_2 and C_3) need to verify the equality of the elements of the following matrices.

$$\begin{bmatrix} C^1{}_{11} & C^1{}_{12} & C^1{}_{13} \\ C^1{}_{21} & C^1{}_{22} & C^1{}_{23} \\ C^1{}_{31} & C^1{}_{32} & C^1{}_{33} \end{bmatrix} = \begin{bmatrix} \dot{\theta_1}^2 & \dot{\theta_1}\dot{\theta_2} & \dot{\theta_1}\dot{\theta_3} \\ \dot{\theta_1}\dot{\theta_2} & \dot{\theta_2}^2 & \dot{\theta_2}\dot{\theta_3} \\ \dot{\theta_3}\dot{\theta_1} & \dot{\theta_3}\dot{\theta_2} & \dot{\theta_3}^2 \end{bmatrix} \tag{2.123}$$

$$\begin{bmatrix} C^2{}_{11} & C^2{}_{12} & C^2{}_{13} \\ C^2{}_{21} & C^2{}_{22} & C^2{}_{23} \\ C^2{}_{31} & C^2{}_{32} & C^2{}_{33} \end{bmatrix} = \begin{bmatrix} \dot{\theta_1}^2 & \dot{\theta_1}\dot{\theta_2} & \dot{\theta_1}\dot{\theta_3} \\ \dot{\theta_1}\dot{\theta_2} & \dot{\theta_2}^2 & \dot{\theta_2}\dot{\theta_3} \\ \dot{\theta_3}\dot{\theta_1} & \dot{\theta_3}\dot{\theta_2} & \dot{\theta_3}^2 \end{bmatrix} \tag{2.124}$$

$$\begin{bmatrix} C^3{}_{11} & C^3{}_{12} & C^3{}_{13} \\ C^3{}_{21} & C^3{}_{22} & C^3{}_{23} \\ C^3{}_{31} & C^3{}_{32} & C^3{}_{33} \end{bmatrix} = \begin{bmatrix} \dot{\theta_1}^2 & \dot{\theta_1}\dot{\theta_2} & \dot{\theta_1}\dot{\theta_3} \\ \dot{\theta_1}\dot{\theta_2} & \dot{\theta_2}^2 & \dot{\theta_2}\dot{\theta_3} \\ \dot{\theta_3}\dot{\theta_1} & \dot{\theta_3}\dot{\theta_2} & \dot{\theta_3}^2 \end{bmatrix} \tag{2.125}$$

The elements of the Coriolis and Centripetal force vector are given as follows:

$$\begin{aligned} C_{11} = {} & I_{zz2}\,\dot{\theta_1}\dot{\theta_2}\sin 2\theta_2 + I_{zz3}\,\dot{\theta_1}\dot{\theta_2}\sin(2\theta_2 + 2\theta_3) + I_{zz3}\,\dot{\theta_1}\dot{\theta_3}\sin(2\theta_2 + 2\theta_3) \\ & + a_{10}\,\dot{\theta_2}^2\sin\theta_2 + \frac{a_2\dot{\theta_1}\dot{\theta_2}\sin 2\theta_2}{4} + a_4\,\dot{\theta_1}\dot{\theta_2}\sin 2\theta_2 + \frac{a_7\dot{\theta_1}\dot{\theta_2}\sin(2\theta_2 + 2\theta_3)}{4} \\ & + \frac{a_7\dot{\theta_1}\dot{\theta_3}\sin(2\theta_2 + 2\theta_3)}{4} - \frac{a_{11}\dot{\theta_2}^2\sin(\theta_2 + \theta_3)}{2} + \frac{a_{11}\dot{\theta_3}^2\sin(\theta_2 + \theta_3)}{2} \\ & + \frac{a_9\dot{\theta_2}^2\sin\theta_2}{2} + a_{11}\,\dot{\theta_2}\dot{\theta_3}\sin(\theta_2 + \theta_3) + a_8\,\dot{\theta_1}\dot{\theta_2}\sin(2\theta_2 + 2\theta_3) \\ & + \frac{a_8\dot{\theta_1}\dot{\theta_3}\sin(2\theta_2 + \theta_3)}{2} - \frac{a_8\dot{\theta_1}\dot{\theta_3}\sin\theta_3}{2} \end{aligned} \tag{2.126}$$

$$\begin{aligned} C_{21} = {} & \frac{-I_{zz2}\dot{\theta_1}^2\sin 2\theta_2}{2} - \frac{I_{zz3}\dot{\theta_1}^2\sin(2\theta_2 + 2\theta_3)}{2} - \frac{a_2\dot{\theta_1}^2\sin 2\theta_2}{8} \\ & - \frac{a_1\dot{\theta_1}^2\sin(2\theta_2 + 2\theta_3)}{8} - \frac{a_4\dot{\theta_1}^2\sin 2\theta_2}{2} - \frac{a_8\dot{\theta_3}^2\sin\theta_3}{2} \\ & - \frac{a_8\dot{\theta_1}^2\sin(2\theta_2 + \theta_3)}{2} - a_8\dot{\theta_3}\dot{\theta_2}\sin\theta_3 \end{aligned} \tag{2.127}$$

$$C_{31} = \frac{a_8\,\dot{\theta_1}^2\sin\theta_3}{4} - \frac{a_1\dot{\theta_1}^2\sin(2\theta_2 + 2\theta_3)}{8} - \frac{I_{zz3}\dot{\theta_1}^2\sin(2\theta_2 + 2\theta_3)}{2}$$

$$+\frac{a_8\dot{\theta_2}^{\,2}\sin\theta_3}{2}-\frac{a_8\dot{\theta_1}^{\,2}\sin(2\theta_2+\theta_3)}{4} \tag{2.128}$$

The expression of Coriolis and Centripetal force vector is given in equation (2.129)

$$C(\theta,\dot{\theta})=\begin{bmatrix}C_{11}\\C_{21}\\C_{31}\end{bmatrix} \tag{2.129}$$

The gravity vector the DLRIP is given in equation (2.130)

$$G=\begin{bmatrix}0\\ \dfrac{-a_{14}\sin(\theta_2+\theta_3)-a_{12}\sin\theta_2-2a_{13}\sin\theta_2}{2}\\ -a_{14}\sin(\theta_2+\theta_3)\end{bmatrix}=\begin{bmatrix}0\\G_{21}\\G_{31}\end{bmatrix} \tag{2.130}$$

The DLRIP has some complex non-linear dynamic equations which can be written in a matrix form given in equation (2.131):

$$\begin{bmatrix}D_{11}&D_{12}&D_{13}\\D_{21}&D_{22}&D_{23}\\D_{31}&D_{32}&D_{33}\end{bmatrix}\begin{bmatrix}\ddot{\theta_1}\\\ddot{\theta_2}\\\ddot{\theta_3}\end{bmatrix}+\begin{bmatrix}C_{11}\\C_{21}\\C_{31}\end{bmatrix}+\begin{bmatrix}0\\G_{21}\\G_{31}\end{bmatrix}=\begin{bmatrix}\tau_1\\0\\0\end{bmatrix} \tag{2.131}$$

2.2.3. Jacobian matrix of the DLRIP

The linear and angular velocities of each link of the DLRIP are used to determine the Jacobian matrix. A formula to compute the Jacobian matrix of the DLRIP is given in equation (2.40) in section (2.1.3). J_v and J_w represents the Jacobian matrices obtained from the linear and angular velocities in the end-link, respectively. The linear velocities are given in equation (2.132).

$$\begin{aligned}{}^0_4V=\ {}^0_4R\,{}^4_4V&=\begin{bmatrix}\cos\theta_1\sin(\theta_2+\theta_3)&\cos\theta_1\cos(\theta_2+\theta_3)&-\sin\theta_1\\\sin(\theta_2+\theta_3)\sin\theta_1&\cos(\theta_2+\theta_3)\sin\theta_1&\cos\theta_1\\\cos(\theta_2+\theta_3)&-\sin(\theta_2+\theta_3)&0\end{bmatrix}\\ \times&\begin{bmatrix}L_2\sin\theta_3\dot{\theta_2}-L_1\sin(\theta_2+\theta_3)\,\dot{\theta_1}\\L_3\dot{\theta_2}+L_3\dot{\theta_3}-\cos(\theta_2+\theta_3)\ L_1\cos\dot{\theta_1}+L_2\cos\theta_3\dot{\theta_2}\\\dot{\theta_1}\,(\sin\theta_2L_2+L_3\sin(\theta_2+\theta_3)\ )\end{bmatrix}=\begin{bmatrix}{}^0_4V_1\\{}^0_4V_2\\{}^0_4V_3\end{bmatrix}\end{aligned} \tag{2.132}$$

The elements of the linear velocities vector (^0_4V) are given as follows:

$$
{}^{0}_{4}V_1 = \left(-L_1C_1 - S_1(L_2S_2 - L_3S_{23})\right)\dot{\theta_1} + \left(C_1(L_3C_{23} + L_3C_2)\right)\dot{\theta_2} + \left(L_3C_{23}C_1\right)\dot{\theta_3} \quad (2.133)
$$

$$
{}^{0}_{4}V_2 = \left(C_1(L_3 + L_2S_2 + S_{23}) - L_1S_1\right)\dot{\theta_1} + \left(S_1(L_3C_{23} + L_2C_2)\right)\dot{\theta_2} + (L_3C_{23}S_1)\dot{\theta_3} \quad (2.134)
$$

$$
{}^{0}_{4}V_3 = (-L_3S_{23} - L_2S_2)\,\dot{\theta_2} - (L_3S_{23})\,\dot{\theta_3} \quad (2.135)
$$

$$
{}^{0}_{4}V = \begin{bmatrix} -L_1C_1 - S_1(L_2S_2 - L_3S_{23}) & C_1(L_3C_{23} + L_3C_2) & L_3C_{23}C_1 \\ C_1(L_3 + L_2S_2 + S_{23}) - L_1S_1 & S_1(L_3C_{23} + L_2C_2) & L_3C_{23}S_1 \\ 0 & -L_3S_{23} - L_2S_2 & -L_3S_{23} \end{bmatrix} \begin{bmatrix} \dot{\theta_1} \\ \dot{\theta_2} \\ \dot{\theta_3} \end{bmatrix} \quad (2.136)
$$

Where

$$
C_1 = \cos\theta_1\,, S_1 = \sin\theta_1\,, C_2 = \cos\theta_2\,, S_2 = \sin\theta_2 \quad (2.137)
$$

$$
S_{23} = \sin(\theta_2 + \theta_3)\,, C_{23} = \cos(\theta_2 + \theta_3) \quad (2.138)
$$

The Jacobian matrix taken from the linear velocities is given in equation (2.139).

$$
J_{v_0}^{4}(\theta) = \begin{bmatrix} -L_1C_1 - S_1(L_2S_2 - L_3S_{23}) & C_1(L_3C_{23} + L_3C_2) & L_3C_{23}C_1 \\ C_1(L_3 + L_2S_2 + S_{23}) - L_1S_1 & S_1(L_3C_{23} + L_2C_2) & L_3C_{23}S_1 \\ 0 & -L_3S_{23} - L_2S_2 & -L_3S_{23} \end{bmatrix} \quad (2.140)
$$

The angular velocities matrix of the system is given in equation (2.141)

$$
{}^{0}_{4}w = {}^{0}_{4}R\,{}^{4}_{4}w = \begin{bmatrix} C_1\,S_{23} & C_1\,C_{23} & -S_1 \\ S_{23}S_1 & S_1\,C_{23} & -C_1 \\ C_{23} & -S_{23} & 0 \end{bmatrix} \begin{bmatrix} \dot{\theta}_1C_{23} \\ -\dot{\theta}_1S_{23} \\ \dot{\theta}_2 + \dot{\theta}_3 \end{bmatrix}
$$

$$
{}^{0}_{4}w = \begin{bmatrix} -S_1\left(\dot{\theta}_2 + \dot{\theta}_3\right) \\ C_1\left(\dot{\theta}_2 + \dot{\theta}_3\right) \\ \dot{\theta}_1 \end{bmatrix} \quad (2.141)
$$

The Jacobian matrix taken from the angular velocities is given as follows:

$$
J_{w_0}^{4}(\theta) = \begin{bmatrix} 0 & -\sin\theta_1 & -\sin\theta_1 \\ 0 & \cos\theta_1 & \cos\theta_1 \\ 1 & 0 & 0 \end{bmatrix} \quad (2.142)
$$

The Jacobian matrix taken from the linear and angular velocities is given in equation (2.143).

$$J_0^4(\theta) = \begin{bmatrix} -L_1C_1 - S_1(L_2S_2 - L_3S_{23}) & C_1(L_3C_{23} + L_3C_2) & L_3C_{23}C_1 \\ C_1(L_3 + L_2S_2 + S_{23}) - L_1S_1 & S_1(L_3C_{23} + L_2C_2) & L_3C_{23}S_1 \\ 0 & -L_3S_{23} - L_2S_2 & -L_3S_{23} \\ 0 & -S_1 & S_1 \\ 0 & C_1 & C_1 \\ 1 & 0 & 0 \end{bmatrix} \quad (2.143)$$

Furthermore, using the determinant of the Jacobian matrix, $w = \left|\det\left(J_0^4(\theta) \times J_0^4(\theta)^T\right)\right|$, the optimal length of each link of the DLRIP is estimated using the PSO optimization algorithm. The optimal lengths are given in Table 2.4.

2.2.4 Dynamic simulation of the DLRIP

According to the equation (2.131), the expression for the angular acceleration vector ($\ddot{\theta}$) can be given in equation (2.144). The three equations of $\ddot{\theta}_1$, $\ddot{\theta}_2$ and $\ddot{\theta}_3$ are derived and simulated in Matlab/Simulink. The Matlab code of the mathematical expression of the three equations is given in the appendix. Figure 2.6 shows the non-linear mathematical model in Matlab/Simulink.

$$\begin{bmatrix} \ddot{\theta}_1 \\ \ddot{\theta}_2 \\ \ddot{\theta}_3 \end{bmatrix} = \begin{bmatrix} D_{11} & D_{12} & D_{13} \\ D_{21} & D_{22} & D_{23} \\ D_{31} & D_{32} & D_{33} \end{bmatrix}^{-1} \left(\begin{bmatrix} \tau_1 \\ 0 \\ 0 \end{bmatrix} - \begin{bmatrix} C_{11} \\ C_{21} \\ C_{31} \end{bmatrix} - \begin{bmatrix} 0 \\ G_{21} \\ G_{31} \end{bmatrix} \right) \quad (2.144)$$

In order to verify the mathematical model, a mechanical dynamic model of the DLRIP was developed by using the MATLAB/SimMechanics toolbox. MATLAB/SimMechanics model of the DLRIP is shown in Figure 2.7 (a). Different views from virtual reality model of the DLRIP in Matlab Simulink is shown in Figure 2.7 (b). Furthermore, for both model, the initial conditions of pendulums' joint positions are chosen as follows $\theta_1 = 0\,°$, $\theta_2 = 20\,°$ and $\theta_3 = 30\,°$. The obtained results from both MATLAB/SimMechanics and the mathematical models match exactly. Figure 2.8 illustrates a comparison of the three joint positions obtained from simulation mathematical and the SimMechanics models without frictions. The simulations are performed by the sampling time 1ms and 5s simulation time. A numerical method Bogacki-Shampine solver is selected with fixed-step.

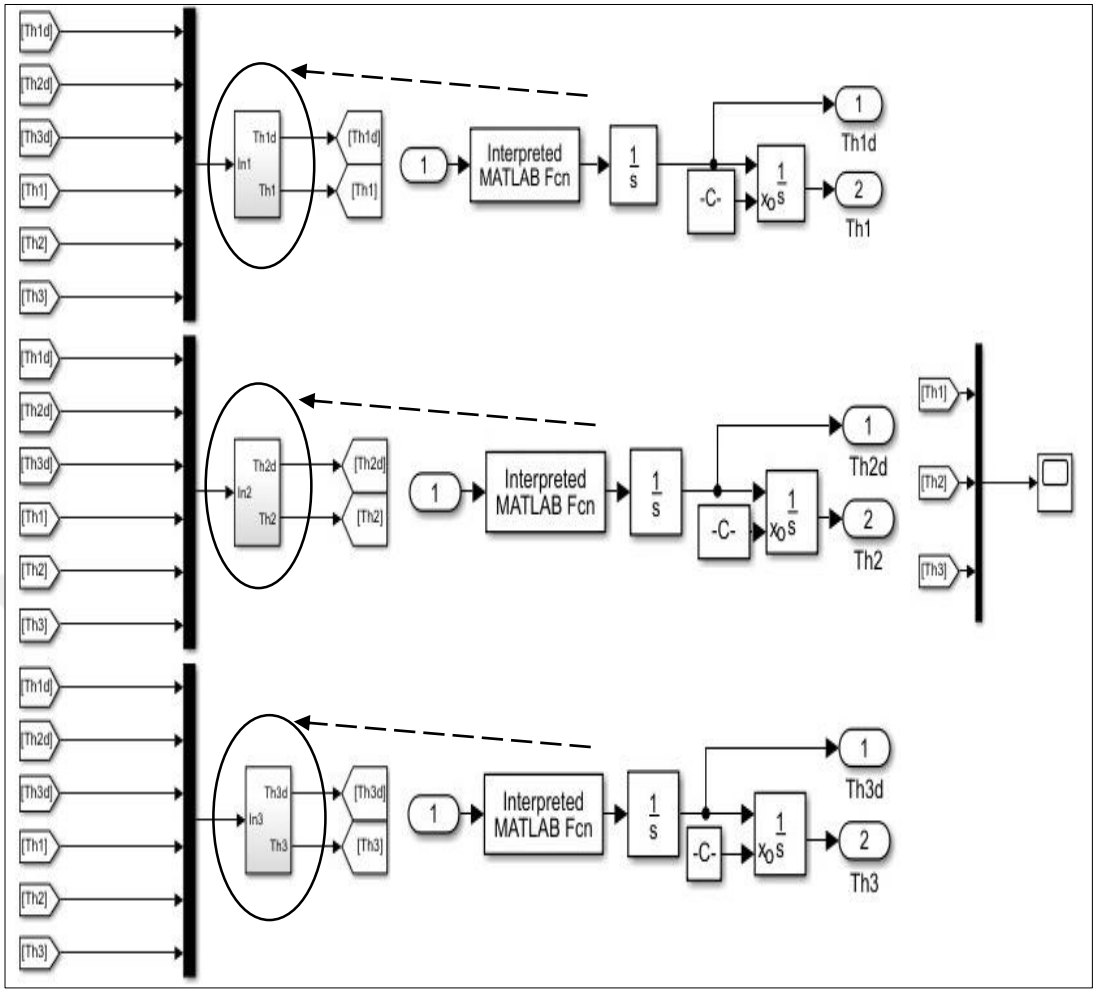

Figure 2.6. Mathematical model of the DLRIP in Matlab/Simulink

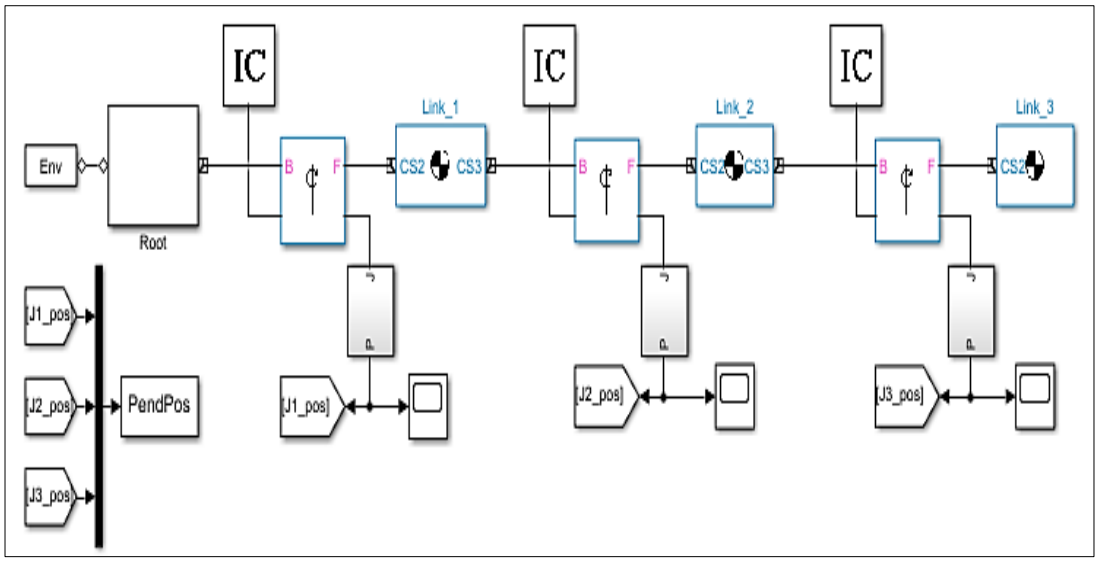

(a)

Figure 2.7. (a) MATLAB/SimMechanics model of the DLRIP, (b) Different views from virtual reality model of the DLRIP in Matlab Simulink

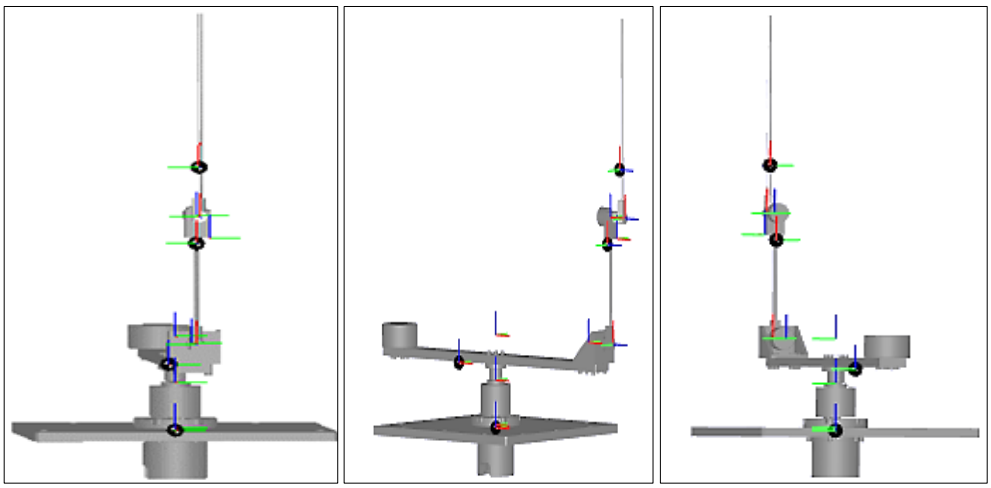

(b)

Figure 2.7.(Cont.) (a) MATLAB/SimMechanics model of the DLRIP, (b) Different views from virtual reality model of the DLRIP in Matlab Simulink

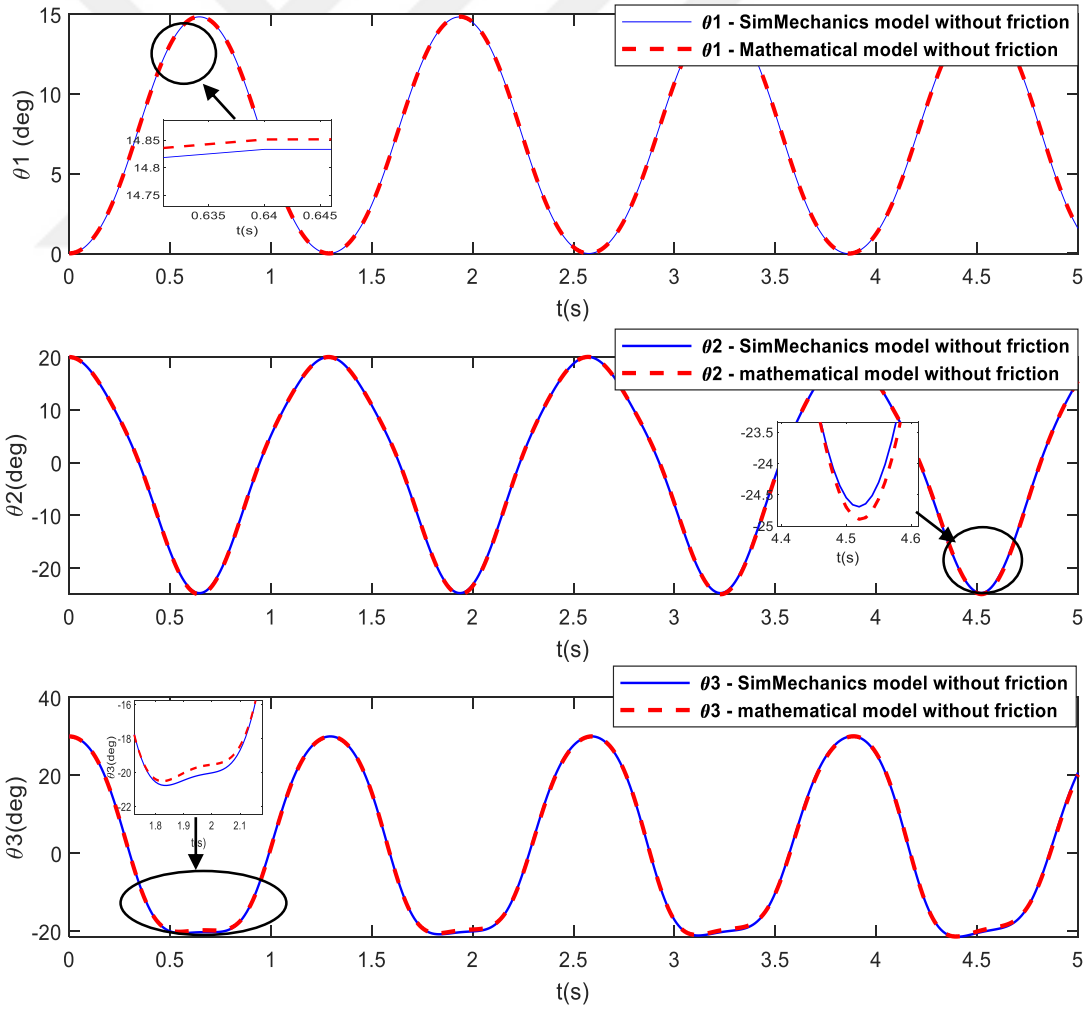

Figure 2.8. Comparison of the pendulum joint positions obtained from the analytic mathematical model and SimMechanics numerical model of the DLRIP

2.3. Modeling of the TLRIP

2.3.1. Kinematic model of the TLRIP

Solid 3D model and kinematics parameters of the TLRIP are shown in Figure 2.9. TLRIP comprises a horizontal rotary link and three pendulum links. A direct drive brushless DC torque motor servo system is mounted to provide torque to the horizontal arm to control the system. The rotary arm rotates in the horizontal plane. Three pendulum links are attached in serial mounted in the extremity of the horizontal arm. Three pendulum links move as an inverted pendulum in a plane perpendicular to the rotary link. A balance mass is attached to the other extremity of the horizontal arm to maintain the balance inertia of the system. The angle of the rotary link (θ_1) and the angles of the three pendulum links (θ_2,θ_3 and θ_4) of the TLRIP are illustrated in Figure 2.9. The kinematic model of the system is derived based on the DH convention. Rotation and homogeneous transformation matrices between coordinates the TLRIP are calculated. The parameters and variables of the model are given in Table 2.1 (in section 2.1.1). The physical parameters of the TLRIP are given in Table 2.7. DH parameters of the TLRIP are given in Table 2.8.

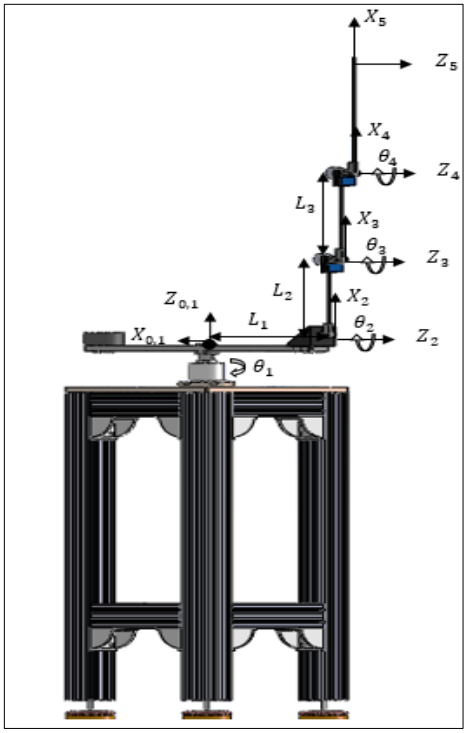

Figure 2.9. Solid 3D model and kinematic parameters of the TLRIP

Table 2.7. Physical parameters of the TLRIP

Parameters	Values	Parameters	Values	Parameters	Values
m_1	3.1129 [kg]	L_1	0.4202 [m]	I_{zz1}	0.25 [kg · m^2]
m_2	0.7268 [kg]	L_2	0.2675 [m]	I_{zz2}	0.04 [kg · m^2]
m_3	0.6789 [kg]	L_3	0.3650 [m]	I_{zz3}	0.05 [kg · m^2]
m_4	0.4500 [kg]	L_4	0.4240 [m]	I_{zz4}	0.05 [kg · m^2]
m_B	3.1469 [kg]	$b_{1,2,3,4}$	0.0024 [N-m-s/Rad]	g	9.81 [N kg^{-1}]

Table 2.8. DH-Parameters of the TLRIP

Coordinate	α_{i-1}	a_{i-1}	d_i	θ_i
1	0	0	0	θ_1
2	$-\frac{\pi}{2}$	0	L_1	$\theta_2 - \frac{\pi}{2}$
3	0	L_2	0	0
4	0	L_3	0	0
5	0	L_4	0	0

The expression of the homogeneous transformation matrix from a coordinate attached to an *i*-th link to a coordinate attached to *i*-1-th link, $i = 1,2,3,4,5$. The expression of ${}^{i-1}_{i}T$ is given in equation (2.1). The homogeneous transformation matrix of the TLRIP is derived in equation (2.145) using the DH-parameters in Table 2.8.

$$ {}^{0}_{5}T = {}^{0}_{1}T\,{}^{1}_{2}T\,{}^{2}_{3}T\,{}^{3}_{4}T\,{}^{4}_{5}T \tag{2.145} $$

Where

$$ {}^{0}_{1}T = \begin{bmatrix} \cos\theta_1 & -\sin\theta_1 & 0 & 0 \\ \sin\theta_1 & \cos\theta_1 & 0 & 0 \\ 0 & 0 & 1 & 0 \\ 0 & 0 & 0 & 1 \end{bmatrix} {}^{1}_{2}T = \begin{bmatrix} \sin\theta_2 & \cos\theta_2 & 0 & 0 \\ 0 & 0 & 1 & L_1 \\ \cos\theta_2 & -\sin\theta_2 & 0 & 0 \\ 0 & 0 & 0 & 1 \end{bmatrix} \tag{2.146} $$

$$ {}^{2}_{3}T = \begin{bmatrix} \cos\theta_3 & -\sin\theta_3 & 0 & L_2 \\ \sin\theta_3 & \cos\theta_3 & 0 & 0 \\ 0 & 0 & 1 & 0 \\ 0 & 0 & 0 & 1 \end{bmatrix} {}^{3}_{4}T = \begin{bmatrix} \cos\theta_4 & -\sin\theta_4 & 0 & L_3 \\ \sin\theta_4 & \cos\theta_4 & 0 & 0 \\ 0 & 0 & 1 & 0 \\ 0 & 0 & 0 & 1 \end{bmatrix} \tag{2.147} $$

$$ {}^{4}_{5}T = \begin{bmatrix} 1 & 0 & 0 & L_4 \\ 0 & 1 & 0 & 0 \\ 0 & 0 & 1 & 0 \\ 0 & 0 & 0 & 1 \end{bmatrix} \tag{2.148} $$

$$ {}^{0}_{5}T = \begin{bmatrix} \frac{1}{2}S_{1234} + \frac{1}{2}S_{2134} & \frac{1}{2}C_{1234} + \frac{1}{2}C_{2134} & -S_1 & P_x \\ \frac{1}{2}C_{2134} - \frac{1}{2}C_{1234} & \frac{1}{2}S_{1234} - \frac{1}{2}S_{2134} & C\theta_1 & P_y \\ C_{234} & -S_{234} & 0 & P_y \\ 0 & 0 & 0 & 1 \end{bmatrix} \tag{2.149} $$

Where

$$ S_1 = \sin\theta_1 , C_1 = \cos\theta_1 , S_2 = \sin\theta_2, C_2 = \cos\theta_2, S_3 = \sin\theta_3 \tag{2.150} $$

$$ C_3 = \cos\theta_3, S\theta_4 = \sin\theta_4 , C\theta_4 = \cos\theta_4 , S_{234} = \sin(\theta_2 + \theta_3 + \theta_4) \tag{2.151} $$

$$ C_{234} = \cos(\theta_2 + \theta_3 + \theta_4), S_{1234} = \sin(\theta_1 + \theta_2 + \theta_3 + \theta_4) \tag{2.152} $$

$$ C_{1234} = \cos(\theta_1 + \theta_2 + \theta_3 + \theta_4) , C_{2134} = \cos(\theta_2 - \theta_1 + \theta_3 + \theta_4) \tag{2.153} $$

$$ S_{2134} = \sin(\theta_2 - \theta_1 + \theta_3 + \theta_4) \tag{2.154} $$

The elements of the position vector are given from the calculated homogeneous transformation matrix ${}^{0}_{5}T$ as follows:

$$ P_x = C_1S_2(L_2 + L_3C_3 + L_4C_3C_4 - L_4S_3S_4) + C_1C_2(L_3S_3 + L_4C_3S_4 + L_4C_4S_3) $$
$$ -L_1S_1 \tag{2.155} $$

$$ P_y = S_1S_2(L_2 + L_3C_3 + L_4C_3C_4 - L_4S_3S_4) $$
$$ +S_1C_2(L_3S_3 + L_4C_3S_4 + L_4C_4S_3) \tag{2.155} $$

$$ P_z = L_3\, C_{23} + L_2C_2 + L_4C_{234} \tag{2.156} $$

The expression of the position vector is given in equation (2.157).

$$ P_v = \begin{bmatrix} P_x \\ P_y \\ P_z \end{bmatrix} \tag{2.157} $$

2.3.2. Dynamic model of the TLRIP

The non-linear motion equations of this TLRIP are derived based on the DH convention and can be given in a matrix form, given in equation (2.7). The dynamic

equations of TLRIP system are derived using the "Euler-Lagrangian" method. The terms of each matrix of equation (2.7) are calculated using the equations (2.8-2.11). The elements of each matrix calculated are calculated as follows:

Δ_{h_1} , Δ_{h_2}, Δ_{h_3} and Δ_{h_4} are center of gravity vectors of the first, second, third and fourth links respectively. The four vectors are given according to the coordinate system of each link.

$$\Delta_{h_1} = \begin{bmatrix} 0 & \frac{L_1}{2} & 0 & 1 \end{bmatrix}^T \quad \Delta_{h_2} = \begin{bmatrix} \frac{L_2}{2} & 0 & 0 & 1 \end{bmatrix}^T \tag{2.158}$$

$$\Delta_{h_3} = \begin{bmatrix} \frac{L_3}{2} & 0 & 0 & 1 \end{bmatrix}^T \quad \Delta_{h_4} = \begin{bmatrix} \frac{L_4}{2} & 0 & 0 & 1 \end{bmatrix}^T \tag{2.159}$$

I_1, I_2, I_3 and I_4 are the inertia tensors of the first, second, third and fourth links, respectively.

$$I_1 = \begin{bmatrix} 0 & 0 & 0 \\ 0 & 0 & 0 \\ 0 & 0 & I_{zz_1} \end{bmatrix} I_2 = \begin{bmatrix} 0 & 0 & 0 \\ 0 & 0 & 0 \\ 0 & 0 & I_{zz_2} \end{bmatrix} I_3 = \begin{bmatrix} 0 & 0 & 0 \\ 0 & 0 & 0 \\ 0 & 0 & I_{zz_3} \end{bmatrix} I_4 = \begin{bmatrix} 0 & 0 & 0 \\ 0 & 0 & 0 \\ 0 & 0 & I_{zz_4} \end{bmatrix} \tag{2.160}$$

The coordinates of the mass center of each link are calculated and given as follows:

$$h_1 = {}^0_1T\,\Delta_{h_1} = \begin{bmatrix} -\frac{L_1 \sin\theta_1}{2} \\ \frac{L_1 \cos\theta_1}{2} \\ 0 \\ 1 \end{bmatrix} \quad h_2 = {}^0_2T\,\Delta_{h_2} = \begin{bmatrix} \frac{L_2 \cos\theta_1 \sin\theta_2}{2} - L_1 \sin\theta_1 \\ \frac{L_2 \sin\theta_1 \sin\theta_2}{2} + L_1 \cos\theta_1 \\ \frac{L_2 \cos\theta_2}{2} \\ 1 \end{bmatrix} \tag{2.161}$$

$$h_3 = {}^0_3T\,\Delta_{h_3}$$

$$= \begin{bmatrix} \frac{L_3 \cos\theta_1 \cos\theta_2 \sin\theta_3}{2} + \frac{L_3 \cos\theta_1 \cos\theta_3 \sin\theta_2}{2} + L_2 \cos\theta_1 \sin\theta_2 - L_1 \sin\theta_1 \\ \frac{L_3 \cos\theta_2 \sin\theta_1 \sin\theta_3}{2} + \frac{L_3 \cos\theta_3 \sin\theta_1 \sin\theta_2}{2} + L_2 \sin\theta_1 \sin\theta_2 + L_1 \cos\theta_1 \\ \frac{L_3 \cos(\theta_2 + \theta_3)}{2} + L_2 \cos\theta_2 \\ 1 \end{bmatrix} \tag{2.162}$$

$$h_4 = {}^0_4T\,\Delta_{h_4}$$

$$= \begin{bmatrix} C_1S_2\left(L_2 + L_3C_3 + \frac{L_4C_3C_4}{2} - \frac{L_4S_3S_4}{2}\right) + C_1C_2\left(L_3S_3 + \frac{L_4C_3S_4}{2} + \frac{L_4S_3C_4}{2}\right) - L_1S_1 \\ S_1S_2\left(L_2 + L_3C_3 + \frac{L_4C_3C_4}{2} - \frac{L_4S_3S_4}{2}\right) + C_2S_1\left(L_3S_3 + \frac{L_4C_3S_4}{2} + \frac{L_4S_3C_4}{2}\right) + L_1C_1 \\ L_3\,C_{23} + L_2\,C_2 + \frac{1}{2}\,L_4C_{234} \\ 1 \end{bmatrix} \quad (2.163)$$

To calculate the Jacobian matrix of the first link, the derivative of the vector h_1 is taken according to θ_1 , θ_2 , θ_3 and θ_4. The first link is a rotational link, so $\xi_1 = 1$, $z^1 = {}^0_1R\, i^4 = [0 \quad 0 \quad 1]^T$ and $b_1 = \xi_1 z^1 = [0 \quad 0 \quad 1]^T$. The Jacobian matrix of the first link is given as follows:

$$J_1 = \begin{bmatrix} \frac{\partial}{\partial\theta_1}\left(-\frac{L_1\sin\theta_1}{2}\right) & \frac{\partial}{\partial\theta_2}\left(-\frac{L_1\sin\theta_1}{2}\right) & \frac{\partial}{\partial\theta_3}\left(-\frac{L_1\sin\theta_1}{2}\right) & \frac{\partial}{\partial\theta_4}\left(-\frac{L_1\sin\theta_1}{2}\right) \\ \frac{\partial}{\partial\theta_1}\left(\frac{L_1\cos\theta_1}{2}\right) & \frac{\partial}{\partial\theta_2}\left(\frac{L_1\cos\theta_1}{2}\right) & \frac{\partial}{\partial\theta_3}\left(\frac{L_1\cos\theta_1}{2}\right) & \frac{\partial}{\partial\theta_4}\left(\frac{L_1\cos\theta_1}{2}\right) \\ 0 & 0 & 0 & 0 \\ 0 & 0 & 0 & 0 \\ 0 & 0 & 0 & 0 \\ 1 & 0 & 0 & 0 \end{bmatrix}$$

$$= \begin{bmatrix} -\frac{L_1\cos\theta_1}{2} & 0 & 0 & 0 \\ -\frac{L_1\sin\theta_1}{2} & 0 & 0 & 0 \\ 0 & 0 & 0 & 0 \\ 0 & 0 & 0 & 0 \\ 0 & 0 & 0 & 0 \\ 1 & 0 & 0 & 0 \end{bmatrix} \quad (2.164)$$

Th Jacobian matrix of the first link can be written in two matrices $A_1$and B_1.

$$A_1 = \begin{bmatrix} -\frac{L_1\cos\theta_1}{2} & 0 & 0 & 0 \\ -\frac{L_1\sin\theta_1}{2} & 0 & 0 & 0 \\ 0 & 0 & 0 & 0 \end{bmatrix} \text{ and } B_1 = \begin{bmatrix} 0 & 0 & 0 & 0 \\ 0 & 0 & 0 & 0 \\ 1 & 0 & 0 & 0 \end{bmatrix} \quad (2.165)$$

To calculate the Jacobian matrix of the second link, the derivative of the vector h_2 is taken according to θ_1 , θ_2 , θ_3 and θ_4. The second link is a rotational link, so $\xi_2 = 1$, $z^2 = {}^0_2R\, i^4 = [0 \quad 0 \quad 1]^T$ and $b_2 = \xi_2 z^2 = [0 \quad 0 \quad 1]^T$. The Jacobian matrix of the second link is given as follows:

$J_2 =$

$$\begin{bmatrix} \frac{\partial}{\partial\theta_1}\left(\frac{L_2\,C_1\,S_2}{2} - L_1S_1\right) & \frac{\partial}{\partial\theta_2}\left(\frac{L_2\,C_1\,S_2}{2} - L_1S_1\right) & \frac{\partial}{\partial\theta_3}\left(\frac{L_2\,C_1\,S_2}{2} - L_1S_1\right) & \frac{\partial}{\partial\theta_4}\left(\frac{L_2\,C_1\,S_2}{2} - L_1S_1\right) \\ \frac{\partial}{\partial\theta_1}\left(\frac{L_2\,S_1\,S_2}{2} + L_1C_1\right) & \frac{\partial}{\partial\theta_2}\left(\frac{L_2\,S_1\,S_2}{2} + L_1C_1\right) & \frac{\partial}{\partial\theta_3}\left(\frac{L_2\,S_1\,S_2}{2} + L_1C_1\right) & \frac{\partial}{\partial\theta_4}\left(\frac{L_2\,S_1\,S_2}{2} + L_1C_1\right) \\ \frac{\partial}{\partial\theta_1}\left(\frac{L_2C_2}{2}\right) & \frac{\partial}{\partial\theta_2}\left(\frac{L_2C_2}{2}\right) & \frac{\partial}{\partial\theta_3}\left(\frac{L_2C_2}{2}\right) & \frac{\partial}{\partial\theta_3}\left(\frac{L_2C_2}{2}\right) \\ 0 & -\sin\theta_1 & 0 & 0 \\ 0 & \cos\ \theta_1 & 0 & 0 \\ 1 & 0 & 0 & 0 \end{bmatrix}$$

$$= \begin{bmatrix} -\frac{L_2\sin\theta_1\sin\theta_2}{2} - L_1\cos\theta_1 & \frac{L_2\cos\theta_1\cos\theta_2}{2} & 0 & 0 & 0 \\ \frac{L_2\cos\theta_1\sin\theta_2}{2} - L_1\sin\theta_1 & \frac{L_2\cos\theta_2\cos\theta_1}{2} & 0 & 0 & 0 \\ 0 & \frac{-L_2\sin\theta_2}{2} & 0 & 0 & 0 \\ 0 & -\sin\theta_1 & 0 & 0 & 0 \\ 0 & \cos\ \theta_1 & 0 & 0 & 0 \\ 1 & 0 & 0 & 0 & 0 \end{bmatrix} \qquad (2.166)$$

The Jacobian matrix of the second link can be written in two matrices A_2 and B_2.

$$A_2 = \begin{bmatrix} -\frac{L_2\sin\theta_1\sin\theta_2}{2} - L_1\cos\theta_1 & \frac{L_2\cos\theta_1\cos\theta_2}{2} & 0 & 0 \\ \frac{L_2\cos\theta_1\sin\theta_2}{2} - L_1\sin\theta_1 & \frac{L_2\cos\theta_2\cos\theta_1}{2} & 0 & 0 \\ 0 & \frac{-L_2\sin\theta_2}{2} & 0 & 0 \end{bmatrix} \qquad (2.167)$$

$$B_2 = \begin{bmatrix} 0 & -\sin\theta_1 & 0 & 0 \\ 0 & \cos\ \theta_1 & 0 & 0 \\ 1 & 0 & 0 & 0 \end{bmatrix} \qquad (2.168)$$

To calculate the Jacobian matrix of the third link, the derivative of the vector h_3 is taken according to θ_1 , θ_2 , θ_3 and θ_4.

The third link is a rotational link, so $\xi_3 = 1$, $z^3 = {}^0_3R\,i^4 = [-\sin\theta_1 \quad \cos\theta_1 \quad 1]^T$ and $b_3 = \xi_3 z^3 = [0 \quad 0 \quad 1]^T$. The Jacobian matrix of the third link is given as follows:

$$J_3 =$$

$$\begin{bmatrix} \frac{\partial}{\partial\theta_1}\left(\frac{L_3\,C_1\;C_2\;S_3}{2}+\frac{L_3C_1\;C_3\;S_2}{2}+L_2\,C_1\,S_2-L_1S_1\right) & \frac{\partial}{\partial\theta_2}\left(\frac{L_3\,C_1\;C_2\;S_3}{2}+\frac{L_3C_1\;C_3\;S_2}{2}+L_2\,C_1\,S_2-L_1S_1\right) \\ \frac{\partial}{\partial\theta_1}\left(\frac{L_3\,C_2\,S_1\;S_3}{2}+\frac{L_3\,C_3\;S_1\;S_2}{2}+L_2S_1\,S_2+L_1C_1\right) & \frac{\partial}{\partial\theta_2}\left(\frac{L_3\,C_2\,S_1\;S_3}{2}+\frac{L_3\,C_3\;S_1\;S_2}{2}+L_2S_1\,S_2+L_1C_1\right) \\ \frac{\partial}{\partial\theta_1}\left(\frac{L_3C_{23}}{2}+L_2C_2\right) & \frac{\partial}{\partial\theta_2}\left(\frac{L_3C_{23}}{2}+L_2C_2\right) \\ 0 & -S_1 \\ 0 & C_1 \\ 1 & 0 \end{bmatrix}$$

$$\begin{bmatrix} \frac{\partial}{\partial\theta_3}\left(\frac{L_3\,C_1\;C_2\;S_3}{2}+\frac{L_3C_1\;C_3\;S_2}{2}+L_2\,C_1\,S_2-L_1S_1\right) & \frac{\partial}{\partial\theta_4}\left(\frac{L_3\,C_1\;C_2\;S_3}{2}+\frac{L_3C_1\;C_3\;S_2}{2}+L_2\,C_1\,S_2-L_1S_1\right) \\ \frac{\partial}{\partial\theta_3}\left(\frac{L_3\,C_2\,S_1\;S_3}{2}+\frac{L_3\,C_3\;S_1\;S_2}{2}+L_2S_1\,S_2+L_1C_1\right) & \frac{\partial}{\partial\theta_4}\left(\frac{L_3\,C_2\,S_1\;S_3}{2}+\frac{L_3\,C_3\;S_1\;S_2}{2}+L_2S_1\,S_2+L_1C_1\right) \\ \frac{\partial}{\partial\theta_3}\left(\frac{L_3C_{23}}{2}+L_2C_2\right) & \frac{\partial}{\partial\theta_4}\left(\frac{L_3C_{23}}{2}+L_2C_2\right) \\ -S_1 & 0 \\ C_1 & 0 \\ 1 & 0 \end{bmatrix}$$

$$= \begin{bmatrix} \frac{L_3\,C_3\;C_1\;S_2}{2}-\frac{L_3C_2\;S_1\,S_3}{2}-L_2\,S_1\;S_2-L_1C_1 & \frac{C_1(L_3C_{23}+2L_2C_2)}{2} & \frac{C_1L_3C_{23}}{2} & 0 \\ \frac{L_3C_1\;C_2\;S_3}{2}+\frac{L_3C_1\;C_3\;S_2}{2}+L_2\,C_1\,S_2-L_1S_1 & \frac{S_1(L_3C_{23}+2L_2C_2)}{2} & \frac{S_1L_3C_{23}}{2} & 0 \\ 0 & \frac{-L_3S_{23}}{2}-L_2S_2 & -\frac{L_3C_{23}}{2} & 0 \\ 0 & -S_1 & -S_1 & 0 \\ 0 & C_1 & C_1 & 0 \\ 1 & 0 & 0 & 0 \end{bmatrix} \quad (2.169)$$

The Jacobian matrix of the third link can be written in two matrices A_3 and B_3.

$$A_3 =$$

$$\begin{bmatrix} \frac{L_3\,C_3\;C_1\;S_2}{2}-\frac{L_3C_2\;S_1\,S_3}{2}-L_2\,S_1\;S_2-L_1C_1 & \frac{C_1(L_3C_{23}+2L_2C_2)}{2} & \frac{C_1L_3C_{23}}{2} & 0 \\ \frac{L_3C_1\;C_2\;S_3}{2}+\frac{L_3C_1\;C_3\;S_2}{2}+L_2\,C_1\,S_2-L_1S_1 & \frac{S_1(L_3C_{23}+2L_2C_2)}{2} & \frac{S_1L_3C_{23}}{2} & 0 \\ 0 & \frac{-L_3S_{23}}{2}-L_2S_2 & -\frac{L_3C_{23}}{2} & 0 \end{bmatrix} \quad (2.170)$$

$$B_3 = \begin{bmatrix} 0 & -S_1 & -S_1 & 0 \\ 0 & C_1 & C_1 & 0 \\ 1 & 0 & 0 & 0 \end{bmatrix} \quad (2.171)$$

To calculate the Jacobian matrix of the fourth link, the derivative of the vector h_4 is taken according to θ_1 , θ_2 , θ_3 and θ_4. The fourth link is a rotational link, so $\xi_4 = 1$, $z^4 = {}^0_4R\,i^4 = [-\sin\theta_1 \quad \cos\theta_1 \quad 1]^T$ and $b_4 = \xi_4 z^4 = [0 \quad 0 \quad 1]^T$. The Jacobian matrix of the fourth link is given as follows:

$$J_4 = \begin{bmatrix} \frac{\partial}{\partial\theta_1}(h_{4_{11}}) & \frac{\partial}{\partial\theta_2}(h_{4_{11}}) & \frac{\partial}{\partial\theta_3}(h_{4_{11}}) & \frac{\partial}{\partial\theta_4}(h_{4_{11}}) \\ \frac{\partial}{\partial\theta_1}(h_{4_{21}}) & \frac{\partial}{\partial\theta_2}(h_{4_{21}}) & \frac{\partial}{\partial\theta_3}(h_{4_{21}}) & \frac{\partial}{\partial\theta_4}(h_{4_{21}}) \\ \frac{\partial}{\partial\theta_1}(h_{4_{31}}) & \frac{\partial}{\partial\theta_2}(h_{4_{31}}) & \frac{\partial}{\partial\theta_3}(h_{4_{31}}) & \frac{\partial}{\partial\theta_4}(h_{4_{31}}) \\ 0 & -S_1 & -S_1 & -S_1 \\ 0 & C_1 & C_1 & C_1 \\ 1 & 0 & 0 & 0 \end{bmatrix}$$

$$= \begin{bmatrix} J_{4_{11}} & J_{4_{12}} & J_{4_{13}} & J_{4_{14}} \\ J_{4_{21}} & J_{4_{22}} & J_{4_{23}} & J_{4_{24}} \\ J_{4_{31}} & J_{4_{32}} & J_{4_{33}} & J_{4_{34}} \\ 0 & -S_1 & -S_1 & -S_1 \\ 0 & C_1 & C_1 & C_1 \\ 1 & 0 & 0 & 0 \end{bmatrix} \quad (2.172)$$

Where:

$h_{4_{11}}$, $h_{4_{21}}$ and $h_{4_{31}}$ are the elments of the vector h_4.

$$J_{4_{11}} = S_1\ S_2\left(\frac{L_4\,S_3S_4}{2} - L_2 - L_3\,C_3 - \frac{L_4\,C_3C_4}{2}\right)$$
$$+\ C_2\ S_1\left(L_3\,S_3 - \frac{L_4\,C_3\,S_4}{2} - \frac{L_4\,C_4\,S_3}{2}\right) - L_1\,C_1 \quad (2.173)$$

$$J_{4_{12}} = C_1\left(\frac{2L_3\,C_{23} + 2L_2\,C_2 + L_4\,C_{234}}{2}\right) \quad (2.174)$$

$$J_{4_{13}} = \frac{L_4\,C_{2134}}{4} + \frac{L_3\,C_{123}}{2} + \frac{L_4\,C_{1234}}{4} + \frac{L_3\,C_{213}}{2} \quad (2.175)$$

$$J_{4_{14}} = \frac{L_4(C_{1234} + C_{2134})}{4} \quad (2.176)$$

$$J_{4_{21}} = C_1S_2\left(L_2 + L_3\,C_3 + \frac{L_4\,C_3C_4}{2} - \frac{L_4\,S_3S_4}{2}\right)$$
$$+\ C_2\ C_1\left(L_3\,S_3 + \frac{L_4\,C_3\,S_4}{2} + \frac{L_4\,C_4\,S_3}{2}\right) - L_1\,S_1 \quad (2.177)$$

$$J_{4_{22}} = S_1\left(\frac{2L_3\,C_{23} + 2L_2\,C_2 + L_4\,C_{234}}{2}\right) \quad (2.178)$$

$$J_{4_{23}} = \frac{L_3\,C_{123}}{2} - \frac{L_4\,S_{2134}}{4} + \frac{L_4\,S_{1234}}{4} - \frac{L_3\,S_{213}}{2} \quad (2.179)$$

$$J_{4_{24}} = \frac{L_4\,S_{1234} - S_{2134}}{4} \quad (2.180)$$

$$J_{4_{31}} = 0 \quad (2.181)$$

$$J_{4_{32}} = -L_3 S_{23} - L_2 S_2 - \frac{L_4 S_{234}}{2} \tag{2.182}$$

$$J_{4_{33}} = -L_3 S_{23} - \frac{L_4 S_{234}}{2} \tag{2.183}$$

$$J_{4_{34}} = -\frac{L_4 S_{234}}{2} \tag{2.184}$$

The Jacobian matrix of the fourd link is written in two matrices A_4 and B_4.

$$A_4 = \begin{bmatrix} J_{4_{11}} & J_{4_{12}} & J_{4_{13}} & J_{4_{14}} \\ J_{4_{21}} & J_{4_{22}} & J_{4_{23}} & J_{4_{24}} \\ J_{4_{31}} & J_{4_{32}} & J_{4_{33}} & J_{4_{34}} \end{bmatrix}, B_4 = \begin{bmatrix} 0 & -S_1 & -S_1 & -S_1 \\ 0 & C_1 & C_1 & C_1 \\ 1 & 0 & 0 & 0 \end{bmatrix} \tag{2.185}$$

The expressions of the mass matrix of the first, second, third and fourth links are given in equations (2.186), (2.187), (2.188) and (2.189), respectively. The inertia tensor of each link is calculated according to the main coordinate system.

$$I_1 = {}^0_1R\, I_{m1}\, {}^0_1R^T, I_2 = {}^0_2R\, I_{m2}\, {}^0_2R^T, I_3 = {}^0_3R\, I_{m3}\, {}^0_3R^T, I_4 = {}^0_4R\, I_{m4}\, {}^0_4R^T \tag{2.186}$$

$$D(\theta_1) = m_1 {A_1}^T A_1 + {B_1}^T I_1 B_1 = \begin{bmatrix} \frac{m_1 {L_1}^2}{4} + I_{zz_1} & 0 & 0 & 0 \\ 0 & 0 & 0 & 0 \\ 0 & 0 & 0 & 0 \\ 0 & 0 & 0 & 0 \end{bmatrix} \tag{2.187}$$

$$D(\theta_2) = m_2 {A_2}^T A_2 + {B_2}^T I_2 B_2$$

$$= \begin{bmatrix} m_2\left(\frac{{L_2}^2 \sin^2\theta_2}{4} + {L_1}^2\right) & -\left(\frac{L_1 L_2 m_2 \cos\theta_2}{2}\right) & 0 & 0 \\ -\left(\frac{L_1 L_2 m_2 \cos\theta_2}{2}\right) & \left(\frac{{L_2}^2 m_2}{4} + I_{zz_2}\right) & 0 & 0 \\ 0 & 0 & 0 & 0 \\ 0 & 0 & 0 & 0 \end{bmatrix} \tag{2.188}$$

$$D(\theta_3) = m_3 {A_3}^T A_3 + {B_3}^T I_3 B_3 \tag{2.189}$$

$$D(\theta_4) = m_4 {A_4}^T A_4 + {B_4}^T I_4 B_4 \tag{2.190}$$

To simplify the equations of TLRIP, Table 2.9 gives the employed parameters used in this section.

Table 2.9. Simplified parameters description of the TLRIP

Parameters	Description	Parameters	Description
a_1	$L_3{}^2 m_3$	a_{16}	$L_1{}^2 m_4$
a_2	$L_2{}^2 m_2$	a_{17}	$L_2{}^2 m_4$
a_3	$L_1{}^2 m_1$	a_{18}	$L_3{}^2 m_4$
a_4	$L_2{}^2 m_3$	a_{19}	$L_4{}^2 m_4$
a_5	$L_1{}^2 m_2$	a_{20}	$L_2 L_3 m_4$
a_6	$L_1{}^2 m_3$	a_{21}	$L_2 L_4 m_4$
a_7	$L_3{}^2 m_3$	a_{22}	$L_3 L_4 m_4$
a_8	$L_2 L_3 m_3$	a_{23}	$L_1 L_3 m_4$
a_9	$L_1 L_2 m_2$	a_{24}	$L_1 L_2 m_4$
a_{10}	$L_1 L_2 m_3$	a_{25}	$L_1 L_4 m_4$
a_{11}	$L_1 L_3 m_3$	a_{26}	$L_3 g m_4$
a_{12}	$L_2 g m_2$	a_{27}	$L_4 g m_4$
a_{13}	$L_2 g m_3$	a_{28}	$L_3 g m_4$
a_{14}	$L_3 g m_3$	a_{29}	$L_2 g m_4$

The elements of $D(\theta_3)$ matrix are given as follows:

$$D^3{}_{11} = \frac{I_{zz3}}{2} + a_6 + \frac{a_4}{2} + \frac{a_7}{8} - \frac{I_{zz3}\cos(2\theta_2 + 2\theta_3)}{2} - \frac{a_4\cos(2\theta_2)}{2} - \frac{a_7\cos(2\theta_2 + 2\theta_3)}{8} + \frac{a_8\cos(\theta_3)}{2} - \frac{a_8\cos(2\theta_2 + \theta_3)}{2} \quad (2.191)$$

$$D^3{}_{12} = -\frac{a_{11}\cos(\theta_2 + \theta_3) + 2\,a_{10}\cos\theta_2}{2} \quad (2.192)$$

$$D^3{}_{13} = -\frac{a_{11}\cos(\theta_2 + \theta_3)}{2} \quad (2.193)$$

$$D^3{}_{22} = a_4 + a_8\cos\theta_3 + \frac{a_1}{4} + I_{zz3} \quad (2.194)$$

$$D^3{}_{23} = \frac{a_1}{4} + \frac{a_8\cos\theta_3}{2} + I_{zz3} \quad (2.195)$$

$$D^3{}_{33} = \frac{a_7}{4} + I_{zz3} \quad (2.196)$$

$$D^3{}_{21} = D^3{}_{12}\,, D^3{}_{31} = D^3{}_{13} \tag{2.197}$$

$$D^3{}_{14} = D^3{}_{24} = D^3{}_{34} = D^3{}_{41} = D^3{}_{42} = D^3{}_{43} = D^3{}_{44} = 0 \tag{2.198}$$

The matrix $D(\theta_3)$ maybe given as follows:

$$D(\theta_3) = \begin{bmatrix} D^3{}_{11} & D^3{}_{12} & D^3{}_{13} & D^3{}_{14} \\ D^3{}_{21} & D^3{}_{22} & D^3{}_{23} & D^3{}_{24} \\ D^3{}_{31} & D^3{}_{32} & D^3{}_{33} & D^3{}_{34} \\ D^3{}_{41} & D^3{}_{42} & D^3{}_{43} & D^3{}_{44} \end{bmatrix} \tag{2.199}$$

The elements of matrix $D(\theta_4)$ are given as follows :

$$\begin{aligned} D^4{}_{11} = {} & \frac{I_{zz4}}{2} + a_{16} + \frac{a_{17}}{2} + \frac{a_{18}}{2} + \frac{a_{19}}{8} - \frac{I_{zz4}\cos(2\theta_2 + 2\theta_3 + 2\theta_4)}{2} \\ & - \frac{a_{17}\cos(2\theta_2)}{2} - \frac{a_{18}\cos(2\theta_2 + 2\theta_3)}{2} + a_{20}\cos(\theta_3) + \frac{a_{22}\cos(\theta_4)}{2} \\ & - \frac{a_{19}\cos(2\theta_2 + 2\theta_3 + 2\theta_4)}{8} + \frac{a_{21}\cos(\theta_3 + \theta_4)}{2} - a_{20}\cos(2\theta_2 + \theta_3) \\ & - \frac{a_{21}\cos(2\theta_2 + \theta_3 + \theta_4)}{2} - \frac{a_{22}\cos(2\theta_2 + 2\theta_3 + \theta_4)}{2} \end{aligned} \tag{2.200}$$

$$D^4{}_{12} = \frac{-2\,a_{23}\cos(\theta_3 + \theta_4) - 2\,a_{24}\cos\theta_2 - a_{25}\cos(\theta_2 + \theta_3 + \theta_4)}{2} \tag{2.201}$$

$$D^4{}_{13} = \frac{-2\,a_{23}\cos(\theta_2 + \theta_3) - a_{25}\cos(\theta_2 + \theta_3 + \theta_4)}{2} \tag{2.202}$$

$$D^4{}_{14} = \frac{-a_{25}\cos(\theta_2 + \theta_3 + \theta_4)}{2} \tag{2.203}$$

$$\begin{aligned} D^4{}_{22} = {} & a_{17} + 2\,a_{20}\cos\theta_3 + a_{21}\cos(\theta_3 + \theta_4) \\ & a_{18} + a_{22}\cos\theta_4 + \frac{a_{19}}{4} + I_{zz4} \end{aligned} \tag{2.204}$$

$$D^4{}_{23} = a_{18} + a_{22}\cos\theta_4 + a_{20}\cos\theta_3 + \frac{a_{19}}{4} + \frac{a_{21}\cos(\theta_3 + \theta_4)}{2} + I_{zz4} \tag{2.205}$$

$$D^4{}_{24} = I_{zz4} + \frac{a_{19}}{4} + \frac{a_{22}\cos\theta_4}{2} + \frac{a_{21}\cos(\theta_3 + \theta_4)}{2} \tag{2.206}$$

$$D^4{}_{33} = I_{zz4} + a_{18} + \frac{a_{22}\cos\theta_4}{2} + \frac{a_{19}}{2} \tag{2.207}$$

$$D^4{}_{34} = I_{zz4} + a_{19} + \frac{a_{22}\cos\theta_4}{2} \tag{2.208}$$

$$D^4{}_{44} = I_{zz4} + \frac{a_{19}}{2} \tag{2.209}$$

$$D^4{}_{21} = D^4{}_{12}, D^4{}_{31} = D^4{}_{13}, D^4{}_{41} = D^4{}_{14}, D^4{}_{42} = D^4{}_{24}, D^4{}_{43} = D^4{}_{34} \tag{2.210}$$

The matrix $D(\theta_4)$ maybe given as follows:

$$D(\theta_4) = \begin{bmatrix} D^4{}_{11} & D^4{}_{12} & D^4{}_{13} & D^4{}_{14} \\ D^4{}_{21} & D^4{}_{22} & D^4{}_{23} & D^4{}_{24} \\ D^4{}_{31} & D^4{}_{32} & D^4{}_{33} & D^4{}_{34} \\ D^4{}_{41} & D^4{}_{42} & D^4{}_{43} & D^4{}_{44} \end{bmatrix} \tag{2.211}$$

The mass matrix of the TLRIP is given as follows :

$$D(\theta) = D(\theta_1) + D(\theta_2) + D(\theta_3) + D(\theta_4) \tag{2.212}$$

The elments of the mass matrix are given as follows

$$\begin{aligned} D_{11} = {} & \frac{a_3}{4} + I_{zz_1} + \frac{a_2 \sin^2\theta_2}{4} + a_5 + \frac{I_{zz3}}{2} + a_6 + \frac{a_4}{2} + \frac{a_7}{8} - \frac{I_{zz3}\cos(2\theta_2 + 2\theta_3)}{2} \\ & - \frac{a_4\cos(2\theta_2)}{2} - \frac{a_7\cos(2\theta_2 + 2\theta_3)}{8} + \frac{a_8\cos(\theta_3)}{2} - \frac{a_8\cos(2\theta_2 + \theta_3)}{2} + \frac{a_{17}}{2} \\ & - \frac{I_{zz4}\cos(2\theta_2 + 2\theta_3 + 2\theta_4)}{2} - \frac{a_{19}\cos(2\theta_2 + 2\theta_3 + 2\theta_4)}{8} - \frac{a_{17}\cos(2\theta_2)}{2} + \frac{I_{zz4}}{2} \\ & + a_{16} + \frac{a_{18}}{2} + \frac{a_{19}}{8} - \frac{a_{18}\cos(2\theta_2 + 2\theta_3)}{2} \\ & + a_{20}\cos(\theta_3) + \frac{a_{22}\cos(\theta_4)}{2} - a_{20}\cos(2\theta_2 + \theta_3) \end{aligned} \tag{2.213}$$

$$\begin{aligned} D_{12} = {} & \frac{-a_9\cos\theta_2}{2} + \frac{-2\,a_{23}\cos(\theta_3 + \theta_4) - 2\,a_{24}\cos\theta_2 - a_{25}\cos(\theta_2 + \theta_3 + \theta_4)}{2} \\ & - \frac{a_{11}\cos(\theta_2 + \theta_3) + 2\,a_{10}\cos\theta_2}{2} \end{aligned} \tag{2.214}$$

$$\begin{aligned} D_{13} = {} & -\frac{a_{11}\cos(\theta_2 + \theta_3)}{2} \\ & + \frac{-2\,a_{23}\cos(\theta_2 + \theta_3) - a_{25}\cos(\theta_2 + \theta_3 + \theta_4)}{2} \end{aligned} \tag{2.215}$$

$$D_{14} = \frac{-a_{25}\cos(\theta_2 + \theta_3 + \theta_4)}{2} \tag{2.216}$$

$$D_{22} = \frac{a_2}{4} + I_{zz_2} + a_4 + a_8\cos\theta_3 + \frac{a_1}{4} + I_{zz3} + a_{17} + 2\,a_{20}\cos\theta_3 + a_{18} + \frac{a_{19}}{4} + I_{zz4} + a_{21}\cos(\theta_3 + \theta_4) + a_{22}\cos\theta_4 \tag{2.217}$$

$$D_{23} = a_{18} + a_{22}\cos\theta_4 + a_{20}\cos\theta_3 + \frac{a_{19}}{4} + \frac{a_{21}\cos(\theta_3 + \theta_4)}{2} + I_{zz4} + \frac{a_1}{4} + \frac{a_8\cos\theta_3}{2} + I_{zz3} \tag{2.218}$$

$$D_{24} = I_{zz4} + \frac{a_{19}}{4} + \frac{a_{22}\cos\theta_4}{2} + \frac{a_{21}\cos(\theta_3 + \theta_4)}{2} \tag{2.219}$$

$$D_{33} = \frac{a_7}{4} + I_{zz3} + I_{zz4} + a_{18} + \frac{a_{22}\cos\theta_4}{2} + \frac{a_{19}}{2} + I_{zz4} + a_{19} + \frac{a_{22}\cos\theta_4}{2} \tag{2.220}$$

$$D_{44} = I_{zz4} + \frac{a_{19}}{2} \tag{2.221}$$

$$D_{21} = D_{12}, D_{31} = D_{13}, D_{41} = D_{14}, D_{42} = D_{24}, D_{43} = D_{34} \tag{2.222}$$

The matrix $D(\theta)$can be given as follows:

$$D(\theta) = \begin{bmatrix} D_{11} & D_{12} & D_{13} & D_{14} \\ D_{21} & D_{22} & D_{23} & D_{24} \\ D_{31} & D_{32} & D_{33} & D_{34} \\ D_{41} & D_{42} & D_{43} & D_{44} \end{bmatrix} \tag{2.223}$$

The elements of the velocity coupling matrix of the first link are calculated as follows:

$$C^1{}_{11} = \frac{1}{2}\frac{\partial}{\partial\theta_1} D_{11}(\theta) = 0 \tag{2.224}$$

$$C^1{}_{12} = \frac{1}{2}\frac{\partial}{\partial\theta_1} D_{12}(\theta) = 0 \tag{2.225}$$

$$C^1{}_{13} = \frac{1}{2}\frac{\partial}{\partial\theta_1} D_{13}(\theta) = 0 \tag{2.226}$$

$$C^1{}_{14} = \frac{1}{2}\frac{\partial}{\partial\theta_1} D_{14}(\theta) = 0 \tag{2.227}$$

$$C^1{}_{21} = \frac{\partial}{\partial\theta_2} D_{11}(\theta) - \frac{1}{2}\frac{\partial}{\partial\theta_1} D_{21}(\theta)$$
$$= I_{zz2}\sin(2\theta_2 + 2\theta_3 + 2\theta_4) + I_{zz2}\sin 2\theta_2 + I_{zz3}\ \sin(2\theta_2 + 2\theta_3)$$
$$+ \frac{a_{19}\sin(2\theta_2 + 2\theta_3 + 2\theta_4)}{4} + \frac{a_2 \sin 2\theta_2}{4} + a_4 + a_{19}\sin 2\theta_2$$
$$+ \frac{a_7 \sin(2\theta_2 + 2\theta_3)}{4} + \ a_{18}\sin(2\theta_2 + 2\theta_3)\ + a_{22}\sin(2\theta_2 + 2\theta_3 + 2\theta_4)$$
$$+ a_8\sin(2\theta_2 + 2\theta_3) + \ 2\ a_{20}\sin(2\theta_2 + 2\theta_3) + a_{21}\sin(2\theta_2 + 2\theta_3 + 2\theta_4) \tag{2.228}$$

$$C^1{}_{22} = \frac{\partial}{\partial\theta_2} D_{12}(\theta) - \frac{1}{2}\frac{\partial}{\partial\theta_1} D_{22}(\theta)$$
$$= \frac{a_{11}\sin(\theta_2 + \theta_3) + \ 2a_{23}\sin(\theta_2 + \theta_3) + \ a_9 \sin\theta_2}{2}$$
$$+ \frac{2a_{10}\sin\theta_2 + \ 2a_{24}\sin\theta_2 + \ a_{25}\sin(\theta_2 + \theta_3 + \theta_4)}{2} \tag{2.229}$$

$$C^1{}_{23} = \frac{\partial}{\partial\theta_2} D_{13}(\theta) - \frac{1}{2}\frac{\partial}{\partial\theta_1} D_{23}(\theta) = \frac{a_{25}\sin(\theta_2 + \theta_3 + \theta_4) + a_{11}\sin(\theta_2 + \theta_3)}{2}$$
$$+ a_{23}\sin(\theta_2 + \theta_3) \tag{2.230}$$

$$C^1{}_{24} = \frac{\partial}{\partial\theta_2} D_{14}(\theta) - \frac{1}{2}\frac{\partial}{\partial\theta_1} D_{24}(\theta) = \frac{a_{25}\sin(\theta_2 + \theta_3 + \theta_4)}{2} \tag{2.231}$$

$$C^1{}_{31} = \frac{\partial}{\partial\theta_3} D_{11}(\theta) - \frac{1}{2}\frac{\partial}{\partial\theta_1} D_{31}(\theta) = \ I_{zz4}\sin(2\theta_2 + 2\theta_3 + 2\theta_4)$$
$$- \frac{a_{20}\sin\theta_3}{2} + \frac{a_8\sin(2\theta_2 + \theta_3)}{2} + a_{20}\sin(2\theta_2 + \theta_3) + \frac{a_{21}\sin(2\theta_2 + \theta_3 + \theta_4)}{2}$$
$$+ \frac{a_{19}\sin(2\theta_2 + 2\theta_3 + 2\theta_4)}{4} + \ \frac{a_1\sin(2\theta_2 + 2\theta_3)}{4}$$
$$+ I_{zz3}\sin(2\theta_2 + 2\theta_3) + a_{18}\sin(2\theta_2 + 2\theta_3) - \frac{a_8\sin\theta_3}{2} \tag{2.232}$$

$$C^1{}_{32} = \frac{\partial}{\partial\theta_3} D_{12}(\theta) - \frac{1}{2}\frac{\partial}{\partial\theta_1} D_{32}(\theta) = \frac{a_{25}\sin(\theta_2 + \theta_3 + \theta_4)}{2}$$
$$+ \frac{a_{11}\sin(\theta_2 + \theta_3)}{2} + \ a_{23}\sin(\theta_2 + \theta_3) \tag{2.233}$$

$$C^1{}_{33} = \frac{\partial}{\partial\theta_3} D_{13}(\theta) - \frac{1}{2}\frac{\partial}{\partial\theta_1} D_{33}(\theta) = \frac{a_{25}\sin(\theta_2+\theta_3+\theta_4)}{2}$$
$$+ \frac{a_{23}\sin(\theta_2+\theta_3)}{2} - a_{23}\sin(\theta_2+\theta_3) \quad (2.234)$$

$$C^1{}_{34} = \frac{\partial}{\partial\theta_3} D_{14}(\theta) - \frac{1}{2}\frac{\partial}{\partial\theta_1} D_{34}(\theta) = \frac{a_{25}\sin(\theta_2+\theta_3+\theta_4)}{2} \quad (2.235)$$

$$C^1{}_{41} = \frac{\partial}{\partial\theta_4} D_{11}(\theta) - \frac{1}{2}\frac{\partial}{\partial\theta_1} D_{41}(\theta) = I_{zz4}\sin(2\theta_2+2\theta_3+2\theta_4)$$
$$+ \frac{a_{21}\sin(2\theta_2+\theta_3+\theta_4) - a_{21}\sin(\theta_3+\theta_4) + a_{22}\sin(2\theta_2+\theta_3+\theta_4)}{2}$$
$$+ \frac{a_{19}\sin(2\theta_2+2\theta_3+2\theta_4)}{4} - \frac{a_{22}\sin\theta_4}{4} \quad (2.236)$$

$$C^1{}_{42} = \frac{\partial}{\partial\theta_4} D_{12}(\theta) - \frac{1}{2}\frac{\partial}{\partial\theta_1} D_{42}(\theta) = \frac{a_{25}\sin(\theta_2+\theta_3+\theta_4)}{2} \quad (2.237)$$

$$C^1{}_{43} = \frac{\partial}{\partial\theta_4} D_{13}(\theta) - \frac{1}{2}\frac{\partial}{\partial\theta_1} D_{43}(\theta) = \frac{a_{25}\sin(\theta_2+\theta_3+\theta_4)}{2} \quad (2.238)$$

$$C^1{}_{44} = \frac{\partial}{\partial\theta_4} D_{14}(\theta) - \frac{1}{2}\frac{\partial}{\partial\theta_1} D_{44}(\theta) = \frac{a_{25}\sin(\theta_2+\theta_3+\theta_4)}{2} \quad (2.239)$$

The velocity coupling matrix of the first link is given in equation (2.240)

$$C_1 = \begin{bmatrix} C^1{}_{11} & C^1{}_{12} & C^1{}_{13} & C^1{}_{14} \\ C^1{}_{21} & C^1{}_{22} & C^1{}_{23} & C^1{}_{24} \\ C^1{}_{31} & C^1{}_{32} & C^1{}_{33} & C^1{}_{34} \\ C^1{}_{41} & C^1{}_{42} & C^1{}_{43} & C^1{}_{44} \end{bmatrix} \quad (2.240)$$

The elements of the velocity coupling matrix of the second link are calculated as follows:

$$C^2{}_{11} = \frac{\partial}{\partial\theta_1} D_{21}(\theta) - \frac{1}{2}\frac{\partial}{\partial\theta_2} D_{11}(\theta) = -\frac{I_{zz4}\sin(2\theta_2+2\theta_3+2\theta_4)}{2} - \frac{I_{zz2}\sin 2\theta_2}{2}$$
$$- \frac{I_{zz3}\sin(2\theta_2+2\theta_3)}{2} - \frac{a_{19}\sin(2\theta_2+2\theta_3+2\theta_4)}{8} - \frac{a_2\sin 2\theta_2}{8} - \frac{a_4\sin 2\theta_2}{2}$$
$$- \frac{a_1\sin(2\theta_2+2\theta_3)}{8} - \frac{a_{18}\sin(2\theta_2+2\theta_3)}{2} - \frac{a_8\sin(2\theta_2+2\theta_3)}{2} - \frac{a_{17}\sin 2\theta_2}{2}$$

$$-\frac{a_{21}\sin(2\theta_2+\theta_3+\theta_4)}{2}-\frac{a_{22}\sin(2\theta_2+2\theta_3+\theta_4)}{2} \quad (2.241)$$

$$C^2{}_{12}=\frac{\partial}{\partial\theta_1}D_{22}(\theta)-\frac{1}{2}\frac{\partial}{\partial\theta_2}D_{12}(\theta)$$
$$=\frac{-a_{11}\sin(\theta_2+\theta_3)-2a_{23}\sin(\theta_2+\theta_3)-a_9\sin\theta_2}{4}$$
$$-\left(\frac{2a_{10}\sin\theta_2+2a_{24}\sin\theta_2+a_{25}\sin(\theta_2+\theta_3+\theta_4)}{4}\right) \quad (2.242)$$

$$C^2{}_{13}=\frac{\partial}{\partial\theta_1}D_{23}(\theta)-\frac{1}{2}\frac{\partial}{\partial\theta_2}D_{13}(\theta)=\frac{-a_{25}\sin(\theta_2+\theta_3)\ -a_{11}\sin(\theta_2+\theta_3)}{4}$$
$$-\frac{a_{23}\sin(\theta_2+\theta_3)}{2} \quad (2.243)$$

$$C^2{}_{14}=\frac{\partial}{\partial\theta_1}D_{24}(\theta)-\frac{1}{2}\frac{\partial}{\partial\theta_2}D_{14}(\theta)=\frac{-a_{25}\sin(\theta_2+\theta_3)}{4} \quad (2.244)$$

$$C^2{}_{21}=\frac{1}{2}\frac{\partial}{\partial\theta_2}D_{21}(\theta)=\frac{1}{4}a_{11}\sin(\theta_2+\theta_3)+\frac{1}{2}a_{23}\sin(\theta_2+\theta_3)+\frac{1}{2}a_{24}\sin\theta_2$$
$$+\frac{1}{2}a_9\sin\theta_2+\frac{1}{2}a_{10}\sin\theta_2+\frac{1}{4}a_{25}\sin(\theta_2+\theta_3+\theta_4) \quad (2.245)$$

$$C^2{}_{22}=\frac{1}{2}\frac{\partial}{\partial\theta_2}D_{22}(\theta)=0 \quad (2.246)$$

$$C^2{}_{23}=\frac{1}{2}\frac{\partial}{\partial\theta_2}D_{23}(\theta)=0 \quad (2.247)$$

$$C^2{}_{24}=\frac{1}{2}\frac{\partial}{\partial\theta_2}D_{24}(\theta)=0 \quad (2.248)$$

$$C^2{}_{31}=\frac{\partial}{\partial\theta_3}D_{21}(\theta)-\frac{1}{2}\frac{\partial}{\partial\theta_2}D_{31}(\theta)=\frac{a_{25}\sin(\theta_2+\theta_3+\theta_4)}{4}+\frac{a_{11}\sin(\theta_2+\theta_3)}{4}$$
$$+\frac{a_{23}\sin(\theta_2+\theta_3)}{2} \quad (2.249)$$

$$C^2{}_{32}=\frac{\partial}{\partial\theta_3}D_{22}(\theta)-\frac{1}{2}\frac{\partial}{\partial\theta_2}D_{32}(\theta)$$
$$=-a_{21}\sin(\theta_3+\theta_4)-a_8\sin\theta_3-2a_{20}\sin\theta_3 \quad (2.250)$$

$$C^2{}_{33} = \frac{\partial}{\partial\theta_3} D_{23}(\theta) - \frac{1}{2}\frac{\partial}{\partial\theta_2} D_{33}(\theta)$$

$$= \frac{-a_{21}\sin(\theta_3+\theta_4) - a_8\sin\theta_3 - 2a_{20}\sin\theta_3}{2} \quad (2.251)$$

$$C^2{}_{34} = \frac{\partial}{\partial\theta_3} D_{23}(\theta) - \frac{1}{2}\frac{\partial}{\partial\theta_2} D_{33}(\theta) = \frac{-a_{21}\sin(\theta_3+\theta_4)}{2} \quad (2.252)$$

$$C^2{}_{41} = \frac{\partial}{\partial\theta_4} D_{21}(\theta) - \frac{1}{2}\frac{\partial}{\partial\theta_2} D_{41}(\theta) = \frac{a_{25}\sin(\theta_2+\theta_3+\theta_4)}{4} \quad (2.253)$$

$$C^2{}_{42} = \frac{\partial}{\partial\theta_4} D_{22}(\theta) - \frac{1}{2}\frac{\partial}{\partial\theta_2} D_{42}(\theta) = -a_{21}\sin(\theta_3+\theta_4) - a_{22}\sin\theta_4 \quad (2.254)$$

$$C^2{}_{43} = \frac{\partial}{\partial\theta_4} D_{23}(\theta) - \frac{1}{2}\frac{\partial}{\partial\theta_2} D_{43}(\theta) = \frac{-a_{21}\sin(\theta_3+\theta_4)}{2} - a_{22}\sin\theta_4 \quad (2.255)$$

$$C^2{}_{44} = \frac{\partial}{\partial\theta_4} D_{24}(\theta) - \frac{1}{2}\frac{\partial}{\partial\theta_2} D_{44}(\theta) = \frac{-a_{21}\sin(\theta_3+\theta_4) - a_{22}\sin\theta_4}{2} \quad (2.256)$$

The velocity coupling matrix of the second link is given in equation (2.257)

$$C_2 = \begin{bmatrix} C^2{}_{11} & C^2{}_{12} & C^2{}_{13} & C^2{}_{14} \\ C^2{}_{21} & C^2{}_{22} & C^2{}_{23} & C^2{}_{24} \\ C^2{}_{31} & C^2{}_{32} & C^2{}_{33} & C^2{}_{34} \\ C^2{}_{41} & C^2{}_{42} & C^2{}_{43} & C^2{}_{44} \end{bmatrix} \quad (2.257)$$

The elements of the velocity coupling matrix of the third link are calculated as follows:

$$C^3{}_{11} = \frac{\partial}{\partial\theta_1} D_{31}(\theta) - \frac{1}{2}\frac{\partial}{\partial\theta_3} D_{11}(\theta)$$

$$= \frac{a_8\sin\theta_3}{4} - \frac{I_{zz3}\sin(2\theta_2+2\theta_3)}{2} - \frac{a_{19}\sin(2\theta_2+2\theta_3+2\theta_4)}{8}$$

$$- \frac{a_7\sin(2\theta_2+2\theta_3)}{8} - \frac{a_{18}\sin(2\theta_2+2\theta_3)}{2} - \frac{I_{zz4}\sin(2\theta_2+2\theta_3+2\theta_4)}{2}$$

$$- \frac{a_8\sin(2\theta_2+\theta_3)}{4} - \frac{a_{20}\sin(2\theta_2+\theta_3)}{2} - \frac{a_{21}\sin(2\theta_2+\theta_3+\theta_4)}{4}$$

$$- \frac{a_{22}\sin(2\theta_2+2\theta_3+\theta_4)}{2} + \frac{a_{20}\sin\theta_3}{2} + \frac{a_{21}\sin(\theta_3+\theta_4)}{4} \quad (2.258)$$

$$C^3{}_{12} = \frac{\partial}{\partial\theta_1} D_{32}(\theta) - \frac{1}{2}\frac{\partial}{\partial\theta_3} D_{12}(\theta)$$

$$= -\frac{a_{25}\ \sin(\theta_2+\theta_3+\theta_4)}{4} - \frac{a_{11}\ \sin(\theta_2+\theta_3)}{4} - \frac{a_{23}\ \sin(\theta_2+\theta_3)}{2} \quad (2.259)$$

$$C^3{}_{13} = \frac{\partial}{\partial\theta_1} D_{33}(\theta) - \frac{1}{2}\frac{\partial}{\partial\theta_3} D_{13}(\theta)$$

$$= -\frac{a_{25}\ \sin(\theta_2+\theta_3+\theta_4)}{4} - \frac{a_{11}\ \sin(\theta_2+\theta_3)}{4} - \frac{a_{23}\ \sin(\theta_2+\theta_3)}{2} \quad (2.260)$$

$$C^3{}_{14} = \frac{\partial}{\partial\theta_1} D_{34}(\theta) - \frac{1}{2}\frac{\partial}{\partial\theta_3} D_{14}(\theta) = -\frac{a_{25}\ \sin(\theta_2+\theta_3+\theta_4)}{4} \quad (2.261)$$

$$C^3{}_{21} = \frac{\partial}{\partial\theta_2} D_{31}(\theta) - \frac{1}{2}\frac{\partial}{\partial\theta_3} D_{21}(\theta) = \frac{a_{25}\ \sin(\theta_2+\theta_3+\theta_4)}{4} + \frac{a_{11}\ \sin(\theta_2+\theta_3)}{4}$$

$$+ \frac{a_{23}\ \sin(\theta_2+\theta_3)}{2} \quad (2.262)$$

$$C^3{}_{22} = \frac{\partial}{\partial\theta_2} D_{32}(\theta) - \frac{1}{2}\frac{\partial}{\partial\theta_3} D_{22}(\theta)$$

$$= \frac{a_{21}\ \sin(\theta_3+\theta_4)}{2} + \frac{a_8\ \sin\theta_3}{2} + a_{20}\ \sin\theta_3 \quad (2.263)$$

$$C^3{}_{23} = \frac{\partial}{\partial\theta_2} D_{33}(\theta) - \frac{1}{2}\frac{\partial}{\partial\theta_3} D_{23}(\theta)$$

$$= \frac{a_{21}\ \sin(\theta_3+\theta_4)}{4} + \frac{a_8\ \sin\theta_3}{4} + \frac{a_{20}\ \sin\theta_3}{2} \quad (2.264)$$

$$C^3{}_{24} = \frac{\partial}{\partial\theta_2} D_{34}(\theta) - \frac{1}{2}\frac{\partial}{\partial\theta_3} D_{24}(\theta) = \frac{a_{21}\ \sin(\theta_3+\theta_4)}{4} \quad (2.265)$$

$$C^3{}_{31} = \frac{1}{2}\frac{\partial}{\partial\theta_3} D_{31}(\theta)$$

$$= \frac{a_{25}\sin(\theta_2+\theta_3+\theta_4)}{4} + \frac{a_{11}\sin(\theta_2+\theta_3)}{4} + \frac{a_{23}\sin(\theta_2+\theta_3)}{2} \quad (2.266)$$

$$C^3{}_{32} = \frac{1}{2}\frac{\partial}{\partial\theta_3} D_{32}(\theta)$$

$$= -\frac{a_{21}\ \sin(\theta_3+\theta_4)}{4} - \frac{a_8\ \sin\theta_3}{4} - \frac{a_{20}\ \sin\theta_3}{2} \quad (2.267)$$

$$C^3{}_{33} = \frac{1}{2}\frac{\partial}{\partial\theta_3}D_{33}(\theta) = 0 \tag{2.268}$$

$$C^3{}_{34} = \frac{1}{2}\frac{\partial}{\partial\theta_3}D_{34}(\theta) = 0 \tag{2.269}$$

$$C^3{}_{41} = \frac{\partial}{\partial\theta_4}D_{31}(\theta) - \frac{1}{2}\frac{\partial}{\partial\theta_3}D_{41}(\theta) = \frac{a_{25}\sin(\theta_2+\theta_3+\theta_4)}{4} \tag{2.270}$$

$$C^3{}_{42} = \frac{\partial}{\partial\theta_4}D_{32}(\theta) - \frac{1}{2}\frac{\partial}{\partial\theta_3}D_{42}(\theta) = \frac{-a_{21}\sin(\theta_3+\theta_4)}{2} - a_{22}\sin\theta_4 \tag{2.271}$$

$$C^3{}_{43} = \frac{\partial}{\partial\theta_4}D_{33}(\theta) - \frac{1}{2}\frac{\partial}{\partial\theta_3}D_{43}(\theta) = -a_{22}\sin\theta_4 \tag{2.272}$$

$$C^3{}_{44} = \frac{\partial}{\partial\theta_4}D_{34}(\theta) - \frac{1}{2}\frac{\partial}{\partial\theta_3}D_{44}(\theta) = \frac{-a_{22}\sin\theta_4}{2} \tag{2.273}$$

The velocity coupling matrix of the third link is given in equation (2.274)

$$C_3 = \begin{bmatrix} C^3{}_{11} & C^3{}_{12} & C^3{}_{13} & C^3{}_{14} \\ C^3{}_{21} & C^3{}_{22} & C^3{}_{23} & C^3{}_{24} \\ C^3{}_{31} & C^3{}_{32} & C^3{}_{33} & C^3{}_{34} \\ C^3{}_{41} & C^3{}_{42} & C^3{}_{43} & C^3{}_{44} \end{bmatrix} \tag{2.274}$$

The elements of the velocity coupling matrix of the fourth link are calculated as follows:

$$\begin{aligned} C^4{}_{11} &= \frac{\partial}{\partial\theta_1}D_{41}(\theta) - \frac{1}{2}\frac{\partial}{\partial\theta_4}D_{11}(\theta) \\ &= -\frac{I_{zz4}\sin(2\theta_2+2\theta_3+2\theta_4)}{2} - \frac{a_{19}\sin(2\theta_2+2\theta_3+2\theta_4)}{8} \\ &\frac{a_{22}\sin\theta_4}{4} - \frac{a_{21}\sin(2\theta_2+\theta_3+\theta_4)}{4} + \frac{a_{21}\sin(\theta_3+\theta_4)}{4} \\ &- \frac{a_{22}\sin(2\theta_2+2\theta_3+2\theta_4)}{4} \end{aligned} \tag{2.275}$$

$$C^4{}_{12} = \frac{\partial}{\partial\theta_1}D_{42}(\theta) - \frac{1}{2}\frac{\partial}{\partial\theta_4}D_{12}(\theta) = -\frac{a_{25}\sin(\theta_2+\theta_3+\theta_4)}{4} \tag{2.276}$$

$$C^4{}_{13} = \frac{\partial}{\partial\theta_1} D_{43}(\theta) - \frac{1}{2}\frac{\partial}{\partial\theta_4} D_{13}(\theta) = -\frac{a_{25}\ \sin(\theta_2+\theta_3+\theta_4)}{4} \quad (2.277)$$

$$C^4{}_{14} = \frac{\partial}{\partial\theta_1} D_{44}(\theta) - \frac{1}{2}\frac{\partial}{\partial\theta_4} D_{14}(\theta) = -\frac{a_{25}\ \sin(\theta_2+\theta_3+\theta_4)}{4} \quad (2.278)$$

$$C^4{}_{31} = \frac{\partial}{\partial\theta_3} D_{41}(\theta) - \frac{1}{2}\frac{\partial}{\partial\theta_4} D_{31}(\theta) = \frac{a_{25}\ \sin(\theta_2+\theta_3+\theta_4)}{4} \quad (2.279)$$

$$C^4{}_{32} = \frac{\partial}{\partial\theta_3} D_{42}(\theta) - \frac{1}{2}\frac{\partial}{\partial\theta_4} D_{32}(\theta) = \frac{-a_{21}\ \sin(\theta_3+\theta_4)}{4} - \frac{a_{22}\ \sin\theta_4}{2} \quad (2.280)$$

$$C^4{}_{33} = \frac{\partial}{\partial\theta_3} D_{43}(\theta) - \frac{1}{2}\frac{\partial}{\partial\theta_4} D_{34}(\theta) = \frac{a_{22}\ \sin\theta_4}{2} \quad (2.281)$$

$$C^4{}_{34} = \frac{\partial}{\partial\theta_3} D_{44}(\theta) - \frac{1}{2}\frac{\partial}{\partial\theta_3} D_{34}(\theta) = \frac{-a_{22}\ \sin\theta_4}{4} \quad (2.282)$$

$$C^4{}_{41} = \frac{1}{2}\frac{\partial}{\partial\theta_4} D_{41}(\theta) = \frac{a_{25}\sin(\theta_2+\theta_3+\theta_4)}{4} \quad (2.283)$$

$$C^4{}_{42} = \frac{1}{2}\frac{\partial}{\partial\theta_4} D_{42}(\theta) = -\frac{a_{22}\ \sin(\theta_3+\theta_4)}{4} - \frac{a_{22}\ \sin\theta_4}{4} \quad (2.284)$$

$$C^4{}_{43} = \frac{1}{2}\frac{\partial}{\partial\theta_4} D_{43}(\theta) = -\frac{a_{22}\ \sin\theta_4}{4} \quad (2.285)$$

$$C^4{}_{44} = \frac{1}{2}\frac{\partial}{\partial\theta_4} D_{44}(\theta) = 0 \quad (2.286)$$

The velocity coupling matrix of the fourth link is given in equation (2.287).

$$C_4 = \begin{bmatrix} C^4{}_{11} & C^4{}_{12} & C^4{}_{13} & C^4{}_{14} \\ C^4{}_{21} & C^4{}_{22} & C^4{}_{23} & C^4{}_{24} \\ C^4{}_{31} & C^4{}_{32} & C^4{}_{33} & C^4{}_{34} \\ C^4{}_{41} & C^4{}_{42} & C^4{}_{43} & C^4{}_{44} \end{bmatrix} \quad (2.287)$$

In ordre to find the Coriolis and Centripetal force vector of the TLRIP, each element of the velocity coupling matrices (C_1, C_2 , C_3 and C_4) need to verified the equality of the elements of the following matrices.

$$\begin{bmatrix} C^1{}_{11} & C^1{}_{12} & C^1{}_{13} & C^1{}_{14} \\ C^1{}_{21} & C^1{}_{22} & C^1{}_{23} & C^1{}_{24} \\ C^1{}_{31} & C^1{}_{32} & C^1{}_{33} & C^1{}_{34} \\ C^1{}_{41} & C^1{}_{42} & C^1{}_{43} & C^1{}_{44} \end{bmatrix} = \begin{bmatrix} \dot{\theta_1}^2 & \dot{\theta_1}\dot{\theta_2} & \dot{\theta_1}\dot{\theta_3} & \dot{\theta_1}\dot{\theta_4} \\ \dot{\theta_1}\dot{\theta_2} & \dot{\theta_2}^2 & \dot{\theta_2}\dot{\theta_3} & \dot{\theta_2}\dot{\theta_4} \\ \dot{\theta_3}\dot{\theta_1} & \dot{\theta_3}\dot{\theta_2} & \dot{\theta_3}^2 & \dot{\theta_3}\dot{\theta_4} \\ \dot{\theta_4}\dot{\theta_1} & \dot{\theta_4}\dot{\theta_2} & \dot{\theta_4}\dot{\theta_3} & \dot{\theta_4}^2 \end{bmatrix} \quad (2.288)$$

$$\begin{bmatrix} C^2{}_{11} & C^2{}_{12} & C^2{}_{13} & C^2{}_{14} \\ C^2{}_{21} & C^2{}_{22} & C^2{}_{23} & C^2{}_{24} \\ C^2{}_{31} & C^2{}_{32} & C^2{}_{33} & C^2{}_{34} \\ C^2{}_{41} & C^2{}_{42} & C^2{}_{43} & C^2{}_{44} \end{bmatrix} = \begin{bmatrix} \dot{\theta_1}^2 & \dot{\theta_1}\dot{\theta_2} & \dot{\theta_1}\dot{\theta_3} & \dot{\theta_1}\dot{\theta_4} \\ \dot{\theta_1}\dot{\theta_2} & \dot{\theta_2}^2 & \dot{\theta_2}\dot{\theta_3} & \dot{\theta_2}\dot{\theta_4} \\ \dot{\theta_3}\dot{\theta_1} & \dot{\theta_3}\dot{\theta_2} & \dot{\theta_3}^2 & \dot{\theta_3}\dot{\theta_4} \\ \dot{\theta_4}\dot{\theta_1} & \dot{\theta_4}\dot{\theta_2} & \dot{\theta_4}\dot{\theta_3} & \dot{\theta_4}^2 \end{bmatrix} \quad (2.289)$$

$$\begin{bmatrix} C^3{}_{11} & C^3{}_{12} & C^3{}_{13} & C^3{}_{14} \\ C^3{}_{21} & C^3{}_{22} & C^3{}_{23} & C^3{}_{24} \\ C^3{}_{31} & C^3{}_{32} & C^3{}_{33} & C^3{}_{34} \\ C^3{}_{41} & C^3{}_{42} & C^3{}_{43} & C^3{}_{44} \end{bmatrix} = \begin{bmatrix} \dot{\theta_1}^2 & \dot{\theta_1}\dot{\theta_2} & \dot{\theta_1}\dot{\theta_3} & \dot{\theta_1}\dot{\theta_4} \\ \dot{\theta_1}\dot{\theta_2} & \dot{\theta_2}^2 & \dot{\theta_2}\dot{\theta_3} & \dot{\theta_2}\dot{\theta_4} \\ \dot{\theta_3}\dot{\theta_1} & \dot{\theta_3}\dot{\theta_2} & \dot{\theta_3}^2 & \dot{\theta_3}\dot{\theta_4} \\ \dot{\theta_4}\dot{\theta_1} & \dot{\theta_4}\dot{\theta_2} & \dot{\theta_4}\dot{\theta_3} & \dot{\theta_4}^2 \end{bmatrix} \quad (2.290)$$

$$\begin{bmatrix} C^4{}_{11} & C^4{}_{12} & C^4{}_{13} & C^4{}_{14} \\ C^4{}_{21} & C^4{}_{22} & C^4{}_{23} & C^4{}_{24} \\ C^4{}_{31} & C^4{}_{32} & C^4{}_{33} & C^4{}_{34} \\ C^4{}_{41} & C^4{}_{42} & C^4{}_{43} & C^4{}_{44} \end{bmatrix} = \begin{bmatrix} \dot{\theta_1}^2 & \dot{\theta_1}\dot{\theta_2} & \dot{\theta_1}\dot{\theta_3} & \dot{\theta_1}\dot{\theta_4} \\ \dot{\theta_1}\dot{\theta_2} & \dot{\theta_2}^2 & \dot{\theta_2}\dot{\theta_3} & \dot{\theta_2}\dot{\theta_4} \\ \dot{\theta_3}\dot{\theta_1} & \dot{\theta_3}\dot{\theta_2} & \dot{\theta_3}^2 & \dot{\theta_3}\dot{\theta_4} \\ \dot{\theta_4}\dot{\theta_1} & \dot{\theta_4}\dot{\theta_2} & \dot{\theta_4}\dot{\theta_3} & \dot{\theta_4}^2 \end{bmatrix} \quad (2.291)$$

The elements of Coriolis and Centripetal force vector of the TLRIP are given as follows:

$$C_{11} = I_{zz4}\,\dot{\theta_1}\dot{\theta_2}\sin(2\theta_2 + 2\theta_3 + 2\theta_4) + I_{zz4}\,\dot{\theta_1}\dot{\theta_3}\sin(2\theta_2 + 2\theta_3 + 2\theta_4)$$
$$I_{zz4}\,\dot{\theta_1}\dot{\theta_4}\sin(2\theta_2 + 2\theta_3 + 2\theta_4) + I_{zz2}\,\dot{\theta_1}\dot{\theta_2}\sin 2\theta_2 + a_{25}\,\dot{\theta_3}\dot{\theta_4}\sin(\theta_3 + \theta_3 + \theta_4)$$
$$+ I_{zz3}\,\dot{\theta_1}\dot{\theta_3}\sin(2\theta_2 + 2\theta_3) + \frac{a_{19}\dot{\theta_1}\dot{\theta_2}\sin(2\theta_2 + 2\theta_3 + 2\theta_4)}{4} - \frac{a_{22}\,\dot{\theta_1}\dot{\theta_4}\sin\theta_4}{2}$$
$$+ \frac{a_{25}\dot{\theta_2}^2\sin(\theta_2 + \theta_3 + \theta_4)}{2} + \frac{a_{25}\dot{\theta_3}^2\sin(\theta_2 + \theta_3 + \theta_4)}{2} + a_8\dot{\theta_1}\dot{\theta_2}\sin(2\theta_2 + \theta_3)$$
$$+ \frac{a_{21}\,\dot{\theta_1}\dot{\theta_4}\sin(2\theta_2 + \theta_3 + \theta_4)}{2} + a_{11}\,\dot{\theta_2}\dot{\theta_3}\sin(\theta_2 + \theta_3) + 2\,a_{23}\,\dot{\theta_2}\dot{\theta_3}\sin(\theta_2 + \theta_3)$$
$$- \frac{a_{21}\,\dot{\theta_1}\dot{\theta_3}\sin(\theta_2 + \theta_3)}{2} - \frac{a_{21}\,\dot{\theta_1}\dot{\theta_4}\sin(\theta_3 + \theta_4)}{2} + \frac{a_{22}\,\dot{\theta_1}\dot{\theta_2}\sin(2\theta_3 + 2\theta_3 + \theta_4)}{2}$$
$$+ \frac{a_{22}\,\dot{\theta_1}\dot{\theta_3}\sin(2\theta_3 + 2\theta_3 + \theta_4)}{2} - \frac{a_8\,\dot{\theta_1}\dot{\theta_3}\sin\theta_3}{2} + \frac{a_{21}\,\dot{\theta_1}\dot{\theta_3}\sin(2\theta_2 + \theta_3 + \theta_4)}{2}$$

$$+a_{20}\,\dot{\theta}_1\dot{\theta}_3\sin(2\theta_2+\theta_3)+\ a_{21}\dot{\theta}_1\dot{\theta}_2\sin(2\theta_2+\theta_3+\theta_4)\ +\frac{a_9\dot{\theta}_2^{\,2}\sin\theta_2}{2}+a_{10}$$

$$+\frac{a_7\dot{\theta}_1\dot{\theta}_3\sin(2\theta_2+2\theta_3)}{4}+a_{18}\dot{\theta}_1\dot{\theta}_3\sin(2\theta_2+2\theta_3)+\frac{a_{11}\dot{\theta}_2^{\,2}\sin(2\theta_2+2\theta_3)}{2}+$$

$$a_8\dot{\theta}_1\dot{\theta}_2\sin(2\theta_2+\theta_3)+\ 2\,a_{20}\,\dot{\theta}_1\dot{\theta}_2\sin(2\theta_2+\theta_3)+\frac{a_8\,\dot{\theta}_1\dot{\theta}_3\sin(2\theta_2+\theta_3)}{2}+$$

$$+a_{18}\dot{\theta}_1\dot{\theta}_2\sin(2\theta_2+2\theta_3)+\ a_{25}\,\dot{\theta}_2\dot{\theta}_4\sin(\theta_3+\theta_3+\theta_4)-\frac{a_{22}\,\dot{\theta}_1\dot{\theta}_3\sin\theta_4}{2}$$

$$+\frac{a_{25}\dot{\theta}_4^{\,2}\sin(\theta_2+\theta_3+\theta_4)}{2}+2\,a_{20}\dot{\theta}_1\dot{\theta}_2\sin(2\theta_2+\theta_3)-\ a_{20}\,\dot{\theta}_1\dot{\theta}_3\sin\theta_3$$

$$+\frac{a_{11}\dot{\theta}_3^{\,2}\sin(\theta_2+\theta_3)}{2}+a_{23}\dot{\theta}_3^{\,2}\sin(\theta_2+\theta_3)\,\dot{\theta}_2^{\,2}\sin\theta_2+a_{21}\dot{\theta}_2^{\,2}\sin\theta_2$$

$$+\frac{a_{19}\dot{\theta}_1\dot{\theta}_3\sin(2\theta_2+2\theta_3+2\theta_4)}{4}+\frac{a_{19}\dot{\theta}_1\dot{\theta}_4\sin(2\theta_2+2\theta_3+2\theta_4)}{4}$$

$$+a_{23}\dot{\theta}_2^{\,2}\sin(\theta_2+\theta_3)+\frac{a_2\dot{\theta}_1\dot{\theta}_4\sin2\theta_2}{4}+I_{zz3}\,\dot{\theta}_1\dot{\theta}_2\sin(2\theta_2+2\theta_3)$$

$$+a_4\dot{\theta}_1\dot{\theta}_2\sin2\theta_2+a_{17}\dot{\theta}_1\dot{\theta}_2\sin2\theta_2+\frac{a_1\dot{\theta}_1\dot{\theta}_2\sin(2\theta_2+2\theta_3)}{4}$$

$$+\,a_{25}\,\dot{\theta}_2\dot{\theta}_3\sin(2\theta_3+2\theta_3+\theta_4) \qquad (2.292)$$

$$C_{21}=\frac{-I_{zz4}\,\dot{\theta}_1^{\,2}\sin(2\theta_2+2\theta_3+2\theta_4)}{2}-\frac{I_{zz2}\,\dot{\theta}_1^{\,2}\sin2\theta_2}{2}-\frac{a_{17}\,\dot{\theta}_1^{\,2}\sin2\theta_2}{2}$$

$$-\frac{a_1\,\dot{\theta}_1^{\,2}\sin(\,2\theta_2+2\theta_3)}{8}-\frac{a_{18}\,\dot{\theta}_1^{\,2}\sin(\,2\theta_2+2\theta_3)}{2}-\frac{a_{21}\,\dot{\theta}_1^{\,2}\sin(\,2\theta_2+2\theta_3)}{2}$$

$$-\frac{a_{21}\,\dot{\theta}_3^{\,2}\sin(\,\theta_3+\theta_4)}{2}-\frac{a_{21}\,\dot{\theta}_4^{\,2}\sin(\,\theta_3+\theta_4)}{2}-\frac{a_{22}\,\dot{\theta}_1^{\,2}\sin(2\theta_2+2\,\theta_3+\theta_4)}{2}$$

$$-a_{21}\,\dot{\theta}_4\dot{\theta}_3\sin(\theta_3+\theta_4)-a_8\,\dot{\theta}_2\dot{\theta}_3\sin\theta_3-2a_{20}\,\dot{\theta}_2\dot{\theta}_3\sin\theta_3-a_{22}\,\dot{\theta}_2\dot{\theta}_4\sin\theta_4$$

$$-\frac{a_8\,\dot{\theta}_3^{\,2}\sin\theta_3}{2}-a_{20}\,\dot{\theta}_3^{\,2}\sin\theta_3-\frac{a_{22}\,\dot{\theta}_4^{\,2}\sin\theta_4}{2}-\frac{a_8\,\dot{\theta}_1^{\,2}\sin(2\theta_2+\theta_3)}{2}$$

$$-a_{20}\,\dot{\theta}_1^{\,2}\sin(2\theta_2+\theta_3)-a_{20}\,\dot{\theta}_2\dot{\theta}_3\sin(\theta_3+\theta_4)-a_{21}\,\dot{\theta}_4\dot{\theta}_2\sin(\theta_3+\theta_4)$$

$$-\frac{a_{19}\,\dot{\theta}_1^{\,2}\sin(2\theta_2+2\theta_3+2\theta_4)}{8}-\frac{a_2\,\dot{\theta}_1^{\,2}\sin2\theta_2}{8}-\frac{a_4\,\dot{\theta}_1^{\,2}\sin2\theta_2}{2}$$

$$-\frac{I_{zz3}\,\dot{\theta}_1^{\,2}\sin(2\theta_2+2\theta_3)}{2}-a_{22}\,\dot{\theta}_3\dot{\theta}_4\sin\theta_4 \qquad (2.293)$$

$$C_{31} = \frac{a_{21}\,\dot{\theta_1}^{2}\sin(\theta_3+\theta_4)}{4} - \frac{I_{zz3}\,\dot{\theta_1}^{2}\sin(2\theta_2+2\theta_3)}{2} - \frac{a_{22}\,\dot{\theta_4}^{2}\sin\theta_4}{2}$$
$$- \frac{a_1\,\dot{\theta_1}^{2}\sin(2\theta_2+2\theta_3)}{8} - \frac{a_{18}\,\dot{\theta_1}^{2}\sin(2\theta_2+2\theta_3)}{2} - \frac{a_{21}\,\dot{\theta_1}^{2}\sin(2\theta_2+\theta_3+\theta_4)}{2}$$
$$- \frac{I_{zz4}\,\dot{\theta_1}^{2}\sin(2\theta_2+2\theta_3+2\theta_4)}{2} + \frac{a_{21}\,\dot{\theta_1}^{2}\sin(\theta_2+\theta_4)}{2} + \frac{a_{20}\,\dot{\theta_2}^{2}\sin\theta_3}{2}$$
$$- \frac{a_8\,\dot{\theta_1}^{2}\sin(2\theta_2+\theta_4)}{4} - \frac{a_{20}\,\dot{\theta_1}^{2}\sin(2\theta_2+\theta_3)}{2} - a_{22}\,\dot{\theta_2}\dot{\theta_4}\sin(2\theta_2+\theta_3)$$
$$- \frac{a_{19}\,\dot{\theta_1}^{2}\sin(2\theta_2+2\theta_3+2\theta_4)}{8} - \frac{a_{22}\,\dot{\theta_1}^{2}\sin(2\theta_2+2\theta_3+2\theta_4)}{2}$$
$$+ \frac{a_8\,\dot{\theta_1}^{2}\sin\theta_3}{4} + \frac{a_{20}\,\dot{\theta_1}^{2}\sin\theta_3}{2} + \frac{a_8\,\dot{\theta_2}^{2}\sin\theta_3}{2} - a_{22}\dot{\theta_3}\dot{\theta_4}\sin\theta_4 \qquad (2.294)$$

$$C_{41} = \frac{a_{21}\,\dot{\theta_1}^{2}\sin(\theta_3+\theta_4)}{4} - \frac{a_{19}\,\dot{\theta_1}^{2}\sin(2\theta_2+2\theta_3+2\theta_4)}{8} + a_{22}\,\dot{\theta_3}\dot{\theta_2}\sin\theta_4$$
$$- \frac{a_{21}\,\dot{\theta_1}^{2}\sin(2\theta_2+\theta_3+\theta_4)}{4} - \frac{a_{22}\,\dot{\theta_1}^{2}\sin(2\theta_2+2\theta_3+2\theta_4)}{4}$$
$$- \frac{I_{zz4}\,\dot{\theta_1}^{2}\sin(2\theta_2+2\theta_3+2\theta_4)}{2} + \frac{a_{21}\,\dot{\theta_2}^{2}\sin(\theta_3+\theta_4)}{2}$$
$$+ \frac{a_{22}\,\dot{\theta_1}^{2}\sin\theta_4}{4} + \frac{a_{22}\,\dot{\theta_2}^{2}\sin\theta_4}{2} + \frac{a_{22}\,\dot{\theta_3}^{2}\sin\theta_4}{2} \qquad (2.295)$$

The Coriolis and Centripetal force vector of the TLRIP can be given in equation (2.296)

$$C(\theta,\dot{\theta}) = \begin{bmatrix} C_{11} \\ C_{21} \\ C_{31} \\ C_{41} \end{bmatrix} \qquad (2.296)$$

The elements of the gravity vector are given as follows:

$$G_{11} = 0 \qquad (2.297)$$

$$G_{21} = -\frac{a_{14}}{2}\sin(\theta_2+\theta_3) - a_{26}\sin(\theta_2+\theta_3) - \frac{a_{12}}{2}\sin\theta_2$$
$$-a_{13}\sin\theta_2 - a_{29}\sin\theta_2 - \frac{a_{27}\sin(\theta_2+\theta_3+\theta_4)}{2} \qquad (2.298)$$

$$G_{31} = -\frac{a_{27}\sin(\theta_2+\theta_3+\theta_4)}{2} - \frac{a_{14}\sin(\theta_2+\theta_3)}{2} - a_{28}\sin(\theta_2+\theta_3) \qquad (2.299)$$

$$G_{41} = -\frac{a_{27}\sin(\theta_2+\theta_3+\theta_4)}{2} \qquad (2.300)$$

The gravity vector of the TLRIP is given in equation (2.301)

$$G = \begin{bmatrix} 0 \\ G_{21} \\ G_{31} \\ G_{41} \end{bmatrix} \qquad (2.301)$$

The TLRIP has some complex non-linear dynamic equations which can be written in a matrix form given in equation (2.302):

$$\begin{bmatrix} D_{11} & D_{12} & D_{13} & D_{14} \\ D_{21} & D_{22} & D_{23} & D_{24} \\ D_{31} & D_{32} & D_{33} & D_{34} \\ D_{41} & D_{42} & D_{43} & D_{44} \end{bmatrix} \begin{bmatrix} \ddot{\theta}_1 \\ \ddot{\theta}_2 \\ \ddot{\theta}_3 \\ \ddot{\theta}_4 \end{bmatrix} + \begin{bmatrix} C_{11} \\ C_{21} \\ C_{31} \\ C_{41} \end{bmatrix} + \begin{bmatrix} 0 \\ G_{21} \\ G_{31} \\ G_{41} \end{bmatrix} = \begin{bmatrix} \tau_1 \\ 0 \\ 0 \\ 0 \end{bmatrix} \qquad (2.302)$$

2.3.3. Jacobian matrix of the TLRIP

The linear and angular velocities of the links of the TLRIP are used to determine the Jacobian matrix. A formula to compute the Jacobian matrix of the TLRIP is given in equation (2.40) in section (2.1.3). J_v and J_w represents the Jacobian matrices obtained from the linear and angular velocities in the end-link, respectively. The linear velocities are given in equation (2.303).

$$ {}^0_5V = {}^0_5R\,{}^5_5V = \begin{bmatrix} \frac{S_{1234}}{2} + \frac{S_{2134}}{2} & \frac{C_{1234}}{2} + \frac{C_{2134}}{2} & -S_1 \\ \frac{C_{2134}}{2} - \frac{C_{1234}}{2} & \frac{S_{1234}}{2} - \frac{S_{2134}}{2} & C_1 \\ C_{234} & -S_{234} & 0 \end{bmatrix} \times$$

$$\begin{bmatrix} L_2\dot{\theta}_2 S_{34} + L_3\dot{\theta}_2 S_4 + L_3\dot{\theta}_3 S_4 - L_1\dot{\theta}_1 S_{234} \\ L_4(\dot{\theta}_2+\dot{\theta}_3+\dot{\theta}_4) + L_2\dot{\theta}_2 C_{34} + L_3\dot{\theta}_2 C_4 + L_3\dot{\theta}_3 C_4 - L_1\dot{\theta}_1 C_{234} \\ \dot{\theta}_1 (L_3 S_{23} + L_2 S_2 + L_4 S_{234}) \end{bmatrix} = \begin{bmatrix} {}^0_5V_1 \\ {}^0_5V_2 \\ {}^0_5V_3 \end{bmatrix} \qquad (2.303)$$

The elements of the linear velocities vector (^0_5V) can be given as follows:

$$ {}^{0}_{5}V = \begin{bmatrix} {}^{0}_{5}V_{11} & {}^{0}_{5}V_{12} & {}^{0}_{5}V_{13} & {}^{0}_{5}V_{14} \\ {}^{0}_{5}V_{21} & {}^{0}_{5}V_{22} & {}^{0}_{5}V_{23} & {}^{0}_{5}V_{24} \\ {}^{0}_{5}V_{31} & {}^{0}_{5}V_{32} & {}^{0}_{5}V_{33} & {}^{0}_{5}V_{34} \end{bmatrix} \begin{bmatrix} \dot{\theta}_1 \\ \dot{\theta}_2 \\ \dot{\theta}_3 \\ \theta_4 \end{bmatrix} \quad (2.304) $$

$$ {}^{0}_{5}V_{11} = S_1 S_2 (L_4 S_3 S_4 - L_2 - L_3 C_3 - L_4 C_3 C_4) $$
$$ -C_2 S_1 (L_3 S_3 + L_4 C_3 S_4 + L_4 C_4 S_3) - L_1 C_1 \quad (2.305) $$

$$ {}^{0}_{5}V_{12} = C_1 (L_3 S_{23} + L_2 C_2 + L_4 C_{234}) \quad (2.306) $$

$$ {}^{0}_{5}V_{13} = \frac{L_4\, C_{2134}}{2} + \frac{L_3\, C_{123}}{2} + \frac{L_4\, C_{1234}}{2} + \frac{L_3\, C_{213}}{2} \quad (2.307) $$

$$ {}^{0}_{5}V_{14} = \frac{L_4\, C_{1234}}{2} + \frac{L_4\, C_{2134}}{2} \quad (2.308) $$

$$ {}^{0}_{5}V_{21} = C_1 S_2 (L_2 + L_3 C_3 + L_4 C_3 C_4 - L_4 S_3 S_4) $$
$$ +C_2 C_1 (L_3 S_3 + L_4 C_3 S_4 + L_4 C_4 S_3) - L_1 S_1 \quad (2.309) $$

$$ {}^{0}_{5}V_{22} = S_1 (L_3 C_{23} + L_2 C_2 + L_4 C_{234}) \quad (2.310) $$

$$ {}^{0}_{5}V_{23} = \frac{L_3\, S_{123}}{2} - \frac{L_4\, S_{2134}}{2} + \frac{L_4\, S_{1234}}{2} + \frac{L_3\, S_{213}}{2} \quad (2.311) $$

$$ {}^{0}_{5}V_{24} = \frac{L_4\, S_{1234}}{2} - \frac{L_4\, S_{2134}}{2} \quad (2.312) $$

$$ {}^{0}_{5}V_{31} = 0 \quad (2.313) $$

$$ {}^{0}_{5}V_{32} = L_3 S_{23} - L_2 S_2 - L_4 S_{234} \quad (2.314) $$

$$ {}^{0}_{5}V_{33} = -L_3 S_{23} - L_4\, S_{234} \quad (2.315) $$

$$ {}^{0}_{5}V_{34} = -L_4\, S_{234} \quad (2.316) $$

Where

$C_{123} = \cos(\theta_1 + \theta_2 + \theta_3)$, $C_{213} = \cos(\theta_2 - \theta_1 + \theta_3)$, $C_{12} = \cos(\theta_1 + \theta_2)$,

$S_{1234} = \sin(\theta_1 + \theta_2 + \theta_3 + \theta_4)$, $C_{1234} = \cos(\theta_1 + \theta_2 + \theta_3 + \theta_4)$,

$C_1 = \cos\theta_1$, $S_1 = \sin\theta_1$ $S_{2134} = \sin(\theta_2 - \theta_1 + \theta_3 + \theta_4)$, $C_3 = \cos\theta_3$

$S_{234} = \sin(\theta_2 + \theta_3 + \theta_4), C_2 = \cos\theta_2, S_2 = \sin\theta_2, S_3 = \sin\theta_3$

$S_{1\_2} = \sin(\theta_1 - \theta_2), C_{1\_2} = \cos(\theta_1 - \theta_2), S_{23} = \sin(\theta_2 + \theta_3)$

$C_{2134} = \cos(\theta_2 - \theta_1 + \theta_3 + \theta_4), C_{234} = \cos(\theta_2 + \theta_3 + \theta_4)$

$C_4 = \cos\theta_4,\ S_4 = \sin\theta_4$ (2.317)

The Jacobian matrix taken from the linear velocities is given in equation (2.318).

$$J_{v_0}^{5}(\theta) = \begin{bmatrix} {}_5^0V_{11} & {}_5^0V_{12} & {}_5^0V_{13} & {}_5^0V_{14} \\ {}_5^0V_{21} & {}_5^0V_{22} & {}_5^0V_{23} & {}_5^0V_{24} \\ {}_5^0V_{31} & {}_5^0V_{32} & {}_5^0V_{33} & {}_5^0V_{34} \end{bmatrix} \quad (2.318)$$

The angular velocities matrix of the TLRIP is given in equation (2.319)

$${}_5^0w = {}_5^0R\ {}_5^5w = \begin{bmatrix} -S_1(\dot{\theta}_2 + \dot{\theta}_3 + \dot{\theta}_4) \\ C_1(\dot{\theta}_2 + \dot{\theta}_3 + \dot{\theta}_4) \\ \dot{\theta}_1 \end{bmatrix} \quad (2.319)$$

The Jacobian matrix taken from the angular velocities is given as follows:

$$J_{w_0}^{5}(\theta) = \begin{bmatrix} 0 & -\sin\theta_1 & -\sin\theta_1 & -\sin\theta_1 \\ 0 & \cos\theta_1 & \cos\theta_1 & \cos\theta_1 \\ 1 & 0 & 0 & 0 \end{bmatrix} \quad (2.320)$$

The Jacobian matrix taken from the linear and angular velocities is given in equation (2.321).

$$J_0^5(\theta) = \begin{bmatrix} {}_5^0V_{11} & {}_5^0V_{12} & {}_5^0V_{13} & {}_5^0V_{14} \\ {}_5^0V_{21} & {}_5^0V_{22} & {}_5^0V_{23} & {}_5^0V_{24} \\ {}_5^0V_{31} & {}_5^0V_{32} & {}_5^0V_{33} & {}_5^0V_{34} \\ 0 & -S_1 & -S_1 & -S_1 \\ 0 & C_1 & C_1 & C_1 \\ 1 & 0 & 0 & 0 \end{bmatrix} \quad (2.321)$$

Furthermore, using the determinant of the Jacobian matrix, $w = \left|\det\left(J_0^5(\theta) \times J_0^5(\theta)^T\right)\right|$, the optimal length of each link of the TLRIP is estimated using the PSO optimization algorithm. The optimal lengths are given in Table 2.7.

2.3.4. Dynamic simulation of the TLRIP

According to the equation (2.302), the expression for the angular acceleration vector ($\ddot{\theta}$) can be given in equation (2.322). The three equations of $\ddot{\theta}_1$, $\ddot{\theta}_2$, $\ddot{\theta}_3$ and $\ddot{\theta}_4$ are derived and simulated in Matlab/Simulink. The Matlab code of the mathematical expression of the three equations is given in the appendix. Figure 2.10 show the non-linear mathematical model in Matlab/Simulink.

$$\begin{bmatrix} \ddot{\theta}_1 \\ \ddot{\theta}_2 \\ \ddot{\theta}_3 \\ \ddot{\theta}_4 \end{bmatrix} = \begin{bmatrix} D_{11} & D_{12} & D_{13} & D_{14} \\ D_{21} & D_{22} & D_{23} & D_{24} \\ D_{31} & D_{32} & D_{33} & D_{34} \\ D_{41} & D_{42} & D_{43} & D_{44} \end{bmatrix}^{-1} \left[\begin{pmatrix} \tau_1 \\ 0 \\ 0 \\ 0 \end{pmatrix} - \begin{pmatrix} C_{11} \\ C_{21} \\ C_{31} \\ C_{41} \end{pmatrix} - \begin{pmatrix} 0 \\ G_{21} \\ G_{31} \\ G_{41} \end{pmatrix} \right] \tag{2.322}$$

In order to verify the mathematical model, a mechanical dynamic model of the TLRIP was developed by using the MATLAB/SimMechanics toolbox. MATLAB/SimMechanics model of the TLRIP is shown in Figure 2.11 (a). Different views from virtual reality model of the TLRIP in Matlab Simulink is shown in Figure 2.11 (b). Furthermore, for both model, the initial conditions of pendulums' joint positions are chosen as follows $\theta_1 = 0\,°$, $\theta_2 = 20\,°$, $\theta_3 = 30\,°$ and $\theta_4 = 40\,°$. The obtained results from both MATLAB/SimMechanics and the mathematical models match exactly. Figure 2.12 illustrates a comparison of the three joint positions obtained from simulation mathematical and the SimMechanics models without frictions. The simulations are performed by the sampling time 1ms and 5s simulation time. A numerical method Bogacki-Shampine solver is selected with fixed-step.

2.4. Inertia Analysis of the Three Link Rotary Pendulum

In order to examine the effects of the inertia of the vertical arms in the TLRIP, the dynamic equations of the TLRIP were solved in different inertia cases. In the first case, the inertia tensor of the links is neglected in the dynamic model. In the second case, only the component I_{zz} of the inertia tensor is considered for each link. In the last case, full inertia tensor ${}^{i}_{i}I$ is taken into consideration in the dynamic model**.** Figure 2.13 shows the joints' positions of the TLRIP obtained by the three different dynamic simulation models for the initial condition of, $\theta_1 = 0\,°$, $\theta_2 = 20\,°$, $\theta_3 = 30°$ and $\theta_4 = 40°$ The simulation results of the dynamic equations with only the component

I_{zz} of the inertia tensor and the full inertia tensor ¦I are almost the same in low velocities of the arms**.**

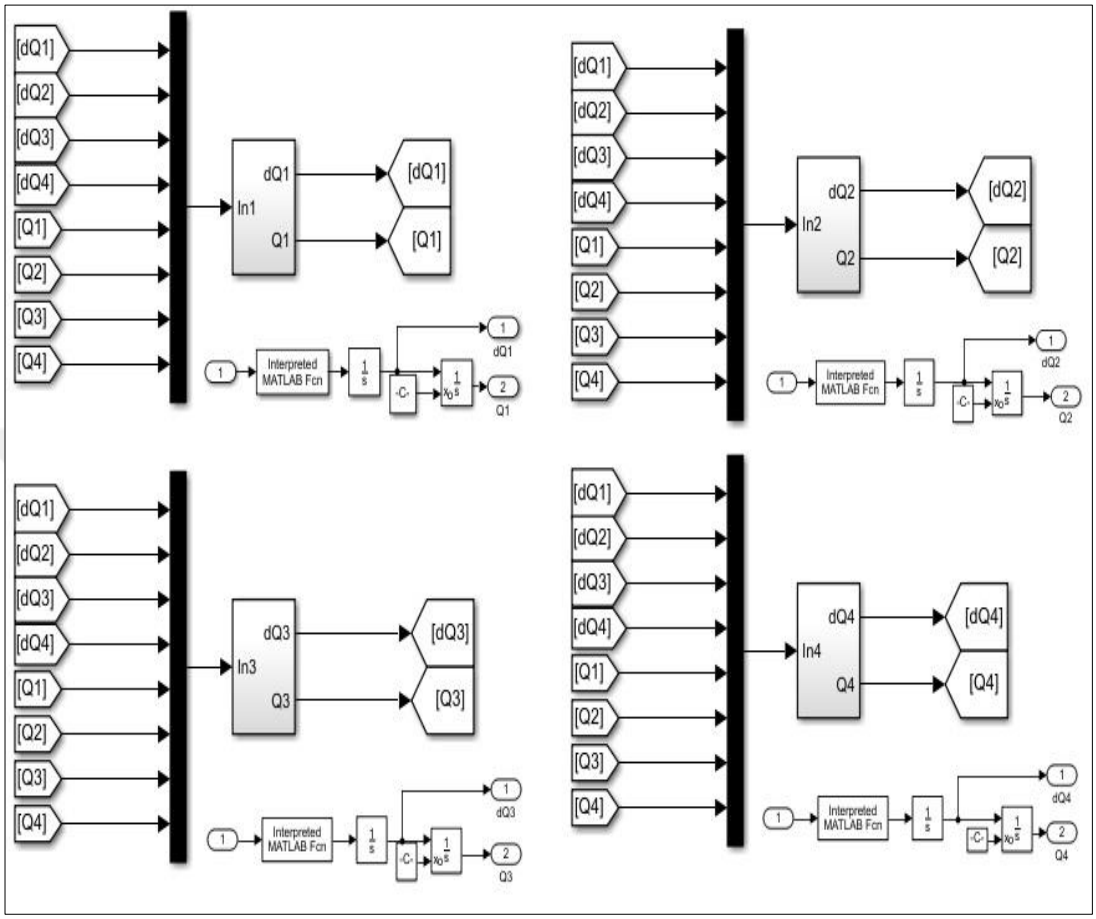

Figure 2.10. Mathematical model of TLRIP in Matlab/Simulink

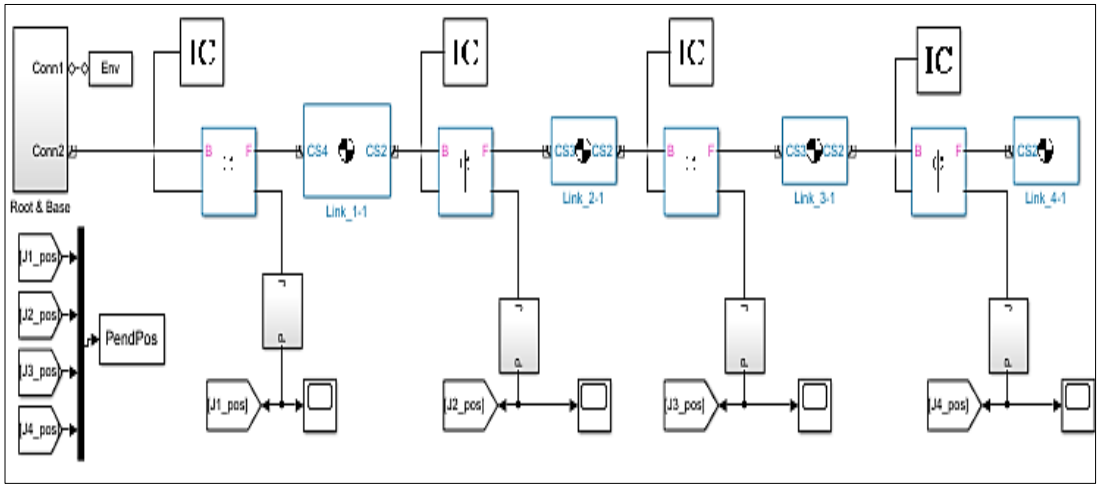

(a)

Figure 2.11. (a) MATLAB/SimMechanics model of the TLRIP, (b) Different views from virtual reality model of the TLRIP in Matlab Simulink

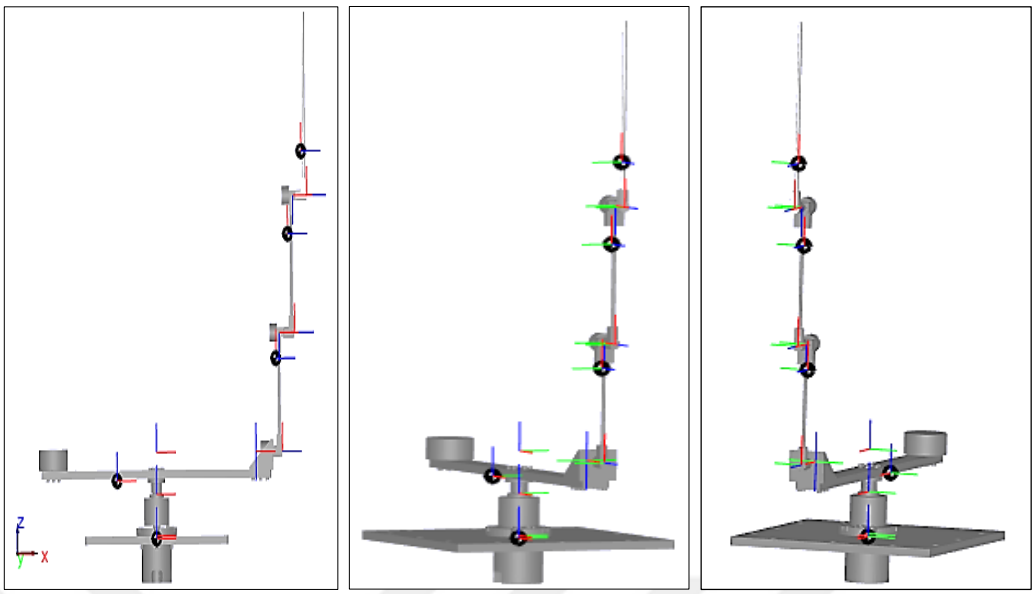

(b)

Figure 2.11.(Cont.) (a) MATLAB/SimMechanics model of the TLRIP, (b) Different views from virtual reality model of the TLRIP in Matlab Simulink

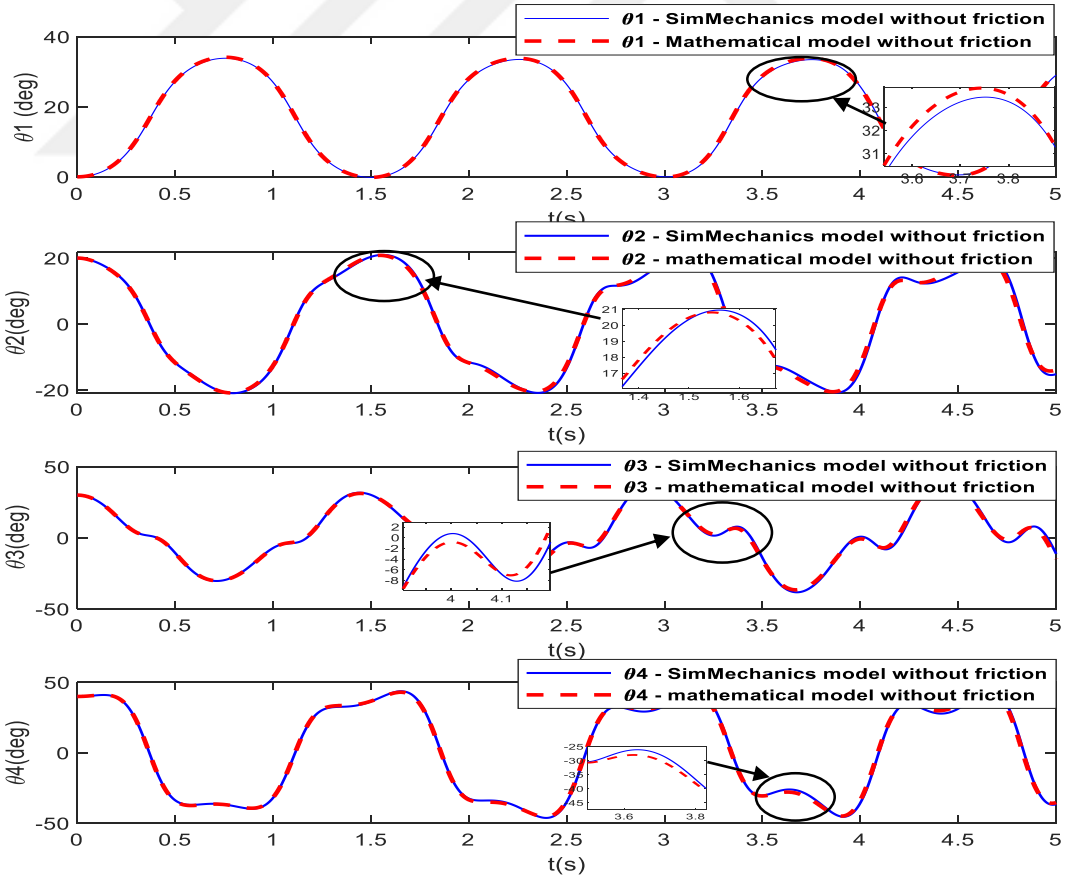

Figure 2.12. Comparison of the pendulum joint positions obtained from the analytic mathematical model and SimMechanics numerical model of the TLRIP

On the other hand, the dynamic model where the inertia is neglected is not acceptable. In order to have a more simplified dynamic model in the equilibrium control of the TLRIP, only the component I_{zz} of the inertia tensor can be employed. On the other hand, the accurate dynamic model in swing-up control of the TLRIP is very important to compute the total energy of the pendulum. Therefore, the full inertia tensor $^{i}_{i}I$ should be taken into consideration in the dynamic model of the pendulum with a complex structure. [92]

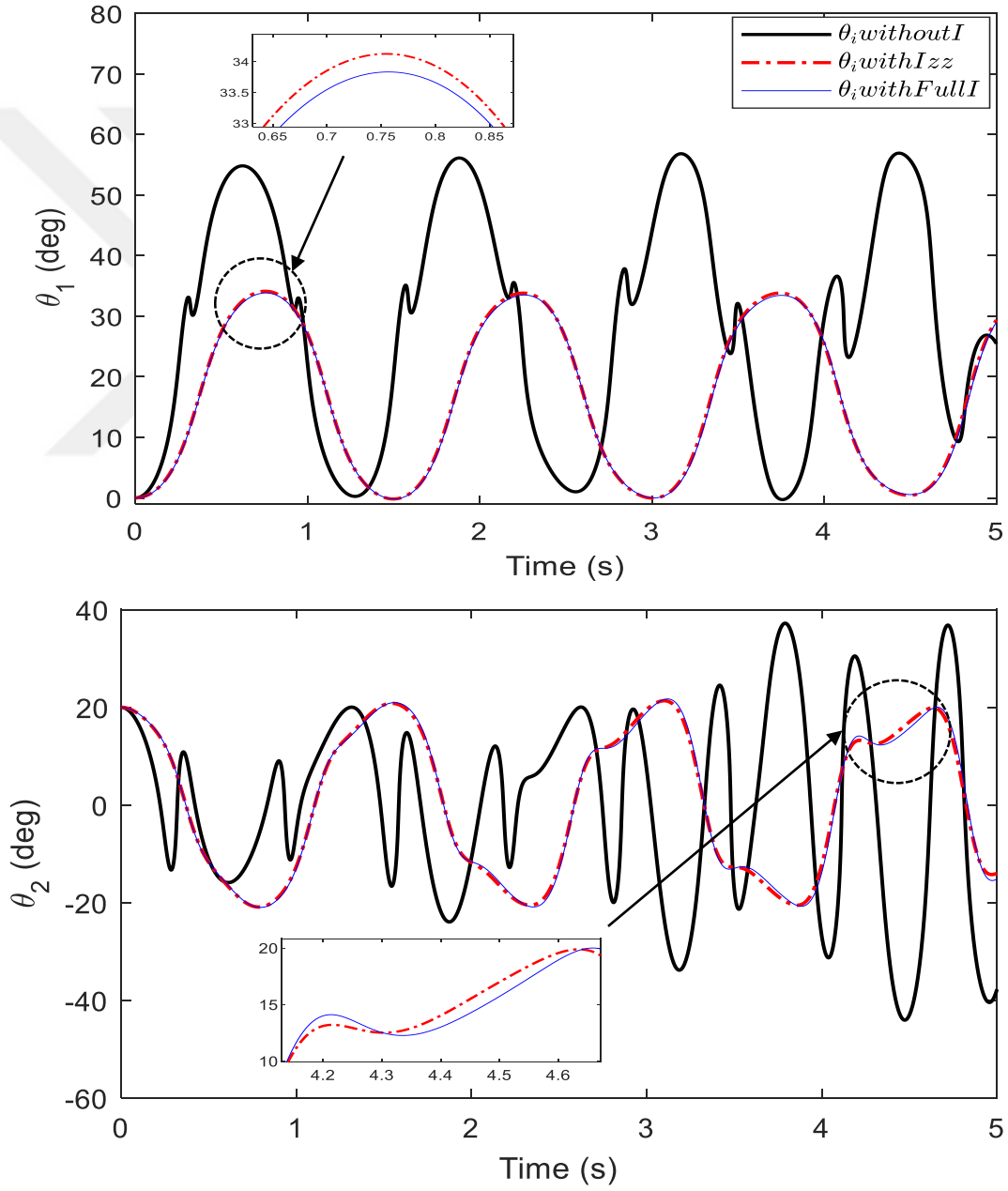

Figure 2.13. Comparison of the joint positions of the TLRIP under different usages of the inertia

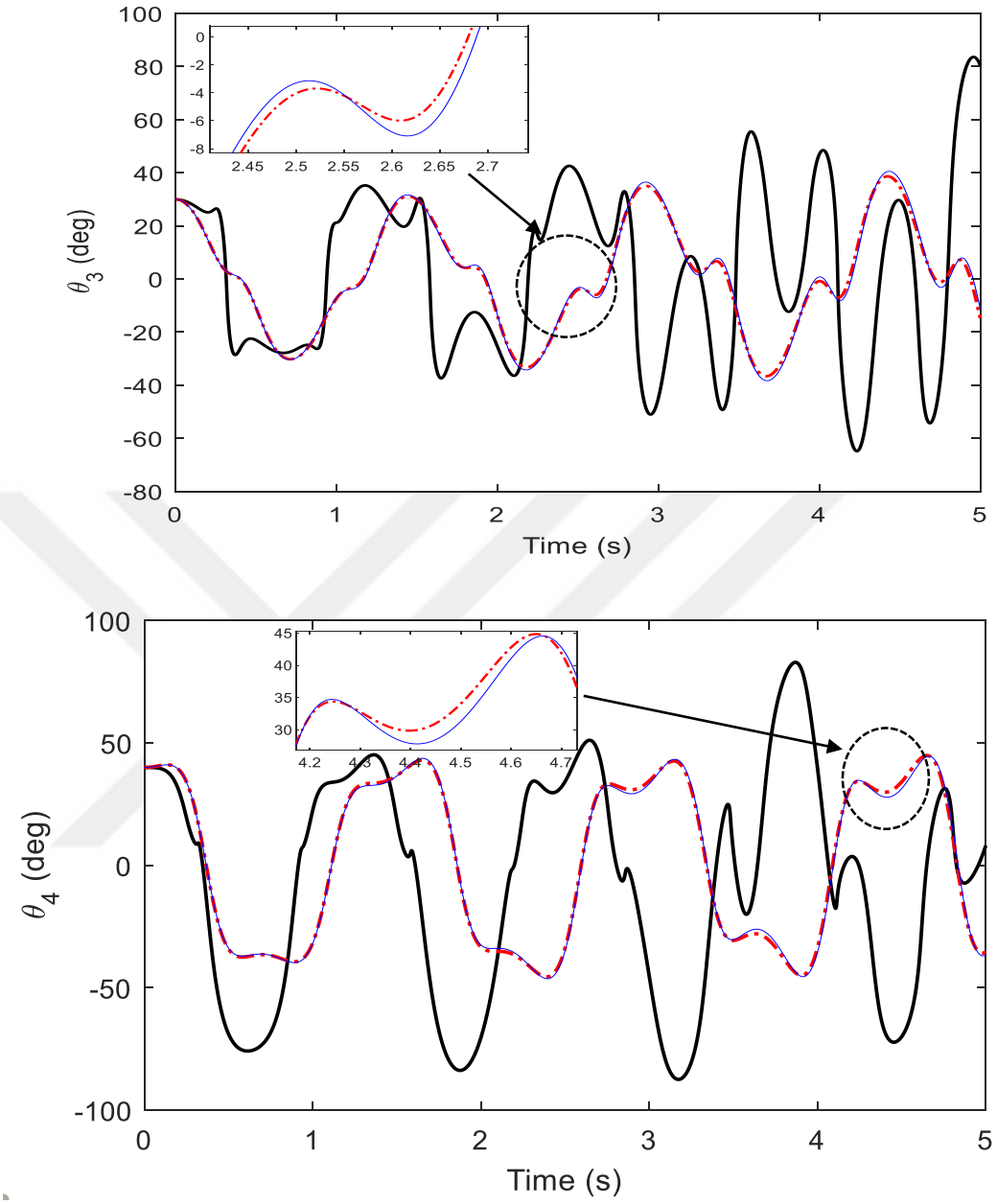

Figure 2.13.(Cont.) Comparison of the joint positions of the TLRIP under different usages of the inertia

Figure 2.14 illustrates a comparison of the three joint positions obtained from simulation (mathematical model and the SimMechanics model without frictions) and experimental results. As can be seen from the figure, position errors of the joints in TLRIP occurred highly since joint friction dynamics are ignored. Therefore, the friction models should be determined explicitly to obtain the most accurate dynamic model of the pendulums. The friction estimation models in the literature will be described in the next chapter.

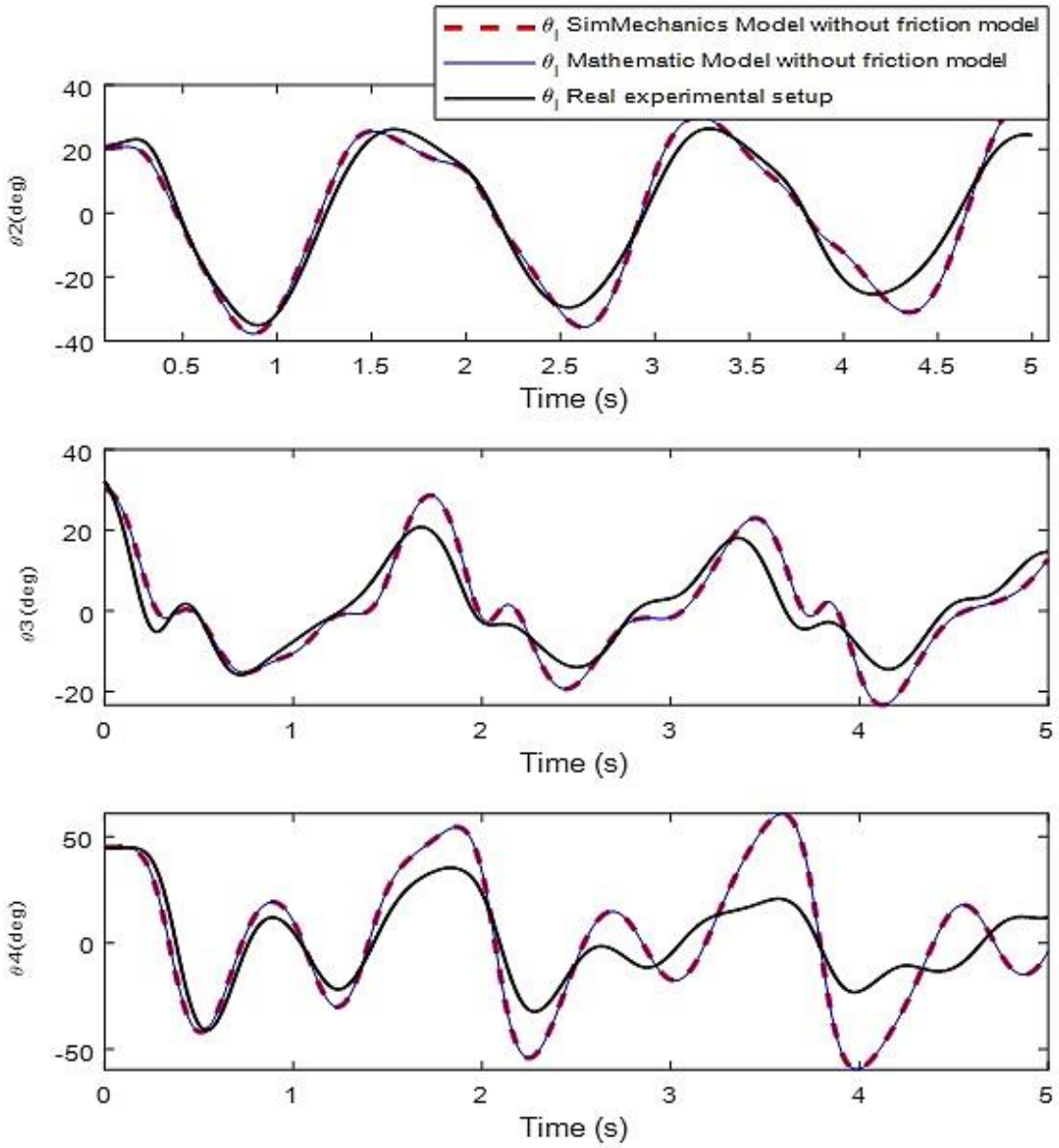

Figure 2.14. Comparison of the joint positions obtained from the mathematical model without frictions, SimMechanics model without frictions and the real experimental setup

3. JOINTS FRICTION ESTIMATION OF THE TLRIP

3.1. Introduction

Frictions are very important in ACE, such as in pneumatic-hydraulic systems, anti-lock brakes for cars and robotic systems. Frictions are highly nonlinear, and they can result in steady-state errors, limit cycles, and poor performance in different systems [93]. It is, therefore, important for control engineers to understand friction phenomena and to estimate the ideal frictions for each system. Today, using the computational power available, it is possible to deal effectively with frictions. Frictions estimation has the potential to ameliorate the quality, economy, and safety of any system. Moreover, due to the gravitational forces and the coupling arising from the Coriolis and centripetal forces, the RIPS is underactuated, unstable and extremely nonlinear. The RIPS include a nonlinearity due to the frictions in the joints. RIPS is the most convenient example to understand the influence of the joint frictions on the design and performance of feedback controllers that aim to stabilize the pendulum in the upright position. The frictions have an influence on the system's response that should be considered seriously [94]. Therefore, friction estimation has the potential to ameliorate the quality and dynamic behavior of the system [95]. In this chapter, friction estimation models are developed to estimate the frictions in the joints of TLRIP. The parameters of frictions models are described with details. The following approach was used to estimate the joint friction of pendulum:

- Comparison of Friction Estimation Models (FEMs) for TLRIP based on three friction models existing in the literature: NCFM, LFM, and NLFM.
- AFEMs were developed to estimate the friction coefficients for TLRIP system. In this approach, the joint accelerations of the TLRIP were classified into three groups: low, medium and high. The adaptive friction coefficients were optimized according to this acceleration classification.
- NFFEMs were developed using the NF system. The joint velocities and accelerations of the TLRIP as the input variables were applied to NF.

3.2. Friction Estimation Models (FEMs)

The joint frictions are dependent on many physical parameters, such as position, velocity and acceleration of the joints [96]. The changes in the positions, velocities and the accelerations of the pendulums can change the friction's characteristics in a complex manner [97]. The dynamic behavior of the joints' frictions is simulated with the different models in the existing literature. Most of these models are defined by friction coefficients. Therefore, it is necessary to develop an accurate friction model to estimate the friction's coefficients in the joints in accordance with the dynamic behavior of positions, velocities and accelerations. NCFM, LFM, and NLFM estimation models were given in this chapter [98], [99], [100-104]. To estimate the constant friction coefficients in the pendulum's joints of the TLRIP, different friction estimation models (NCFM, LFM, and NLFM) were examined. These friction models consist of different important components. Each component takes care of certain aspects of the friction force in the joints [105-106]. Mostly used friction model in the literature is the generalized static friction model which depends only on the velocity (v). It describes only the steady-state behavior of the friction force F_f in the sliding regime, and it is given the equation below [107]:

$$F_f = \sigma_2 v + \text{sign}(v)\left(F_c + (F_s - F_c)\exp\left(-\left|\frac{v}{V_s}\right|^{\delta}\right)\right) \tag{3.1}$$

The first term represents the viscous friction force, and the second term equals the Stribeck effect. F_s , F_c , V_s , δ and σ_2 are the static force, the Coulomb force, the Stribeck force, the shape factor and the viscous friction coefficient, respectively. this model has the discontinuity at velocity reversal which causes errors or even instability during friction compensation.

3.2.1. Non-conservative friction model

NCFM is a classical friction model. It has been used in the first works related to the control of pendulums to estimate the friction in the joints, which based only on one type of friction coefficient [99]. The non-conservative torques due to natural damping of the pendulums called viscous friction torque, and it is introduced through Rayleigh's dissipation function $Ð(\theta_i)$ [98]. The non-conservative friction torque is given in

equation (3.1).

$$F_v = \frac{d\,Đ(\theta_i)}{d\theta_i} = \frac{d}{d\theta_i}\left(\frac{1}{2}\overline{C_p}\dot{\theta_i}^2\right) = \overline{C_p}\dot{\theta_i} \tag{3.2}$$

where $\overline{C_p}$ is the viscous friction coefficient and $\dot{\theta_i}$ is the angular velocity of the i-th pendulum.

3.2.2. Linear friction model

LFM is a combination of the Viscous friction presented in the non-conservative model and another type of friction called Coulomb friction [101], the LFM, which is presented by equation (3.3).

$$F_l = F_v + F_c \tag{3.3}$$

Where F_c is the Coulomb frictions and F_v is the viscous friction torque which is proportional to the angular velocity $\dot{\theta}_i$, and given by equation (3.4). [102]

$$F_v = B_i\,\dot{\theta}_i \tag{3.4}$$

where B_i are the constant viscous coefficients. The Coulomb friction is proportional to the normal load force N_f which is derived as follows:

$$N_f = m\omega^2 l + mg\cos(\theta) \tag{3.5}$$

l is the distance from the pendulum rotation center to the mass center. The pendulum parameters are given in Figure 3.1. The Coulomb frictions F_c is given by equation (3.6).

$$F_c = C_i\,\mathrm{sgn}(\dot{\theta}_i).(ml\,\dot{\theta}_i^{\,2} + mg\cos(\theta_i)) \tag{3.6}$$

where C_i are the dynamic friction coefficients and $\mathrm{sgn}(.)$is the signum function.

3.2.3. Non-linear friction model

The new researches in the field of friction estimation have found that the frictions in the joints can be affected by several factors such as temperature, force/torque, position, velocity and acceleration. Since friction has a complex nonlinear nature [103], the

LFM becomes an oversimplified model in friction structure. The TLRIP system can move in trajectories which have high and suddenly changing, position speed, acceleration and jerk. The LFM cannot cover these characteristics, especially at sudden motion reversal [104]. Therefore, the NLFM reflects a better description of the joint friction characteristics. This model can be described in the following nonlinear equation (3.7). [108]

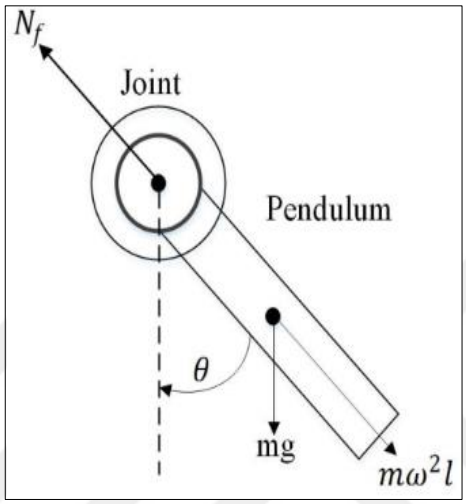

Figure. 3.1. Pendulum parameters

$$\tau_f = f_o + f_c \, \mathrm{sgn}(\dot{\theta}_i) + f_v \, \dot{\theta}_i + f_a \mathrm{atan}(f_b \, \dot{\theta}_i) \tag{3.7}$$

where $f_o$the zero-drift error of friction torque, f_c is the Coulomb friction coefficient, f_v is the viscous friction coefficient. $f_a \mathrm{atan}(f_b \, \dot{\theta}_i)$ present the experimental friction in zero velocity behavior, which f_a and f_b are the experimental friction coefficients. $\dot{\theta}_i$ is the angular velocity, $\mathrm{sgn}(.)$ is the signum function and atan is the arctangent function. In fact, it appears that this nonlinear friction model is derived from the generalized friction model (equation (3.1)). The only difference between the two equations (3.1 and 3.7), the third term in equation (3.7) is modelled with the first and fourth term in equation (3.7). The reason for using the arctangent function in equation (3.7) is to overcome the discontinuity at zero velocity equation (3.1).

3.3. Comparison of the Friction Estimation Models of the TLRIP

In this section, a comparison of the three different models applied to estimate the joint friction of The TLRIP: Non-Conservative, Linear and Non-linear friction estimation

models. A dynamic mechanical simulation without the integration of joints friction of links is explained in chapter 2. The friction estimation models explained in section (3.2) will be compared in this section. The nonlinear dynamic equations of the TLRIP which contain the friction vector can be written in a matrix form, as follows:

$$D(\theta)\ddot{\theta} + C(\theta,\dot{\theta})\dot{\theta} + \tau_f\left(\theta,\dot{\theta}\right) + G(\theta) = \tau_1 \tag{3.8}$$

where $\theta, \dot{\theta}$ and $\ddot{\theta}$ are the vectors of joint angles, the angular velocities, and the angular accelerations, respectively. $D(\theta)$ is the mass matrix, $C(\theta,\dot{\theta})$ is the Coriolis and centrifugal force vector, $\tau_f\left(\theta,\dot{\theta}\right)$ is the friction torque vector, $G(\theta)$ is the gravity vector and τ_1 is the input torque vector in the first joint. The friction vector can be expressed in equation (3.9).

$$\tau_f\left(\theta,\dot{\theta}\right) = \begin{bmatrix} \tau_{f_{11}} \\ \tau_{f_{21}} \\ \tau_{f_{31}} \\ \tau_{f_{41}} \end{bmatrix} \tag{3.9}$$

$\tau_{f_{11}}, \tau_{f_{21}}, \tau_{f_{31}}$ and $\tau_{f_{41}}$ are the components of the friction vector in each joint of the TLRIP.

In the dynamic model, some parameters like body masses, inertia, and lengths of the pendulums can be directly measured. However, the friction coefficients should be determined experimentally to have the most accurate dynamic model of the TLRIP. The MATLAB/SimMechanics model of the TLRIP which contain the friction in joints is shown in Figure 3.2. In our SimMechanics model, the fixed part and the horizontal arm of the TLRIP are connected with one revolution joint which has one rotational degree of freedom. Moreover, three pendulums 1, 2 and 3 are connected by revolution joints 1, 2 and 3, respectively, which also have one rotational degree of freedom. For system simulation, friction model blocks were added to each pendulum joint; they contain joint sensors and joint actuators, see Figure 3.3. Furthermore, the initial conditions can be given directly by specifying the initial position and orientation of rigid bodies. The orientation position of the horizontal arm is represented by the angle θ_1, and the positions of the three pendulums by the angles θ_2, θ_3 and θ_4 respectively.

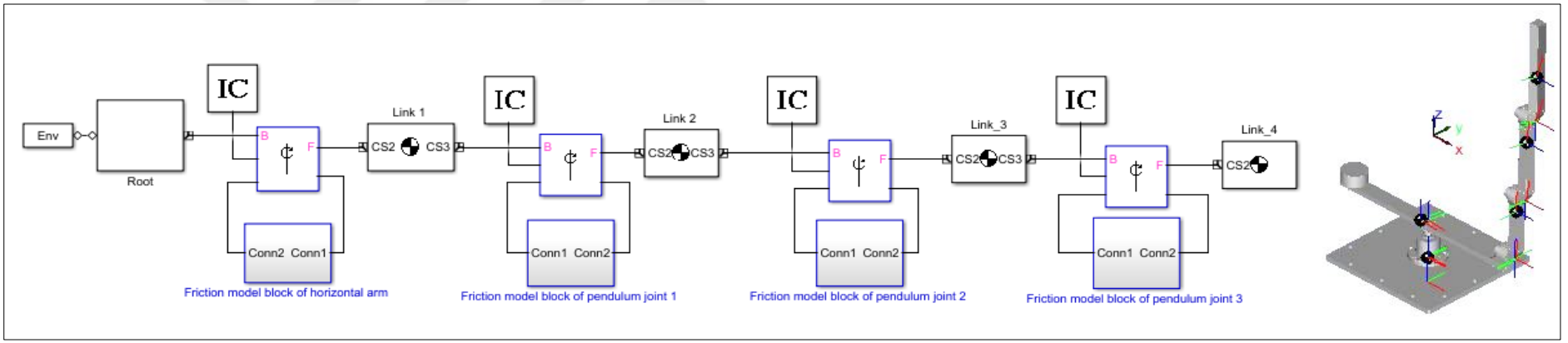

(a) (b)

Figure. 3.2. (a) MATLAB/SimMechanics model of the TLRIP with friction blocks, (b) solid model of the TLRIP

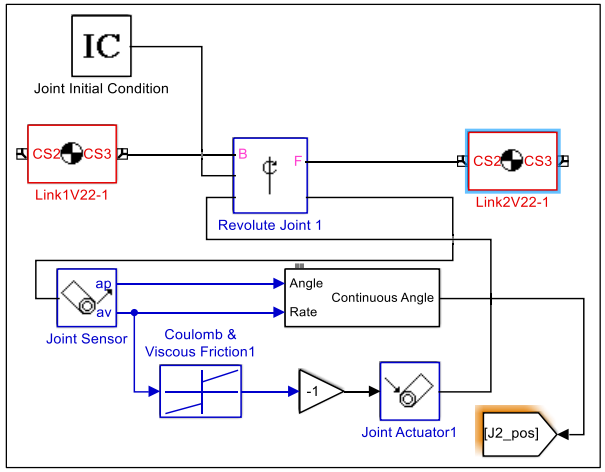

Figure. 3.3. Example of a friction model block

3.3.1. Data collection for the FEMs

The horizontal arm of the TLRIP is driven by a direct drive brushless DC torque motor (Type: TMH-130-050-NC). In this type of motor, since there is no use of transmission or gearbox, the frictions in the horizontal arm can be considered negligible. During the collection of the experimental data, the arm joint θ_1 is fixed at zero position. The pendulums' angles (θ_2, θ_3 and θ_4) are measured with three encoders having a resolution of 2048 pulses per revolution. The signals obtained from the encoder passes through the slip ring mounted in the joints. A dSPACE-DS1103 controller board treats the received signals from the encoders. The friction in the joints of the TLRIP depends on their velocities and the accelerations. In this case, the friction coefficients should be determined experimentally. The initial positions of the pendulums will be taken in cases with the value of θ_2 at 45 degrees along with θ_3 and θ_4 at an angle of 0 degrees. The sampling interval is 1 ms. The experimental simulation time of θ_2, θ_3 and θ_4 is taken at t=80 seconds. The block diagram of the experimental hardware configuration structure is shown in Figure 3.4.

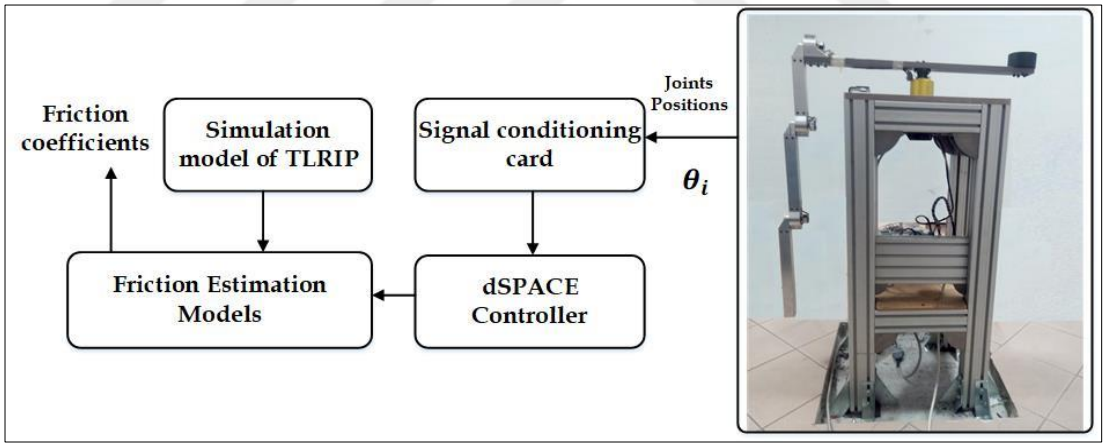

Figure. 3.4. Block diagram of the experimental hardware configuration structure for FEMs

3.3.2. Estimation results of the FEMs

The estimated results of the friction coefficients for the NCFM are given in Table 3.1. The Gradient Descent (GD) method is selected for the current optimization case. This method is based on a sequential quadratic programming (SQP) algorithm to estimate the viscous friction coefficients $C_{p\,(i)}$, which minimizes the value of the function $e = \left\|\theta_i(t) - \hat{\theta}_i(t)\right\|$. $\theta_i(t)$ is the position value of the angles obtained experimentally and

$\widehat{\theta_1}(t)$ is the position value of the angles obtained from the SimMechanics model of The TLRIP. The experiments are carried out during the 80s, however, for the graphs' clarity, only the [0, 10s] intervals are shown. Figure 3.5 shows an angular position comparison between experimental and NLFM simulation results. Furthermore, to estimate the friction coefficients of the LFM and NLFM, the Pattern Search (PS) method is selected for optimization. The PS algorithm starts by calculating a sequence of points that may or may not reach the optimal value. The PS proceeds by creating a group of points around the given initial point, called mesh. If a point in the mesh is found to improve the estimation of the experiment's output at that current point, the algorithm sets the new point as the current point at the next iteration [109]. The friction coefficients obtained by the LFM and NLFM are given in Tables 3.2 and 3.3, respectively. Figure 3.6 shows an angular position comparison between experimental and LFM simulation results. Figure 3.7 shows an angular position comparison between experimental and NLFM simulation results.

Table 3.1. Friction coefficients obtained by the NCFM

Friction coefficients	Joints		
	Joint (2)	Joint (3)	Joint (4)
C_p [Nm.s/rad]	5.6178e-04	2.9319e-10	9.0673e-04

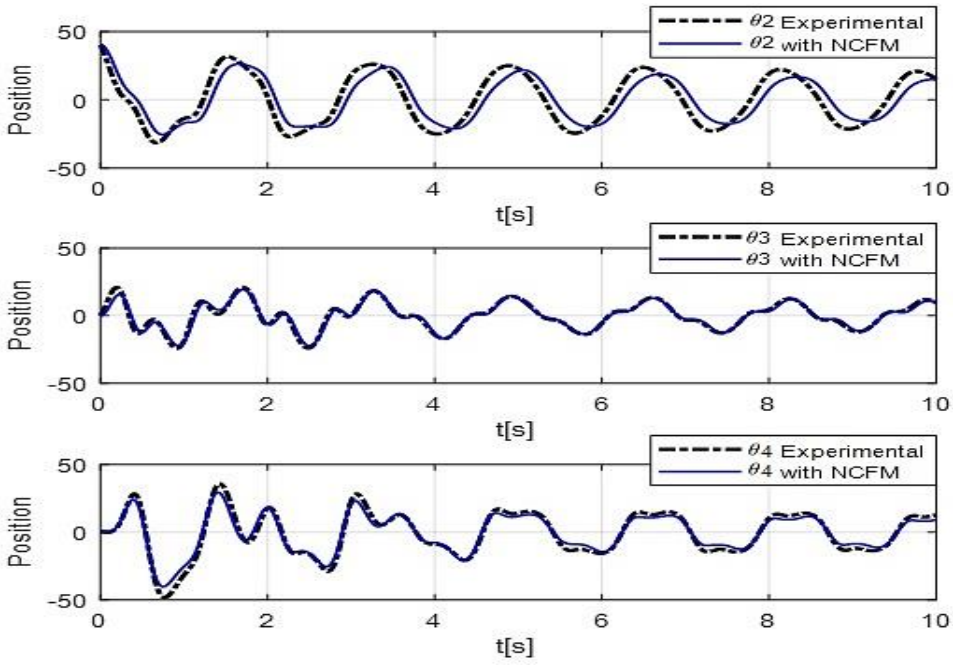

Figure 3.5. Angular position comparison between experimental and NCFM simulation results

Table 3.2. Friction coefficients obtained by the LFM

Friction coefficients	Joints		
	Joint (2)	Joint (3)	Joint (4)
B_i [Nm.s/rad]	6.1865e-04	3.1009e-07	2.2292e-04
C_i [Nm]	2.7550e-05	4.9864e-09	0.0168

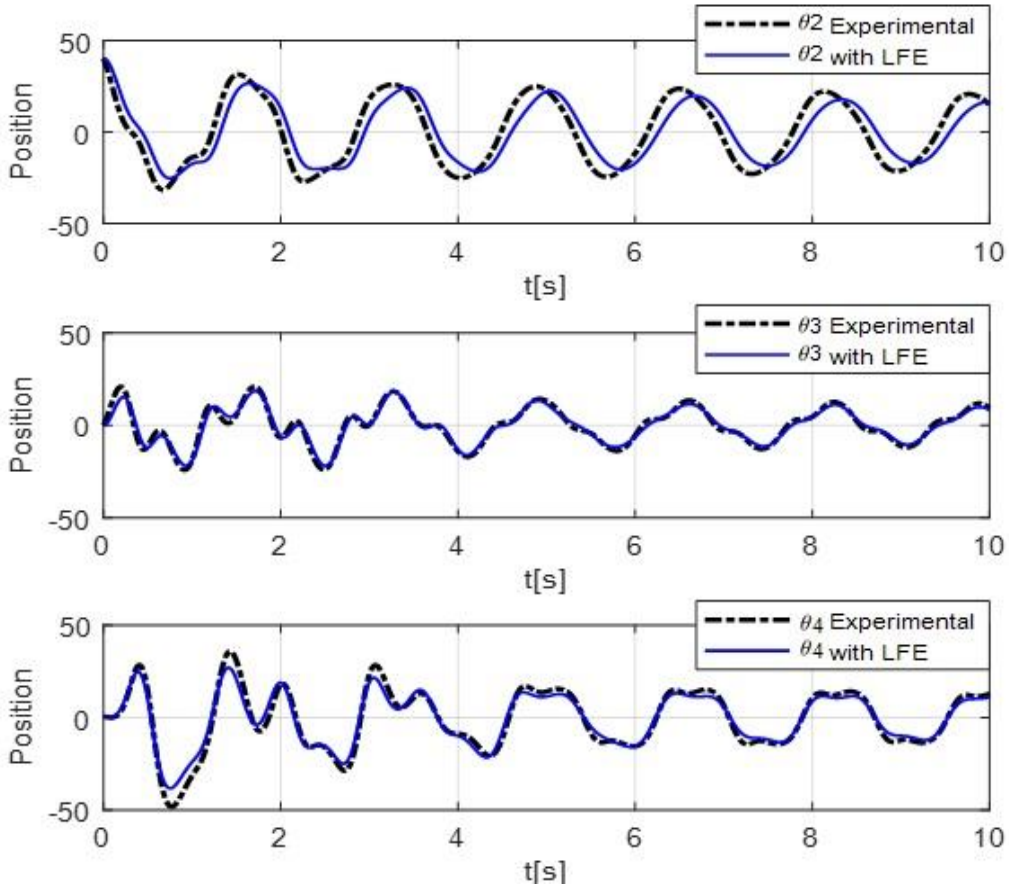

Figure 3.6. Angular position comparison between experimental and LFM simulation results

Table 3.3. Friction coefficients obtained by the NLFM

Friction coefficients	Joints		
	Joint (2)	Joint (3)	Joint (4)
f_o [Nm]	0.0038	1.5280e-06	0.001
f_c [Nm]	9.5940e-04	8.8846e-04	0.0165
f_v [Nm.s/rad]	0.0011	0.0315	0.0577
f_a [Nm]	0.0869	0.1876	7.2715e-04
f_b [Nm]	0.0159	0.1876	0.0456

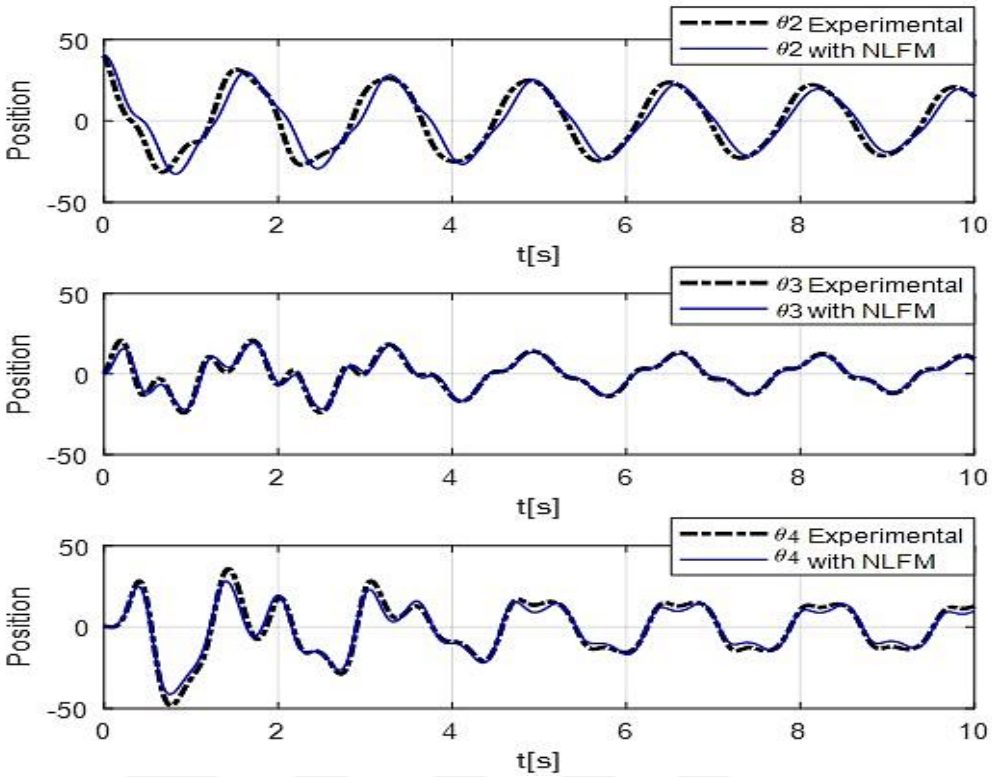

Figure 3.7. Angular position comparison between experimental and NLFM simulation results

To evaluate the performance of the LFM, NLFM and NCFM, the position RMSEs between these simulation and experimental results were calculated based on equation (3.10). The RMSEs are given in Table 3.4.

$$\mathrm{RMSE} = \sqrt{\frac{1}{\mathrm{N}}\sum_{\mathrm{i}=1}^{\mathrm{N}}(\theta_{\mathrm{i}} - \hat{\theta}_i)^2} \tag{3.10}$$

Where θ_{i} are modelled signals, $\hat{\theta}_{\mathrm{i}}$ are measured signals, and N is the number of sampling.

Table 3.4. Position RMSEs obtained by the NCFM, LFM and NLFM

Joints	RMSE		
	NCFM	LFM	NLFM
Joint (2)	0.0052	0.0049	0.0025
Joint (3)	0.0071	0.0065	0.0047
Joint (4)	0.0085	0.0079	0.0035

In order to understand the dynamic friction behaviors in the TLRIP, the friction forces and velocities in each joint are given in Figure 3.8. The nonlinear relationship between the calculated friction forces and the joint velocities may be observed in this figure. This relationship should be explained with more complex models for an accurate friction estimation.

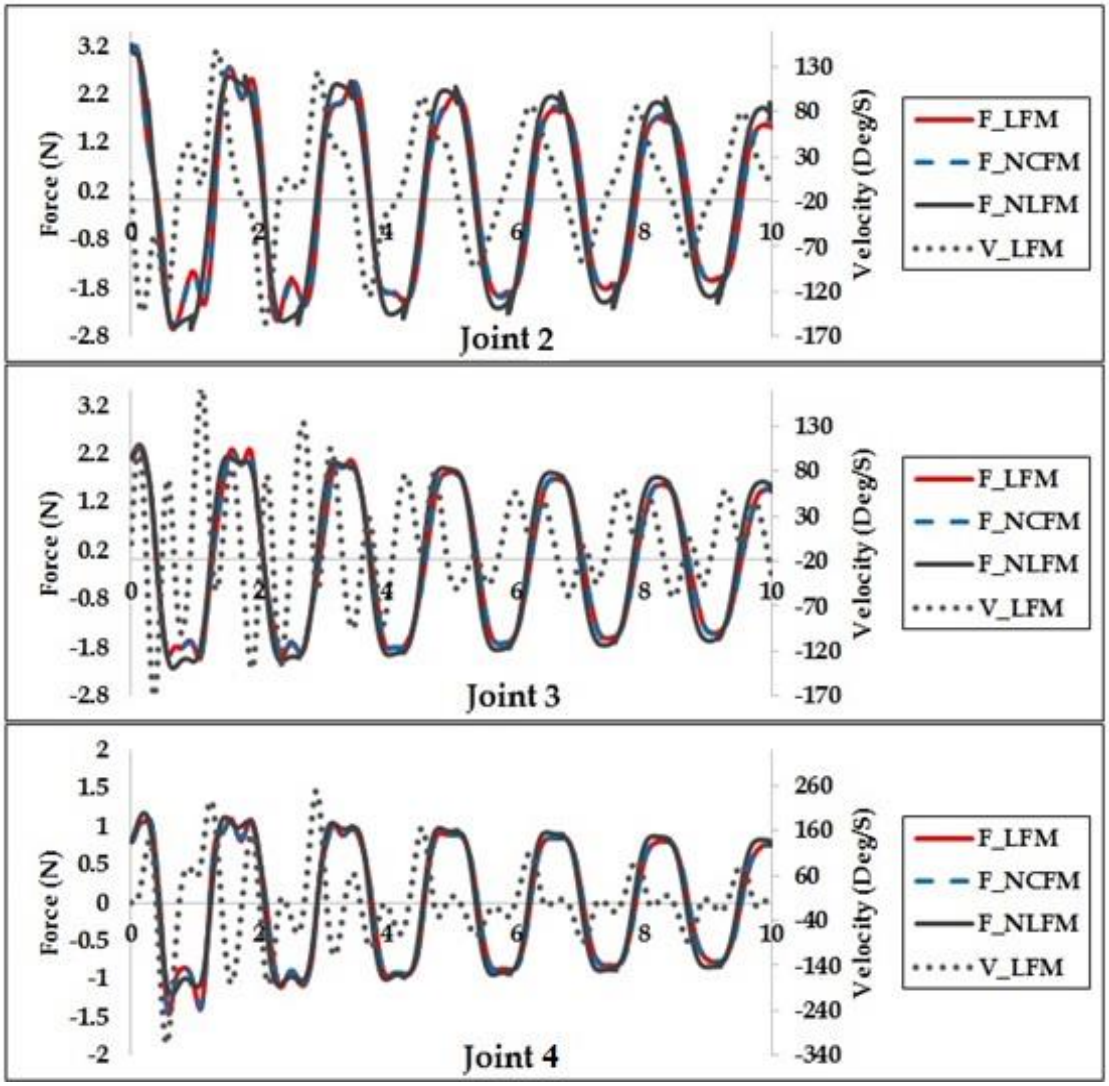

Figure 3.8. Friction forces and the velocity in each joint of the TLRIP

In this study, the performances of three different friction estimation models (NCFM, LFM and NLFM) are compared in terms of RMSEs of joints of the TLRIP. Based on the performance comparison, the NLFM produces the least RMSE in the results for all joints of the TLRIP. The RMSE of LFM becomes less than that of the NCFM. In next section, a better friction estimation model needs to be enhanced in the control of the

complex robotic systems such as an adaptive friction estimation model, which is developed using the joint velocities and accelerations of the TLRIP.

3.4. Adaptive Friction Coefficients for the TLRIP

In this section, AFEMs are developed to estimate the friction coefficients in three pendulums' joints of a TLRIP. The position signals of the joints obtained experimentally from a dSPACE controller board were classified based on their: low, medium and high accelerations. The adaptive friction coefficients' estimation method was studied in four initial angle positions of the second joint (θ_2) as follows: 45, 90, 135 and 180 degrees along with third joint (θ_3) and fourth joint (θ_4) at an angular position of 0 degrees. The adaptive friction coefficients were studied and compared with the existing friction estimation models: NCFM, LFM and NLFM. A Mechanical simulation carried out with estimated friction coefficients is compared with respect to the real experimental position signals [96].

3.4.1. Data collection for the AFEMs

The horizontal arm of the TLRIP is driven by a direct drive brushless DC torque motor (Type: TMH-130-050-NC). In this type of motor, since there is no use of transmission or gearbox, the frictions in the horizontal arm can be considered negligible. During the collection of the experimental data, the arm joint θ_1 is fixed at zero position. The pendulums' angles (θ_2, θ_3 and θ_4) are measured with three encoders having a resolution of 2048 pulses per revolution. The signals obtained from the encoder passes through the slip ring mounted in the joints. A dSPACE -DS1103 controller board treats the received signals from the encoders. The friction in the joints depends on the positions and the accelerations of the pendulums. In this case, an adaptive friction coefficients estimation should be determined experimentally. The initial positions of the system will be taken in four cases with the value of θ_2 as follows: 45, 90, 135 and 180 degrees along with θ_3 and θ_4 at an angle of 0 degrees. For each case, joints acceleration was classified into three groups such as low, medium and high. The adaptive friction coefficients were optimized based on this acceleration classification. The experimental hardware configuration is shown in Figure 3.9.

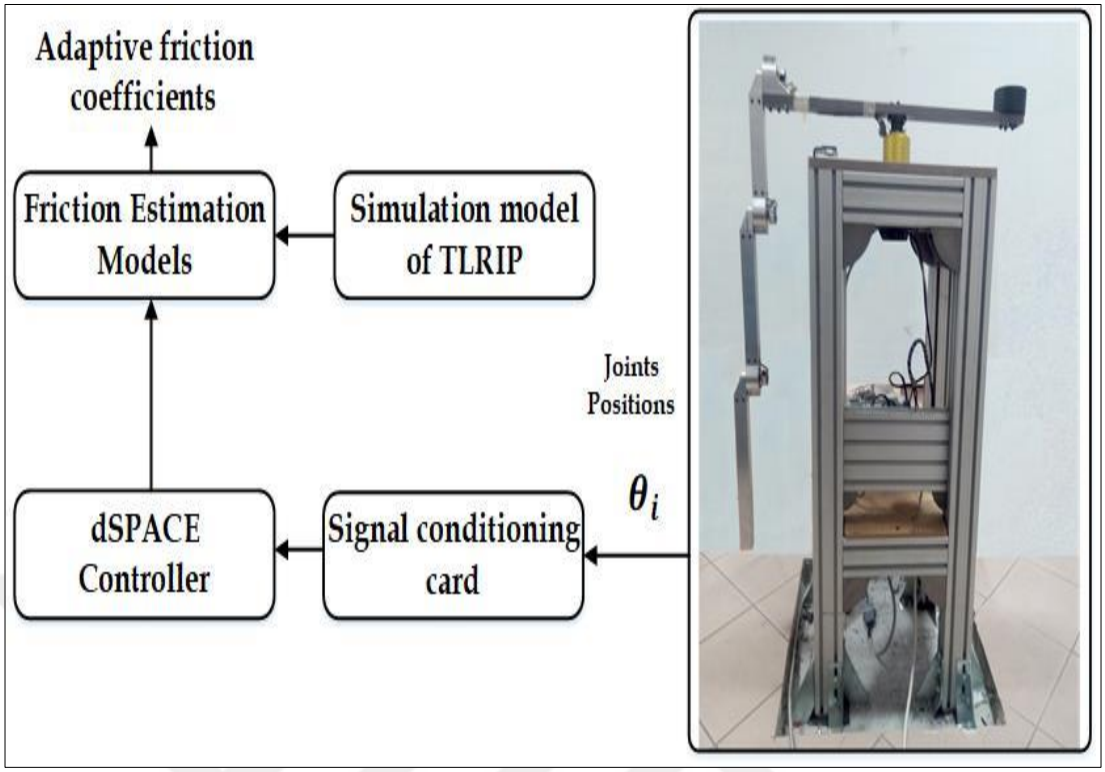

Figure 3.9. Block diagram of the experimental hardware configuration structure of the AFEMs.

3.4.2. Estimation results of the AFEMs

For each optimization simulation, the Pattern Search (PS) method was used to optimize the adaptive frictions coefficients. The PS method allows the optimization of a number of parameters at the same time. The adaptive friction coefficients were optimized and compared with the existing friction estimation models such as NCFM, LFM and NLFM based on the RMSEs.

- Initial positions for: $\theta_2 = 45^{\circ}, \theta_3 = 0^{\circ}, \theta_4 = 0^{\circ}$

Table 3.5 gives the classification of joints accelerations and their values into three groups: High [0-4s], Medium [4-30s] and low [30-70s]. Table 3.6 gives adaptive friction coefficients using the NCFM, LFM, and NLFM.

The RMSEs between the modelled signals and the measured signals were calculated using the adaptive friction coefficients. It was compared by the RMSEs obtained with existing friction estimation models given in Table 3.7.

Table 3.5. Classification of joints accelerations for the initial positions $\theta_2 = 45^{\circ}, \theta_3 = 0^{\circ}$ and $\theta_4 = 0^{\circ}$

Time [s]		[0-4]		[4-30]		[30-80]	
		Max values	Min values	Max values	Max values	Max values	Min values
Positions [Deg]	Joint (2)	44.2539	31.4648	25.0488	24.9609	10.5029	10.3271
	Joint (3)	24.0820	20.9180	16.9629	14.1943	5.6250	5.5371
	Joint (4)	48.2080	35.7715	20.6982	17.0508	4.1309	3.7793
Accelerations [Deg/s^2]	Joint (2)	$1.0236 \cdot 10^3$	$0.8620 \cdot 10^3$	458.2001	438.3131	223.9769	219.7110
	Joint (3)	$2.0793 \cdot 10^3$	$2.0663 \cdot 10^3$	525.8127	492.9399	199.7988	194.0725
	Joint (4)	$3.0302 \cdot 10^3$	$2.1231 \cdot 10^3$	$1.0578 \cdot 10^3$	$0.9651 \cdot 10^3$	146.9310	134.2073

Table 3.6. Adaptive friction coefficients for the initial positions $\theta_1 = 45^{\circ}, \theta_2 = 0^{\circ}$ and $\theta_3 = 0^{\circ}$

Time [s]		[0-4]			[4-30]			[30-80]		
Joints		(2)	(3)	(4)	(2)	(3)	(4)	(2)	(3)	(4)
NCFM	C_p [Nm.s/rad]	$3.1791 \cdot 10^{-4}$	$1.9256 \cdot 10^{-1}$	$4.7143 \cdot 10^{-5}$	$1.3760 \cdot 10^{-4}$	$6.8645 \cdot 10^{-4}$	$6.9828 \cdot 10^{-5}$	0.0001	0.0019	0.0021
LFM	B_i [Nm.s/rad]	$9.5160 \cdot 10^{-5}$	$5.8693 \cdot 10^{-5}$	$1.8693 \cdot 10^{-8}$	5.053110^{-5}	$5.7791 \cdot 10^{-4}$	$37055 \cdot 10^{-4}$	$6.8060 \cdot 10^{-7}$	0.0010	$5.7407 \cdot 10^{-4}$
	C_i [Nm]	0.0258	$1.3539\ 10^{-6}$	0.0074	$6.1448 \cdot 10^{-6}$	0.0094	0.00120	$1.2805 \cdot 10^{-5}$	0.0060	0.0091

Table 3.6.(Cont.) Adaptive friction coefficients for the initial positions $\theta_1 = 45^{\circ}, \theta_2 = 0^{\circ}$ and $\theta_3 = 0^{\circ}$

NLFM	f_o [Nm]	0.0023	0.0037	$5.8992 \cdot 10^{-4}$	0.0044	0.0024	$3.3741 \cdot 10^{-4}$	0.0062	0.0033	$1.9146 \cdot 10^{-4}$
	f_c [Nm]	0.0082	0.0118	0.0097	0.0054	0.0085	0.0232	$2.4567\ 10^{-4}$	0.0070	0.0176
	f_v [Nm.s/rad]	0.1188	0.0012	$5.6466 \cdot 10^{-4}$	0.0159	0.0362	0.0133	0.0141	0.0384	0.0287
	f_a [Nm]	0.2314	0.3456	$5.1595 \cdot 10^{-4}$	0.0585	0.0341	0.0042	0.0460	0.1139	0.0045
	f_b [Nm]	0.0039	0.0047	$1.4124 \cdot 10^{-5}$	0.1396	0.0526	$3.1141 \cdot 10^{-5}$	0.4062	0.2119	$9.5165 \cdot 10^{-5}$

Table 3.7. RMSEs obtained using existing friction estimation models, and the RMSEs obtained with adaptive friction coefficients for initial position $\theta_2 = 45^{\circ}, \theta_3 = 0^{\circ}$ and $\theta_4 = 0^{\circ}$

Joints	RMSEs obtained with existing FEMs			RMSEs obtained with AFEMs		
	NCFM	LFM	NLFM	ANCFM	ALFM	ANLFM
Joint (2)	0.0052	0.0049	0.0025	0.0045	0.0041	0.0020
Joint (3)	0.0071	0.0065	0.0047	0.0068	0.0055	0.0037
Joint (4)	0.0085	0.0079	0.0035	0.0083	0.0076	0.0032

- Initial positions for: $\theta_2 = 90^{\circ}, \theta_3 = 0^{\circ}, \theta_4 = 0^{\circ}$

Table 3.8 gives presents the classification of joints accelerations and their values into three groups: High [0-10s], Medium [10-30s] and low [30-90s]. Table 3.9 gives adaptive friction coefficients using the NCFM, LFM, and NLFM. The RMSEs between the modeled signals and the measured signals were calculated using the adaptive friction coefficients. It was compared by the RMSEs obtained with existing friction estimation models see Table 3.10.

- Initial positions for: $\theta_2 = 135^{\circ}, \theta_3 = 0^{\circ}, \theta_4 = 0^{\circ}$

Table 3.11 presents the classification of joints accelerations and their values into different groups as follows: High [0-12s], medium [12-20s] and low [20-30s] for joint of the first pendulum; high [0-6s], medium [6- 16s] and low [16-40s] for joint of the second pendulum 2; low [0-1.3s], high [1.3- 4.5s], medium [4.5-13s] and low [13-30s] for joint of the third pendulum 3. Tables 3.12, 3.13, and 3.14 present the adaptive friction coefficients using the NCFM, LFM, and NLFM, respectively. The RMSEs between the modeled signals and the measured signals were calculated using the adaptive friction coefficients. It was compared by the RMSEs obtained with existing friction estimation models see Table 3.15.

- Initial positions for: $\theta_2 = 180^{\circ}, \theta_3 = 0^{\circ}, \theta_4 = 0^{\circ}$

Table 3.16 presents the classification of joints accelerations and their values into different groups as follows: High [0-7s], medium [7-14s] and low [14-40s] for joint of the first pendulum; high [0-6s], medium [6- 16s] and low [16-40s] for joint of the second pendulum 2; low [0-1.3s], high [1.3-4.5s], medium [4.5-13s] and low [13-30s] for joint of the Third pendulum 3. Tables 3.17, 3.18, and 3.19 present the adaptive friction coefficients using the NCFM, LFM, and NLFM, respectively. The RMSEs between the modeled signals and the measured signals were calculated using the adaptive friction coefficients. It was compared by the RMSEs obtained with existing friction estimation models see Table 3.20.

Table 3.8. Classification of joints accelerations for the initial positions $\theta_2 = 90^{\circ}, \theta_3 = 0^{\circ}$ and $\theta_4 = 0^{\circ}$

Time [s]		[0-10]		[10-30]		[30-90]	
		Max values	Min values	Max values	Max values	Max values	Min values
Positions [Deg]	Joint (2)	90.0	70.0488	29.3994	20.8740	12.1729	12.0850
	Joint (3)	82.4414	75.2783	19.6436	14.0186	6.9873	6.8115
	Joint (4)	851.0889	124.4971	750.2344	689.0186	725.3613	714.3311
Accelerations [Deg/s^2]	Joint (2)	$4.7139 \cdot 10^3$	$3.8975 \cdot 10^3$	720.6739	679.7878	255.7555	245.4379
	Joint (3)	$9.30571 \cdot 10^3$	$6.9768 \cdot 10^3$	$0.9210 \cdot 10^3$	$1.0719 \cdot 10^3$	263.0684	258.5020
	Joint (4)	$1.1358 \cdot 10^4$	$0.9275 \cdot 10^4$	$1.5944 \cdot 10^3$	$2.1159 \cdot 10^3$	194.7493	179.8465

Table 3.9. Adaptive friction coefficients for the initial positions $\theta_2 = 90^{\circ}, \theta_3 = 0^{\circ}$ and $\theta_4 = 0^{\circ}$

Time [s]		[0-10]			[10-30]			[30-90]		
Joints		(2)	(3)	(4)	(2)	(3)	(4)	(2)	(3)	(4)
NCFM	C_p [Nm.s/rad]	$4.7380 \cdot 10^{-4}$	$7.4014 \cdot 10^{-5}$	$1.7182 \cdot 10^{-5}$	$5.7604 \cdot 10^{-4}$	0.0088	$4.0350 \cdot 10^{-5}$	$3.5793 \cdot 10^{-6}$	0.0011	$8.117 \cdot 10^{-4}$
LFM	B_i [Nm.s/rad]	0.0016	$2.0847 \cdot 10^{-4}$	0.0011	$3.1140 \cdot 10^{-4}$	$3.7497 \cdot 10^{-4}$	0.1114	$1.2252 \cdot 10^{-4}$	6.9792 e-04	$1.1903 \cdot 10^{-4}$
	C_i [Nm]	0.0238	0.0843	0.0798	0.0028	0.0299	0.7761	0.0024	0.0029	0.0066

Table 3.9.(Cont.) Adaptive friction coefficients for the initial positions $\theta_2 = 90^\circ$, $\theta_3 = 0^\circ$ and $\theta_4 = 0^\circ$

NLFM	f_o [Nm]	0.0023	0.0037	$5.8992 \cdot 10^{-4}$	0.0044	0.0024	$3.3741 \cdot 10^{-4}$	0.0062	0.0033	$1.9146 \cdot 10^{-4}$
	f_c [Nm]	0.0082	0.0118	0.0097	0.0054	0.0085	0.0232	$2.4567 \cdot 10^{-4}$	0.0070	0.0176
	f_v [Nm.s/rad]	0.1188	0.0012	$5.6466 \cdot 10^{-4}$	0.0159	0.0362	0.0133	0.0141	0.0384	0.0287
	f_a [Nm]	0.2314	0.3456	$5.1595 \cdot 10^{-4}$	0.0585	0.0341	0.0042	0.0460	0.1139	0.0045
	f_b [Nm]	0.0039	0.0047	$1.4124 \cdot 10^{-5}$	0.1396	0.0526	$3.1141 \cdot 10^{-5}$	0.4062	0.2119	$9.5165 \cdot 10^{-5}$

Table 3.10. RMSEs obtained using existing friction estimation models, and the RMSEs obtained with adaptive friction coefficients for initial position $\theta_2 = 90^\circ$, $\theta_3 = 0^\circ$ and $\theta_4 = 0^\circ$

Joints	RMSEs obtained with existing FEMs			RMSEs obtained with AFEMs		
	NCFM	LFM	NLFM	ANCFM	ALFM	ANLFM
Joint (2)	0.0274	0.0245	0.0227	0.0232	0.0216	0.0188
Joint (3)	0.0242	0.0211	0.0201	0.0225	0.0209	0.0186
Joint (4)	0.2087	0.1474	0.1275	0.1978	0.1425	0.1093

Table 3.11. Classification of joints accelerations for the initial positions $\theta_2 = 135^{\circ}$, $\theta_3 = 0^{\circ}$ and $\theta_4 = 0^{\circ}$

Joint 2				
Time [s]	Positions value [Deg]		Accelerations value [Deg/s^2]	
	Max values	Min values	Max values	Min values
[0-12]	134.2969	91.9775	$6.911 \cdot 10^3$	$4.2371 \cdot 10^3$
[12 -20]	14.3701	8.7451	$1.115 \cdot 10^3$	$0.9755 \cdot 10^3$
[20 -30]	3.7793	3.6914	59.0392	56.8847
Joint 3				
[0-6]	159.5215	128.6279	$1.242 \cdot 10^4$	$1.1017 \cdot 10^4$
[6-16]	77.1680	53.7891	$6.160 \cdot 10^3$	$4.9842 \cdot 10^3$
[16-30]	2.3730	2.1094	63.8500	52.9298
Joint 4				
[0-1.9]	489.6387	120.1465	$1.709 \cdot 10^4$	$1.5173 \cdot 10^4$
[1.9-4.3]	877.2803	489.6387	$1.468 \cdot 10^4$	$0.8899 \cdot 10^4$
[4.3-9]	1.2357	0.8773	$8.633 \cdot 10^3$	$6.2568 \cdot 10^3$
[9-25]	$1.13 \cdot 10^3$	$1.01 \cdot 10^3$	$3.488 \cdot 10^3$	$3.3282 \cdot 10^3$

Table 3.12. Adaptive friction coefficients obtained by NCFM for the initial positions $\theta_2 = 135^{\circ}$, $\theta_3 = 0^{\circ}$ and $\theta_4 = 0^{\circ}$

Time of Joint 2 [s]	[0-12]		[12-20]	[20-30]
C_p [Nm.s/rad]	$2.794 \cdot 10^{-4}$		$4.075 \cdot 10^{-4}$	$9.145 \cdot 10^{-4}$
Time of Joint 3 [s]	[0-6]		[6-16]	[16-30]
C_p [Nm.s/rad]	$9.6129 \cdot 10^{-5}$		$1.2685 \cdot 10^{-4}$	0.0012
Time of Joint 4 [s]	[0-1.9]	[1.9-4.3]	[4.3-9]	[9-25]
C_p [Nm.s/rad]	$5.7581 \cdot 10^{-6}$	$5.9433 \cdot 10^{-5}$	$1.2119 \cdot 10^{-4}$	0.0032

Table 3.13. Adaptive friction coefficients obtained by LFM for the initial positions $\theta_2 = 135^{\circ}$, $\theta_3 = 0^{\circ}$ and $\theta_4 = 0^{\circ}$

Time of Joint 2 [s]	[0-12]	[12-20]	[20-30]	
B_i [Nm.s/rad]	$8.2357 \cdot 10^{-5}$	0.0011	$9.0762 \cdot 10^{-4}$	
C_i [Nm]	$3.0576\ 10^{-5}$	0.0232	$2.9533 \cdot 10^{-7}$	
Time of Joint 3 [s]	[0-6]	[6-16]	[16-30]	
B_i [Nm.s/rad]	$2.1210 \cdot 10^{-5}$	$6.8167 \cdot 10^{-4}$	0.0147	
C_i [Nm]	$9.6368 \cdot 10^{-5}$	0.0389	0.0037	
Time of Joint 4 [s]	[0-1.9]	[1.9-4.3]	[4.3-9]	[9-25]
B_i [Nm.s/rad]	$5.9536 \cdot 10^{-6}$	$1.2175 \cdot 10^{-5}$	$1.1514 \cdot 10^{-4}$	$1.587 \cdot 10^{-5}$
C_i [Nm]	0.0042	$1.3634 \cdot 10^{-4}$	0.0045	0.0047

Table 3.14. Adaptive friction coefficients obtained by NLFM for the initial positions $\theta_2 = 135^{\circ}, \theta_3 = 0^{\circ}$ and $\theta_4 = 0^{\circ}$

Time of Joint 2 [s]	[0-12]	[12-20]	[20-30]
f_o [Nm]	0.0017	0.0734	$1.787 \cdot 10^{-4}$
f_c [Nm]	0.0506	0.1146	$1.1557 \cdot 10^{-4}$
f_v [Nm.s/rad]	0.1147	0.3952	$1.9678 \cdot 10^{-4}$
f_a [Nm]	0.2035	0.0012	0.6379
f_b [Nm]	0.0448	0.0478	$2.2041 \cdot 10^{-4}$
Time of Joint 3 [s]	[0-6]	[6-16]	[16-30]
f_o [Nm]	0.0645	0.0275	0.0030
f_c [Nm]	$3.5524 \cdot 10^{-4}$	0.0026	0.0157
f_v [Nm.s/rad]	0.0001	0.0066	$7.4236 \cdot 10^{-4}$
f_a [Nm]	$1.3782 \cdot 10^{-4}$	$1.3036 \cdot 10^{-4}$	$1.0042 \cdot 10^{-4}$
f_b [Nm]	$1.8377 \cdot 10^{-4}$	$1.5460 \cdot 10^{-5}$	$1.0042 \cdot 10^{-4}$

Time of Joint 4 [s]	[0-1.9]	[1.9-4.3]	[4.3-9]	[9-25]
f_o [Nm]	0.00205	$9.0605 \cdot 10^{-4}$	$8.3410 \cdot 10^{-4}$	0.0042
f_c [Nm]	$4.7384 \cdot 10^{-6}$	$9.2100 \cdot 10^{-6}$	$1.1303 \cdot 10^{-5}$	0.0382
f_v [Nm.s/rad]	0.0162	0.0047	0.0040	0.0246
f_a [Nm]	0.1575	0.1187	0.2343	0.0012
f_b [Nm]	$3.7107 \cdot 10^{-4}$	$5.5206 \cdot 10^{-6}$	$1.5688 \cdot 10^{-6}$	0.0535

Table 3.15. RMSEs obtained using existing friction estimation models, and the RMSEs obtained with adaptive friction coefficients for initial position $\theta_2 = 135^{\circ}, \theta_3 = 0^{\circ}$ and $\theta_4 = 0^{\circ}$

Joints	RMSEs obtained with existing FEMs			RMSEs obtained with AFEMs		
	NCFM	LFM	NLFM	ANCFM	ALFM	ANLFM
Joint (2)	0.1686	0.1149	0.1116	0.1645	0.1105	0.1096
Joint (3)	0.2102	0.2004	0.1892	0.2008	0.1894	0.1852
Joint (4)	0.6217	0.5606	0.4079	0.5007	0.4852	0.4032

Table 3.16. Classification of joints accelerations for the initial positions $\theta_2 = 180^{\circ}, \theta_3 = 0^{\circ}$ and $\theta_4 = 0^{\circ}$

Joint 2				
Time [s]	Positions value [Deg]		Accelerations value [Deg/s^2]	
	Max	Min	Max	Min
[0-7]	134.2969	91.9775	$6.911 \cdot 10^3$	$4.2371 \cdot 10^3$
[7 -14]	14.3701	8.7451	$1.115 \cdot 10^3$	$0.9755 \cdot 10^3$
[14 -40]	3.7793	3.6914	59.0392	56.8847
Joint 3				
[0-6]	159.5215	128.6279	$1.242 \cdot 10^4$	$1.1017 \cdot 10^4$
[6-16]	77.1680	53.7891	$6.160 \cdot 10^3$	$4.9842 \cdot 10^3$
[16 -40]	2.3730	2.1094	63.8500	52.9298
Joint 4				

Table 3.16.(Cont.) Classification of joints accelerations for the initial positions $\theta_2 = 180^{\circ}, \theta_3 = 0^{\circ}$ and $\theta_4 = 0^{\circ}$

[0-1.3]	489.6387	120.1465	$1.709 \cdot 10^4$	$1.5173 \cdot 10^4$
[1.3-4.5]	877.2803	489.6387	$1.468 \cdot 10^4$	$0.8899 \cdot 10^4$
[4.5 -13]	1.2357	0.8773	$8.633 \cdot 10^3$	$6.2568 \cdot 10^3$
[13-30]	$1.13 \cdot 10^3$	$1.01 \cdot 10^3$	$3.488 \cdot 10^3$	$3.3282 \cdot 10^3$

Table 3.17. Adaptive friction coefficients obtained by NCFM for the initial positions $\theta_2 = 180^{\circ}, \theta_3 = 0^{\circ}$ and $\theta_4 = 0^{\circ}$

Time of Joint 2 [s]	[0-7]	[7-14]	[14-40]	
C_p [Nm.s/rad]	0.0040	0.0033	0.0335	
Time of Joint 3 [s]	[0- 6]	[6 -16]	[16 - 40]	
C_p [Nm.s/rad]	2.4410^{-4}	0.0015	0.001514	
Time of Joint 4 [s]	[0 -1.3]	[1.3-4.5]	[4.5-13]	[13 - 40]
C_p [Nm.s/rad]	0.00100	7.4710^{-5}	1.10^{-4}	$7.3\ 10^{-6}$

Table 3.18. Adaptive friction coefficients obtained by LFM for the initial positions $\theta_2 = 180^{\circ}, \theta_3 = 0^{\circ}$ and $\theta_4 = 0^{\circ}$

Time of Joint 2 [s]	[0-7]	[7-14]	[14-40]	
B_i [Nm.s/rad]	0.0015	0.0037	0.0314	
C_i [Nm]	0.0209	0.0429	0.0174	
Time of Joint 3 [s]	[0 to 6]	[6 to 16]	[16 - 40]	
B_i [Nm.s/rad]	0.0030	0.0018	0.001497	
C_i [Nm]	$2.4\ 10^{-4}$	0.00277	$1.000\ 10^{-4}$	
Time of Joint 4 [s]	[0 - 1.3]	[1.3- 4.5]	[4.5 - 13]	[13 - 30]
B_i [Nm.s/rad]	5.4910^{-5}	$7.4\ 10^{-5}$	$8.6\ 10^{-5}$	$8.\ 7\ 10^{-5}$
C_i [Nm]	0.0050	$6.3\ 10^{-4}$	$1.5\ 10^{-4}$	$1.5\ 10^{-4}$

Table 3.19. Adaptive friction coefficients obtained by NLFM for the initial positions $\theta_2 = 180^{\circ}$, $\theta_3 = 0^{\circ}$ and $\theta_4 = 0^{\circ}$

Time of Joint 2 [s]	[0- 7]		[7-14]	[14 - 40]
f_o [Nm]	$9.03\ 10^{-5}$		0.0040	$1.11\ 10^{-4}$
f_c [Nm]	$2.3530\ 10^{-4}$		0.2421	0.01534
f_v [Nm.s/rad]	$3.91191\ 10^{-6}$		$3.60\ 10^{-6}$	$3.51961 \cdot 10^{-5}$
f_a [Nm]	$2.8946\ 10^{-6}$		$1.43\ 10^{-2}$	$9.1137 \cdot 10^{-5}$
f_b [Nm]	$6.4761\ 10^{-5}$		8.8510^{-5}	$2.9317 \cdot 10^{-7}$
Time of Joint 3 [s]	[0- 6]		[6- 16]	[16 - 40]
f_o [Nm]	$6.5109\ 10^{-5}$		$1.61\ 10^{-4}$	0.00843
f_c [Nm]	$9.7363\ 10^{-5}$		8.1410^{-5}	0.01538
f_v [Nm.s/rad]	$1.1790\ 10^{-5}$		$1.54\ 10^{-6}$	0.00585
f_a [Nm]	$2.3295\ 10^{-4}$		2.7210^{-4}	$2.23\ 10^{-5}$
f_b [Nm]	$7.7406\ 10^{-5}$		$3.58\ 10^{-5}$	$1.49\ 10^{-4}$
Time of Joint 4 [s]	[0-1.3]	[1.3 - 4.5]	[4.5-13]	[13-30]
f_o [Nm]	0.0454	0.0468	0.0085	$1.3362 \cdot 10^{-5}$
f_c [Nm]	0.2768	0.2541	$4.32\ 10^{-5}$	9.7910^{-5}
f_v [Nm.s/rad]	$8.08\ 10^{-4}$	0.0028	$4.6348 \cdot 10^{-5}$	2.1810^{-4}
f_a [Nm]	0.7500	0.36377	$1.2 \cdot 10^{-5}$	$1.09\ 10^{-4}$
f_b [Nm]	$3.55\ 10^{-4}$	7.9510^{-4}	0.0077	$1.85 \cdot 10^{-4}$

Table 3.20. RMSEs obtained using existing friction estimation models, and the RMSEs obtained with adaptive friction coefficients for initial position $\theta_2 = 180^\circ, \theta_3 = 0^\circ$ and $\theta_4 = 0^\circ$

Joints	RMSEs obtained with existing FEMs			RMSEs obtained with AFEMs		
	NCFM	LFM	NLFM	ANCFM	ALFM	ANLFM
Joint (2)	0.1467	0.1231	0.1003	0.1397	0.1127	0.0983
Joint (3)	1.8120	1.8056	0.1341	1.8105	1.8032	0.1115
Joint (4)	0.7212	0.6945	0.6390	0.6995	0.6743	0.6248

According to the calculated RMSEs, the Adaptive Non-Conservative Friction Estimation Model (ANCFM), the Adaptive Linear Friction Estimation Model (ALFM) and the Adaptive Non-Linear Friction Estimation Model (ANLFM) returned more accurately than the existing friction models (NCFM, LFM, and NLFM). Comparison in term of improvement of RMSE percentage between existing friction models and AFEMs are given in Tables 3.21, 3.22 and 3.23.

Table 3.21. Comparison in term of improvement of RMSE percentage between NCFM and ANCFM

NCFM-ANCFM / Cases	Improvement of RMSE percentages between NCFM and ANCFM		
	Joint 2	Joint 3	Joint 4
$\theta_2 = 45^\circ, \theta_3 = 0^\circ, \theta_4 = 0^\circ$	13.45%	4.2 %	2.3 %
$\theta_2 = 90^\circ, \theta_3 = 0^\circ, \theta_4 = 0^\circ$	15.3 %	7.02%	5.22%
$\theta_2 = 135^\circ, \theta_3 = 0^\circ, \theta_4 = 0^\circ$	2.43%	4.47%	19.46%
$\theta_2 = 180^\circ, \theta_3 = 0^\circ, \theta_4 = 0^\circ$	4.9%	0.08%	3%

Table 3.22. Comparison in term of improvement of RMSE Percentage between LFM and ALFM

LFM-ALFM / Cases	Improvement of RMSE percentages between LFM and ALFM		
	Joint 2	Joint 3	Joint 4
$\theta_2 = 45^\circ, \theta_3 = 0^\circ, \theta_4 = 0^\circ$	16.32%	15.38 %	3.79 %
$\theta_2 = 90^\circ, \theta_3 = 0^\circ, \theta_4 = 0^\circ$	11.83 %	0.9 %	3.39%
$\theta_2 = 135^\circ, \theta_3 = 0^\circ, \theta_4 = 0^\circ$	3.8 %	5.48 %	13.44%
$\theta_2 = 180^\circ, \theta_3 = 0^\circ, \theta_4 = 0^\circ$	8.44%	0.13%	2.9%

Table 3.23. Comparison in term of improvement of RMSE Percentage between NLFM and ANLFM.

NLFM-ANLFM / Cases	Improvement of RMSE percentages between NCFM and ANLFM		
	Joint 2	Joint 3	Joint 4
$\theta_2 = 45^\circ, \theta_3 = 0^\circ, \theta_4 = 0^\circ$	20%	21.27 %	8.57 %
$\theta_2 = 90^\circ, \theta_3 = 0^\circ, \theta_4 = 0^\circ$	17.18 %	7.46 %	14.27%
$\theta_2 = 135^\circ, \theta_3 = 0^\circ, \theta_4 = 0^\circ$	2.1 %	2.11 %	1.14%
$\theta_2 = 180^\circ, \theta_3 = 0^\circ, \theta_4 = 0^\circ$	1.9%	16.85%	2.22%

Figure 3.10 illustrates the experiment's position signals obtained from the dSPACE controller for the cases : $\theta_2 = 180^\circ, \theta_3 = 0^\circ, \theta_4 = 0^\circ$, the signals with the adaptive non-linear friction coefficients estimation model and the signals with the existing non-linear friction coefficients estimation model.

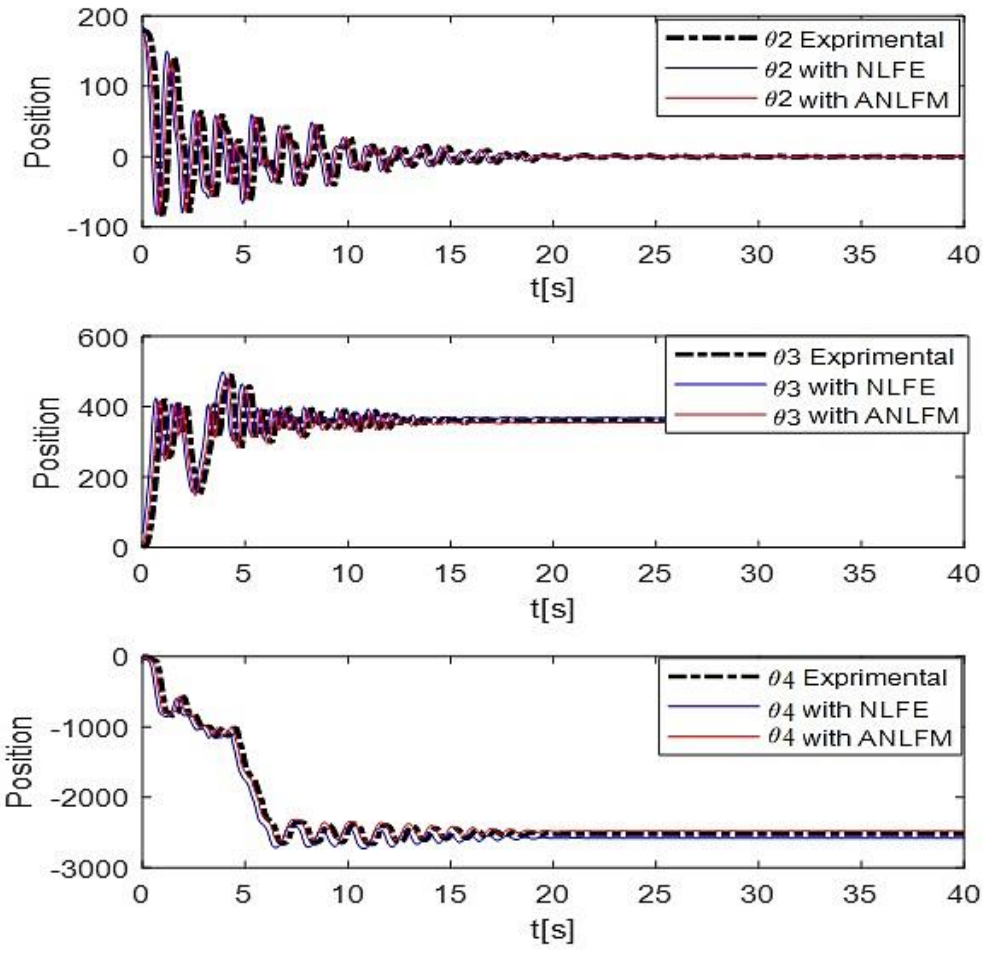

Figure 3.10. Experimental position signals, the NLFM simulation and the ANLFM simulation for initial position $\theta_2 = 180^\circ, \theta_3 = 0^\circ, \theta_4 = 0^\circ$

In this section, novel AFEMs have been developed based on the classification of joints accelerations of the TLRIP into three groups such as low, medium and high. The adaptive friction coefficients estimation was compared with the existing friction estimation models (NCFM, LFM, and NLFM) based on the RMSEs of joints of the TLRIP. According to the comparison performance, the ANLFM has given the best results for all joints of the TLRIP. A better AFEM needs to be applied to the inverse dynamic model to control the system. In the next section, an NFFEMs based on velocities, accelerations will be developed and applied to the system in order to observe more accurate results.

3.5. Neuro-Fuzzy Friction Models for the TLRIP

In the last section, the AFEMs were developed to estimate the friction coefficients for TLRIP system. In the AFEM approach, the joint accelerations of the TLRIP were classified into three groups: low, medium and high. The adaptive friction coefficients were optimized according to this acceleration classification. In this study, the NFFEMs were developed using the NF system. The joint velocities and accelerations of the TLRIP as the input variables were applied to NF. Membership functions of input and output variables and fuzzy rules in the fuzzy estimation system were trained using an RBANN. The variable friction coefficients of NFFEMs were estimated and verified through several simulation and experimental results. These proposed friction estimation models are compared with AFEMs. This work has three important contributions to the literature. Firstly, all friction models in the literature depend only on velocity. However, the friction model developed here depends on both velocity and acceleration. This approach has enabled us to obtain a two-dimensional friction model. Secondly, the coefficients of all friction models in the literature were constant when the physical quantities change. On the other hand, the coefficients of the friction models in this work vary depending on the state of the velocity and acceleration. Hence, this friction model allows for better estimation of the effects of friction in different velocity and acceleration conditions. Thirdly, much of existing papers in the literature have studied only the frictions of the linear motion which depends on linear velocity and force. This section examines frictions on the joints which have hard rotational motions.

3.5.1. Implementation of the neuro-fuzzy friction estimation model

A fuzzy logic inference system is developed to estimate the friction coefficients in the pendulum joints of the TLRIP. For each joint, an FLC (Fuzzy Logic Controller) implemented to estimate the friction coefficients. Figure 3.11 depicts the implementation of the FLC in the joints of the TLRIP. Two inputs of FLC are the joints velocities and accelerations. The typical steps in developing the FLC system involve fuzzification, rule formation and defuzzification is explained briefly in this section. The input variables such as velocities and accelerations are suitably partitioned and converted into linguistic variables, as following (NL-negative medium, Z-zero, PM-positive medium, PH- positive high, VS-very slow, S-slow, F-fast, VF-very fast, M-medium). The output variables (friction coefficients of the models) are partitioned and represented as fuzzy sets with linguistic terms as following (M-medium, L-large, VL-very large, H-high and VH-very high). The maximal absolute experimental velocities and acceleration of the pendulums' joints are 1000 deg/s and 8000 deg/s2, respectively. The membership functions and ranges of the input variables are obtained based on the experimental velocities and accelerations classification. Also, the membership functions and ranges of the output variables is obtained relatively from friction coefficients of the AFEM of the case ($\theta_2 = 180^\circ, \theta_3 = 0^\circ, \theta_4 = 0^\circ$) are given in Tables 3.17, 3.18, and 3.19 in section (3.4.2). The fuzzy rules are the most important part of the entire method, which affect the output results crucially. They are set based on the experimental velocities and acceleration classification knowledge and results obtained theoretically by the AFEM for each class. An example of the range selections for the input and output variables in LFM are shown in Table 3.24. Gaussian membership functions were used for graphical inference of the input and the output variables. As an example of many membership functions of the joints in the friction models used here, the membership functions of the first joint in LFM are illustrated in Figure 3.12. A fuzzy rule is a standard form of expressing knowledge based on the logic of IF and Then functions. A set of rules have been constructed based on the input variables (velocities and accelerations) and output variables (friction coefficients) for the three joints of TLRIP. The fuzzy rules used here are given in Table 3.25. The FLC rules for each of pendulum joint were obtained based on the experimental results from velocities and accelerations in AFEM. The defuzzification is the conversion of a fuzzy

quantity to a crisp value. The centroid method was applied for defuzzification. Figure 3.13 shows the FLC surface relationship between velocities, accelerations and friction coefficients of the three joints in LFM.

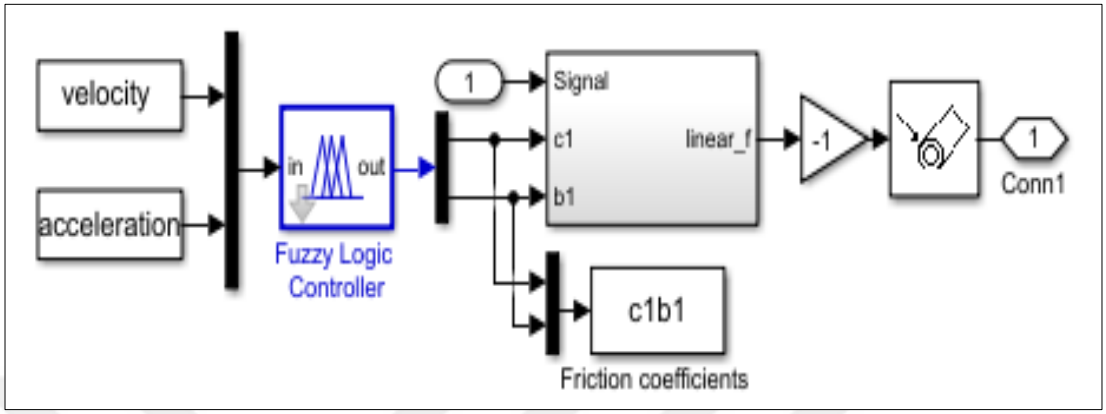

Figure 3.11. Simulink implementation of FLC in each joint of the TLRIP

Table 3.24. FLC Rules For Pendulums' Joints

Velocities / Accelerations	VS		S		M		F		VF	
F.Cof	B1	C1	B1	C1	B1	C1	B1	C1	B1	C1
NH	VH	H	VH	VH	H	VH	M	H	L	M
NM	VH	H	H	VH	H	H	M	M	VL	L
ZE	VH	VH	H	H	M	H	L	M	VL	L
PM	VH	VH	H	H	M	H	L	L	VL	VL
PH	H	H	M	M	L	H	VL	L	VL	VL

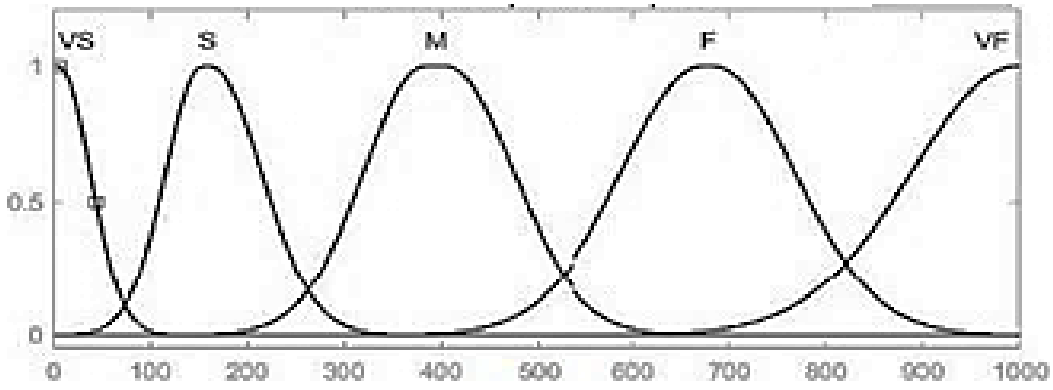

(a)

Figure 3.12. FLC membership functions of the first joint in LFM. (a) Velocity membership functions. (b) Acceleration membership functions. (c) Friction coefficient (B) membership functions. (d) Friction coefficient (C) membership functions.

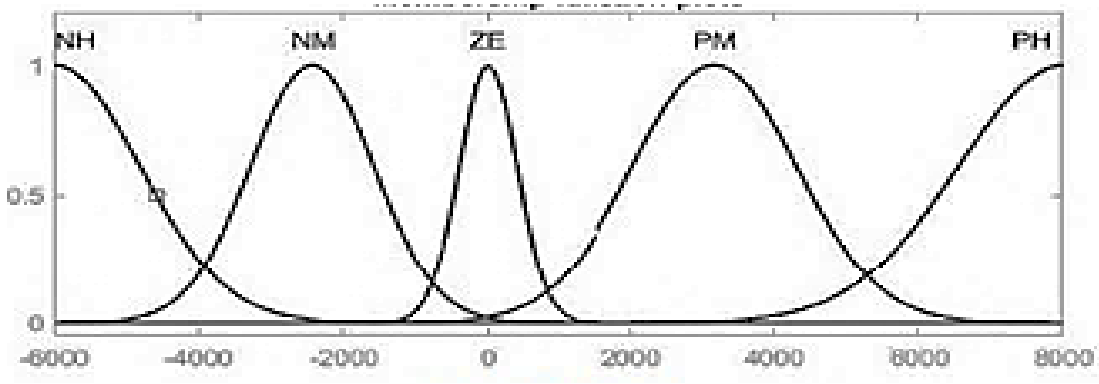

(b)

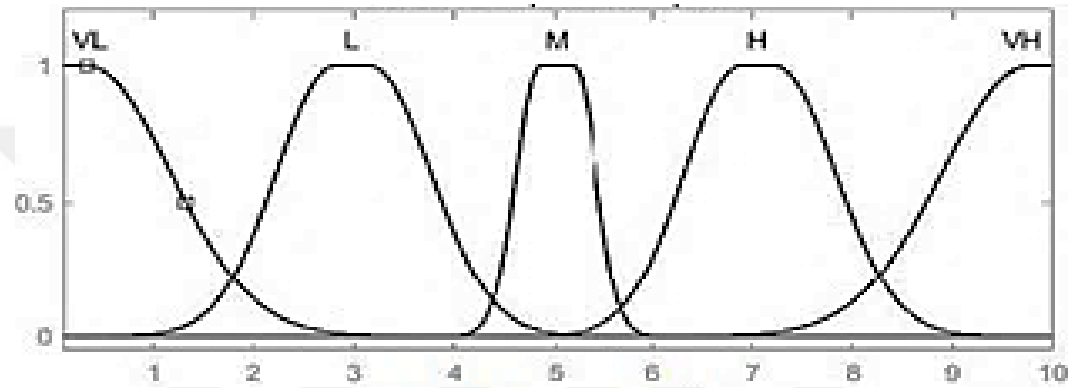

(c)

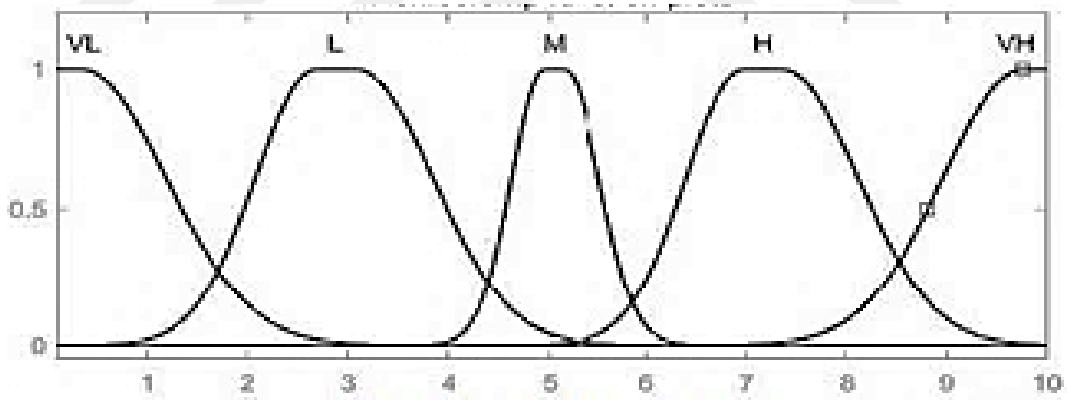

(d)

Figure 3.12.(Cont.) FLC membership functions of the first joint in LFM. (a) Velocity membership functions. (b) Acceleration membership functions. (c) Friction coefficient (B) membership functions. (d) Friction coefficient (C) membership functions.

The friction coefficients obtained by the fuzzy logic inference system was trained by using a RBNN. The sampling rate is chosen as 1khz (sampling time) for the 40s (experiment test time) the velocities and accelerations inputs data are 40000 simples, respectively. The RBFNN method produces better training for a big number of data.

RBFNN have the advantages of an easy design (just three-layer architecture), good generalization, and high tolerance of input noises and the ability of online learning. RBFNNs are simpler than other networks existing in the literature [110-111]. This network uses the Bayesian Regularization (BR) algorithm [112] to treat the joint velocities and accelerations as inputs and the resultant frictions coefficients of fuzzy logic as targets. The BR algorithm performance is dependent by the minimal Means Squared Error (MSE). The RBNN model expressed by two neurons in the input layer, ten neurons in the hidden layer, and two neurons in the output layer. The RBANN model is developed in each pendulum's joint of the TLRIP. Figure 3.14 illustrates the block diagram of the NFFEM architecture for the TLRIP. The filter seen in Figures 3.14 and 3.15 is an IIR (Infinite Impulse Response) filter. $\theta_i, \dot{\theta}_i$ and $\ddot{\theta}_i$ are the joints' angles positions, the angular velocities and the angular accelerations of the i-th pendulums.

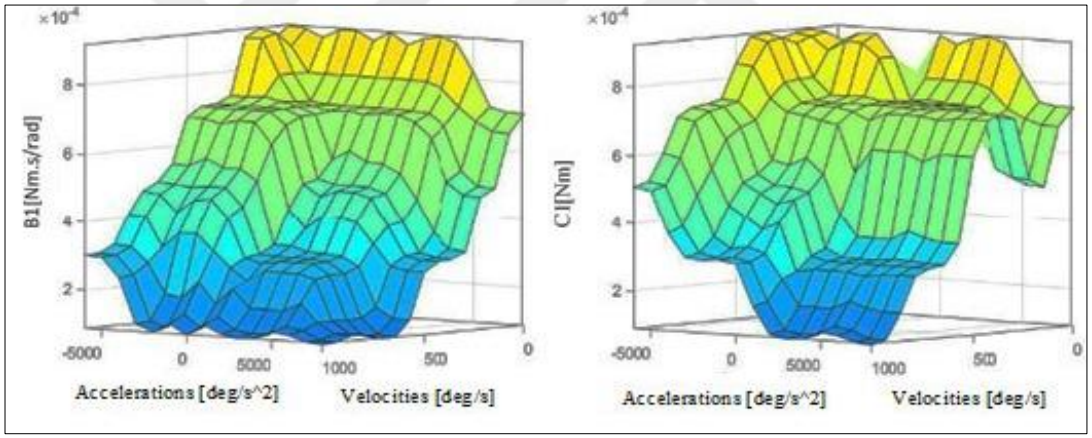

(a)

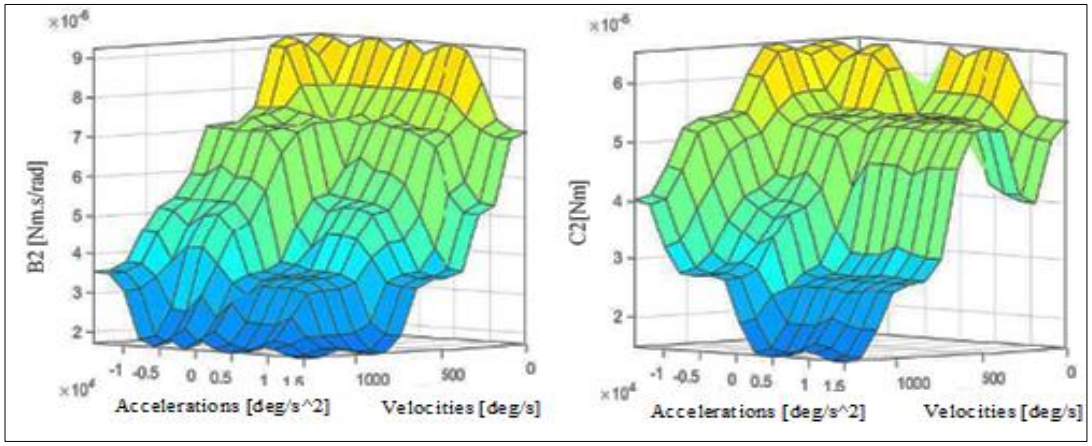

(b)

Figure 3.13. FLC surface in LFM for i-th joints (a) Joint 2 (b) Joint 3 (c) Joint 4

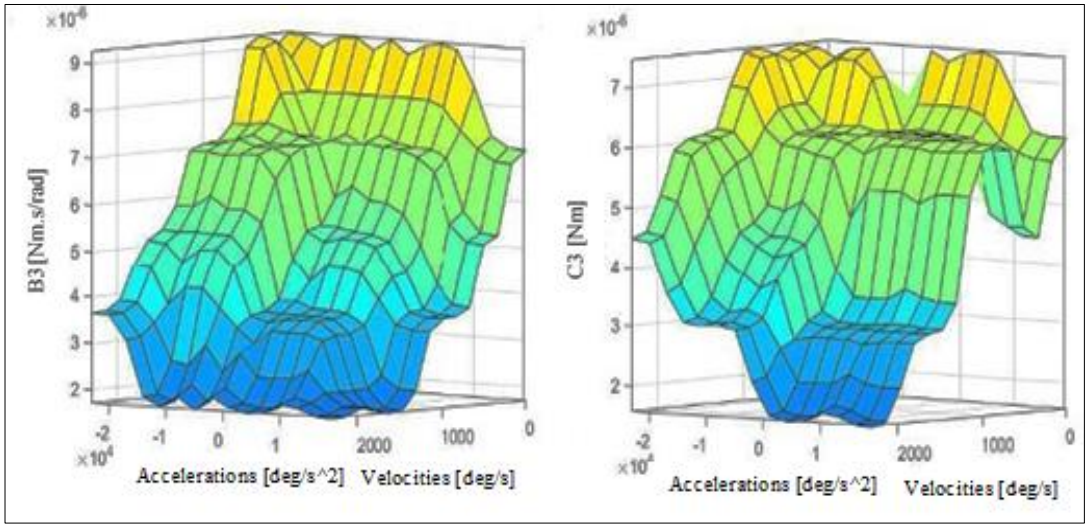

(c)

Figure 3.13.(Cont.) FLC surface in LFM for i-th joints (a) Joint 2 (b) Joint 3 (c) Joint 4

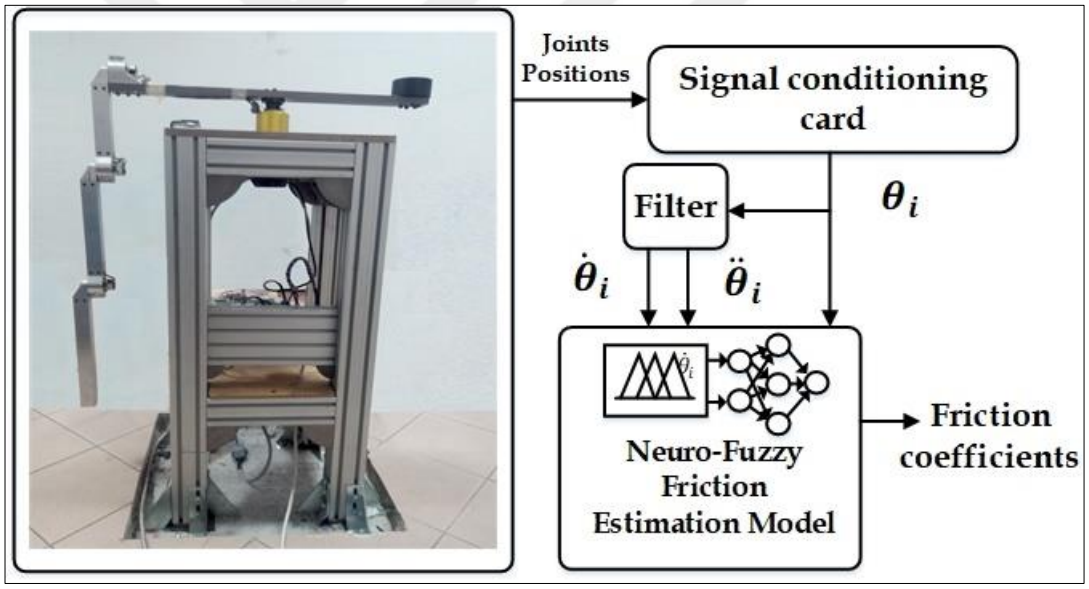

Figure 3.14. Block diagram of the NFFEM architecture for the TLRIP

3.5.2. Data collection for the NFFEMs

The horizontal arm of the TLRIP is driven by a direct drive brushless DC torque motor (Type: TMH-130-050-NC). In this type of motor, since there is no use of transmission or gearbox, the frictions in the horizontal arm can be considered negligible. During the collection of the experimental data, the arm joint θ_1 is fixed at zero position. The pendulums' angles (θ_2, θ_3 and θ_4) are measured with three encoders having a resolution of 2048 pulses per revolution.

Table 3.25. Selection of range for the input and output variables

	İnput variables				Output variables		
Joints	Velocity	Ranges	Acceleration	Ranges	B and C	B-Ranges	C- Ranges
Joint 2	VS	[0 95]	NH	[-6000 -2300]	VH	$[0\ \ 2{,}53.10^{-4}]$	$[0\ 2{,}601.10^{-4}]$
	S	[85 280]	NM	[-5000 -200]	H	$[1{,}263.\ 10^{-4}\ \ 4{,}778.\ 10^{-4}]$	$[1{,}073\ .10^{-4}\ \ 5{,}121.10^{-4}]$
	M	[200 600]	ZE	[-1000 1000]	M	$[4{,}086.\ 10^{-4}\ \ 5{,}916.\ 10^{-4}]$	$[4{,}087.10^{-4}\ \ 6{,}139.10^{-4}]$
	F	[450 920]	PM	[-200 6500]	L	$[5{,}396.\ 10^{-4}\ \ 8{,}837.\ 10^{-4}]$	$[5{,}449.10^{-4}\ \ 9{,}378.10^{-4}]$
	VF	[690 1000]	PH	[3800 8000]	VL	$[7{,}457\ .\ 10^{-4}\ \ 10\ .\ 10^{-4}\ ]$	$[7{,}624.10^{-4}\ 10\ .\ 10^{-4}]$
Joint 3	VS	[0 110]	NH	[-14000 -8177]	VH	$[1.\ 10^{-6}\ \ 3.236.\ 10^{-6}]$	$[1.\ 10^{-6}\ 2.516.\ 10^{-6}]$
	S	[69 400]	NM	[-10880-2483]	H	$[1.757.\ 10^{-6}\ 5.254.\ 10^{-6}]$	$[1.59.\ 10^{-6}\ 4.043.\ 10^{-6}]$
	M	[280 800]	ZE	[-3546 375.9]	M	$[4.624.\ 10^{-6}\ 6.288.\ 10^{-6}]$	$[3.416.\ 10^{-6}\ \ 4.66.\ 10^{-6}]$
	F	[590 1200]	PM	[-611.2 10610]	L	$[5.814.\ 10^{-6}\ \ \ 9.344.\ 10^{-6}]$	$[4.23.\ 10^{-6}\ \ 6.61.\ 10^{-6}]$
	VF	[900 1300]	PH	[7793 22330]	VL	$[7.688.\ 10^{-6}\ 1.002.\ 10^{-5}]$	$[5.56.\ 10^{-6}\ \ \ 7.\ 10^{-6}\ \ ]$
Joint 4	VS	[0 355]	NH	$[-2.3.\ 10^{4}\ \ -1.457.\ 10^{4}]$	VH	$[0\ \ \ 3.232.\ 10^{-6}]$	$[0\ \ 2.769.\ 10^{-6}]$
	S	[138 669]	NM	$[-1.84.\ 10^{4}\ -6242]$	H	$[2.057.\ 10^{-6}\ \ 5.252.\ 10^{-6}]$	$[1.688.\ 10^{-6}\ 4.55.\ 10^{-6}]$
	M	[510 1337]	ZE	[-7860 -2180]	M	$[4.624.\ 10^{-6}\ \ 6.287.\ 10^{-6}]$	$[3.782.\ 10^{-6}\ 5.233.\ 10^{-6}]$
	F	[1075 2043]	PM	$[-3610\ \ 1.264.\ 10^{4}]$	L	$[5.815.\ 10^{-6}\ \ 8.942.\ 10^{-6}]$	$[4.781.\ 10^{-6}\ 7.561.\ 10^{-6}]$
	VF	[1608 3026]	PH	$[8566\ 1.909.\ 10^{4}]$	VL	$[7.687.\ 10^{-6}\ \ 1.002.\ 10^{-5}\ \ ]$	$[6.32.\ 10^{-6}\ 8.\ 10^{-6}]$

The signals obtained from the encoder passes through the slip ring mounted in the joints. A dSPACE-DS1103 controller board treats the received signals from the encoders. The friction in the joints of the TLRIP depends on their velocities and the accelerations. In this case, NFFEM should be determined experimentally. The initial positions of the pendulums will be taken in cases with the value of θ_2 at 180 degrees along with θ_3 and θ_4 at an angle of 0 degrees. The experimental hardware configuration is shown in Figure 3.15. In this work, the frequency counting [113] technique was used to obtain velocity and acceleration from an incremental encoder. This technique is useful for medium and high speeds but degrades in performance at low speed since the relative error increases at low speed. For this reason, a second-order IIR filter was used to smooth the signal.

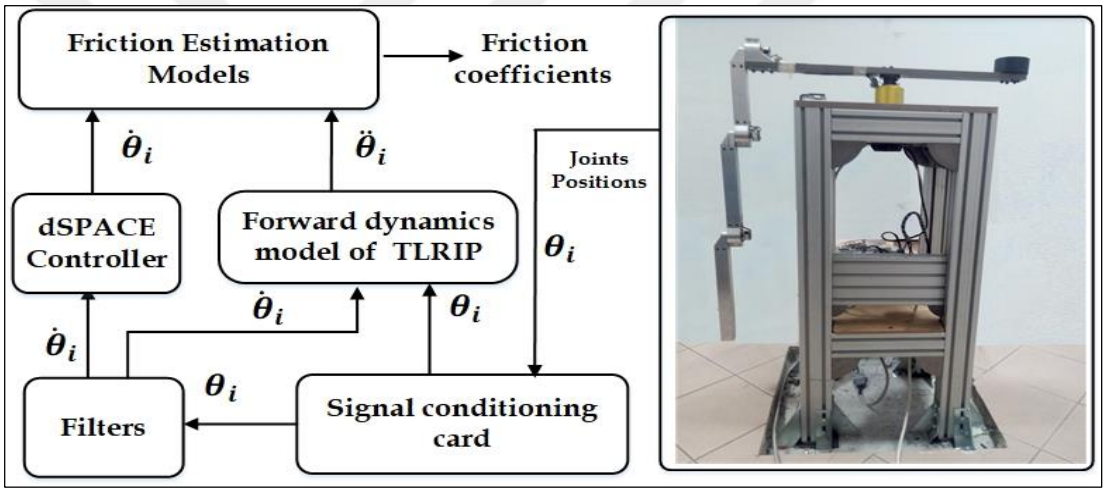

Figure 3.15. Block diagram of the experimental hardware configuration structure for the NFFEMs

3.5.3. Estimation results of the NFFEMs

The simulation results obtained from the AFEMs and NFFEMs based on NCFM, LFM and NLFM were compared with the experimental results. For each joint, position RMSEs between these simulation and experimental results were calculated. Figure 3.16, 3.17 and 3.18 illustrate the friction coefficients obtained by the: Neuro-Fuzzy Non-Conservative Friction Model (NFNCFM), Neuro-Fuzzy Linear Friction Model (NFLFM) and Neuro-Fuzzy Non-Linear Friction Model (NFNLFM) for the joints of the TLRIP, respectively. Figure 3.19 illustrates the angular position comparison between experimental and NFNLFM simulation results. As can be seen from the

figure, a high estimation performance is produced with the use of NFNLFM for each joint.

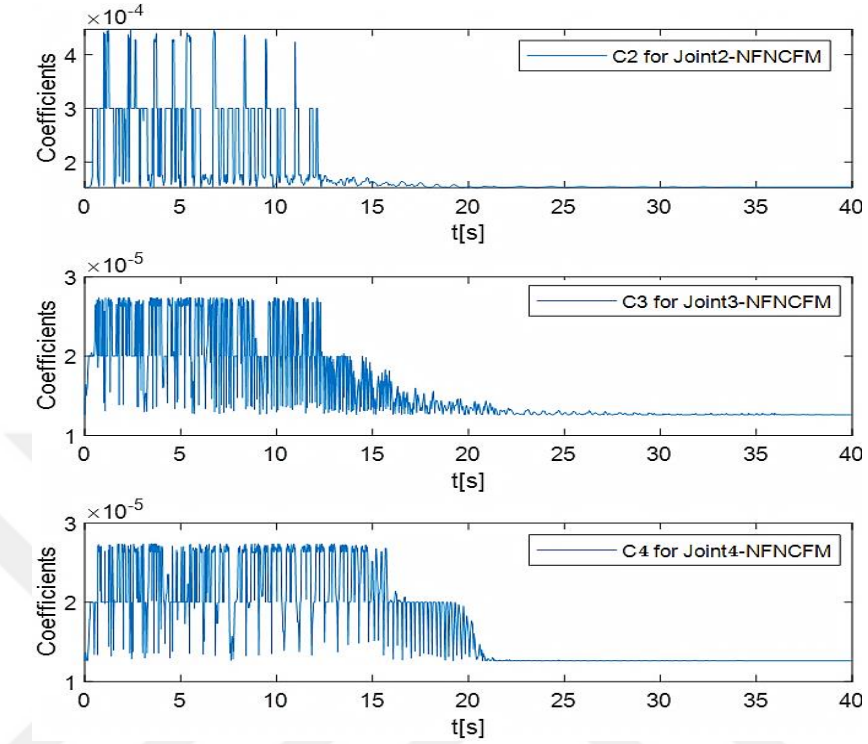

Figure 3.16. Friction coefficients obtained by NFNCFM for pendulums' joints

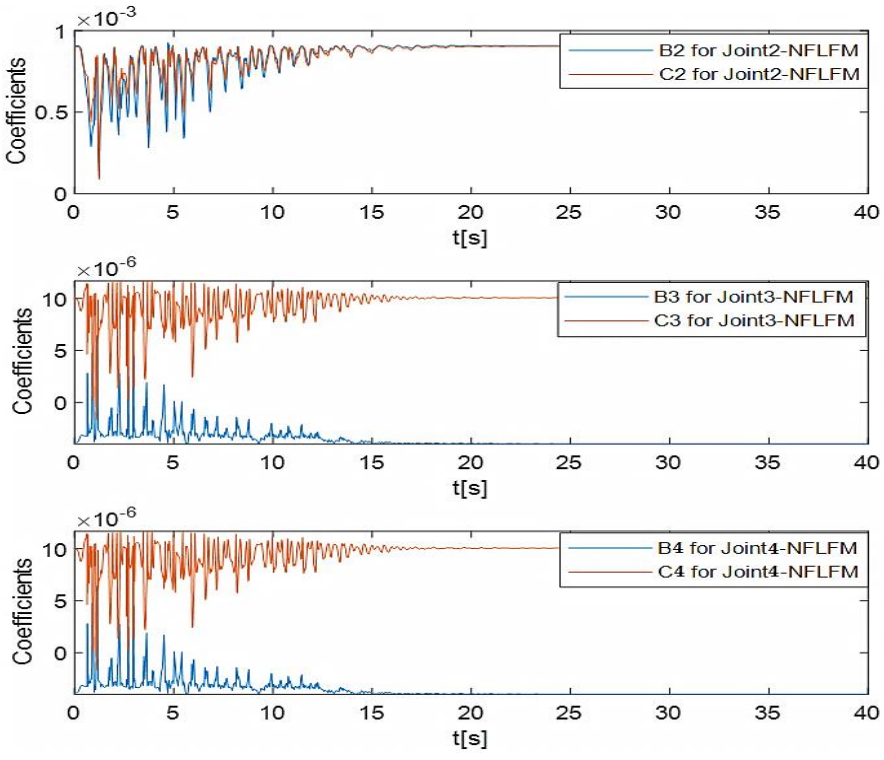

Figure 3.17. Friction coefficients in NFLFM for pendulums' joints

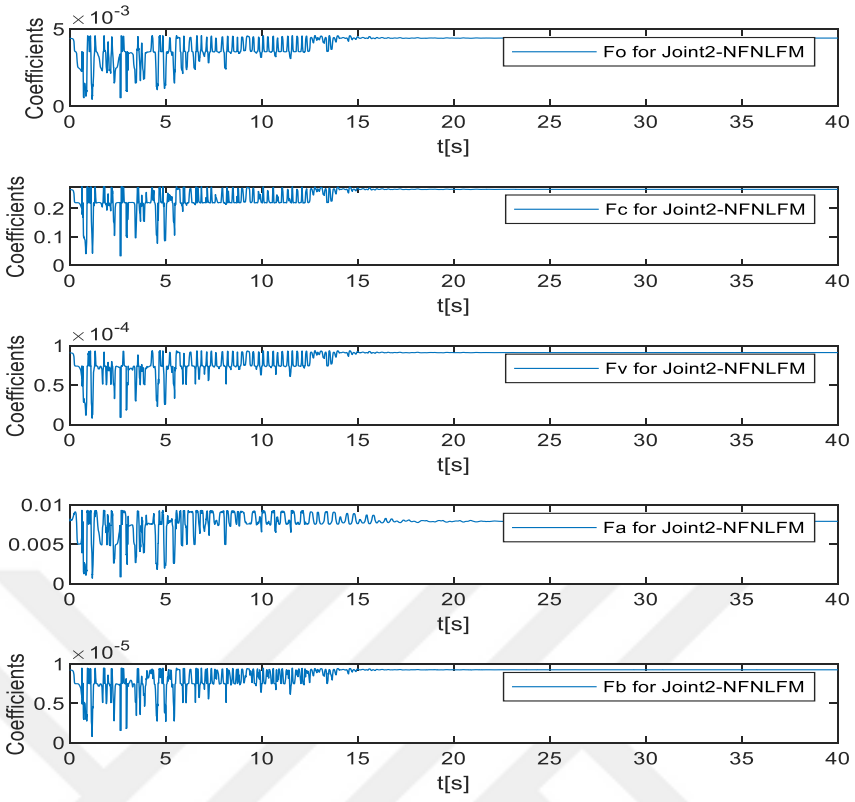

(a)

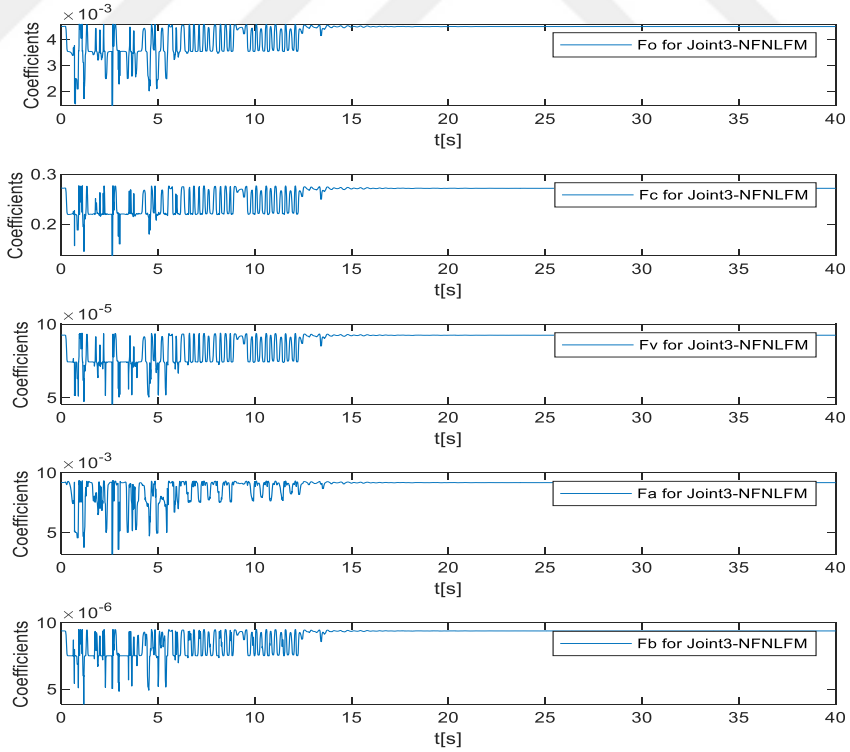

(b)

Figure 3.18. Friction coefficients in NFNLFM: (a) Joint 2, (b) Joint 3 and (c) Joint 4.

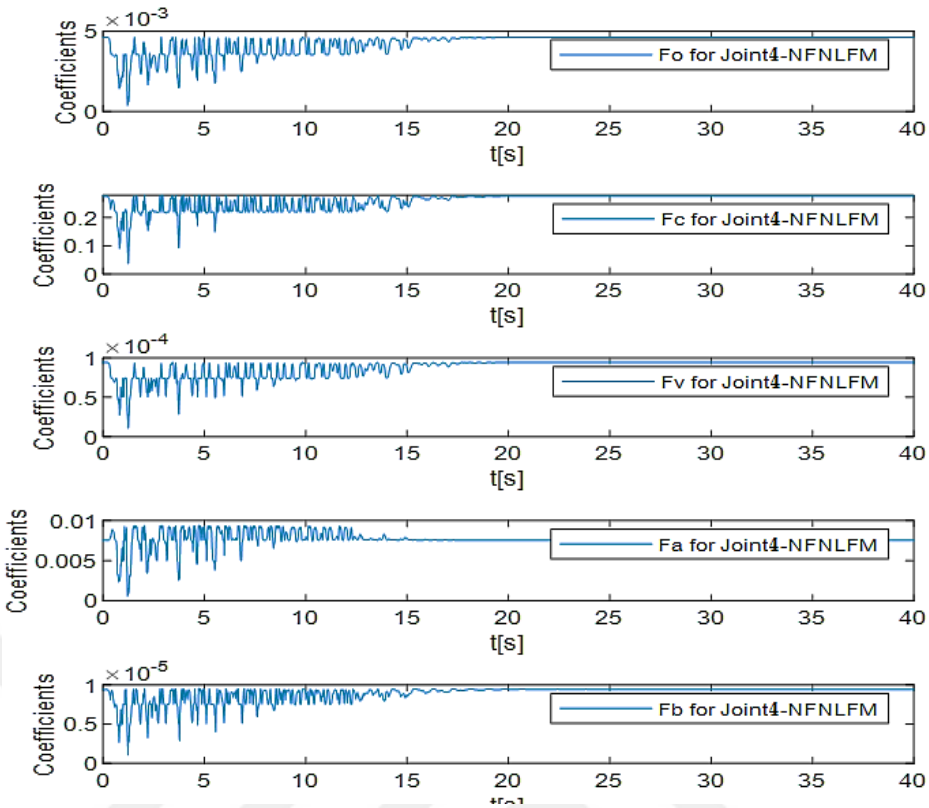

(c)

Figure 3.18.(Cont.) Friction coefficients in NFNLFM: (a) Joint 2, (b) Joint 3 and (c) Joint 4

The joint position RMSEs between the simulation and experimental results of the AFEM and NFFEM were calculated. For comparison purpose, these position RMSEs are given in Table 3.26. According to the calculated position RMSEs, the NFNLFM produces more accurate results than the ANCFM, ALFM, ANLFM, NFNCFM, and NFLFM. In order to see the NFNLFM performance compared with other friction models, percentages of position RMSEs were computed for each joint, and they are given in Table 3.27. Considering the RMSEs of position in all joints, NFNLFM between 11.56 of percentage and 94.55 of percentage yields better results.

Table 3.26. Position RMSES in AFEMS and NFFEMS

Friction Models \ Joints		Joint 2	Joint 3	Joint 4
Adaptive friction coefficients	ANCFM	0.1397	1.8105	0.6995
	ALFM	0.1127	1.8032	0.6743

Table 3.26.(Cont.) Position RMSES in AFEMS and NFFEMS

	ANLFM	0.0983	0.1115	0.6248
Neuro-Fuzzy coefficients	NFNCFM	0.1259	0.8105	0.5480
	NFLFM	0.0987	0.1794	0.4372
	NFNLFM	0.0829	0.0986	0.3304

Table 3.27. Comparison in TERMS of RMSE Percentage between NFNLFM and other friction models

Friction Models	RMSE Percentages between NFNLFM and other friction models		
	Joint 2	Joint 3	Joint 4
ANCFM	40.65 %	94.55%	52.76%
ALFM	26.44%	94.53%	51.00%
ANLFM	15.66%	11.56%	47.11%
NFNCFM	34,15%	87,83%	39,70%
NFLFM	16,00%	45,03%	24,42%

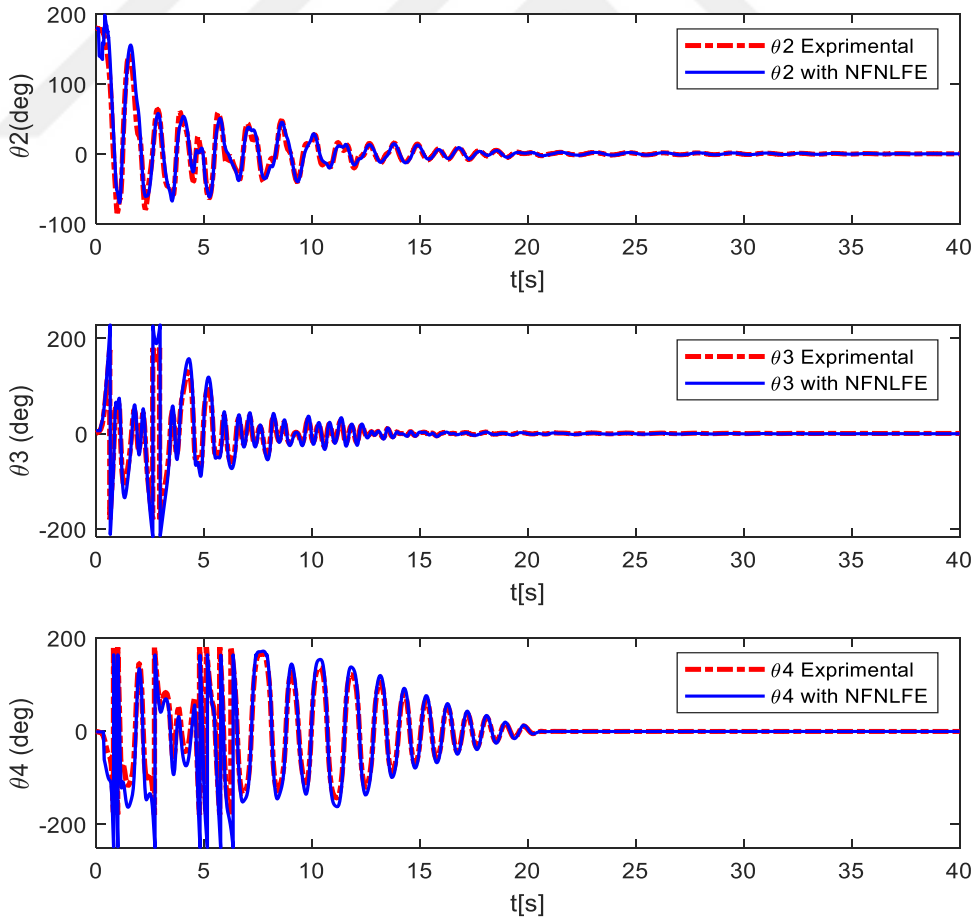

Figure 3.19. Angular position comparison between experimental and NFNLFM simulation results

In this study, novel NFFEMs are developed based on NCFM, LFM and NLFM to estimate the joint friction coefficients in the TLRIP system. The simulation results obtained from NFFEMs were compared with AFEMs. For wide ranges of velocity and acceleration of joints, the variable friction coefficients were estimated with the NFFEMs and AFEMs. All of the friction models were verified and compared using the calculated position RMSEs. According to the performance comparison, the NFNLFM in NFFEMs produced the best results for all joints of the TLRIP. In other future works, the fuzzification ranges and rules of the NF system can be tuned with evolutionary algorithms to enhance the estimation performance of the NFFEMs. Furthermore, more inputs such as jerks and snaps of the joints can be applied to the NF system, and the TLRIP system will be controlled using the proposed friction models.

4. SYSTEM CONTROL AND SIMULATION RESULTS

4.1. Introduction

IPS are widely used in Non-Linear Control Theory (NLCT) education. Many control problems in the field of NLCT have been studied with the IPS which was installed in a research laboratory. A vast range of contributions in the literature exists for the stabilization of different types of IPS. Besides the stabilization problem aspect, the anti-swing problem, especially of the classical SLRIP has gained increasing attention in the recent studies. Therefore, the DLRIP and TLRIP are more complex than SLRIP in terms of dynamic control problem. DLRIP and TLRIP systems have a three and four DOFs, respectively. The RIP systems have two stable points, such as downward (stable equilibrium point) and upward positions (unstable equilibrium point). According to the complicated nonlinearity and the high coupling effect between the pendulum links, the control problem of the DLRIP and TLRIP is still considered as a challenging research topic. Underactuation structure of the systems (driven by a single actuator) makes the control actions more difficult and hence it needs a more complicated controller design. Furthermore, the classical controllers may not control this type of systems effectively. A robust nonlinear controller should be applied to control the system. The development of effective controllers for the highly nonlinear and complex coupled dynamic behaviour systems is needed. One solution widely used in literature to alleviate this control problem is to linearize the complex nonlinear system and applied classical linear control methods to stabilize the system. Moreover, the control performance of the real system can be degraded depending on the differences between the linearized and the real nonlinear systems [114]. Recently, the fuzzy controllers seem to be a good alternative to simplify the control of a nonlinear complex system such as IPS for desired control performance. By using the fuzzy control, the nonlinear systems are approximated by the combination of several linear subsystems in the corresponding fuzzy state-space regions. For this reason, the linear subsystems are fuzzily combined. The fuzzy control of the IPS is shown that robust under internal and external disturbances [115-116]. In the first works existing in the literature [117-118],

the fuzzy controller was used for swing up and stabilization control of a SLRIP. The rules for the swing-up of the pendulum were chosen to each swing results in order to have greater energy build up. The stabilization of the pendulum was achieved by switching at an LQR control law to the fuzzy inference to make the stability in the unstable equilibrium point. The objective of the new studies in the literature [119-120] is to determine a non-linear control strategy to obtain better performance applied to SLLIP. An LQR based fuzzy controller was designed, and its performance was compared with LQR controller. The results in this new control technique show that LQR based fuzzy controller produced better response as compared to LQR control strategy. In this section, a non-linear FLQR and FLQG controllers are developed to stabilize the pendulum links of the DLRIP and TLRIP systems in the upward vertical position. In order to obtain the desired angular position of pendulums with a better dynamic response, compared to the classical LQR and LQG controllers, the fuzzy controllers were combined with the LQR and LQG in objective to adjust the closed-loop controller feedback gains. respectively. This paper examines the control performance of the controllers in terms of T_s, PO, E_{ss} and the RMSE position errors of the joints (position error between the equilibrium point and the dynamic responses obtained from each joint). Moreover, several simulations were conducted to study the effectiveness of the FLQR and FLQG controllers under the internal and external disturbances. ANNs have been presented good solutions for the anti-swing control problem of IPS [121]. Recently, both approaches, Fuzzy and ANN are combined with the NF model. NF control has become a popular research topic for the IPS control problem. Takagi-Sugeno Fuzzy model called the ANFIS is used for the nonlinear anti-swing control of IPS [122-124]. In recent works, the use of LQR based NF model has been suggested to improve the performance of the controller [125]. In this section, a novel RBNF-LQR controller is developed for an anti-swing control of a DLRIP and TLRIP systems. The objective of this work is to study the RBNF-LQR controller and to compare it with FLQR and the classical LQR controllers. In the proposed RBNF-LQR controllers, the positions and velocities of state variables multiplied by their LQR gains trained by using two RBNNs architecture. The output of the two RBNNs are used as the input variables of the fuzzy controller. The novel architecture of the RBNF controller is developed in order to obtain better control performance than the classical ANFIS. To determine the control performance of the anti-swing controllers, different

control parameters are computed such as E_{ss}, T_s, MP, RMSEs. Moreover, the performance of controllers was compared based on robustness analysis under external disturbance. Figure 4.1 shows the applied controllers to the SLRIP, DLRIP and TLRIP systems.

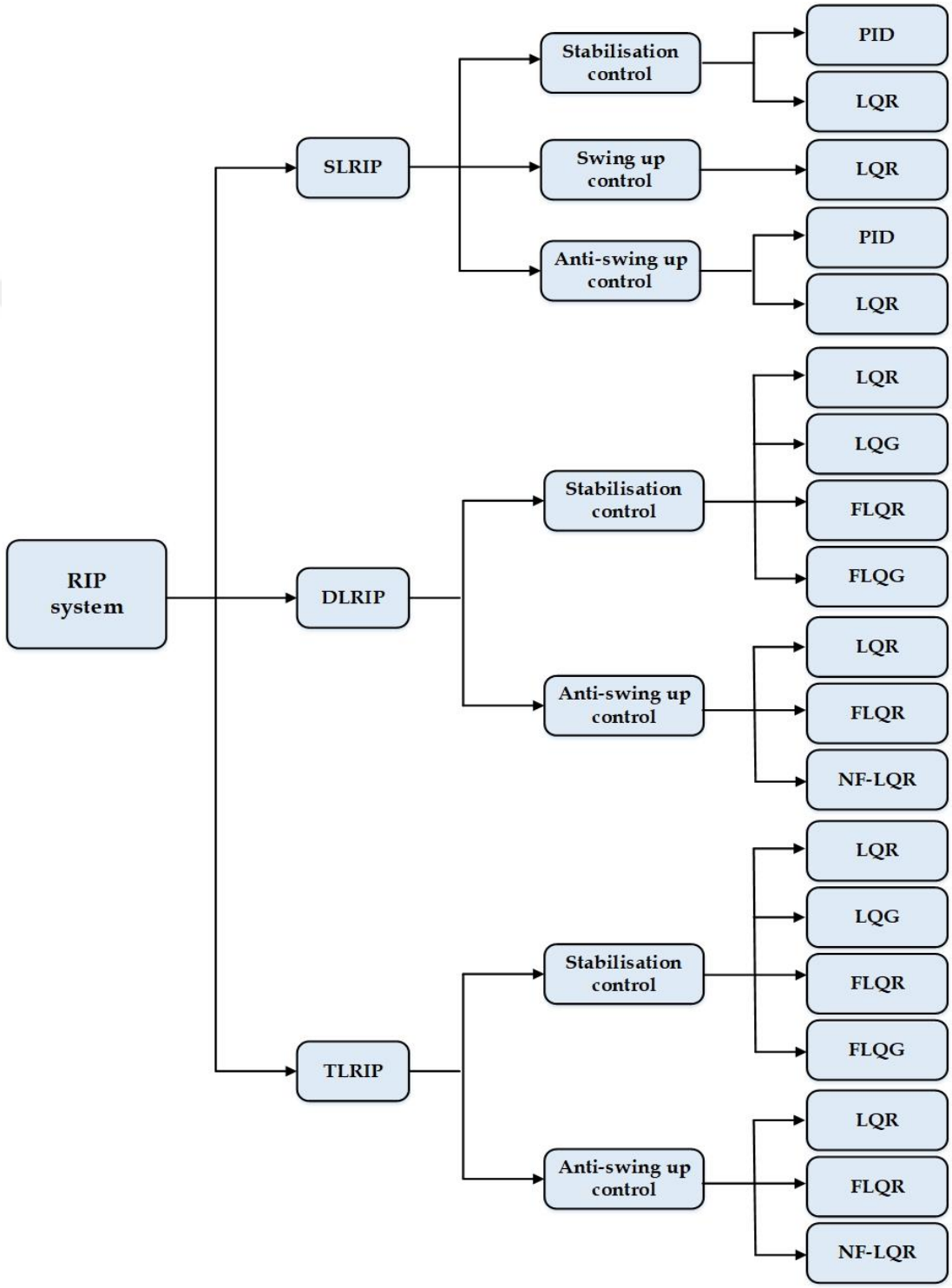

Figure 4.1. Control methods applied for the SLRIP, DLRIP and TLRIP

4.2. Design of Controllers for the RIPS

In this section, the controller methods applied to control our RIPS are explained with details.

4.2.1. PID controller

To stabilize the inverted pendulum of the SLRIP in the upright position and to control the horizontal link at the desired position using the PID control approach, two PID controllers: Angle PID controller and horizontal link PID controller have been designed for the two control loops of the system. The equations of the PID control are given as follows: [126]

$$u_p = K_{pp}\, e_{\theta_2}(t) + K_{ip} \int e_{\theta_2}(t)\, dt + K_{dp}\, \frac{d\, e_{\theta_2}(t)}{dt} \tag{4.1}$$

$$u_l = K_{pl}\, e_{\theta_1}(t) + K_{il} \int e_{\theta_1}(t)\, dt + K_{dl}\, \frac{d\, e_{\theta_1}(t)}{dt} \tag{4.2}$$

where $e_{\theta_2}(t)$and $e_{\theta_1}(t)$are the angle error of the pendulum link and the angle error of the horizontal link, respectively. K_{pp} , K_{ip}, K_{dp} are the PID controller parameters of the proportional, integral and derivative terms of the pendulum link respectively. Moreover, K_{pl} , K_{il}, K_{dl} are the PID controller parameters of the proportional, integral and derivative terms of the horizontal link respectively. Since the dynamics of the angle of pendulum link and horizontal link dynamics are coupled to each other, the change in any controller parameters affects both the pendulum angle and horizontal arm position, which makes the tuning tedious. The tuning of controller parameters is done by using trial and error methods and observing the responses of the Simulink model to be optimal. The tuning of controller parameters is done by minimizing the error methods using an optimization algorithm such as PSO.

4.2.2. Linear quadratic regulator

The State Feedback Control (SFC) technique is based on the placement of the system poles. A gain matrix (K) and the state variables are used for the pole placement of the system. In SFC the poles of the closed-loop system may be placed at any chosen

position. Nevertheless, for the methods of output feedback control, the poles of systems may be given to a definite point [127]. In this technique, the state variables are implemented by a state feedback controller. The state variables of the system are feedback. All feedbacks multiplied by a state feedback gain matrix are compared to the reference input. The important point in the SFC design is to calculate a gain matrix (K). In this purpose, the LQR controller is one of the most used methods. In the LQR controller, the optimal feedback parameters of K matrix are taken by the cost function (J), which optimize states, x(t) and the control signal $u(t)$ of the system. $u(t)$ and J are given in equations (4.3) and (4.4), respectively. [128]

$$u(t) = -K\,x(t) \tag{4.3}$$

$$J = \frac{1}{2}\int_0^{\infty} (x^T Q x + u^T R u)\,dt \tag{4.4}$$

J depends on the matrix Q and R. Q and R are defined as a positive semi-defined matrix. Furthermore, the K gain matrix is determined based on Q and R. The control signal is shown below. [129]

$$u(t) = -R^{-1}B^T P(t)x(t) = -Kx(t) \tag{4.5}$$

where P is obtained by the differential equation of Riccati:

$$PA + A^T - PBR^{-1}P + Q = 0 \tag{4.6}$$

K matrix is determined with P. It is the solution of the Riccati equation given in (4.7).

$$K = R^{-1}B^T P = [k_1 \quad K_2 \quad K_3 \ldots . . K_n] \tag{4.7}$$

n is the number of state variables. LQR controller performance is dependent on the choice of weight matrices. In the literature, there exist many different approaches for the choice of Q and R, for example, the Bryson's Rule. A simple choice approach can be Q=I and R=ρ I. Also, several optimization algorithms can be used to obtain the optimal value of Q and R. [130]

4.2.3. Fuzzy linear quadratic regulator

This controller is a combination of the optimal control approach (LQR) and fuzzy

control method [131]. The FLQR controller transform the variables into error (e) and derivation of the error (ė), which simplified the fuzzy controller. e and ė are the summings of positions and velocities of state variables multiplied by their LQR gains, respectively. An example of the block diagram of FLQR controller applied to DLRIP is shown in Figure 4.2. e and ė can be calculated as follows:

$$\begin{bmatrix} e \\ \dot{e} \end{bmatrix} = Kx^T = \begin{bmatrix} K_{\theta_1}\theta_1 + K_{\theta_2}\theta_2 + K_{\theta_3}\theta_3 + \cdots K_{\theta_i}\theta_i \\ K_{\dot{\theta_1}}\dot{\theta_1} + K_{\dot{\theta_2}}\dot{\theta_2} + K_{\dot{\theta_3}}\dot{\theta_3} + \cdots K_{\dot{\theta_1}}\dot{\theta_1} \end{bmatrix} \tag{4.8}$$

$$K = \begin{bmatrix} K_{\theta_1} & K_{\theta_2} & K_{\theta_3} \ldots K_{\theta_i} & 0 & 0 & 0 \ldots \\ 0 & 0 & 0 \ldots K_{\dot{\theta_1}} & K_{\dot{\theta_2}} & K_{\dot{\theta_3}} & \ldots K_{\dot{\theta_1}} \end{bmatrix} \tag{4.9}$$

Where i is the number of state variables and x^T is the state vector.

$$e = K_{\theta_1}\theta_1 + K_{\theta_2}\theta_2 + K_{\theta_3}\theta_3 + \cdots K_{\theta_i}\theta_i \tag{4.10}$$

$$\dot{e} = K_{\dot{\theta_1}}\dot{\theta_1} + K_{\dot{\theta_2}}\dot{\theta_2} + K_{\dot{\theta_3}}\dot{\theta_3} + \cdots K_{\dot{\theta_1}}\dot{\theta_1} \tag{4.11}$$

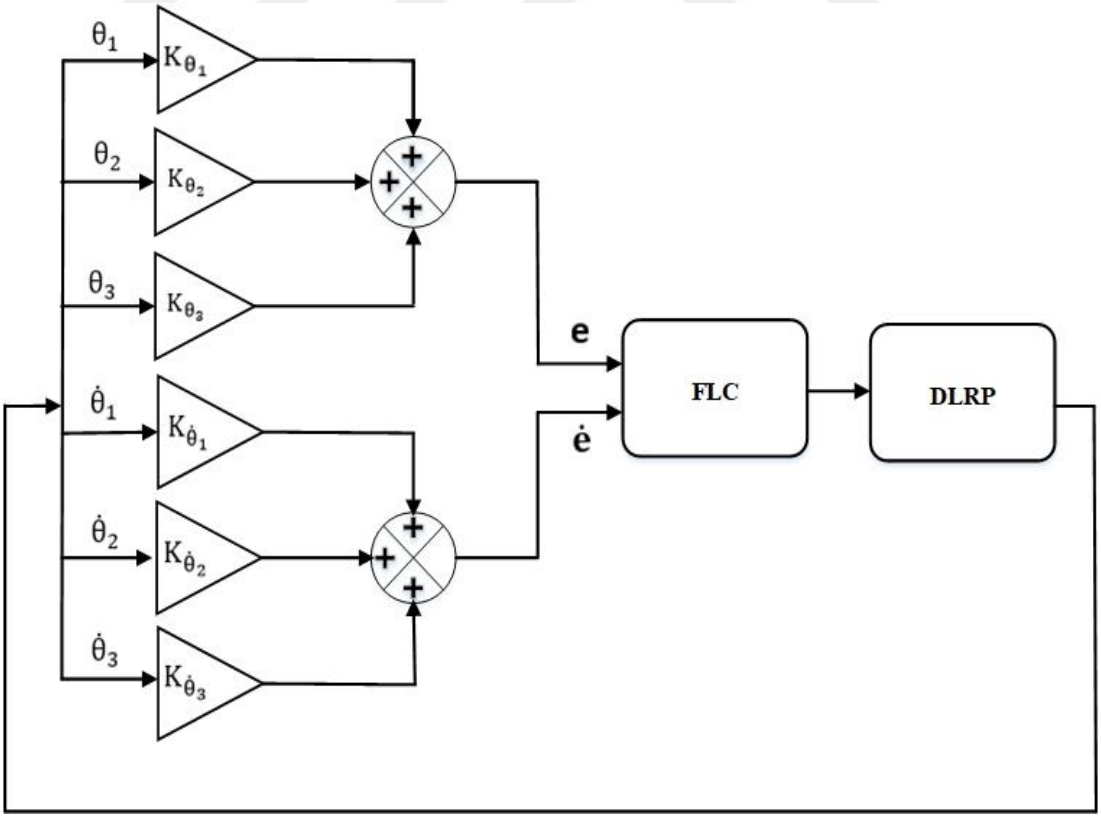

Figure 4.2. Example of the block diagram of FLQR controller applied to DLRIP

Mamdani type fuzzy model was developed in objective to adjust the closed-loop

controller feedback gains of our system. The input variables (e and ė) and the output variable (Control signal-U) are converted into linguistic variables, as follows: (NB-negative big, NM-negative medium, NM-negative small, Z-zero, PS-positive small, PM-positive medium, PB- positive big) [132]. The range of the input variables are [-15 15 (degree)], [-6 6 (degree/s)] for e and ė, respectively. Also, the range of the output variable is [-10 10 (v)]. Triangular membership functions are used for the graphical inference of the input and the output variables [133-134]. Table 4.1 present the fuzzy rules applied to the controller of the system. Tables 4.2 show the range of the input and output variables. Figure 4.3 shows the relationship between inputs and output of the FLC (FLC surface). The membership of the input and output variables are presented in Figure 4.4.

Table 4.1. Fuzzy rules

ė / e	NB	NM	NS	ZE	PS	PM	PB
NB	NB	NB	NB	NM	NM	NS	ZE
NM	NB	NB	NM	NM	NS	ZE	PS
NS	NB	NM	NM	NS	ZE	PS	PM
ZE	NM	NM	NS	ZE	PS	PM	PM
PS	NM	NS	ZE	PS	PM	PM	PB
PM	NS	ZE	PS	PM	PM	PB	PB
PB	ZE	PS	PM	PB	PB	PB	PB

Table 4.2. Range of the input and output variables

Ranges / Symbols	Input variables		Output variables
	Ranges of input (e)	Ranges of input (ė)	Ranges of output (U)
NB	[-15 -12 -7.5]	[-6 -5 -3.5]	[-10 -8 -5]
NM	[-9 -6 -2]	[-4 -3 -1.5]	[-6 -4 -1.8]
NS	[-3 -1.5 0]	[-2 -1 0]	[-2 -1 0]
ZE	[-0.75 0 0.75]	[-0.5 0 0.5]	[-1 0 1]
PS	[0 -1.5 3]	[0 1 2]	[0 1 2]
PM	[2 6 9]	[1.5 3 4]	[1.8 4 6]
PB	[7.5 12 15]	[3.5 5 6]	[5 8 10]

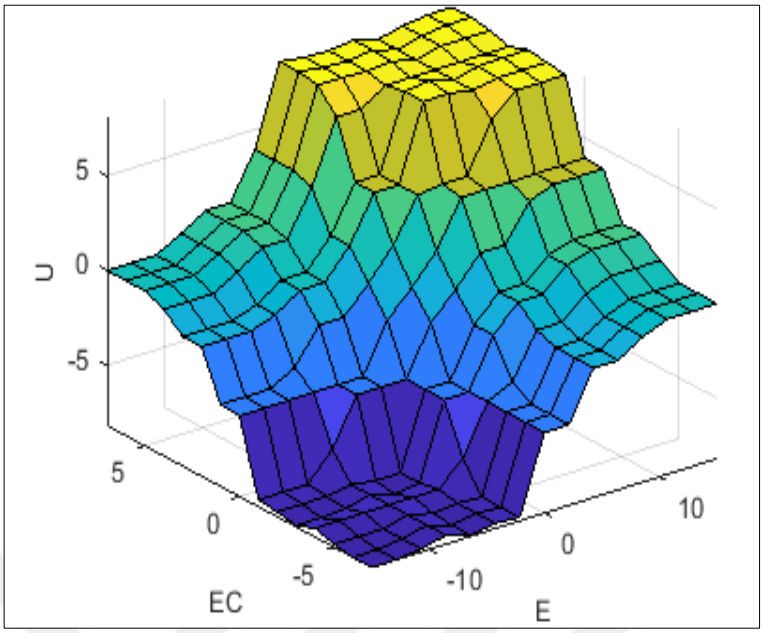

Figure 4.3. FLC surface

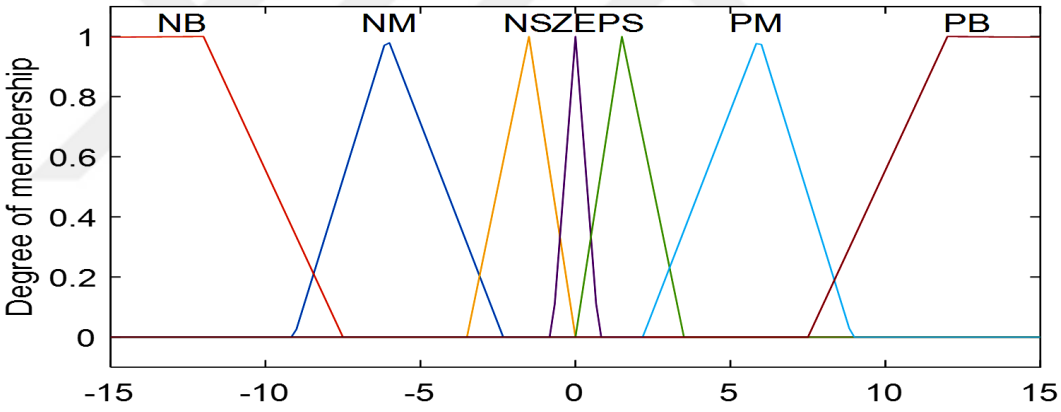

(a)

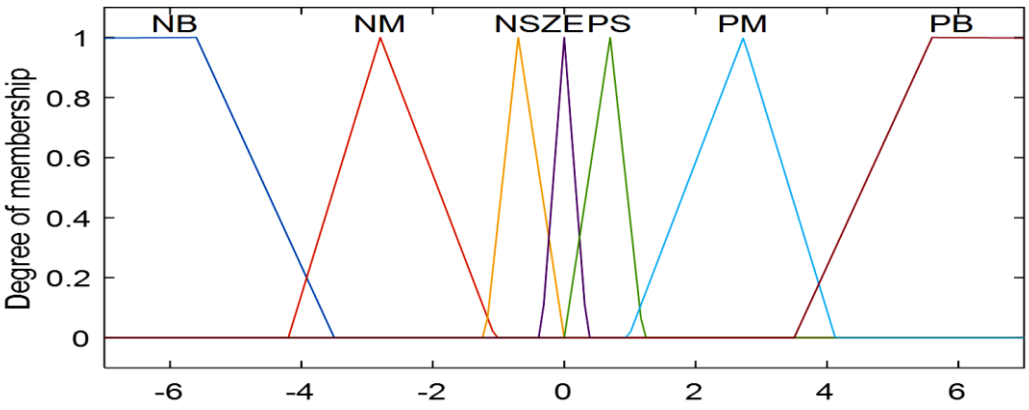

(b)

Figure 4.4. The membership functions of (a) the input e, (b) the input ė and (c) the output U

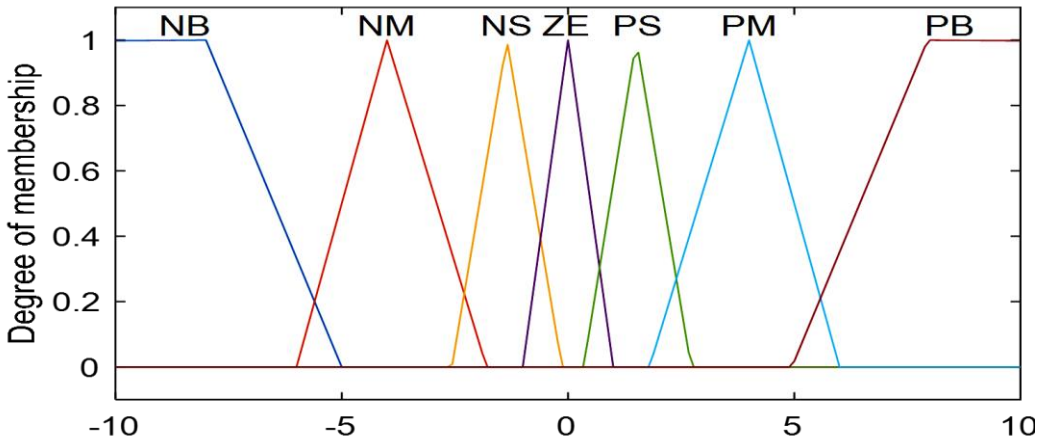

(c)

Figure 4.4.(Cont.) The membership functions of (a) the input e, (b) the input ė and (c) the output U

4.2.4. Linear quadratic gaussian

In a linear dynamic system, Kalman Filter (KF) estimates the system states from the information of input and output. Figure 4.5 (a) shows the block diagram of the KF. Noised signals (W_d, W_n) are combined with the linear dynamic system to get more increased system construction necessary to the KF algorithm [135]. According to the add noised signal, the state-space model of RIPS can be the system given as follows:

$$\begin{cases} \dot{x} = Ax + Bu + W_d \\ y = Cx + Du + W_n \end{cases} \tag{4.12}$$

The dynamic equation of KF is added to the state space and it is given by the equation:

$$\begin{cases} \dot{\hat{x}} = A\hat{x} + Bu + K_f(y - \hat{y}) \\ \hat{y} = C\hat{x} \end{cases} \tag{4.13}$$

The KF gain K_f is calculated as follows:

$$K_f = PC^T R^{-1} \tag{4.14}$$

P and R are an algebraic constant calculated with the Riccati equation and the output covariance matrix, respectively. $\hat{x}$ and $\hat{y}$ are the estimated state variables and outputs, respectively. The error can be given in equation (4.15).

$$e = \hat{x} - x \tag{4.15}$$

By using equations (4.12) and (4.15) equation (4.16) is obtained.

$$\dot{e} = (A - K_f C)e \tag{4.16}$$

An optimal K_f the gain matrix must be determined to the KF design. The structure of LQG is taken by the added KF to the LQR, as can be seen in Figure 4.5 (b). The KF is obligatory if the state variables of the LQR needed to be estimated. LQG is an optimal controller method for some systems which have uncertainty. the KF is used to estimate the state variables according to the system input and the measured output variables. The state variables will be multiplied by the K matrix to generate the control signal (u), given in equation (4.17). [136-137]

$$u = -K\hat{x} \tag{4.17}$$

If the control signal is applied to the state-space model and the noise signals added to the system, the closed-loop model is given as follows:

$$\dot{x} = Ax - BKx + BK(x - \hat{x}) + W_d \tag{4.18}$$

The KF state-space model is

$$\dot{\varepsilon} = (A - K_f C)\varepsilon + W_d - K_f W_n \tag{4.19}$$

The new space model can be defined in equation (4.20)

$$\begin{bmatrix}\dot{x}\\ \dot{\varepsilon}\end{bmatrix} = \begin{bmatrix}(A - BK) & BK\\ 0 & (A - K_f C)\end{bmatrix}\begin{bmatrix}x\\ \varepsilon\end{bmatrix} + \begin{bmatrix}1 & 0\\ 1 & -K_f\end{bmatrix}\begin{bmatrix}W_d\\ W_n\end{bmatrix} \tag{4.20}$$

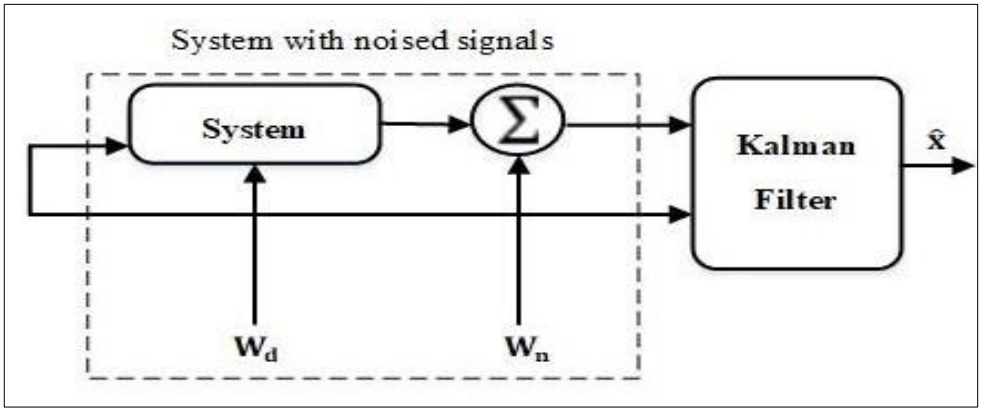

(a)

Figure 4.5. (a) Block diagram of the KF, (b) Block diagram of the LQG

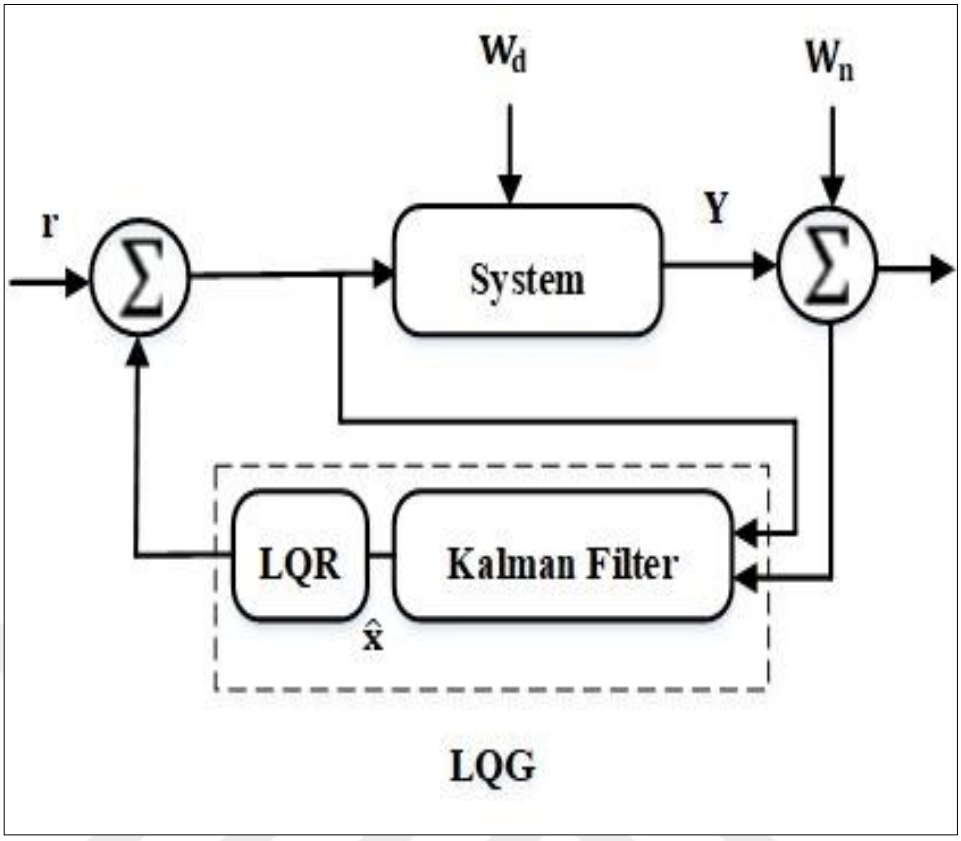

(b)

Figure 4.5.(Cont.) (a) Block diagram of the KF, (b) Block diagram of the LQG

4.2.5. Fuzzy linear quadratic gaussian controller

This FLQG controller structure is based on the combination of the LQG controller given in section (4.2.4) and FLQR controller given in section (4.2.3). However, for certain cases, the state variables are not measured for real experimental systems. But it is possible to estimate the non-measurable state by using the measurement data if the system is observable. Furthermore, the estimation of state variables can be preferred because of the noisy measurement data.

The structure of FLQG is obtained by adding the KF to the FLQR, as can be seen in Figure 4.6. However, the KF is obligatory if some state variables needed for the FLQR are estimated. KF estimates the state variables according to the RIPS input and the measured output variables. The estimated state variables are the input of the FLQR controller. The Block diagram of FLQG controller is shown in Figure 4.6. [138-139]

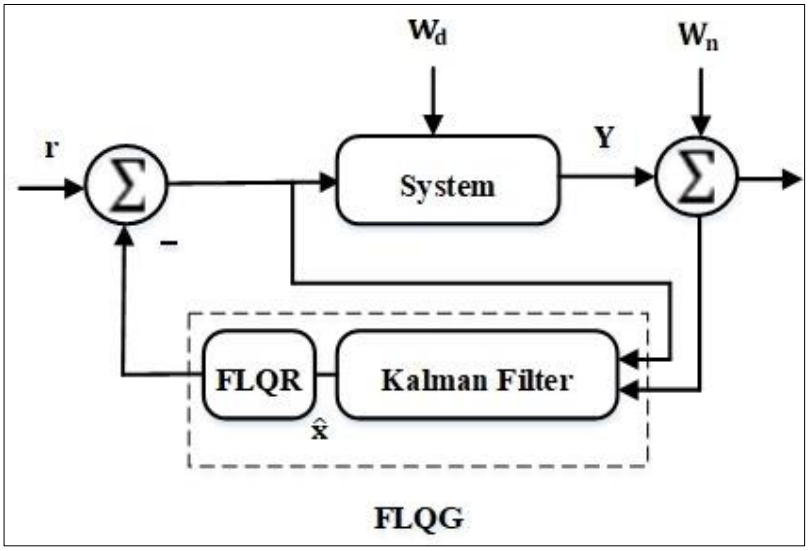

Figure 4.6. Block diagram of FLQG controller for the RIPS

4.2.6. ANFIS based LQR controller

In this section, the design aspect of ANFIS based LQR (ANFIS-LQR) controller is explained in details. The procedure of ANFIS is considered into three steps, given in Figure 4.7.

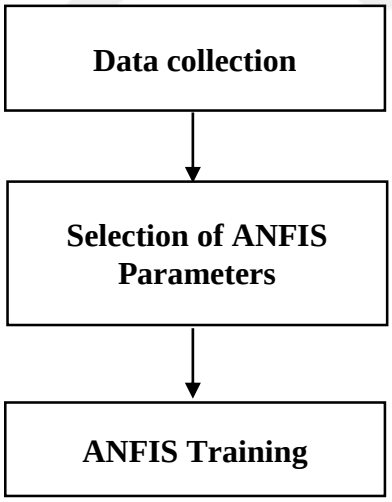

Figure 4.7. Procedure to design ANFIS-LQR controller

In the step of data collection, the data must be in the form of multiple-inputs and single-output column vector [140]. For the data collection, the inputs and output data of the non-linear FLQR controller are used. The FLQR controller transforms the variables into error (e) and derivation of the error (ė), e and ė are the summing of positions and

velocities of state variables multiplied by their LQR gains, respectively. U is the output control signal of the FLQR controller. The input data vectors are obtained from e and ė. The output data vector is obtained from U. An example of a block diagram of ANFIS-LQR controller applied to DLRIP is shown in Figure 4.8. In the second step, ANFIS parameters such as the number and type of membership functions, error tolerance, epochs number and learning method must be chosen. In the last step, a fuzzy inference system is trained by the ANFIS [141]. ANFIS training is easily obtained in MATLAB using the pre-defined function "anfisedit". The obtained fuzzy inference system can be exported in a .fis file is created, which acts as a non-linear controller for the system.

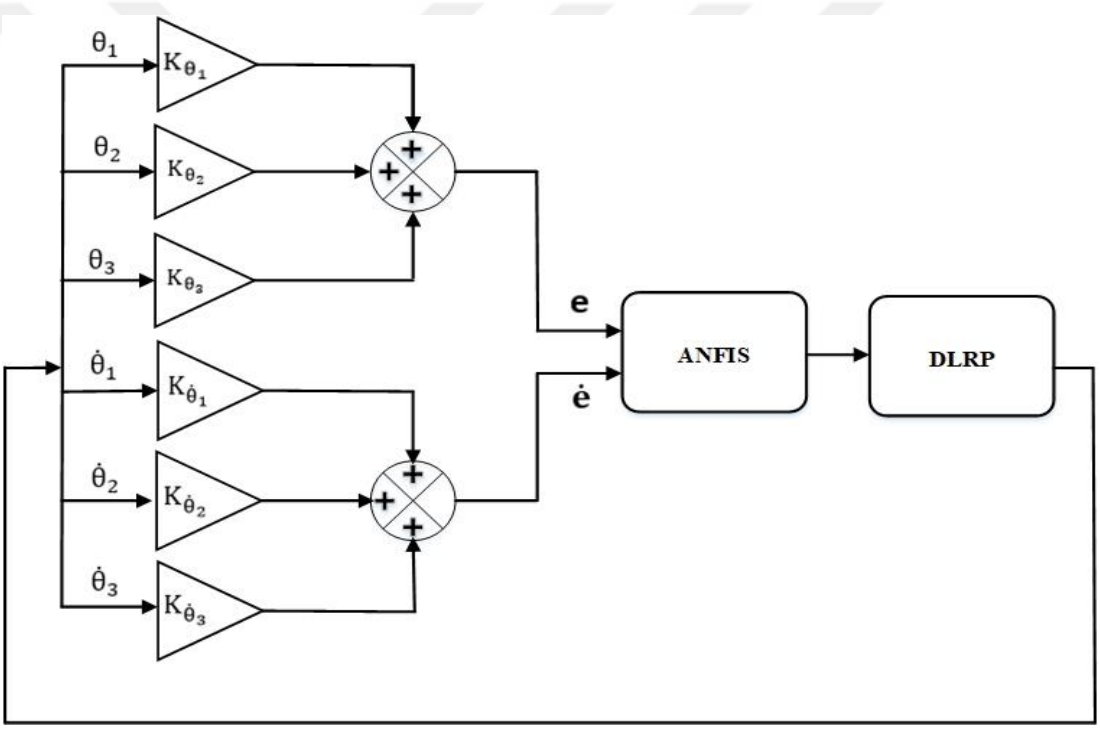

Figure 4.8. Example of a block diagram of the ANFIS-LQR controller in a DLRIP

4.2.7. Radial-basis neuro-fuzzy based LQR controller

In this section, RBNF-LQR controller is explained in details. The RBNF-LQR is developed in order to obtain better control performance than the classical ANFIS-LQR controller. Two RBNNs are used to train the positions and velocities of state variables multiplied by their LQR gains, respectively. The inputs and output (u) data obtained from the non-linear FLQR controller are used for the training of both RBNNs. RBNN is a universal approximator based on the simple and fixed three-layer architecture.

RBNNs are easier to be developed and trained compared to other ANNs. RBNNs have a very strong tolerance to the noised inputs, which improve the stability control of the systems. RBNN can be used as a method of nonlinear controller design [142-143]. An example of the block diagram of RBNF-LQR controller applied to DLRIP is shown in Figure 4.9.

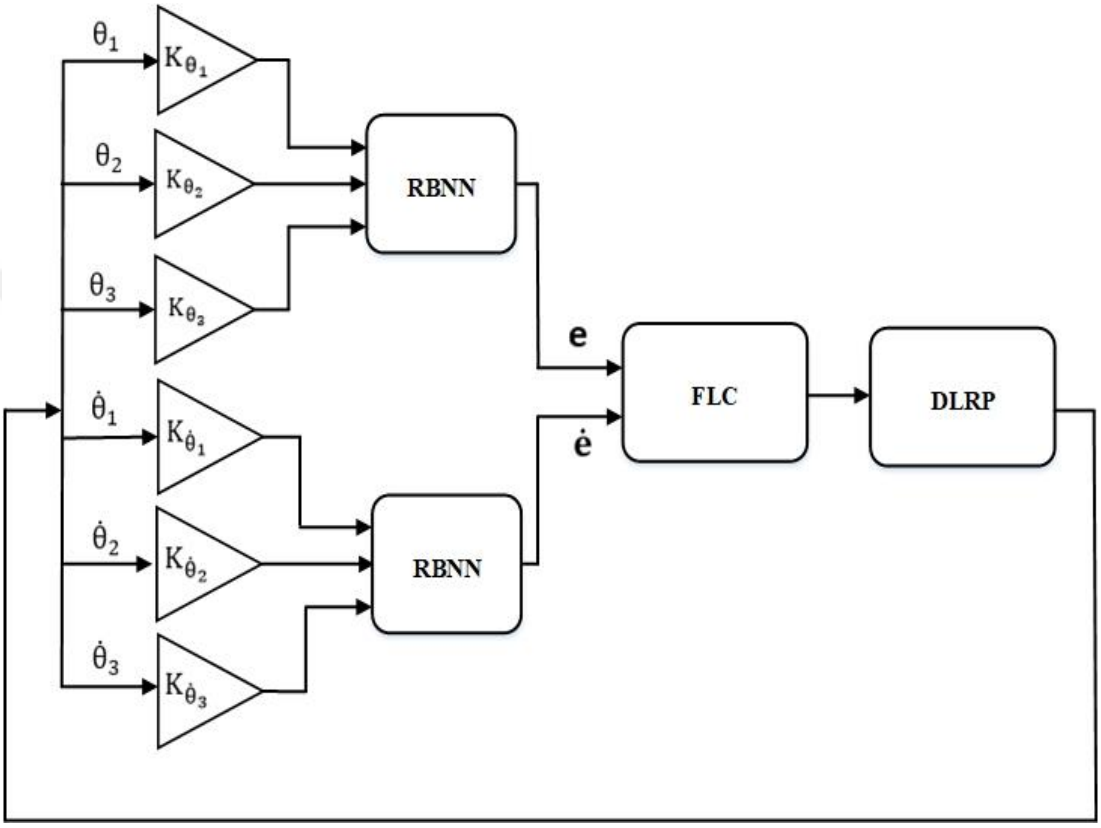

Figure 4.9. Example of a block diagram of the RBNF-LQR controller in a DLRIP

The two output of both RBNNs (e, ė) are used as the input of a Mamdani type fuzzy model explained in 4.2.3.

4.3. Stabilisation Control of the SLRIP

4.3.1. Model linearization of the SLRIP

The nonlinear state-space form of RIPS is as follows:

$$\dot{x} = f(x, u) \tag{4.21}$$

x is the state vector of SLRIP, $x^T = [\theta_1 \quad \theta_2 \quad \dot{\theta_1} \quad \dot{\theta_2}]$. u is the control input $u = \tau$ (τ is the applied input vector), it is a scalar because there is only one actuator that

provides torque input to the system. The expression for the angular acceleration, $\ddot{\theta} = [\ddot{\theta}_1 \ ; \ddot{\theta}_2 \ ]^T$, was obtained by solving for $\ddot{\theta}$ in equation (4.22).

$$\ddot{\theta} = M^{-1}\left[\tau - C\left(\theta, \dot{\theta}\right) - G(\theta)\right] \tag{4.22}$$

Equation (4.21) is of the form $\dot{x} = f(x, u)$. The term $\dot{x}$ is a 2×1 matrix, which contains nonlinear elements. In this forms the first two elements of $\dot{x}$ are just the last two elements of x. To linearize the last two elements about an operating point vector (OP), Taylor's expansion is used: [144]

$$\delta\dot{x}(t) = \left(\frac{\partial f(x, u)}{\partial x}\right)_{x=OP,u=0} \delta x(t) + \left(\frac{\partial f(x, u)}{\partial u}\right)_{x=OP,u=0} \delta u(t) \tag{4.23}$$

x is the state vector, $\dot{x}(t)$ is a small deviation of the states from the operating point. The coefficients of $\delta x(t)$ and $\delta u(t)$, termed A and B, respectively, are evaluated at the operating point. Thus, the linear state-space model of the system is given in the equation system becomes:

$$\begin{cases} \dot{x} = Ax + Bu \\ y = Cx + Du \end{cases} \tag{4.24}$$

A, B, C and D are matrices for the state-space representation. The aim is to design a robust controller for stabilizing the pendulum links in the upright position with minimum deflection. The stable equilibrium point corresponds to a state in each pendulum is downward position ($\theta_1 = 0^\circ$ and $\theta_2 = 180^\circ$). The unstable equilibrium corresponds to the state in each pendulum points vertically upwards which is against gravity ($\theta_1 = \theta_2 = 0^\circ$). Substituting system parameters and constants for respective terms, A, B, C and D state-space matrices of the SLRIP become:

$$A = \begin{bmatrix} 0 & 0 & 1 & 0 \\ 0 & 0 & 0 & 1 \\ 0 & 2.6358 & -0.4215 & -0.0064 \\ 0 & 35.4759 & -0.6253 & 0.0865 \end{bmatrix} B = \begin{bmatrix} 0 \\ 0 \\ 1.0095 \\ 1.7227 \end{bmatrix} \tag{4.25}$$

$$C = \begin{bmatrix} 1 & 0 & 0 & 0 \\ 0 & 1 & 0 & 0 \\ 0 & 0 & 1 & 0 \\ 0 & 0 & 0 & 1 \end{bmatrix} D = [0] \tag{4.26}$$

Bryson's method is used to determine the initial weighting matrices (Q and R). According to the Bryson's Rule, Q and R are diagonal matrices. The diagonal elements are expressed as the reciprocals of the squares of the maximum acceptable values of the state variable (x) and the input control variable (u). The diagonal elements Q_{ii} of matrix Q, can be given as:

$$Q_{ii} = \frac{1}{\text{maximum acceptable value of } x_i^2} \tag{4.28}$$

Where $i = 1,2,..n$. The diagonal elements R_{jj} of matrix R, also can be given as:

$$R_{jj} = \frac{1}{\text{maximum acceptable value of } u_i^2} \tag{4.29}$$

The initial choice of Q and R matrix are:

$$Q = \begin{bmatrix} 1 & 0 & 0 & 0 \\ 0 & 1 & 0 & 0 \\ 0 & 0 & 1 & 0 \\ 0 & 0 & 0 & 1 \end{bmatrix} \text{ and } R = 0.01 \tag{4.30}$$

The characteristic roots of the open-loop system are of the SLRIP are located at 5.9914, -6.0246 and -0.3749. therefore, the open-loop system is unstable, since 1 pole of the SLRIP system lies in the right half of s plane. the LQR gain vector of the SLRIP is obtained as follows:

$$K = [-13.5047 \quad 221.4027 \quad -261.7301 \quad 160.1331] \tag{4.31}$$

In the next parts, PID, LQR, and swing-up based LQR controllers are developed and simulated in the MATLAB/Simulink environment for the stabilization of the SLRIP. The simulation is performed by the sampling time 1ms and 5s simulation time. A numerical method Bogacki-Shampine solver is selected with fixed-step. According to simulation results, a comparative study of all controllers is given. The controllers are tested for robustness under external disturbances. The simulation results can provide a good background and feasibility for a real experimental implementation to the stabilization control problem of the SLRIP.

4.3.2. PID controller of the SLRIP

The turned PID parameters are optimized using PSO algorithm in order to obtain more robust PID gains. The optimized PID controller parameters are given in Table 4.3. To test the performance of the PID controller, an external disturbance is given to the system at t=3s. The SimMechanics model of the SLRIP using PID controller is shown in Figure 4.10. Figure 4.11 shows the responses of the pendulum angle (θ_2), the angle of horizontal link (θ_1) and the control signal (U) of SLRIP with PID controller under external disturbance.

Table 4.3. Optimal PID controller parameters of the SLRIP

Parameters of PID controller of the pendulum link	K_{pp}	K_{ip}	K_{dp}
	4.0698	0.605	0.176
Parameters of PID controller of the horizontal link	K_{pl}	K_{il}	K_{dl}
	−1.25	0.02	3.6

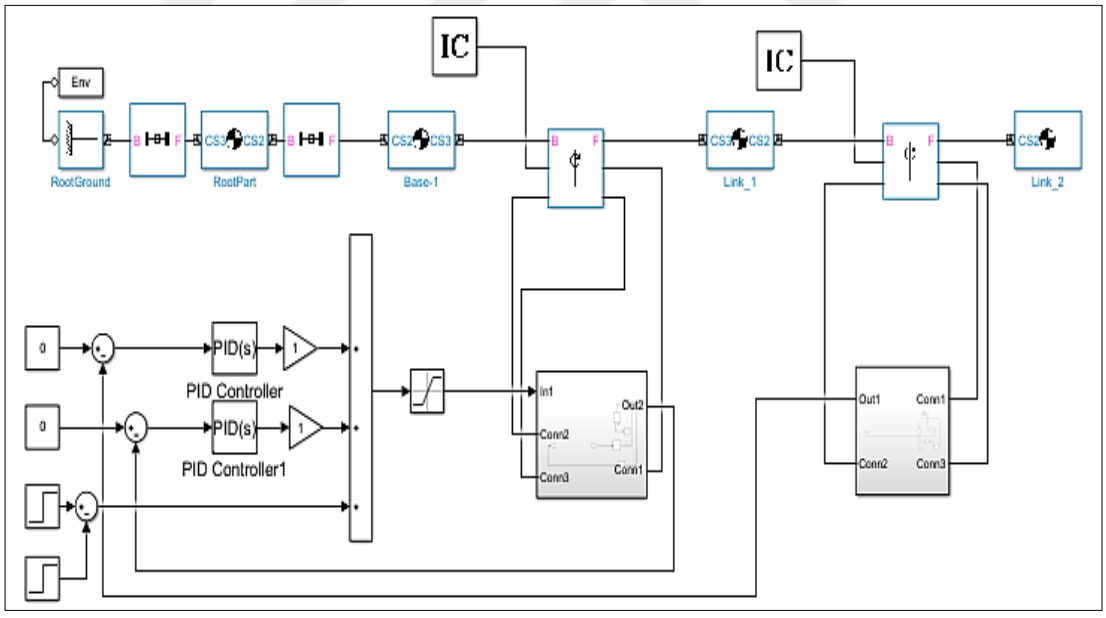

Figure 4.10. SimMechanics model of the SLRIP with PID controller

4.3.3. LQR controller of the SLRIP

The simulation of the LQR controller is performed with a calculated gain matrix (K) given in equation (4.31) and an initial condition vector which is $x^T = [0\ 10\ 0\ 0\ ]°$. The output variables of LQR controllers are stabilized at the reference

points. To test the performance of the LQR controller, an external disturbance is given to the system at t=3s. The SimMechanics model for control of SLRIP using LQR controller method with disturbance input is shown in Figure 4.12. Figure 4.13 show the responses of the pendulum angle (θ_2), the angle of the horizontal link (θ_1) and control force (U) of the SLRIP with LQR controller under external disturbance.

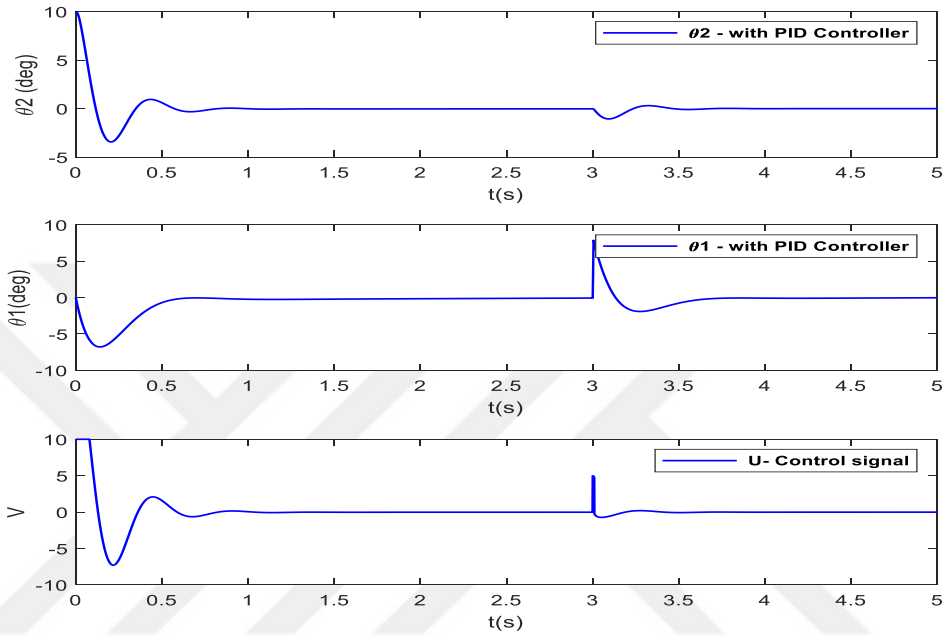

Figure 4.11. Responses of pendulum angle (θ_2), the angle of the horizontal link (θ_1) and control force (U) of the SLRIP with PID controller under external disturbance

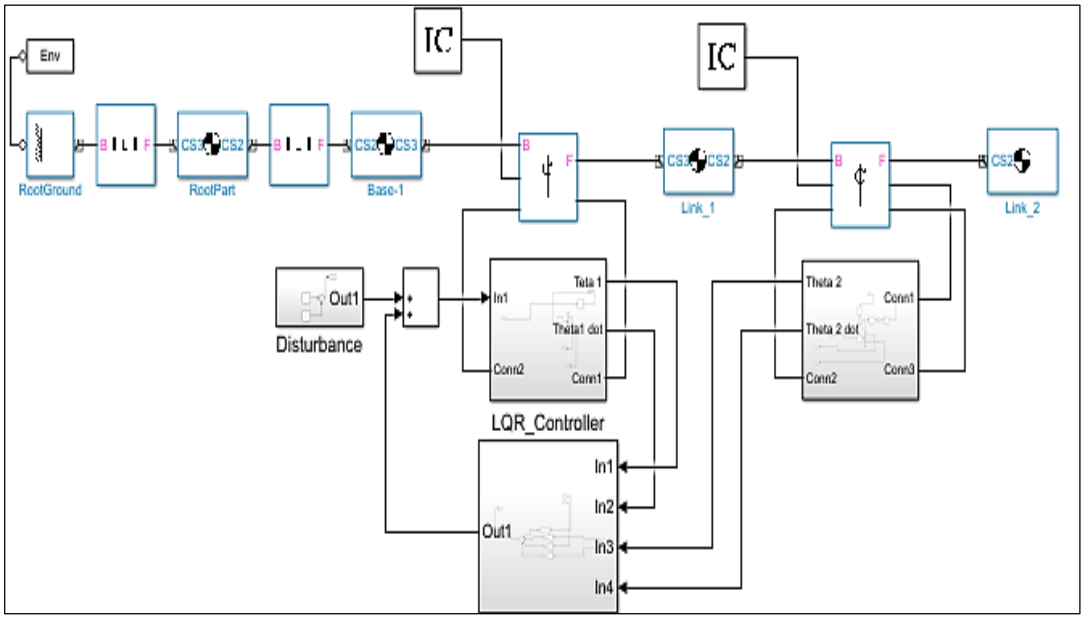

Figure 4.12. SimMechanics model of the SLRIP with LQR controller

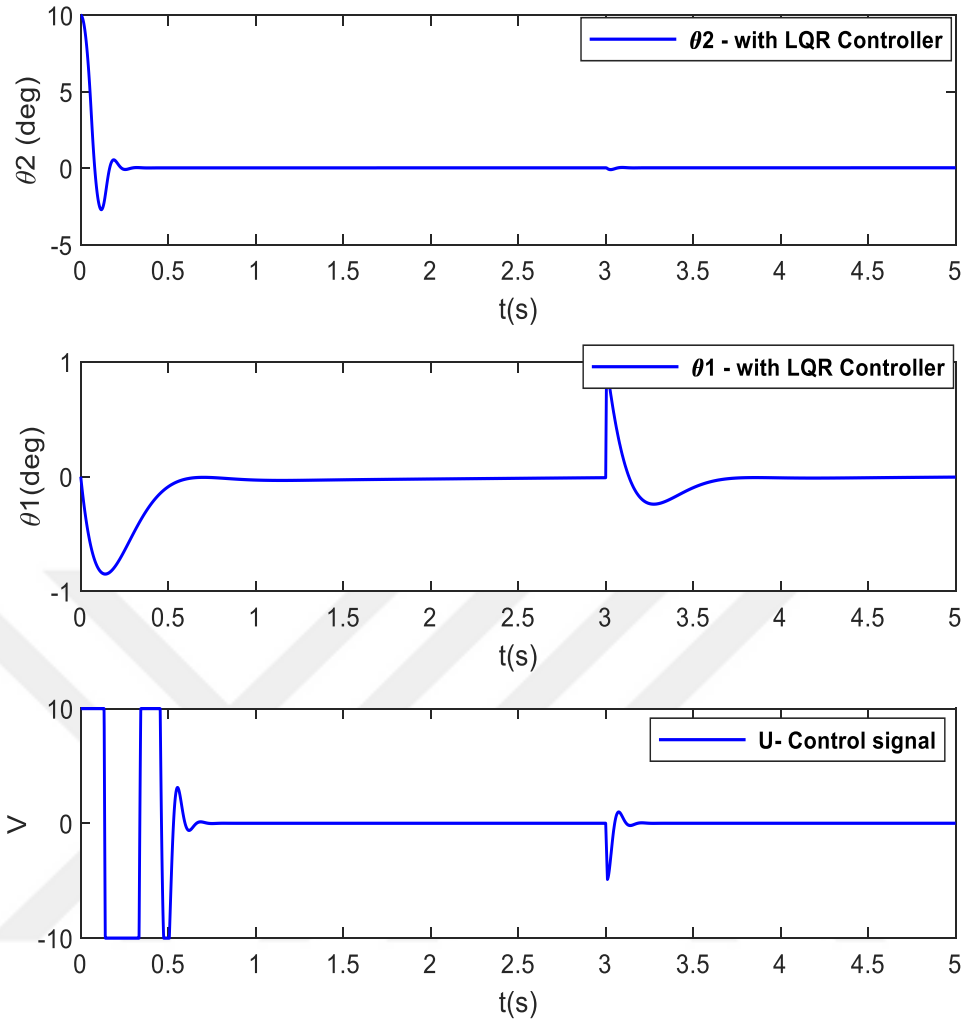

Figure 4.13. Responses of pendulum angle (θ_2), the angle of the horizontal link (θ_1) and control force (U) of the SLRIP with LQR controller under external disturbance

4.3.4. Performance evaluation of PID and LQR controllers

According to the obtained results, the PID is robust, and it has successfully maintained the control of the SLRIP. The LQR controller is developed to give us better T_s, PO, E_{ss} and the RMSEs than the classical PID controllers. The two controllers are under external disturbance. Table 4.4 shows the comparison of PID and LQR controllers in terms of T_s, PO, E_{ss} and the RMSEs under external disturbance. Furthermore, the performance of the two controllers' effort is determined by the RMSEs between the control signal and zero voltage. The calculated RMSEs are given in Table 4.5. According to the obtained signals results, the system controlled with LQR needs more effort to control the system.

Table 4.4. Quantitative comparison of the performance of the PID and LQR controllers under external disturbance

Controllers under external disturbance	Parameters	Joints	
		First Link (θ_1)	Second Link (θ_2)
PID	T_s (s)	1.3009	0.7289
	PO %	1.51	47
	E_{ss} (°)	0.2	0.035
	RMSE (°)	0.0229	0.0159
LQR	T_s (s)	1.2007	0.5295
	PO %	0.8	23
	E_{ss} (°)	0.0365	0.03
	RMSE (°)	0.0057	0.0210

Table 4.5. RMSEs of the control signals of the PID and LQR controllers

Controllers under external disturbances	RMSE (°)
LQR	0.0447
PID	0.0255

According to the calculated T_s, PO, E_{ss} and position RMSEs, the LQR controller produces more accurate results than the PID controller. In order to see the performance of the LQR compared with PID; The improvement percentages of T_s, PO, E_{ss} and position RMSEs were computed, and they are given in Table 4.6 Considering the T_s, PO, E_{ss} and position RMSEs in all joints, the percentage obtained by the LQR controller yields better results.

Table 4.6. Comparison of the performance parameters in terms of percentage between LQR and PID under external disturbance

Controllers under external disturbance	Parameters	Joints	
		First Link (θ_1)	Second Link (θ_2)
LQR versus PID	T_s	7.702 %	27.39 %
	PO	47.01 %	51.06 %
	E_{ss}	81.75 %	14.28 %
	RMSE	75,28 %	24.28 %

According to the calculated improvement percentages in Table 4.6, the LQR returned more accurately than the PID controller under external disturbance for all joints. The T_s improvement percentages are 7.702% for the first link and 27.39% for the second link. The PO improvement percentages are 47.01% for the first link and 51.06% for the second link. The E_{ss} improvement percentages are 81.75% for the first link and 14.28% for the second link. The RMSEs improvement percentages are 75,28% for the first link and 24.28% for the second link. Moreover, according to the incremental calculated percentages of RMSEs of the control signals in Table 4.5, the LQR returned more effort than PID with 42.95 % under external disturbance.

4.3.5. Swing-up control based on LQR

One of the most effective approaches existing in the literature is to swing-up the pendulum to make it controlled at the stability point. This method is based on energy considerations. The goal is to bring the total mechanical energy of the pendulum to zero, which corresponds to the upright position. The basic energy-based control law is given in equation (4.32).

$$U_{sw} = u_m \left|\theta_2^{\,3}\right| \operatorname{sng}\left(\cos\theta_2 \dot{\theta}_2\right) \tag{4.32}$$

Where θ_2 , $\dot{\theta_2}$ are angle and velocity of the pendulum link, respectively. u_m is the swing coefficients. The following swing-up/stabilizing control strategy is proposed for the torque model. For the control objective, the freely hanging pendulum had to be brought into the upright equilibrium, and the arm needed to be stabilized at the origin (θ_2 must be stable at 180°). The initial conditions of θ_1 ,θ_2 are zero degrees. Once the pendulum link was approaching the upright position, the control is switched to balancing the LQR controller. The SimMechanics model to control the SLRIP using the swing-up controller-based LQR is shown in Figure 4.14. Figure 4.15 show the responses of the pendulum angle θ_2, horizontal link θ_1 and the torque input signal of SLRIP with swing-up controller-based LQR. An external disturbance is given to the system at 7s to see the performance controller. As can be seen from Figure 4.15, the swing up controller-based LQR is robust and can control the system.

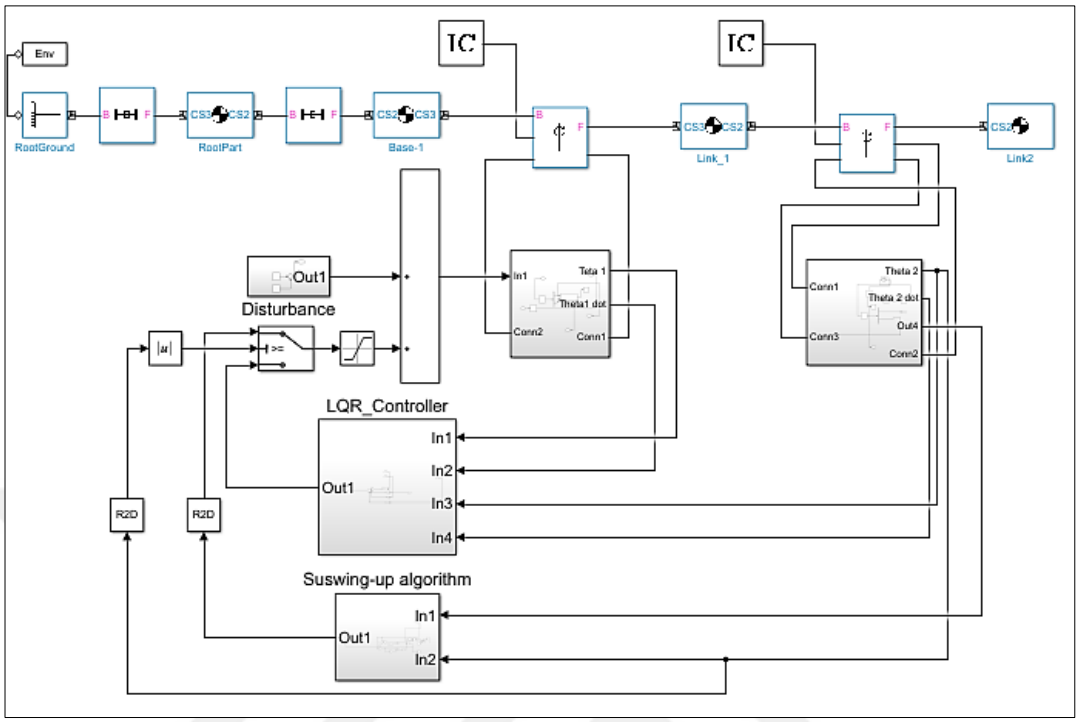

Figure 4.14. SimMechanics model of the SLRIP using the swing-up based LQR controller

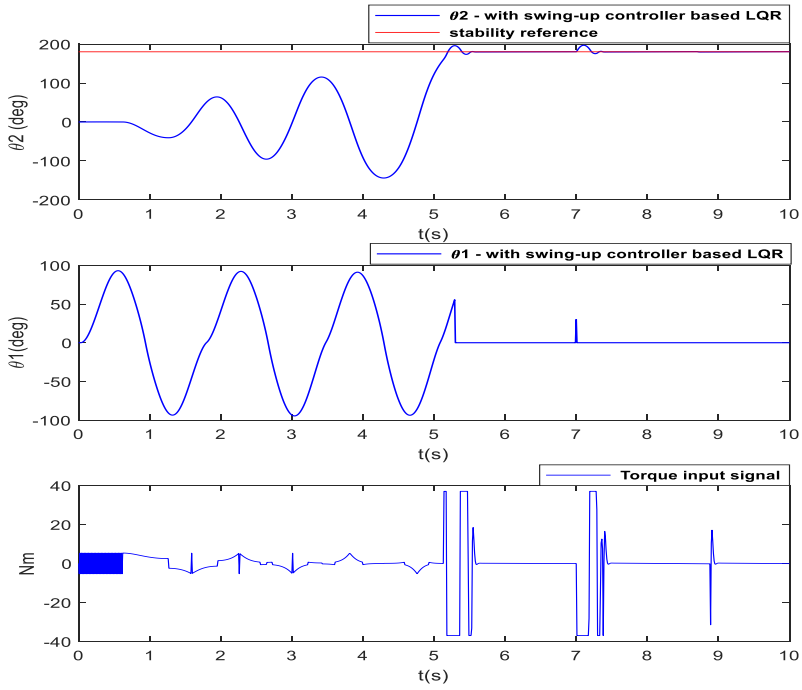

Figure 4.15. Responses of the angle of pendulum (θ_2), the angle of the horizontal link (θ_1) and the torque input signal of the SLRIP with swing-up controller-based LQR under external disturbance

4.4. Anti-swing Control of the SLRIP

PID and LQR controllers are developed for the anti-swing control of the SLRIP. Two controllers are modelled and simulated in the MATLAB/SimMechanics Simulink environment. The initial conditions of the links are taken with $\theta_1 = 0\ °$ and $\theta_2 = 60°$. The optimized PID controller parameters for the anti-swing controller are given in Table 4.7.

Table 4.7. Optimal PID controller parameters for the anti-swing controller of the SLRIP

Parameters of PID controller of the pendulum link	K_{pp}	K_{ip}	K_{dp}
	2.01	0.369	0.05
Parameters of PID controller of the horizontal link	K_{pl}	K_{il}	K_{dl}
	−0.75	0.0047	1.007

The anti-swing LQR controller is performed with K= [-0.2586 46.3074 1.136 -1.9724]. All output variables of the SLRIP system must be stabilized at the reference zero position by the both PID and LQR anti-swing controllers. As can be seen from Figure 4.16, the link arm and the pendulum link were stabilized at the reference position with minimum vibrations.

4.4.1. Performance evaluation of the anti-swing PID and LQR controllers

Moreover, Figure 4.16 presents a comparison between the angle signals (θ_1 and θ_2) with PID and LQR anti-swing controllers of the SLRIP. According to the obtained results, the PID has successfully maintained the control of the SLRIP with minimum vibrations.

The LQR controller is developed to give better T_s, MP, E_{ss} and the RMSEs than the PID controller. Table 4.8 shown the comparison of PID and LQR controllers in terms of T_s, MP, E_{ss} and RMSEs. According to the calculated T_s, MP, E_{ss} and position RMSEs, the LQR produces more perfect results than the PID. To understand the LQR performance compared with PID; The improvement percentages of all parameters were calculated for each case and given in Table 4.9.

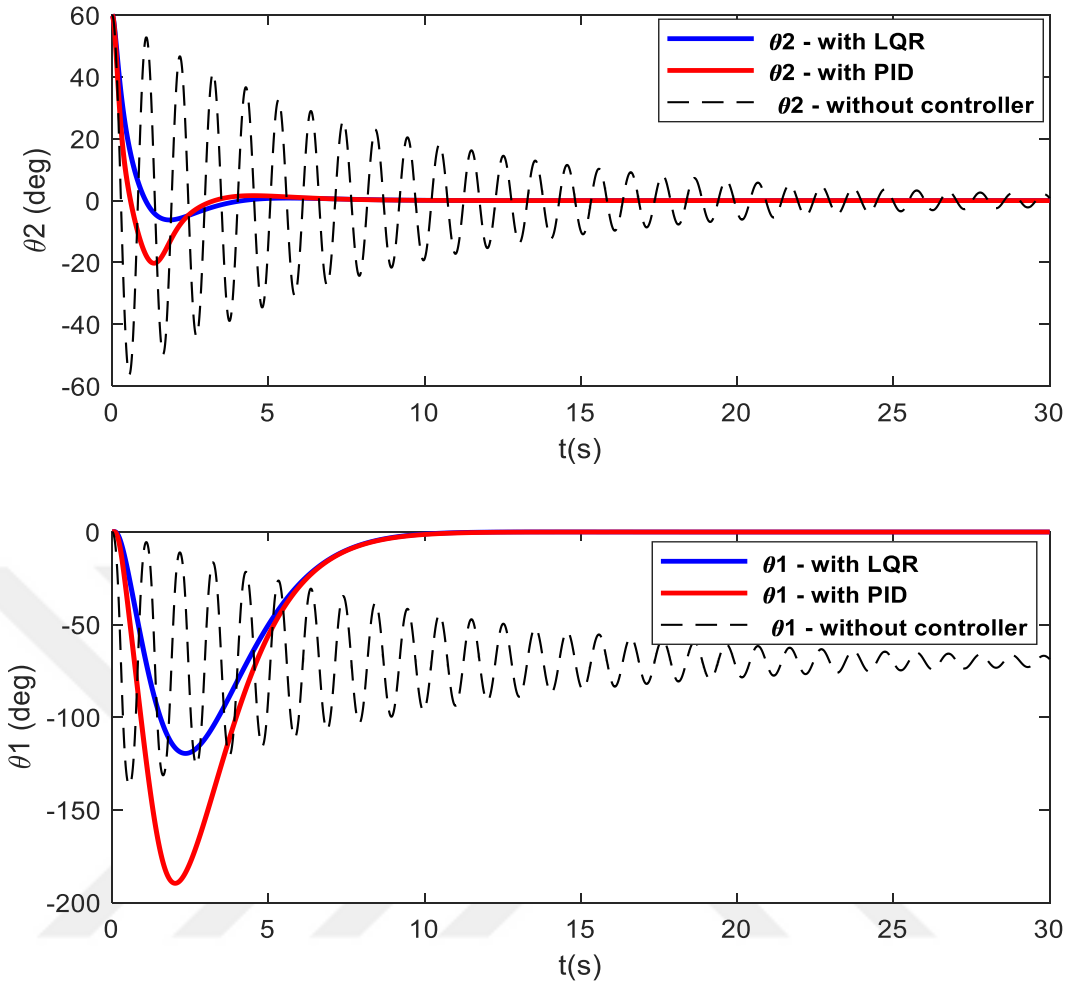

Figure 4.16. Angle signals (θ_1 and θ_2) with PID and LQR anti-swing controllers for the SLRIP

Table 4.8. Quantitative comparison of the performance of PID and LQR anti-swing controllers

Anti-swing controllers	Parameters	Joints	
		First Link (θ_1)	Second Link (θ_2)
PID	T_s (s)	9.1903	5.6238
	MP (°)	195	20
	E_{ss} (°)	0.0978	0.01
	RMSE (°)	0.9756	0.1067
LQR	T_s (s)	8.7535	3.5475
	MP (°)	128	5
	E_{ss} (°)	0.0865	0.0029
	RMSE (°)	0.6651	0.1002

Table 4.9. Quantitative comparison of the performance parameters in terms of percentage between PID-LQR anti-swing controllers

Anti-swing controllers	Parameters	Joints	
		First Link (θ_1)	Second Link (θ_2)
LQR versus PID	T_s	4.75 %	36.91%
	MP	34,35 %	75 %
	E_{ss}	12.36 %	71 %
	RMSE	31.82 %	6.091 %

According to the calculated improvement percentages in Table 4.9, the LQR returned more accurately than PID for all joints.

The T_s improvement percentages are 4.75% for the first link and 36.91 % for the second link. The MP improvement percentages are 34.36 % for the first link and 75 % for the second link. The E_{ss} improvement percentages are 12.36 % for the first link, and 71% for the second link. The RMSEs improvement percentages are 31.82% for the first link and 6.091% for the second link.

The developed anti-swing controllers are tested for robustness under external disturbances. The pendulum angles (θ_2) and the link angle (θ_1) are stabilized at zero positions. Figure 4.17 shows the angle signals (θ_1 and θ_2) with PID and LQR anti-swing controllers for the SLRIP under external disturbance in zero position at T=1s.

Both anti-swing controllers are robust, and it has successfully maintained the control of the SLRIP under external disturbance. Table 4.10 shows the comparison of PID and LQR controllers in terms of Ts, MP, Ess and the RMSEs under external disturbance.

According to the calculated parameters, the LQR yields perfect results than the PID under external disturbance. To see the performance of the PID compared with LQR; The improvement percentages of all parameters were calculated and given in Table 4.11.

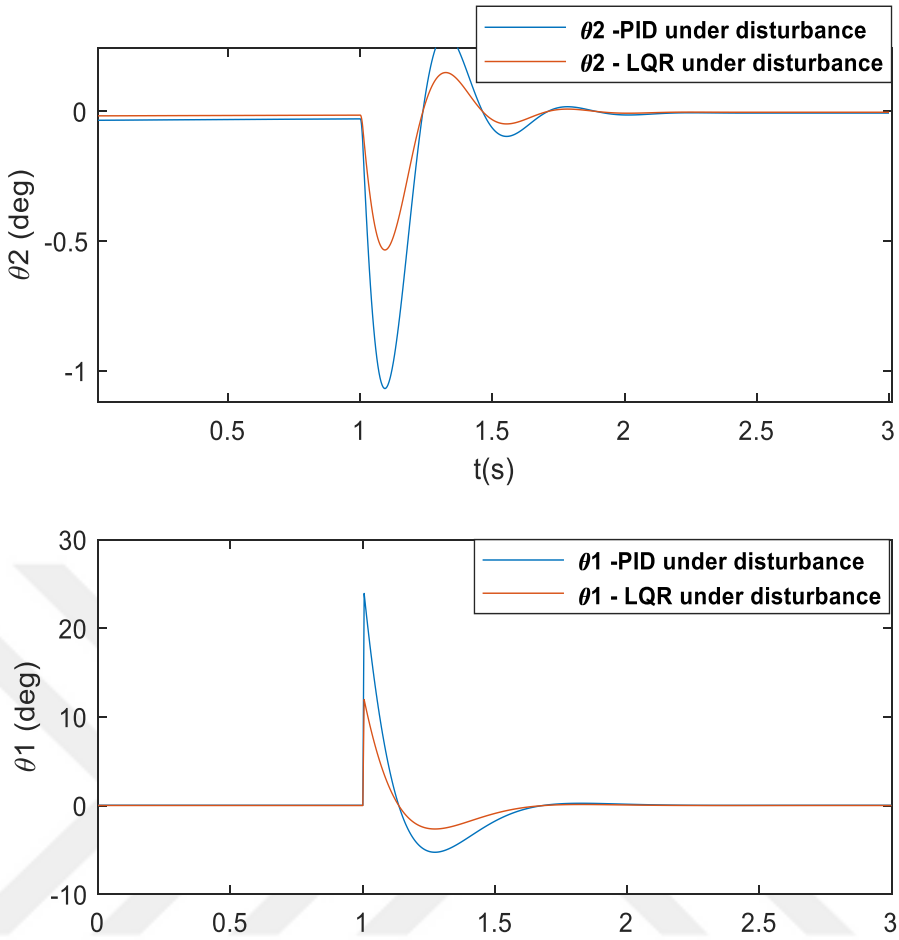

Figure 4.17. Comparison between the angle signals (θ_1 and θ_2) under external disturbance with PID and LQR anti-swing controllers to the SLRIP

Table 4.10. Quantitative comparison of the performance of the PID and LQR anti-swing controllers under external disturbance

Anti-swing controllers under external disturbance	Parameters	Joints	
		First Link (θ_1)	Second Link (θ_2)
PID	T_s (s)	0.5	0.81
	MP (°)	22	1
	E_{ss} (°)	0.043	0.0065
	RMSE (°)	0.0535	0.0039
LQR	T_s (s)	0.3	0.59
	MP (°)	10	0.6
	E_{ss} (°)	0.022	0.0041
	RMSE (°)	0.0267	0.0019

Table 4.11. Quantitative comparison of the performance parameters in terms of percentage between PID-LQR anti-swing controllers

Anti-swing controllers under external disturbance	Parameters	Joints	
		First Link (θ_1)	Second Link (θ_2)
LQR versus PID	T_s	40%	27.16%
	MP	54.54 %	40%
	E_{ss}	48.83%	36.92%
	RMSE	50.09%	51.28%

According to the calculated improvement percentages in Table 4.11, the LQR returned more accurately than PID for all joints. The T_s improvement percentages are 40% for the first link and 27.16% for the second link. The PO improvement percentages are 29.8% for the first link and 7.66% for the second link. The E_{ss} improvement percentages are 48.83 % for the first link, and 36.92% for the second link. The RMSEs improvement percentages are 50.09% for the first link and 51.28% for the second link.

4.5. Stabilisation Control of the DLRIP

4.5.1. Model linearization of the DLRIP

The linear state-space model of the system is given in equation (4.24). x is the state vector of the DLRIP, $x^T = [\theta_1 \quad \theta_2 \quad \theta_3 \quad \dot{\theta_1} \quad \dot{\theta_2} \quad \dot{\theta_3}]$. u is the control input $u = \tau_1$ (τ_1 is torque input of the first link). A, B, C and D are matrices for the state-space representation. The aim is to design a robust controller for stabilizing the pendulum links in the upright position with minimum deflection. The stable equilibrium point corresponds to a state in each pendulum is downward position ($\theta_1 = 0°$ and θ_2=θ_3 = 180°). The unstable equilibrium corresponds to the state in each pendulum points vertically upwards which is against gravity ($\theta_1 = \theta_2$ =θ_3 = 0°). Substituting system parameters and constants for respective terms, A, B, C and D state-space matrices of the DLRIP become:

$$A = \begin{bmatrix} 0 & 0 & 0 & 1 & 0 & 0 \\ 0 & 0 & 0 & 0 & 1 & 0 \\ 0 & 0 & 0 & 0 & 0 & 1 \\ 0 & 2.5966 & -0.0729 & -0.0279 & -0.0093 & 0.0136 \\ 0 & 43.3634 & -18.9777 & -0.0476 & -0.2172 & 1.3321 \\ 0 & -63.3307 & 318.9279 & 0.0695 & 1.3321 & -20.0673 \end{bmatrix} \quad (4.33)$$

$$B = \begin{bmatrix} 0 \\ 0 \\ 0 \\ 1.0095 \\ 1.7227 \\ -2.5160 \end{bmatrix} \quad C = \begin{bmatrix} 1 & 0 & 0 & 0 & 0 & 0 \\ 0 & 1 & 0 & 0 & 0 & 0 \\ 0 & 0 & 1 & 0 & 0 & 0 \\ 0 & 0 & 0 & 1 & 0 & 0 \\ 0 & 0 & 0 & 0 & 1 & 0 \\ 0 & 0 & 0 & 0 & 0 & 1 \end{bmatrix} \quad D = [0 \quad 0 \quad 0 \quad 0 \quad 0 \quad 0]^T \quad (4.34)$$

The initial choice of the Q and R matrices are given in equation (4.35):

$$Q = \begin{bmatrix} 1 & 0 & 0 & 0 & 0 & 0 \\ 0 & 1 & 0 & 0 & 0 & 0 \\ 0 & 0 & 1 & 0 & 0 & 0 \\ 0 & 0 & 0 & 1 & 0 & 0 \\ 0 & 0 & 0 & 0 & 1 & 0 \\ 0 & 0 & 0 & 0 & 0 & 1 \end{bmatrix} \text{ and } R = 0.01 \quad (4.35)$$

The characteristic roots of the open-loop system of the DLRIP are located at -30.6879, -6.3174, 10.5355, 6.1825, -0.0250. The open-loop system is unstable since two poles of the DLRIP system lie in the right half of s plan.

The LQR gain vector of the DLRIP is obtained as follows:

$$K = [0.12 \quad -3.24 \quad -37.68 \quad 0.4314 \quad -12.545 \quad -10.99] \quad (4.36)$$

4.5.2. Robustness analyze of the DLRIP

In the next part, LQR, FLQR, LQG and FLQG are modelled and simulated in the MATLAB/Simulink environment for the stabilization control problem of the DLRIP. The simulation is performed by 1ms sampling time and 25s simulation time. A numerical method Bogacki-Shampine solver is selected with fixed-step. According to simulation results, a comparative study of all controllers is given. The controllers are tested for robustness under internal, external disturbances and noise. The simulation results can provide a good background and feasibility for a real experimental implementation to the stabilization control problem of the DLRIP. The SimMechanics model of the DLRIP with the controller is shown in Figure 4.18.

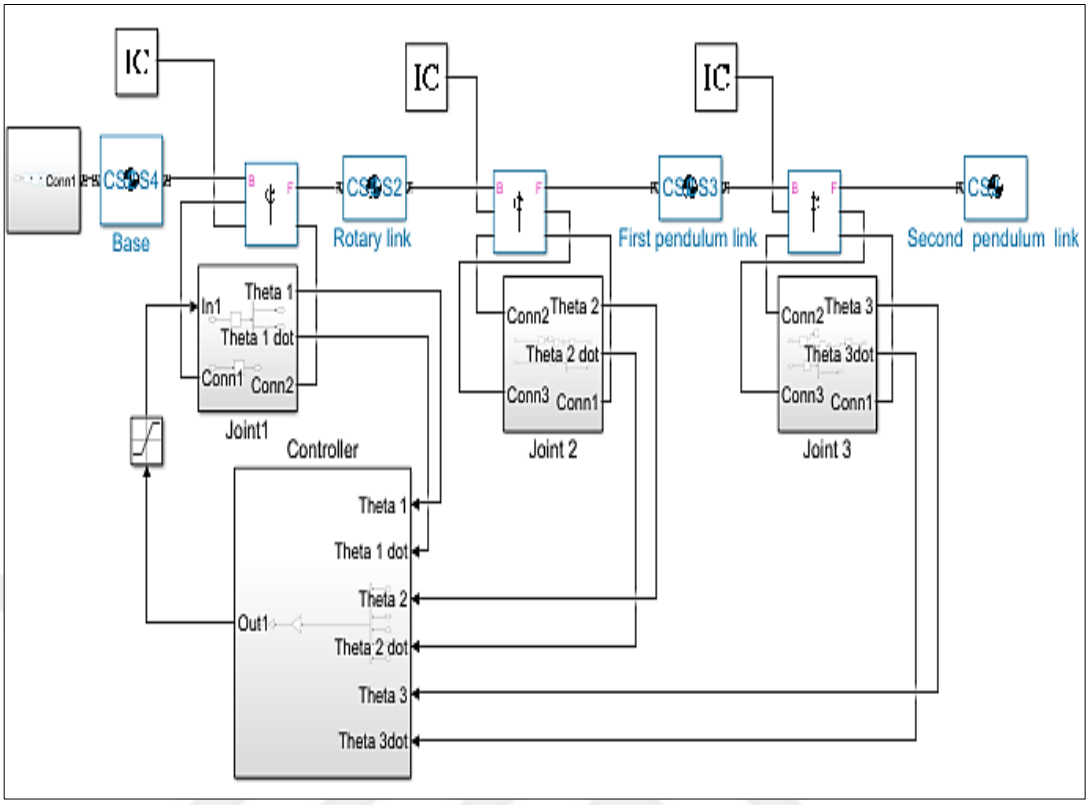

Figure 4.18. SimMechanics model of the DLRIP with the controller

a) External disturbance

The simulation of LQR and FLQR controllers is performed with the calculated gain matrix K given in equation (4.36) and an initial condition vector which is $x^T = [0\ 0 - 0.05\ 0\ 0\ 0]$. As can be seen from Figure 4.19, the output variables of two controllers are stabilized at the reference points, the two pendulum angles (θ_2 and θ_3) are stabilized. Similarly, the horizontal arm stabilized at a reference trajectory $\pm 100°$ each 6.24s. Figure 4.19 shows the angle signals (θ_1, θ_2 and θ_3) with LQR and FLQR controllers for the DLRIP system.

According to the obtained results using the LQR controller, the LQR is robust, and it has successfully maintained the control of the DLRIP. An FLQR controller is developed to give us better T_s, PO, E_{ss} and the RMSEs than the classical LQR controllers. The two controllers are robust under external disturbance. Table 4.12 shows the comparison of LQR and FLQR controllers in terms of T_s, PO, E_{ss} and the RMSEs under external disturbance.

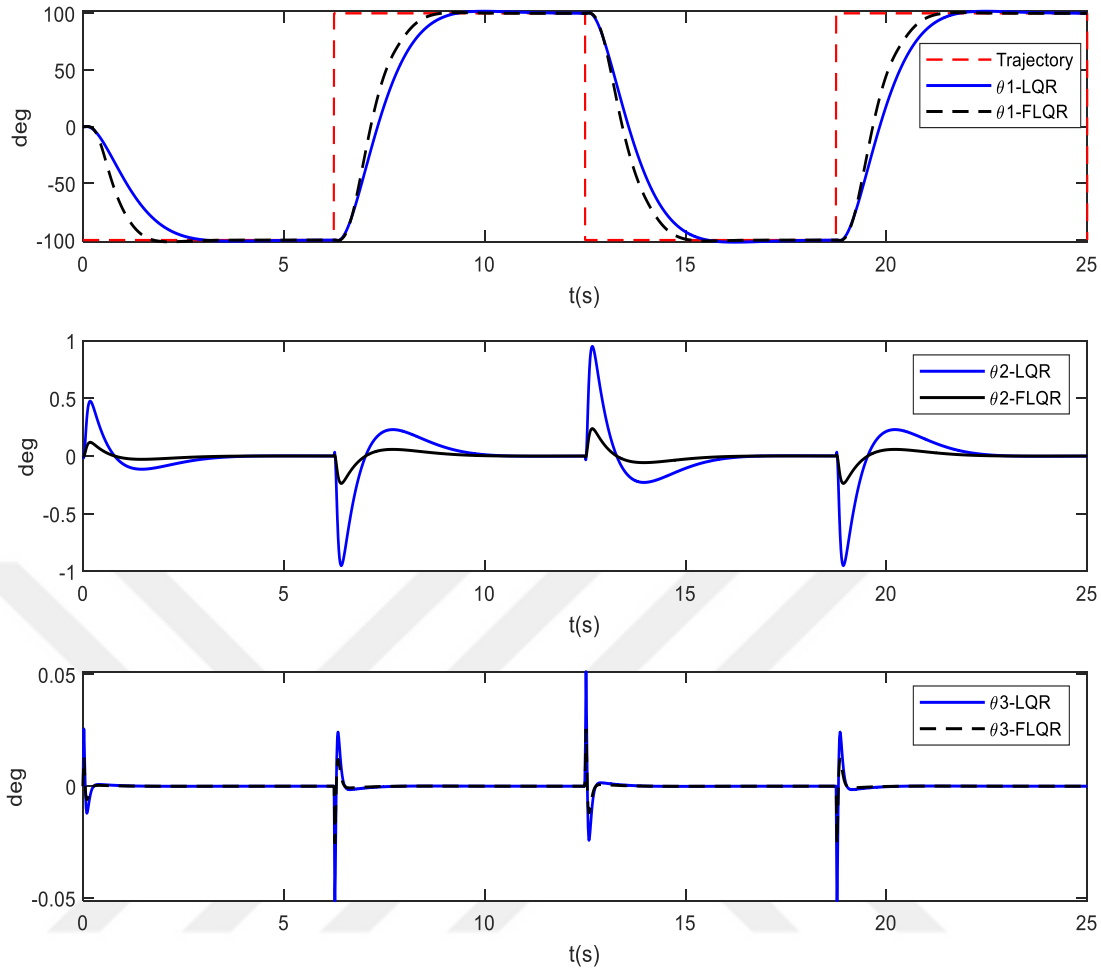

Figure 4.19. The angle signals (θ_1, $\theta_2$and θ_3) with LQR and FLQR controllers

Table 4.12. Quantitative comparison of the performance of LQR and FLQR controllers under external disturbance

Controllers under external disturbance	Parameters	Joints		
		First Link (θ_1)	Second Link (θ_2)	Third link (θ_3)
LQR	T_s (s)	3.154 s	3.9 s	1.55 s
	PO %	1.51%	47 %	52.4%
	E_{ss} (°)	0.1	0.005	0.00005
	RMSE (°)	0.2077	6.2047e-04	1.1698e-05
FLQR	T_s (s)	2.375 s	3.43 s	1.37 s
	PO %	0.8%	23 %	37.5 %
	E_{ss} (°)	0.01	0.001	0.00002
	RMSE (°)	0.1938	1.5512e-04	2.9244e-06

b) Internal disturbance

The robustness of two controllers LQR and FLQR is tested under external disturbance. To test the controllers' response under internal disturbance, the mass of the third link is varied from [10-20%] to the initial mass of the third link in time of 10s. Also, the two controllers are robust under the internal disturbance. The variation of mass of the third link is given in Table 4.13. Figure 4.20. shows an example of the response of LQR and FLQR controllers under internal disturbance. Table 4.14 shows the comparison of LQR and FLQR controllers in terms of T_s, PO, E_{ss} and the RMSEs under internal disturbance.

Table 4.13. Variation of the mass of the third link

Variation of the mass of the third link	Values
Initial mass	0.0832 [kg]
Initial mass + 10% of the third link	0.09152[kg]
Initial mass + 15% of the third link	0.09568[kg]
Initial mass + 20% of the third link	0.09984 [kg]

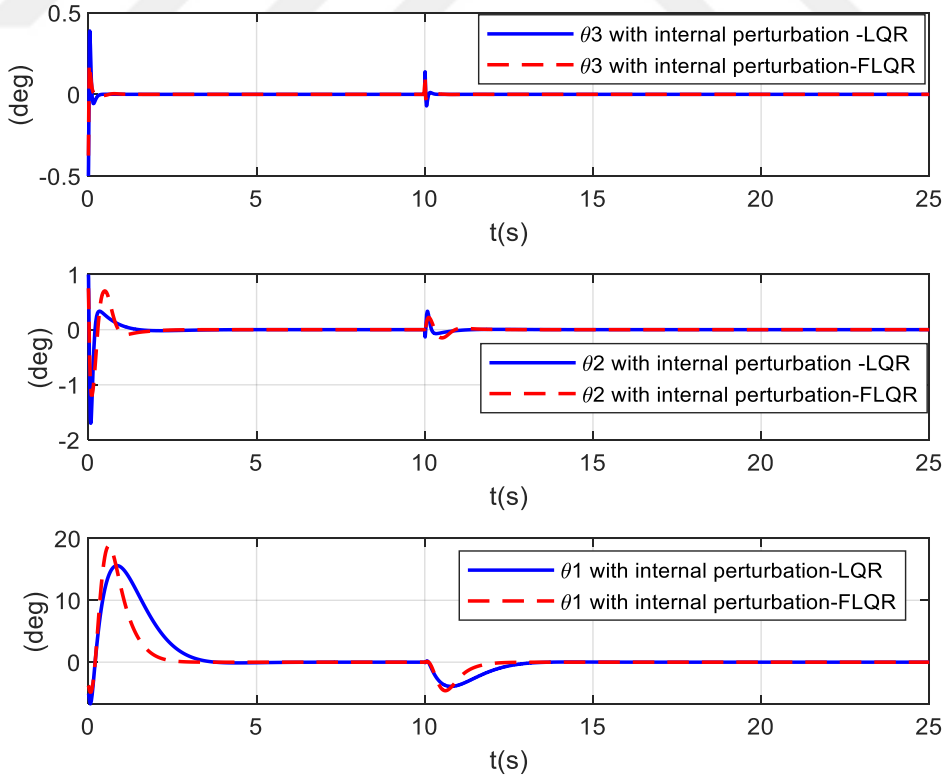

Figure 4.20. Example of the response of LQR and FLQR controller under internal disturbance with a variation of mass of the third link in T=10s (Initial mass + 15% of the third link)

Table 4.14. Quantitative Comparison of Performance of LQR and FLQR controllers under internal disturbance

Controllers under internal disturbance	Parameters	Joints		
		First Link (θ_1)	Second Link (θ_2)	Third link (θ_3)
LQR	T_s (s)	3.657	4.31	1.3
	PO %	47.82	35	37,94
	E_{ss} (°)	0.008	0.0025	0.00216
	RMSE (°)	0.0107	3.3523e-04	5.8010e-05
FLQR	T_s (s)	2.441	2.46	1
	PO %	46.9	28	18,78
	E_{ss} (°)	0.0001	0.000019	0.00006
	RMSE (°)	0.0080	2.4495e-04	2.0152e-05

The performance of the two controllers' effort is determined by the RMSEs between the control signal and zero voltage. The calculated RMSEs are given in Table 4.15. According to the obtained signals results, the system controlled with FLQR needs more effort to control the system. Figure 4.21 show the control signals of LQR and FLQR controllers under internal and external disturbances.

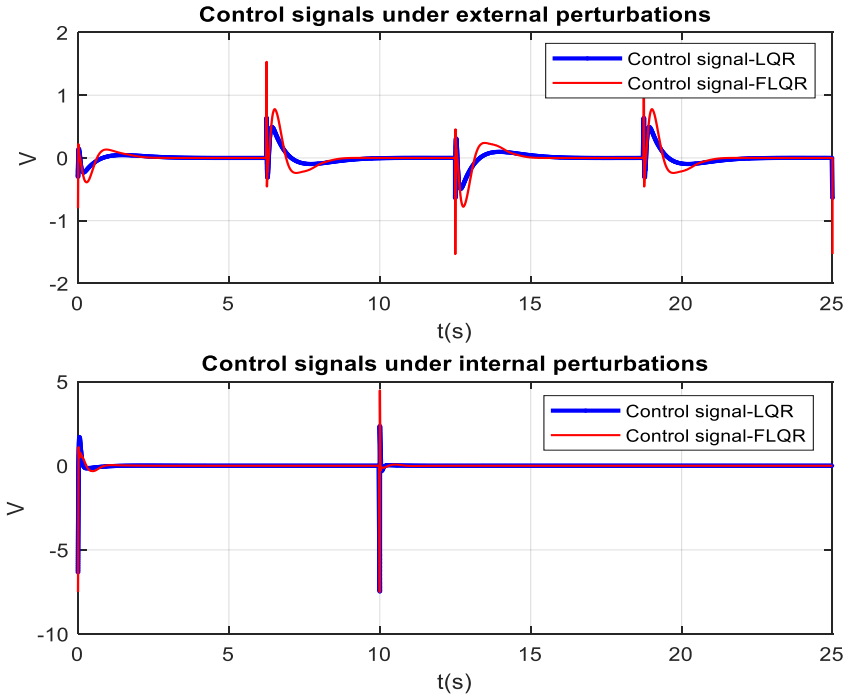

Figure 4.21. The control signals of LQR and FLQR controllers under internal and external disturbances

Table 4.15. RMSEs of the control signals for the controllers

Disturbances	Controller	RMSE
External disturbance	LQR	3.1030e-04
	FLQR	5.1703e-04
Internal disturbance	LQR	4.4932e-04
	FLQR	6.0451e-04

c) Noise and external disturbance

The simulation results obtained by LQR and FLQR controllers are obtained in the case without noise; it is not always the same case for a real experimental system. In the other hand, in a real experimental implementation, the system can be affected by noise. However, all situations cannot be measurable. White noise with different SNR is added to the system in the simulation to approach to a real experimental system. The level of added noise to the system is a critical point in the design of the controller. The LQR and FLQR controllers' performance is tested by adding white noise to the DLRIP. In the LQG and FLQG controllers, the KF has succeeded to estimate the states in the noise cases applied to the system. The reference trajectory signal ($\pm 100°$ each $6.24s$) shown in Figures 4.22 and 4.23 is applied to a horizontal arm when the pendulums are stabilized in the equilibrium point.

The initial condition vector is $x^T = [0 \; -0.05 \; 0 \; 0 \; 0 \; 0]$. The LQG and FLQG controllers are capable of eliminating noise, and the system remains stable for the determined time. The most important difference point between the LQR, FLQR controllers and LQG, FLQG controllers results is the effect of noise. LQR and FLQR controllers don't contain any algorithm to ignore the noise combined to the DLRIP. As can be seen from Figures 4.22 and 4.23, the added noise reflect the outputs of the system, which is eliminated by the LQG and FLQG controllers, respectively. Table 4.16 shows a comparison of LQG and FLQG controllers under noise and external disturbance in terms of T_s, PO, E_{ss} and RMSEs.

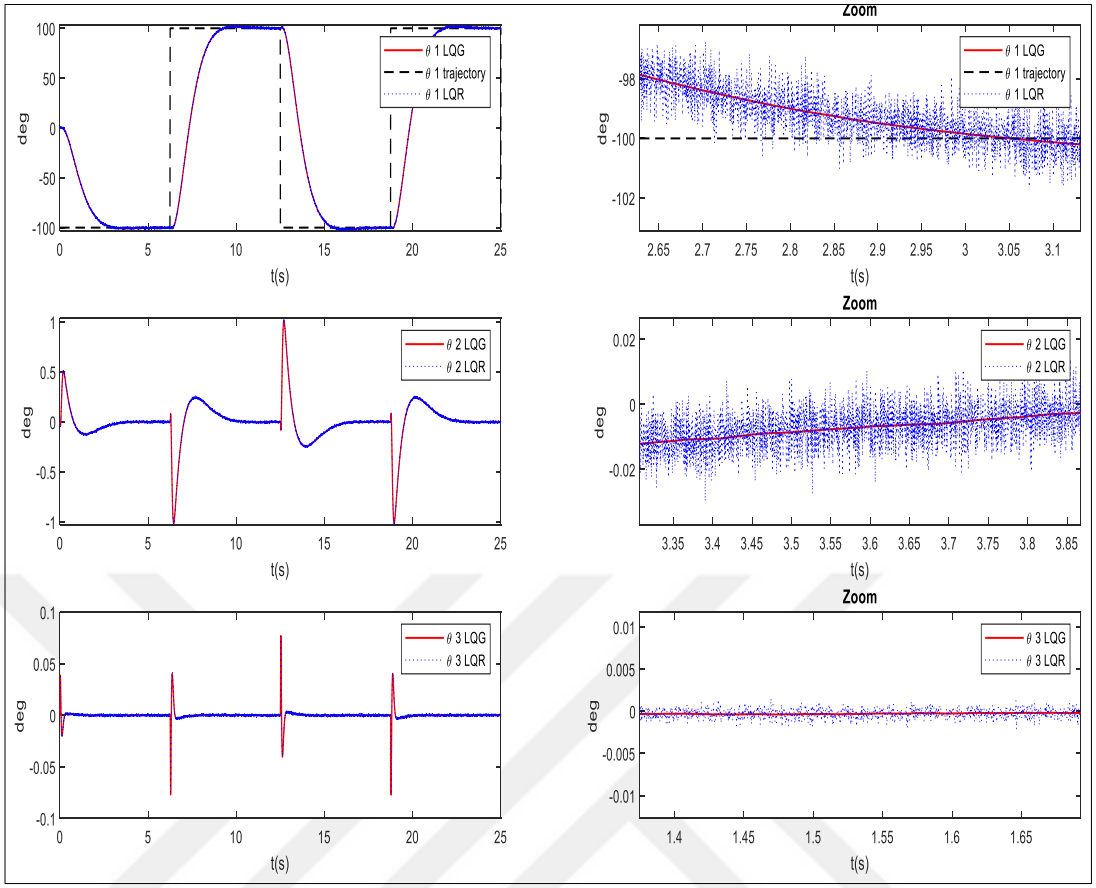

Figure 4.22. The angle signals (θ_1 , θ_2 and θ_3) with noised LQR and LQG controllers

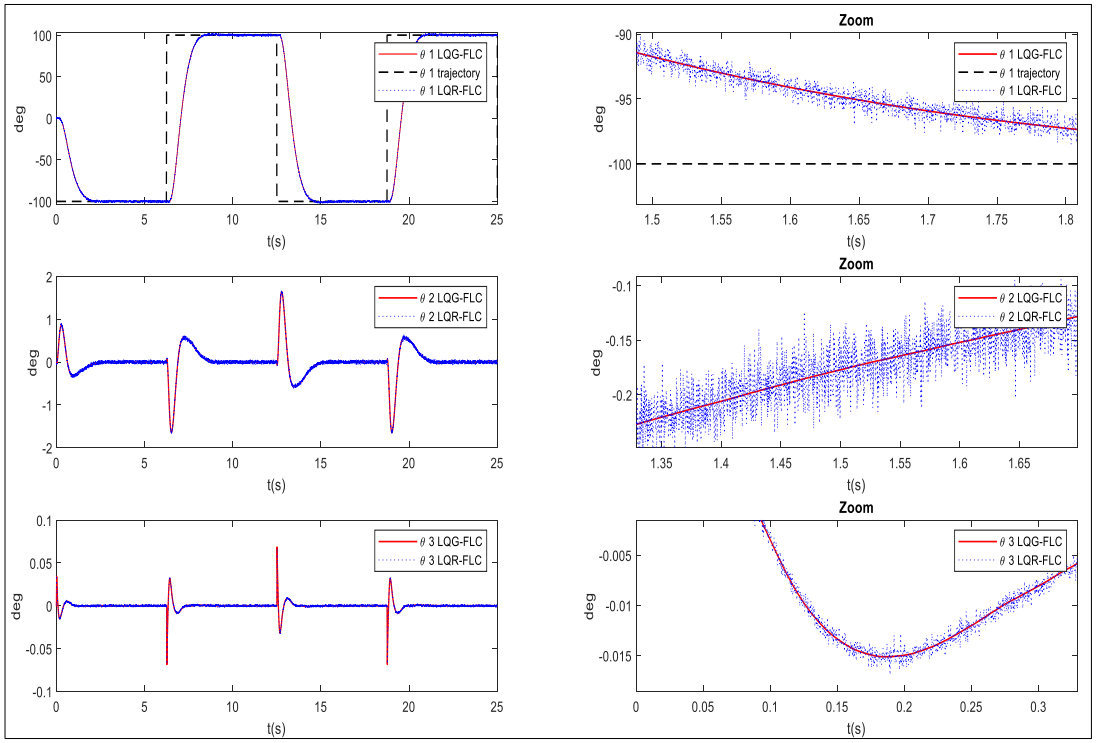

Figure 4.23. The angle signals (θ_1 , θ_2 and θ_3) with noised FLQR and FLQG controllers

Table 4.16. Quantitative Comparison of Performance of LQG and FLQG controllers under noise and external disturbance

Controllers under noise and external disturbance	Parameters	Joints		
		First Link (θ_1)	Second Link (θ_2)	Third link (θ_3)
LQG	T_s(s)	3.26	3.01	2.15
	PO %	1.57	48	3.8
	E_{ss} (°)	0.2	0.008	0.001
	RMSE (°)	0.1891	6.7008e-04	6.0974e-05
FLQG	T_s(s)	2.23	2.3	1.25
	PO %	0.76	46	3
	E_{ss} (°)	0.001	0.003	0.0002
	RMSE (°)	0.1614	4.3504e-04	1.5244e-05

d) Noise and internal disturbance

In part (c), the robustness of the two controllers LQG and FLQG is tested under noise and external disturbance. To test the controllers' response under noise and external disturbance, also the mass of the third link is varied from [10-20%] to the initial mass of the third link in time of 10s. The two controllers are robust under the internal disturbance. The variation of mass of the third link is given in Table 4.13. Figure 4.24 shows an example of the response of LQG and FLQG controllers under internal disturbance. Table 4.17 shows the comparison of LQG and FLQG controllers in terms of T_s, PO, E_{ss} and RMSEs under internal disturbance.

Table 4.17. Quantitative Comparison of Performance of LQG and FLQG controllers under noise and internal disturbance.

Controllers under noise and internal disturbance	Parameters	Joints		
		First Link (θ_1)	Second Link (θ_2)	Third link (θ_3)
LQG	T_s(s)	3.48	2.81	1.1
	PO %	68.1	45.6	27.5
	E_{ss} (°)	0.07	0.05	0.003

Table 4.17.(Cont.) Quantitative Comparison of Performance of LQG and FLQG controllers under noise and internal disturbance.

	RMSE (°)	0.0085	2.6818e-04	4.6408e-05
FLQG	T_s(s)	2.2	2.14	0.95
	PO %	45.2	41.1	21.8
	E_{ss} (°)	0.001	0.0010	0.00009
	RMSE (°)	0.0043	1.7146e-04	3.4258e-05

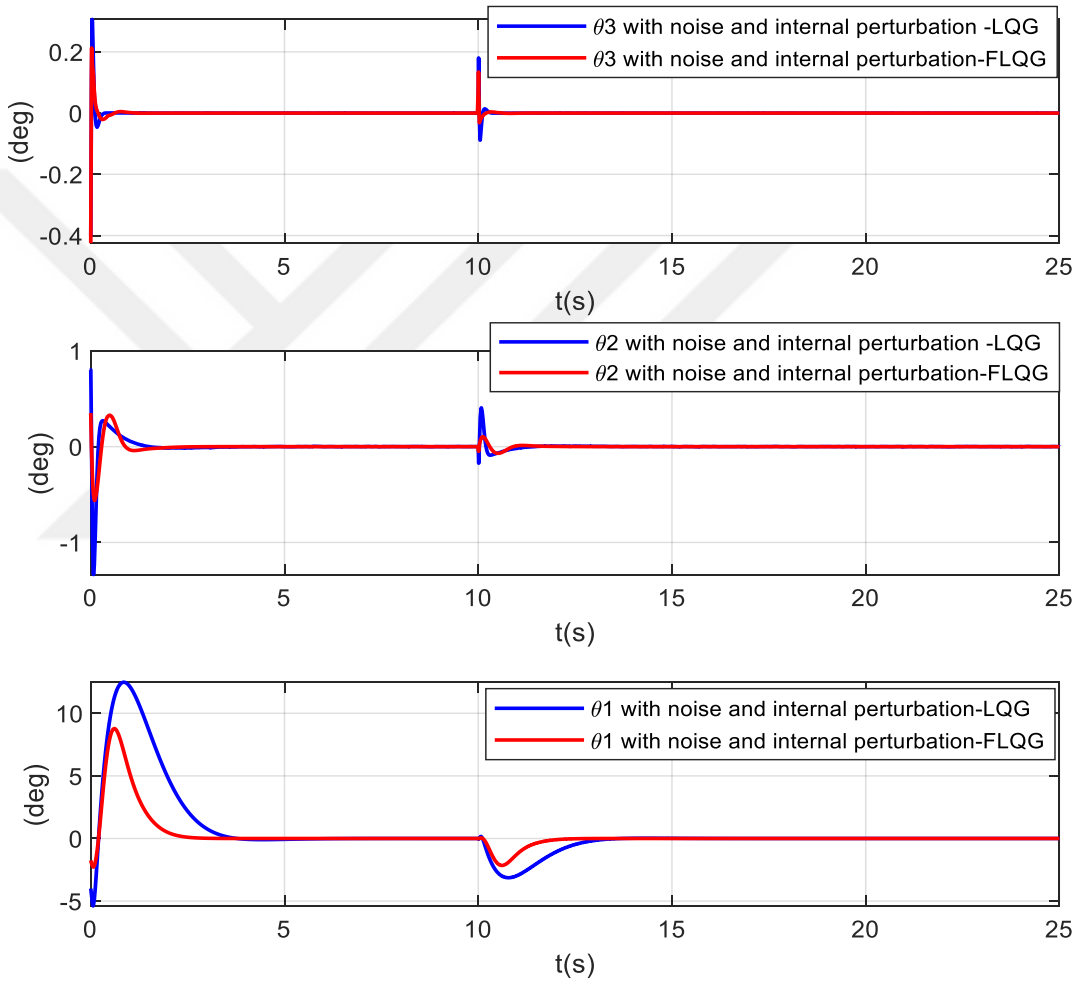

Figure 4.24. Example of the response of LQG and FLQG controller under internal disturbance with a variation of mass of the third link in T=10s (Initial mass + 15% of the Third link)

Figure 4.25. shows the control signals of LQG and FLQG controllers under noise, internal and external disturbances. The performance of the two controllers' effort is determined by the RMSEs between the control signal and zero voltage. The calculated RMSEs are given in Table 4.18. According to the obtained signals results, the system controlled with FLQG needs more effort to control the system.

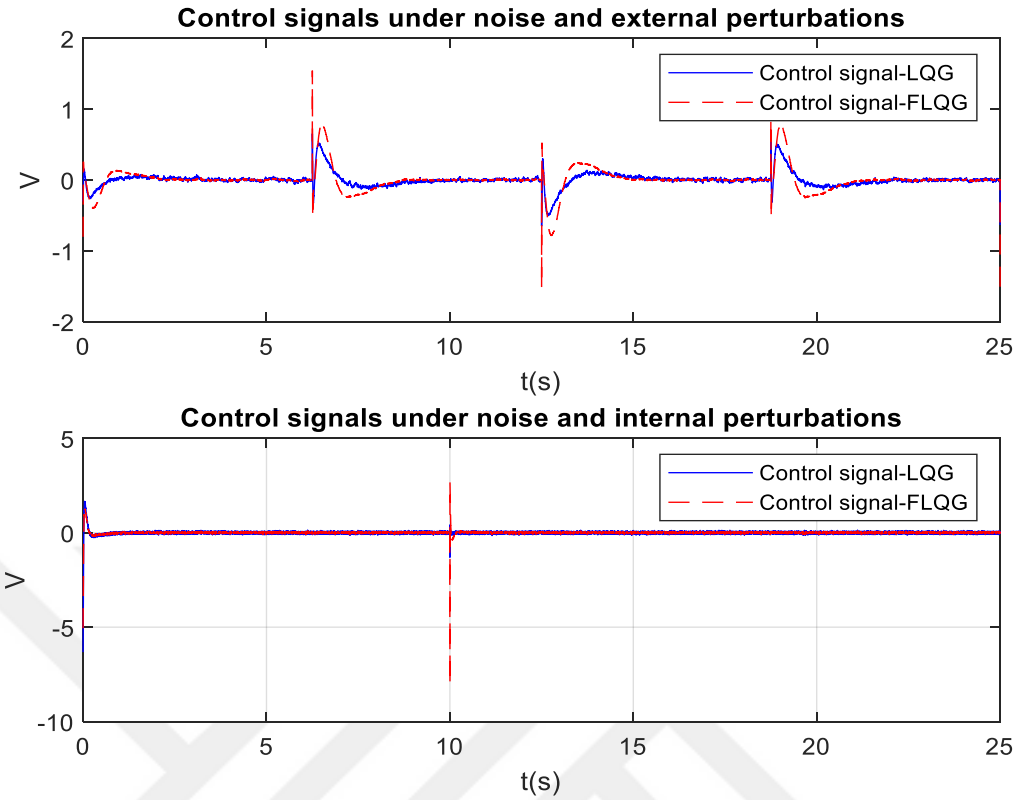

Figure 4.25. The control signals of LQG and FLQG controllers under noise, internal and external disturbances

Table 4.18. RMSEs of the control signals for the controllers

Disturbances	Controller	RMSE
Noise and external disturbance	LQG	3.1331e-04
	FLQG	5.1696e-04
Noise and internal disturbance	LQG	3.9782e-04
	FLQG	5.4488e-04

e) LQG and FLQG controllers under different variances of SNR white noise

To test the LQG and FLQG algorithms in the presence of white noise, the DLRIP system is tested for three different variances of SNR of white noise. The LQR and FLQR algorithm takes into account the presence of the noise. The LQG and FLQG controllers show very good noise rejection feature. Even in the presence of very high noise, the LQG and FLQG can trace the desired response. Figure 4.26 shows an example of LQR and LQG responses with different variances of SNR of white noise: (a) SNR =0.001dB, (b) SNR =0.01dB and(c) SNR =0.1dB.

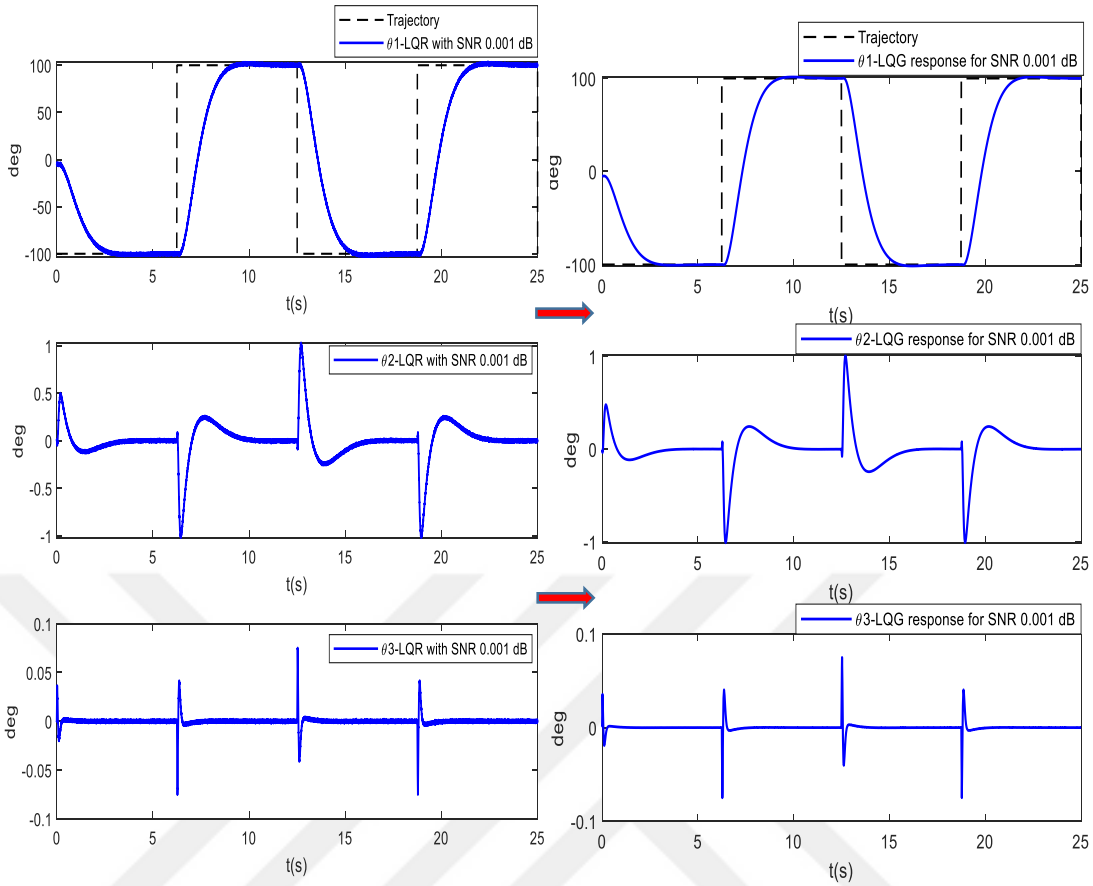

(a)

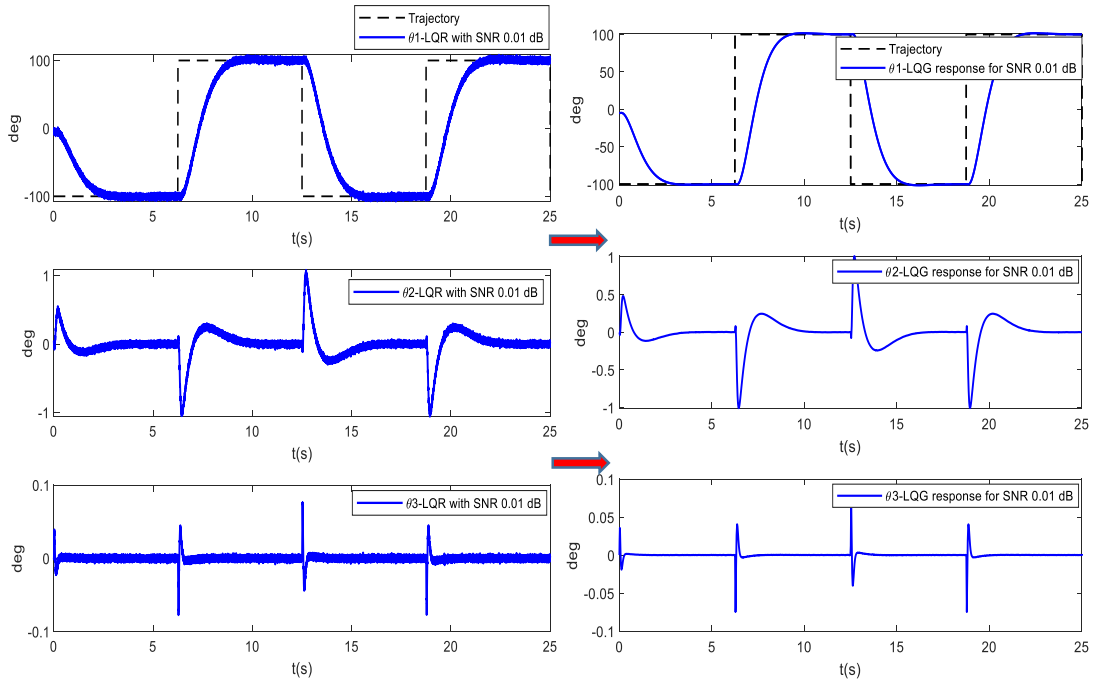

(b)

Figure 4.26. Examples of LQR and LQG responses: (a) witch SNR =0.001dB, (b) witch SNR =0.1dB and (c) witch SNR =0.1dB

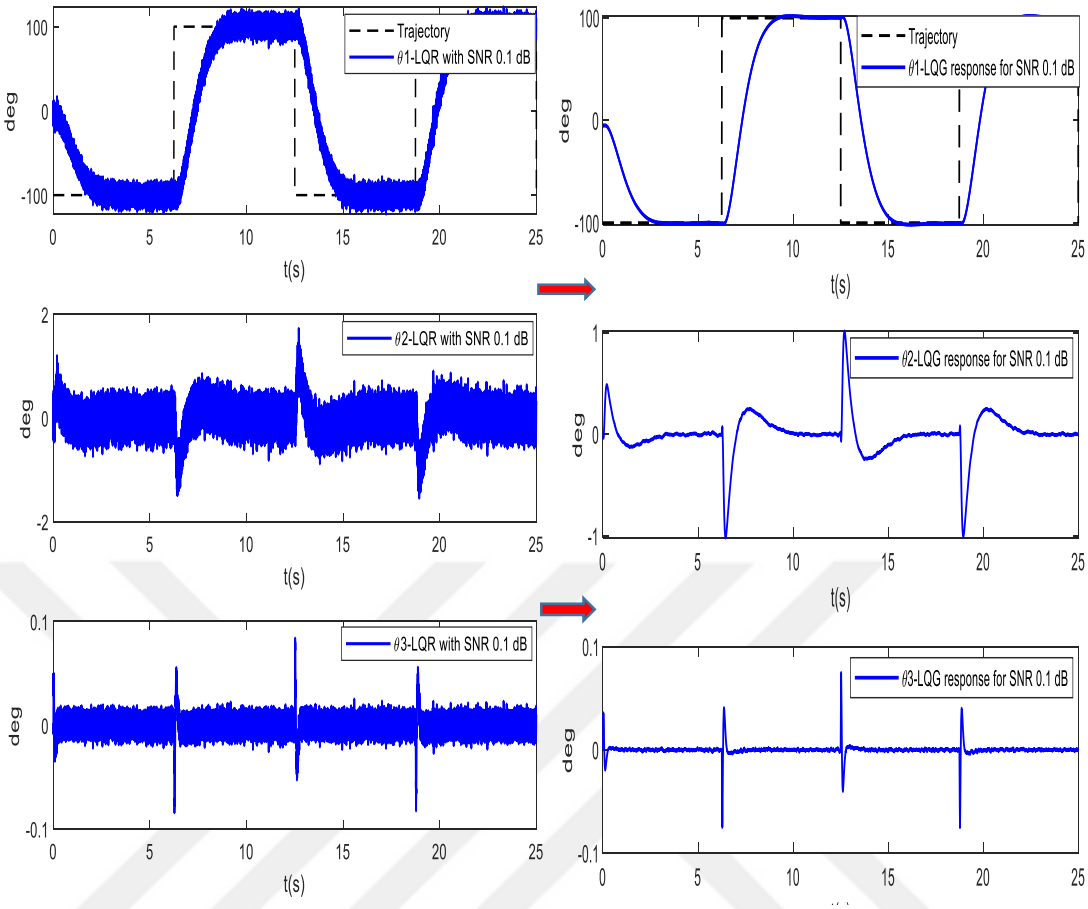

(c)

Figure 4.26.(Cont.) Examples of LQR and LQG responses: (a) witch SNR =0.001dB, (b) witch SNR =0.1dB and (c) witch SNR =0.1dB

4.5.3. Performance evaluation of controllers of the DLRIP

T_s, PO, E_{ss} and the position RMSEs of the joints of both groups of controllers (LQR-FLQR and LQG-FLQG) under external and internal disturbances are given in Tables 4.12, 4.14, 4.16 and 4.17. According to the calculated T_s, PO, E_{ss} and position RMSEs, the nonlinear controllers (FLQR and FLQG) produce more accurate results than the linear controllers (LQR and LQG). In order to see the performance of the FLQR and FLQG compared with LQR and LQG respectively; The improvement percentages of T_s, PO, E_{ss} and position RMSEs were computed for each disturbance cases, and they are given in Tables 4.19, 4.20, 4.21 and 4.22. Considering the T_s, PO, E_{ss} and position RMSEs in all joints, the percentage obtained by the FLQR and FLQG controllers yields better results.

Table 4.19. Comparison of the performance parameters in terms of percentage between LQR-FLQR under external disturbance

Controllers	Parameters	Joint		
		First Link (θ_1)	Second Link (θ_2)	Third link (θ_3)
LQR- FLQR under external disturbance	T_s	24.69 %	12.05 %	11.61%
	PO	47.01 %	51.06 %	28.43 %
	E_{ss}	90 %	80 %	60 %
	RMSE	6.69 %	74.99 %	75 %

According to the calculated improvement percentages in Table 4.19, the FLQR returned more accurately than LQR under external disturbance for all joints. The T_s improvement percentages are 24.69% for the first link, 12.05% for the second link and 11.61% for the third link. The PO improvement percentages are 47.01% for the first link, 51.06% for the second link and 28.43% for the third link. The E_{ss} improvement percentages are 90% for the first link, 80% for the second link and 60% for the third link. The RMSEs improvement percentages are 6.69% for the first link, 74.99% for the second link and 75% for the third link.

Table 4.20. Comparison of the performance parameters in terms of percentage between LQR-FLQR under internal disturbance

Controllers	Parameters	Joint		
		First Link (θ_1)	Second Link (θ_2)	Third link (θ_3)
LQR-FLQR under internal disturbance	T_s	33.25 %	42.92 %	23.07 %
	PO	1.92 %	20 %	50.50 %
	E_{ss}	98.75%	99.24%	97.22%
	RMSE	25.23 %	26.93 %	65.26%

According to the calculated rate of improvement percentages in Table 4.20, the FLQR returned more accurately than LQR under internal disturbance for all joints. The T_s improvement percentages are 33.25% for the first link, 42.92% for the second link and 23.07% for the third link. The PO improvement percentages are 1.92% for the first link, 20% for the second link and 50.50% for the third link. The E_{ss} improvement percentages are 98.75% for the first link, 99.24% for the second link and 97.22% for the third link. The RMSE improvement percentages are 25.23% for the first link,

26.93% for the second link and 65.26% for the third link.

Table 4.21. Comparison of the performance parameters in terms of percentage between LQG-FLQG under noise and external disturbance

Controllers	Parameters	Joint		
		First Link (θ_1)	Second Link (θ_2)	Third link (θ_3)
LQG-FLQG under noise and external disturbance	T_s	31.59 %	23.58 %	41.86 %
	PO	51.59 %	4.16 %	21.05 %
	E_{ss}	99.5 %	62.5%	80%
	RMSE	14.64 %	35.07 %	74.99 %

According to the calculated rate of improvement percentages in Table 4.21, the FLQG returned more accurately than LQG under external disturbance for all joints. The T_s improvement percentages are 31.59% for the first link, 23.58% for the second link and 41.86% for the third link. The PO improvement percentages are 51.59% for the first link, 4.16% for the second link and 21.06% for the third link. The E_{ss} improvement percentages are 99.5% for the first link, 62.5% for the second link and 80% for the third link. The RMSE improvement percentages are 14.64% for the first link, 35.07% for the second link and 74.99% for the third link.

Table 4.22. Comparison of the performance of parameters in terms of percentage between LQG-FLQG under noise and internal disturbance

Controllers	Parameters	Joint		
		First Link (θ_1)	Second Link (θ_2)	Third link (θ_3)
LQG-FLQG under noise and internal disturbance	T_s	36.78%	23.84%	13.63%
	PO	33.62%	9.86%	20.72%
	E_{ss}	98.57%	98%	97%
	RMSE	49.41%	36.06%	26.18%

According to the calculated rate of improvement percentages in Table 4.22, the FLQG returned more accurately than LQG under noise and internal disturbance for all joints. The T_s improvement percentages are 36.78% for the first link, 23.84% for the second link and 13.63% for the third link. The PO improvement percentages are 33.62% for the first link, 9.86% for the second link and 20.72% for the third link. The E_{ss} improvement percentages are 98.57% for the first link, 98% for the second link and

97% for the third link. The RMSE improvement percentages are 49.41% for the first link, 36.06% for the second link and 26.18% for the third link. Moreover, the RMSEs of the control signals for the controllers (LQR-FLQR and LQG-FLQG) under external and internal disturbances are given in Tables 4.15 and 4.18. According to the calculated RMSEs of the control signals, the controllers (FLQR and FLQG) produce more effort than the (LQR and LQG) to control the DLRIP. The incremental percentages of RMSEs of the control signals are computed for each disturbance cases, and they are given in Table 4.23.

Table 4.23. Comparison of the controllers based on Incremental percentages of RMSE control signal

Controllers	Rate
FLQR versus LQR	34.53% - 66.62%
FLQG versus LQG	36.96% - 64.99%

According to the incremental calculated percentages of RMSEs of the control signals in Table 4.23, the FLQR returned more effort than LQR with 34.53 % under internal disturbance and with 66.62% under external disturbance. The FLQG returned more effort than LQG with 36.96 % under noise and internal disturbance; Also, with 64.99 % under noise and external disturbance.

In this section, both FLQR and FLQG controllers were developed for the stability control of the DLRIP and they were compared with LQR and LQG controllers, respectively. The developed controllers were tested under internal and external disturbances to determine the robustness performance of the controllers. According to the obtained simulation results the nonlinear FLQR and FLQG controllers are robust and produce better results than the LQR and LQG controllers in terms of T_s, PO, E_{ss} and RMSEs. RMSEs improvement percentages between FLQR and LQR range from 6.69% to 75% and 25.23% to 65.26% under external and internal disturbances, respectively. Similarly, RMSEs improvement percentages between FLQG and LQG range from 14.64% to 74.99 % and 25.23 % to 49.41 % under external and internal disturbances, respectively. Moreover, the LQG and FLQG controllers in the DLRIP were tested in the presence of white noise with different SNRs. The LQG and FLQG controllers show very good noise rejection feature. The increment percentages of

RMSEs of the control signals for the FLQR and FLQG compared with LQR and LQG is from 34.53% to 66.62%. Accordingly, the FLQR and FLQG controllers need more control efforts than the classical LQR and LQG. The design compromise between controller performance and efforts should be made based on which one is more important than others. Generally, the performance of the controller is a more crucial aspect of control applications.

4.6. Anti-swing Control of The DLRIP

4.6.1. Anti-swing ANFIS-LQR controller of the DLRIP

The design aspect and the procedure of the ANFIS-LQR controller are explained with details in section (4.2.6). In this section, only the ANFIS-LQR parameters used for the anti-swing control of the DLRIP will be explained. The ANFIS parameters such as the number and type of membership functions, error tolerance, epochs number and learning method applied to the DLRIP are given in Table 4.24.

Table 4.24. ANFIS parameters to the DLRIP

ANFIS parameter	Value
Number of membership functions	7
Type of membership function	Triangular
Error tolerance	Zero
Epochs number	1000
Learning method	Hybrid

e and ė are of the DLRIP calculated as follows:

$$\begin{bmatrix} e \\ \dot{e} \end{bmatrix} = Kx^T = \begin{bmatrix} K_{\theta_1}\theta_1 + K_{\theta_2}\theta_2 + K_{\theta_3}\theta_3 \\ K_{\dot{\theta_1}}\dot{\theta_1} + K_{\dot{\theta_2}}\dot{\theta_2} + K_{\dot{\theta_3}}\dot{\theta_3} \end{bmatrix} \quad (4.37)$$

Where

$$K = \begin{bmatrix} K_{\theta_1} & K_{\theta_2} & K_{\theta_3} & 0 & 0 & 0 \\ 0 & 0 & 0 & K_{\dot{\theta_1}} & K_{\dot{\theta_2}} & K_{\dot{\theta_3}} \end{bmatrix} \quad (4.38)$$

$$x = \begin{bmatrix} \theta_1 & \theta_2 & \theta_2 & \dot{\theta}_1 & \dot{\theta}_2 & \dot{\theta}_3 \end{bmatrix} \quad (4.39)$$

The sampling rate is chosen as 1khz for the 50s. (e, ė) and (U) are the inputs and output of ANFIS, respectively. For one example, the loaded data for training, the training

error, and the trained data in ANFIS editor are shown in Figure 4.27. The network structure and the surface relationship of the two inputs and one output are shown in Figure 4.28. The block diagram of the ANFIS-LQR of the DLRIP is given as an example in Figure 4.8 in section (4.2.6).

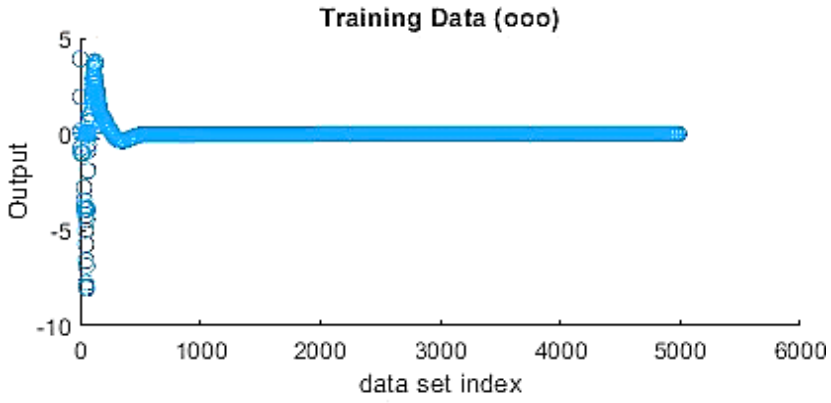

(a)

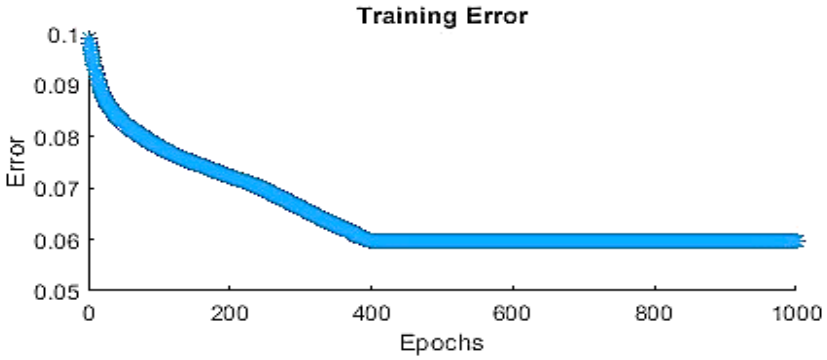

(b)

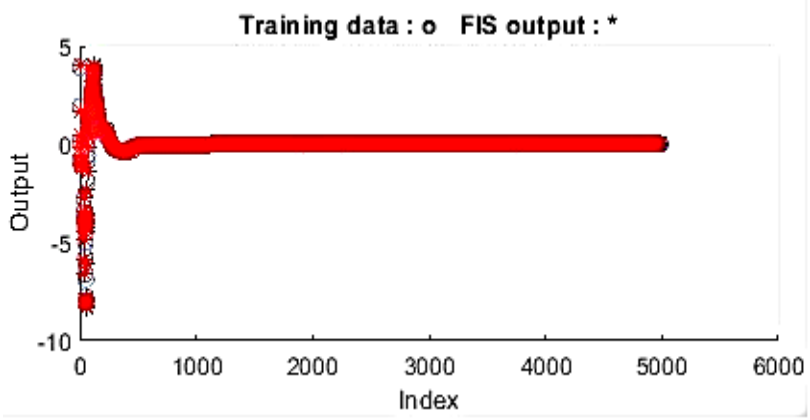

(c)

Figure 4.27. One example (a) the loaded data for training (b) the training error and (c) the trained data

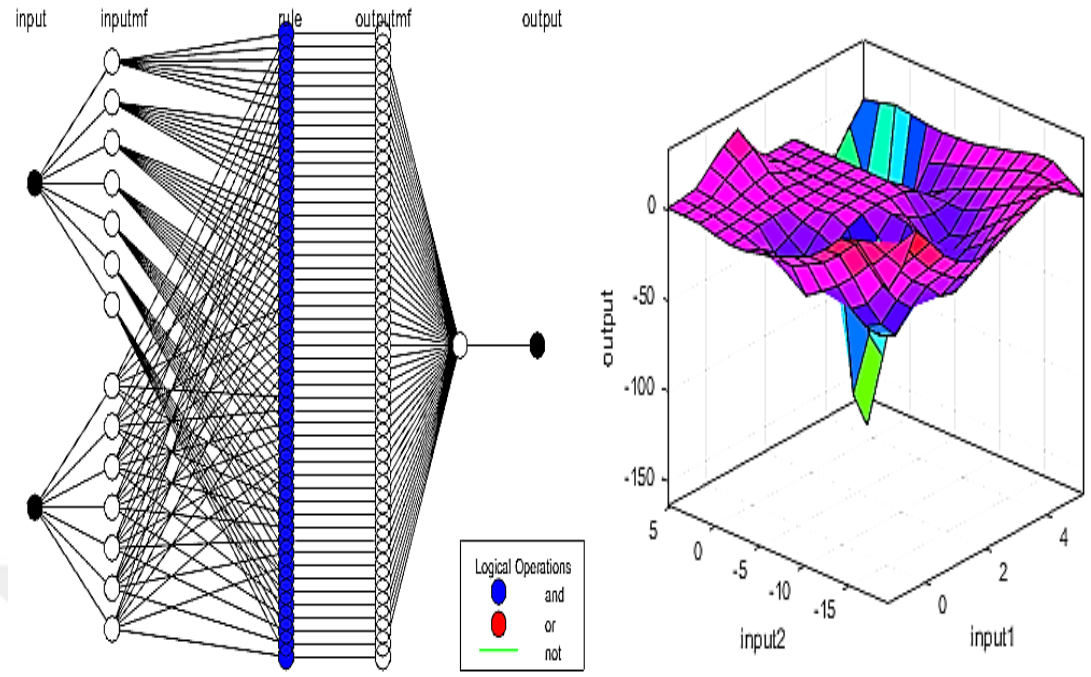

(a) (b)

Figure 4.28. ANFIS: (a) network structure (b) inputs-output surface

4.6.2. Anti-swing RBNF-LQR controller of the DLRIP

The RBNF-LQR controller is explained in details in section (4.2.6). The RBNF-LQR is developed to obtain better control performance than the classical ANFIS-LQR controller. Two RBNNs are used to train the positions and velocities of state variables multiplied by their LQR gains, respectively. The inputs and output (u) data obtained from the non-linear FLQR controller are used for the training of both RBNNs. The block diagram of RBNF-LQR controller is shown as an example in Figure 4.9 in section (4.2.7). 300000 data of each input and 100000 data of output are used to train for RBNNs. For the two RBNNs, Bayesian Regularization (BR) algorithm is used to treat the inputs and the output. 70% of the data used for simulation were used for training, 15% for validation, and 15% for the testing for each RBFNN. The realized values and calculated values of all data for each RBNN are shown in Figure 4.29. The regression value for all data is 0.99 for both RBNNs. As can be seen in Figure 4.30, the best validation performance value is obtained at the 66-ith and 66-ith iterations for both RBNNs, respectively. The Mamdani type fuzzy model is developed and explained in section (4.2.6).

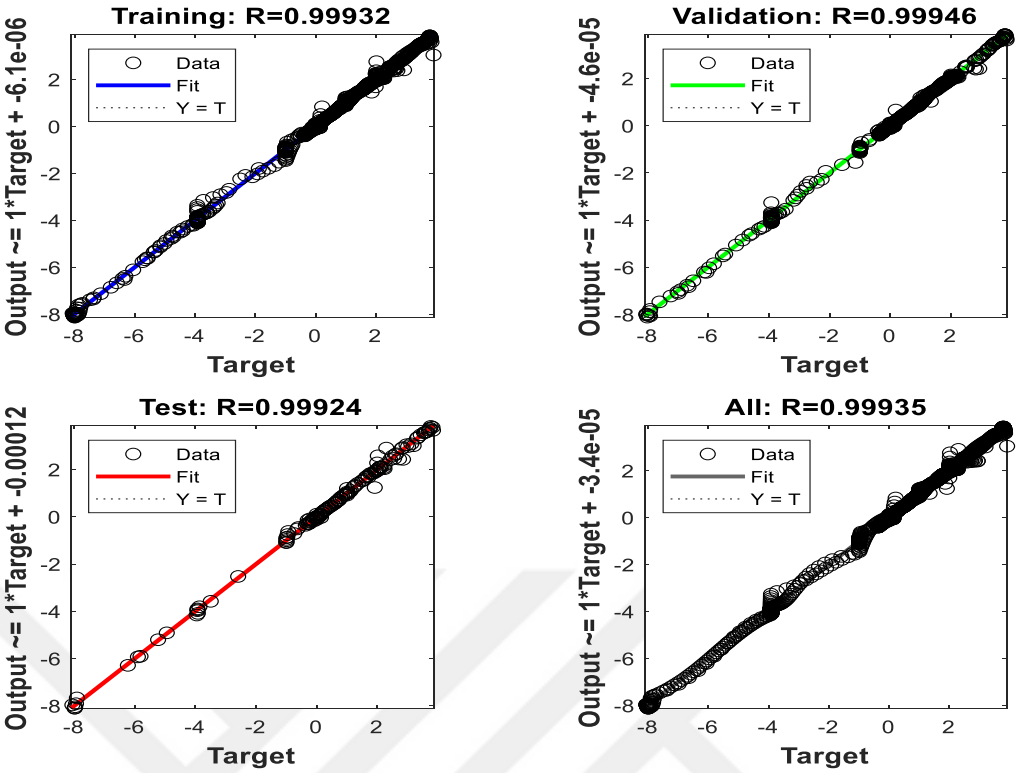

(a)

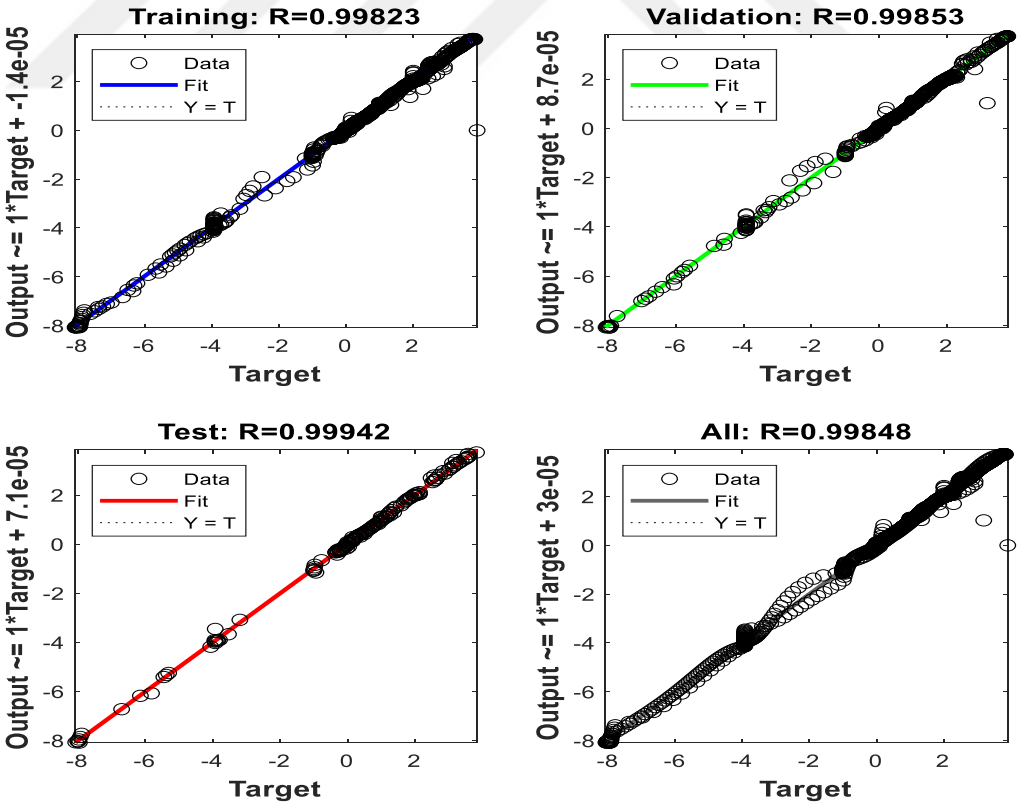

(b)

Figure 4.29. Regression graphs for : (a) positions RBNN (b) velocities RBNN

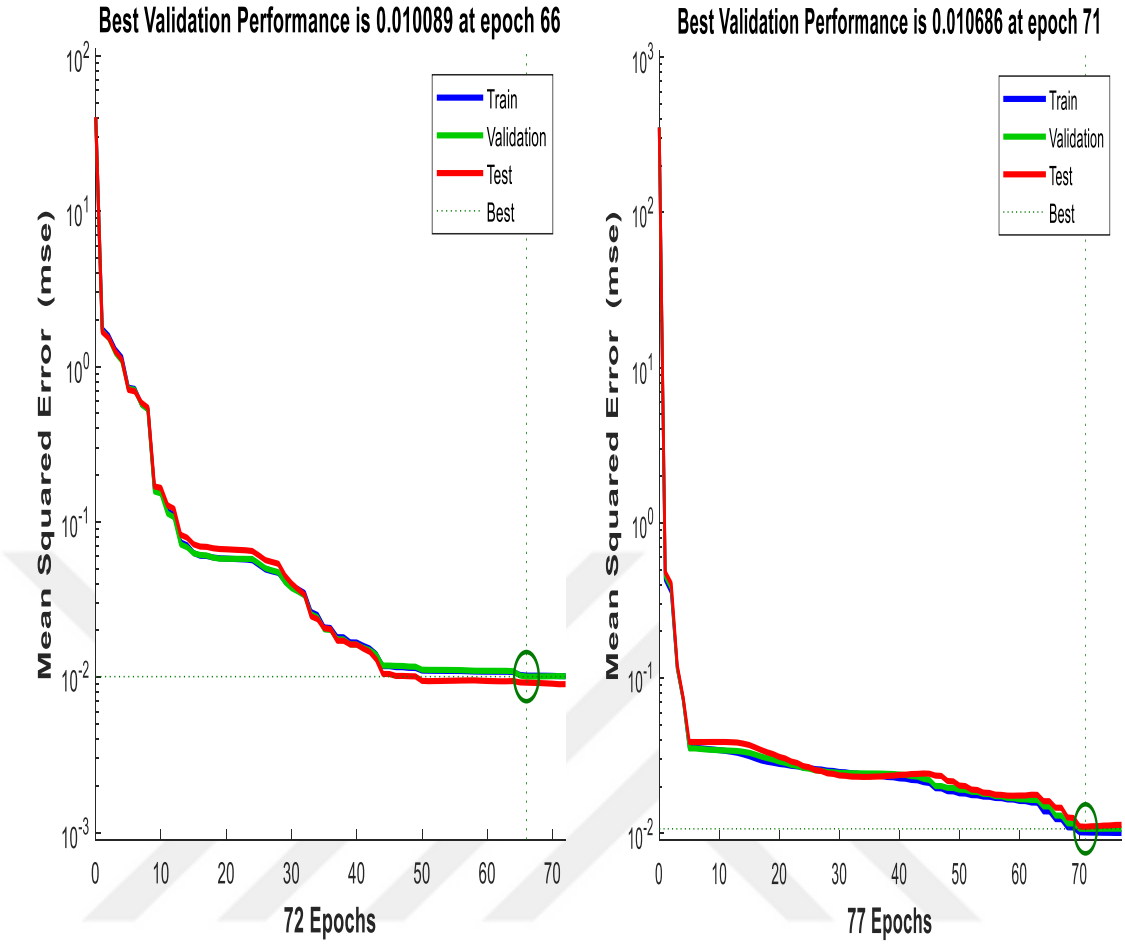

(a) (b)

Figure 4.30. Convergence behavior of the RBNNs during training iterations : (a) positions RBNN (b) velocities RBNN

4.6.3. Comparison between the two anti-swing NF controllers of the DLRIP

In this section, both anti-swing NF controllers (ANFIS-LQR and RBNF-LQR) are compared based on the performance of the control signal obtained from the three joints of the DLRIP. According to the obtained results, the RBNF-LQR controller returned better control performance than ANFIS-LQR controller. Furthermore, the RBNF-LQR controller is chosen as our NF controller applied to the DLRIP. Figure 4.31. shown a comparison between the ANFIS-LQR and RBNF-LQR based on the performance of the control signal. In the next section, three controllers (RBNF-LQR, FLQR and LQR) are developed for the anti-swing control of the DLRIP. The three controllers are modelled and simulated in MATLAB/Simulink.

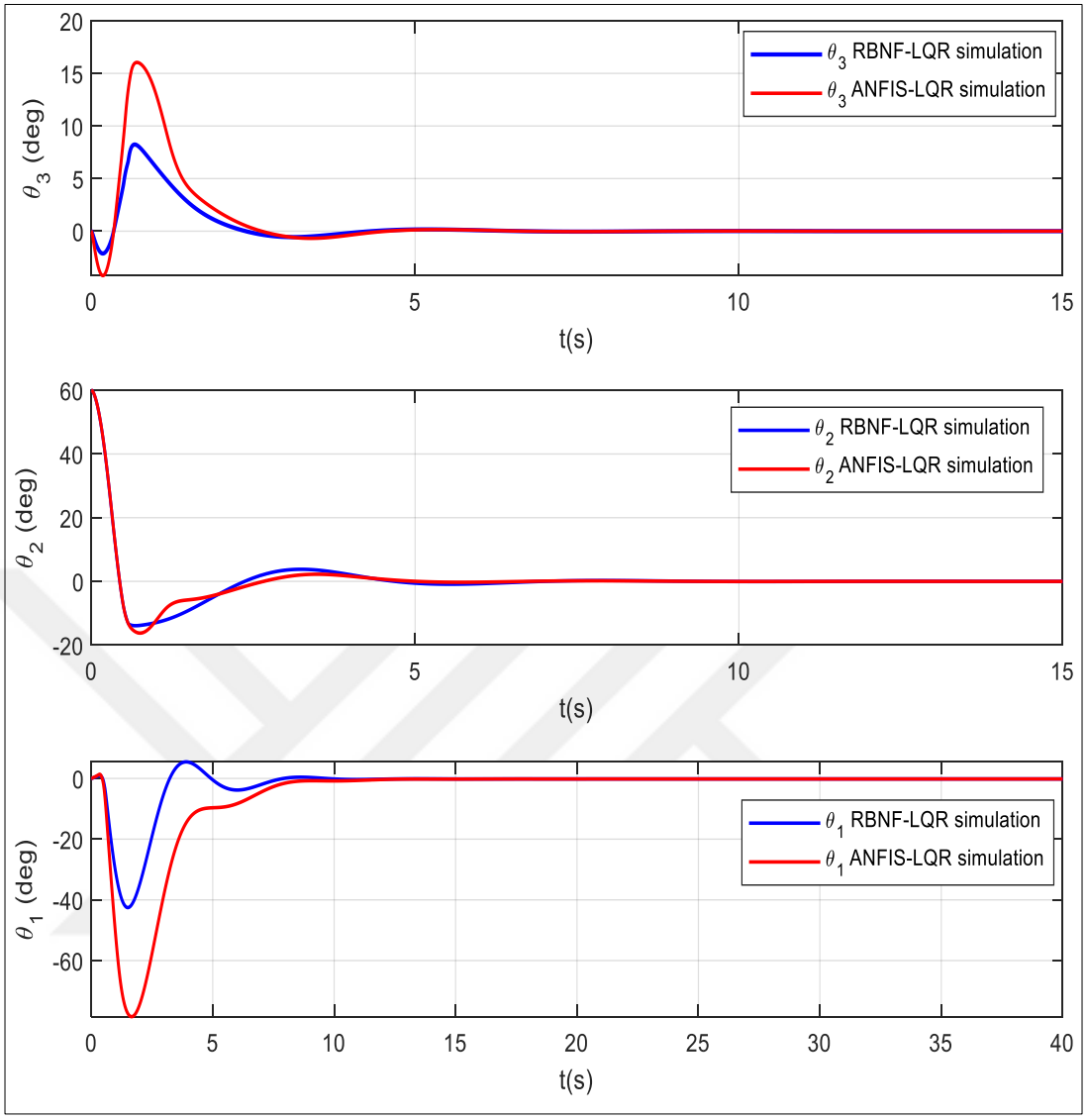

Figure 4.31. Control signal obtained by the ANFIS-LQR and RBNF-LQR

4.6.4. Anti-swing control results and robustness analysis of the DLRIP

The developed controllers (RBNF-LQR, FLQR and LQR) for the anti-swing control of the DLRIP are modeled and simulated using the SimMechanics Toolbox in MATLAB/Simulink. The anti-swing control is performed by the initial conditions of $\theta_1 = 0°$, $\theta_2 = 60°$, $\theta_3 = 0°$, and gain matrix K=[-0.1826 56.1059 1.3411 -0.8416 8.8488 0.4982]. All output variables of the DLRIP need to be stabilized at the reference point by all anti-swing controllers. Moreover, a comparison between the angle signals (θ_1,θ_2 and θ_3) with anti-swing controllers in simulation given in Figures 4.32.

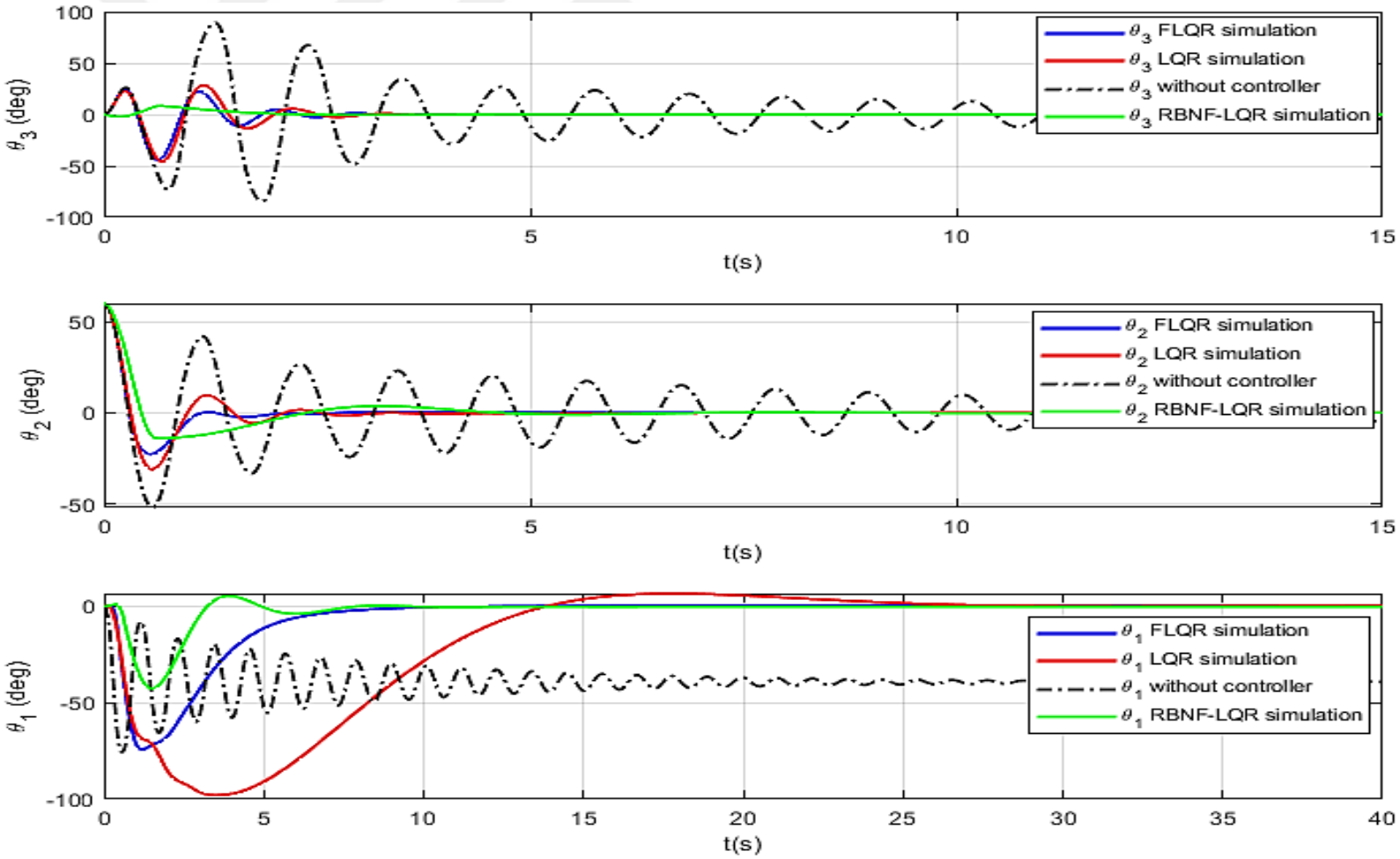

Figure 4.32. Comparison between the angle signals (θ_1,θ_2 and θ_3) with LQR, FLQR and RBNF-LQR anti-swing controllers for DLRIP

According to the obtained results, all controllers have effectively maintained the anti-swing control of the DLRIP with minimum vibration. The RBNF-LQR controller is developed in order to give the best results in terms of T_s, MP, E_{ss} and the RMSEs than the FLQR and LQR controllers. Table 4.25 shows the comparison of LQR, FLQR and RBNF-LQR anti-swing controllers in terms of T_s, MP, E_{ss} and the RMSEs in simulation.

Table 4.25. Comparison of the performance of LQR, FLQR and RBNF-LQR anti-swing controllers for the DLRIP

Controllers	Parameters	Joints		
		First Link (θ_1)	Second Link (θ_2)	Third link (θ_3)
LQR	T_s(s)	24.07	2.9841	3.34
	MP (°)	97.91	30.76	45.65
	E_{ss} (°)	0.263	0.5	0.1
	RMSE (°)	0.1845	0.0619	0.2004
FLQR	T_s(s)	8.7760	1.8947	3.0847
	MP (°)	74.26	22.49	44.09
	E_{ss} (°)	0.01	0.08	0.05
	RMSE (°)	0.0833	0.0581	0.0576
RBNF-LQR	T_s(s)	7.3811	4.26	2.72
	MP (°)	42.54	13.91	15
	E_{ss} (°)	0.001	0.0051	0.0027
	RMSE (°)	0.0372	0.0637	0.0133

According to the calculated parameters, the RBNF-LQR produces better results than the FLQR and LQR. To verify the RBNF-LQR performance compared with other anti-swing controllers; the improvement percentages of all parameters are calculated and given in Table 4.26.

Table 4.26. Comparison of the performance parameters in terms of percentage between RBNF-LQR versus FLQR and RBNF-LQR versus LQR

Controllers	Parameters	Joints		
		First Link (θ_1)	Second Link (θ_2)	Third link (θ_3)
RBNF-LQR versus LQR	T_s	69.33%	29.95%	18.62%
	MP	56.55%	54.77%	67.14%

Table 4.26.(Cont.) Comparison of the performance parameters in terms of percentage between RBNF-LQR versus FLQR and RBNF-LQR versus LQR

	E_{ss}	99.61%	98.98%	97.30%
	RMSE	79.83%	2.82%	93.36%
RBNF-LQR versus FLQR	T_s	15.89%	55.52%	11.82%
	MP	42.71%	38.15%	65.97%
	E_{ss}	90.00%	93.62%	94.60%
	RMSE	55.34%	8.79%	73.40%

According to the calculated rate of improvement percentages in Table 4.26, the RBNF-LQR returned more accurately than LQR for the anti-swing control of the DLRIP. The T_s improvement percentages are 69.33% for the first link, 29.95% for the second link and 18.62 % for the third link. The MP improvement percentages are 56.55% for the first link, 54.77% for the second link and 67.14% for the third link. The E_{ss} improvement percentages are 99.61% for the first link, 98.98% for the second link and 97.30% for the third link. The RMSE improvement percentages are 79.83% for the first link, 2.82% for the second link and 93.36% for the third link. Furthermore, the RBNF-LQR returned more accurately than FLQR for the anti-swing control of the DLRIP. The T_s improvement percentages are 15.98% for the first link, 55.52% for the second link and 11.82 % for the third link. The MP improvement percentages are 42.71% for the first link, 38.15% for the second link and 65.97% for the third link. The E_{ss} improvement percentages are 99 % for the first link, 93.62% for the second link and 94.60% for the third link. The RMSE improvement percentages are 55.34% for the first link, 8.79% for the second link and 73.40% for the third link.

- Robustness analysis:

In this part, the developed controllers are tested for robustness under external disturbance. Figure 4.33 shows the angle signals (θ_1, θ_2 and θ_3) with LQR, FLQR and RBNF-LQR controllers for the DLRIP under external disturbance. Based on the obtained results, all controllers are robust under external disturbance. The external disturbance is applied to the system at t=25s when the system is stable at zero position. The RBNF-LQR controller is developed to provide better control parameters than the FLQR and LQR. Table 4.27 shows a comparison of controllers in terms of Ts, MP, Ess and the RMSEs under external disturbance. According to the obtained results, the

RBNF-LQR yields more perfect results than the LQR and FLQR. To analyze the performance of the RBNF-LQR compared with FLQR and LQR under external disturbance; The improvement percentages of T_s, MP, Ess and position RMSEs are calculated and given in Table 4.28.

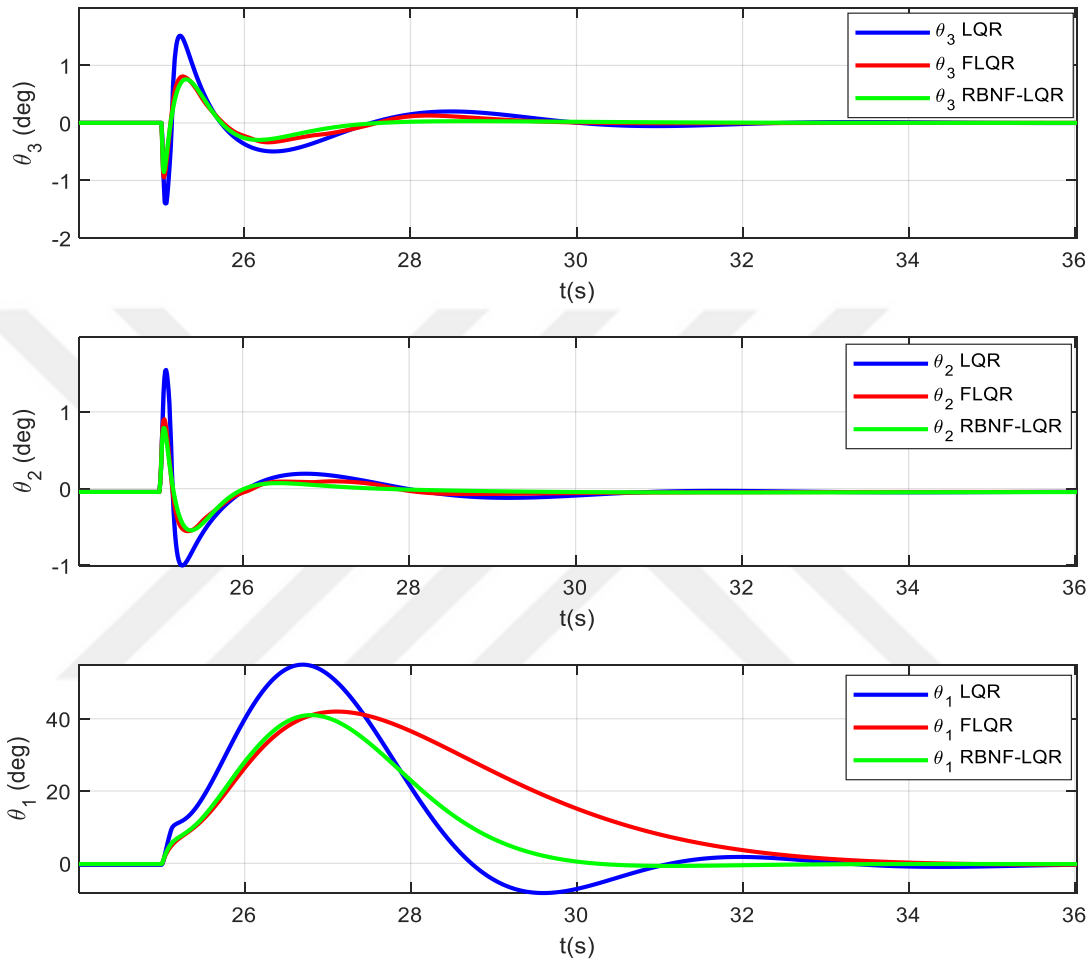

Figure 4.33. Comparison between the angle signals (θ_1,θ_2 and θ_3) with LQR, FLQR and RBNF-LQR anti-swing controllers under external disturbance for DLRIP

Table 4.27. Comparison of the performance of LQR, FLQR and RBNF-LQR anti-swing controllers under external for the DLRIP

Controllers under external disturbance	Parameters	Joints		
		First Link (θ_1)	Second Link (θ_2)	Third link (θ_3)
LQR	T_s(s)	18.9	7.5	8.3
	MP (°)	55	1.5	1.5
	E_{ss} (°)	0.4	0.046	0.00223

Table 4.27.(Cont.) Comparison of the performance of LQR, FLQR and RBNF-LQR anti-swing controllers under external for the DLRIP

	RMSE (°)	0.1396	0.0015	0.0019
FLQR	T_s(s)	16.8	6.1	5.1
	MP (°)	43	1	0.8
	E_{ss} (°)	0.19	0.044	0.0017
	RMSE (°)	0.1378	0.0010	0.0011
RBNF-LQR	T_s(s)	12.5	5.1	2.5
	MP (°)	41	0.8	0.7
	E_{ss} (°)	0.02	0.043	0.0016
	RMSE (°)	0.1094	9.5958e-04	0.0010

Table 4.28. Comparison of the performance parameters in terms of percentage between RBNF-LQR versus FLQR and RBNF-LQR versus LQR under external disturbance

Controllers	Parameters	Joints		
		First Link (θ_1)	Second Link (θ_2)	Third link (θ_3)
RBNF-LQR versus LQR	T_s	11.11%	32.00%	69.87%
	MP	21.81%	46.66%	53.33%
	E_{ss}	95%	6.52%	28.25%
	RMSE	21.63%	4.042%	47.36%
RBNF-LQR versus FLQR	T_s	33.86%	16.39%	50.98%
	MP	25.45%	19.99%	12.50%
	E_{ss}	89.47	2.27%	5.882%
	RMSE	20.60%	36.02%	9.090%

According to the calculated rate of improvement percentages in Table 4.28, the RBNF-LQR returned more accurately than LQR for the anti-swing control under the external disturbance of the DLRIP. The T_s improvement percentages are 11.11% for the first link, 32% for the second link and 68.87% for the third link. The MP improvement percentages are 21.81% for the first link, 46.66% for the second link and 53.33% for the third link. The E_{ss} improvement percentages are 95% for the first link, 6.52% for the second link and 28.25% for the third link. The RMSE improvement percentages are 21.63% for the first link, 4.042% for the second link and 47.36% for the third link. Furthermore, the RBNF-LQR returned more accurately than FLQR for the anti-swing control under the external disturbance of the DLRIP. The T_s improvement percentages

are 33.86% for the first link, 16.39% for the second link and 50.98% for the third link. The MP improvement percentages are 25.45% for the first link, 19.99% for the second link and 12.50% for the third link. The E_{ss} improvement percentages are 89.47% for the first link, 2.27% for the second link and 5.882% for the third link. The RMSE improvement percentages are 20.60% for the first link, 36.02% for the second link and 9.090% for the third link.

In this section, a RBNF-LQR was developed and compared with FLQR and the classical LQR controller for the anti-swing control of the DLRIP. According to the obtained simulation results the RBNF-LQR controller gives better results than the FLQR and LQR controller in terms of T_s, MP, E_{ss} and RMSE. RMSEs improvement percentages between RBNF-LQR versus FLQR and RBNF-LQR versus LQR are from 8.79% to 73.40% and 2.82% to 93.36%, respectively. Furthermore, the RBNF-LQR controller produces better results than the FLQR and LQR controllers under external disturbance. RMSEs improvement percentages between RBNF-LQR versus FLQR and RBNF-LQR versus LQR are from 4.042% to 47.36% and 9.090% to 36.02% under external disturbance, respectively.

4.7. Stabilisation Control of the TLRIP

4.7.1. Model linearization of the TLRIP

The linear state-space model of the system is given in equation (4.24). x is the state vector of the TLRIP, $x^T = [\theta_1 \quad \theta_2 \quad \theta_3 \quad \theta_4 \quad \dot{\theta_1} \quad \dot{\theta_2} \quad \dot{\theta_3} \quad \dot{\theta_4}]$. u is the control input $u = \tau_1$, (τ_1 is torque input of the first link). A, B, C and D are matrices for the state-space representation.

The aim is to design a robust controller for stabilizing the pendulum links in the upright position with minimum deflection. The stable equilibrium point corresponds to a state in each pendulum is downward position ($\theta_1 = 0°$ and θ_2=$\theta_3 = \theta_4 = 180^\circ$). The unstable equilibrium corresponds to the state in each pendulum points vertically upwards which is against gravity ($\theta_1 = \theta_2 = \theta_3 = \theta_4 = 0^\circ$). Substituting system parameters and constants for respective terms, A, B, C and D state-space matrices of the TLRIP become:

$$A = \begin{bmatrix} 0 & 0 & 0 & 0 & 1 & 0 & 0 & 0 \\ 0 & 0 & 0 & 0 & 0 & 1 & 0 & 0 \\ 0 & 0 & 0 & 0 & 0 & 0 & 1 & 0 \\ 0 & 0 & 0 & 0 & 0 & 0 & 0 & 1 \\ 0 & 5.5966 & -4.0879 & -1.0158 & -1.1279 & -1.4723 & 0.0136 & 0.0568 \\ 0 & 49.87 & -18.977 & -10.418 & -1.3476 & -1.8172 & 2.3321 & 2.3285 \\ 0 & -368.337 & 40.9279 & 25.674 & 1.0695 & 1.3321 & -3.673 & -2.0427 \\ 0 & -477.853 & 518.368 & 260.418 & 1.448 & 1.748 & -2.747 & -4.067 \end{bmatrix} \quad (4.40)$$

$$B = \begin{bmatrix} 0 \\ 0 \\ 0 \\ 0 \\ 1.0095 \\ 1.7227 \\ -2.516 \\ -4.5160 \end{bmatrix} \quad C = \begin{bmatrix} 1 & 0 & 0 & 0 & 0 & 0 & 0 & 0 \\ 0 & 1 & 0 & 0 & 0 & 0 & 0 & 0 \\ 0 & 0 & 1 & 0 & 0 & 0 & 0 & 0 \\ 0 & 0 & 0 & 1 & 0 & 0 & 0 & 0 \\ 0 & 0 & 0 & 0 & 1 & 0 & 0 & 0 \\ 0 & 0 & 0 & 0 & 0 & 1 & 0 & 0 \\ 0 & 0 & 0 & 0 & 0 & 0 & 1 & 0 \\ 0 & 0 & 0 & 0 & 0 & 0 & 0 & 1 \end{bmatrix} \quad D = \begin{bmatrix} 0 \\ 0 \\ 0 \\ 0 \\ 0 \\ 0 \\ 0 \\ 0 \end{bmatrix} \quad (4.41)$$

The initial choice of the Q and R matrices are given as follows:

$$Q = \begin{bmatrix} 1 & 0 & 0 & 0 & 0 & 0 & 0 & 0 \\ 0 & 1 & 0 & 0 & 0 & 0 & 0 & 0 \\ 0 & 0 & 1 & 0 & 0 & 0 & 0 & 0 \\ 0 & 0 & 0 & 1 & 0 & 0 & 0 & 0 \\ 0 & 0 & 0 & 0 & 1 & 0 & 0 & 0 \\ 0 & 0 & 0 & 0 & 0 & 1 & 0 & 0 \\ 0 & 0 & 0 & 0 & 0 & 0 & 1 & 0 \\ 0 & 0 & 0 & 0 & 0 & 0 & 0 & 1 \end{bmatrix} \text{ and } R = 0.01 \quad (4.42)$$

The LQR gain vector of the TLRIP is given in equation (4.43).

$$K = [-3.1623\ 214.0004\ -252.2487\ -138.1634\ -5.3538\ 1.7422\ -9.7926\ -7.5319] \quad (4.43)$$

The proposed controller for the stabilization control TLRIP will be described in the next section.

4.7.2. Robustness analyze of the TLRIP

In this section, LQR, FLQR, LQG and FLQG are modelled and simulated in the MATLAB/Simulink environment for the stabilization control of the TLRIP. The simulation is performed by the sampling time 1ms and 50s simulation time. A numerical method Bogacki-Shampine solver is selected with fixed-step. According to simulation results, a comparative study of all controllers is given. The controllers are tested for robustness under internal, external disturbances and noise. The simulation

results can provide a good background and feasibility for a real experimental implementation to the stabilization control problem of the TLRIP. SimMechanics model for control of TLRIP with the controller is shown in Figure 4.34.

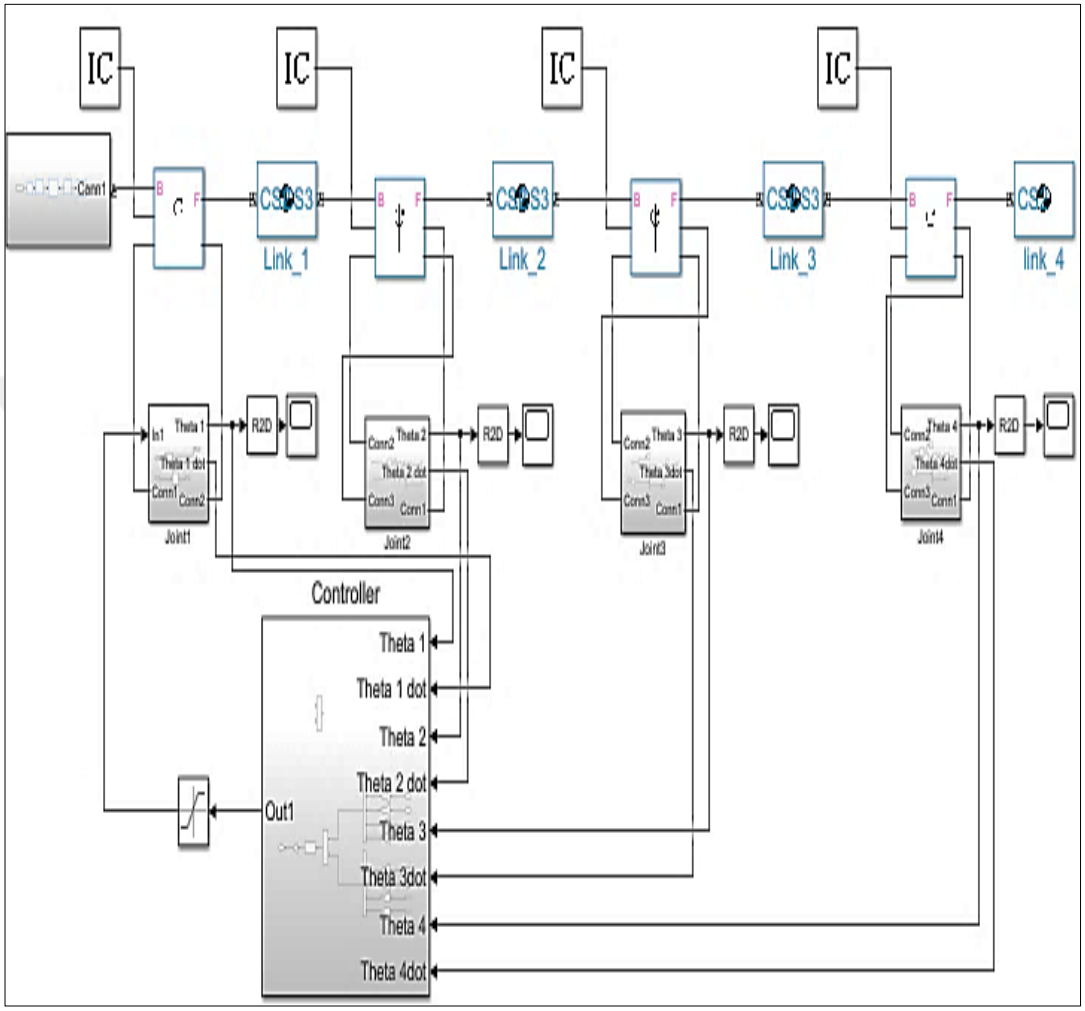

Figure 4.34. SimMechanics model of the TLRIP with the controller

a) External disturbance

The simulation of LQR and FLQR controllers is performed with the calculated gain matrix K given in equation (392) and an initial condition vector which is $x^T = [0\ 0\ 0\ -0.05\ 0\ 0\ 0\ 0]$. As can be seen from Figure 4.33, The output variables of two controllers are stabilized at the reference points, the three pendulum angles (θ_2 , θ_3 and θ_4) are stabilized. Similarly, the horizontal arm stabilized at a reference trajectory $\pm 50°$ each 25s. Figure 4.35 shows the angle signals (θ_1, θ_2 , θ_3 and θ_4) with LQR and FLQR controllers for the TLRIP system.

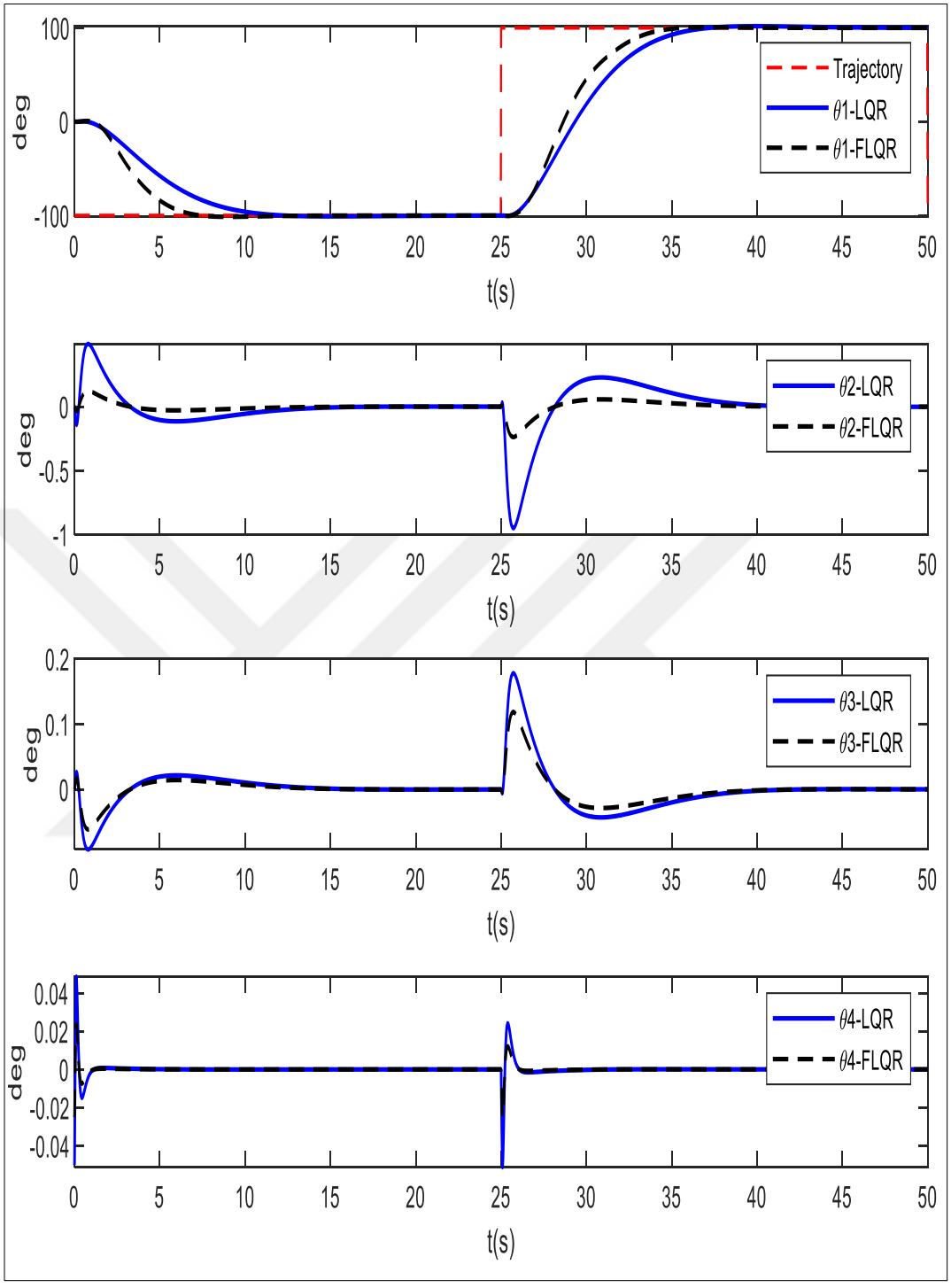

Figure 4.35. The angle signals (θ_1, θ_2, θ_3 and θ_4) with LQR and FLQR controllers

According to the obtained results using the LQR controller, the LQR is robust, and it has successfully maintained the control of the TLRIP. An FLQR controller is developed to give us more best T_s, PO, E_{ss} and the RMSEs than the classical LQR controllers. The two controllers are robust under external disturbance. Table 4.29 shows the comparison of LQR and FLQR controllers in terms of T_s, PO, E_{ss} and the

RMSEs under external disturbance.

Table 4.29. Quantitative Comparison of Performance of LQR and FLQR controllers under external disturbance for the TLRIP

Controllers under external disturbance	Parameters	Joints			
		First Link (θ_1)	Second Link (θ_2)	Third link (θ_3)	Fourth link (θ_4)
LQR	T_s(s)	9.54	9.10	8.9	1.33
	PO (%)	1.4	40	19	4.1
	E_{ss} (°)	0.89	0.019	5.5 e^{-5}	2.44 e^{-5}
	RMSE (°)	0.4472	7.745e^{-4}	1.4522e^{-4}	1.7575e^{-5}
FLQR	T_s(s)	5.21	4.55	3.50	1.1s
	PO (%)	0.7	15	10	3.2
	E_{ss} (°)	0.35	0.000232	1,15 e^{-5}	9.8 e^{-6}
	RMSE (°)	0.3920	1.9363e^{-4}	9.6814e^{-5}	8.7876e^{-6}

b) Internal disturbance

The robustness of two controllers LQR and FLQR is tested under external disturbance. To test the controllers' response under internal disturbance, the mass of the fourth link is varied from [10-20%] to the initial mass of the fourth link in time of 20s.

The two controllers are robust under the internal disturbance. Figure 4.36. shows an example of the response of LQR and FLQR controllers under internal disturbance. Table 4.30 shows the comparison of LQR and FLQR controllers in terms of T_s, PO, E_{ss} and the RMSEs under internal disturbance.

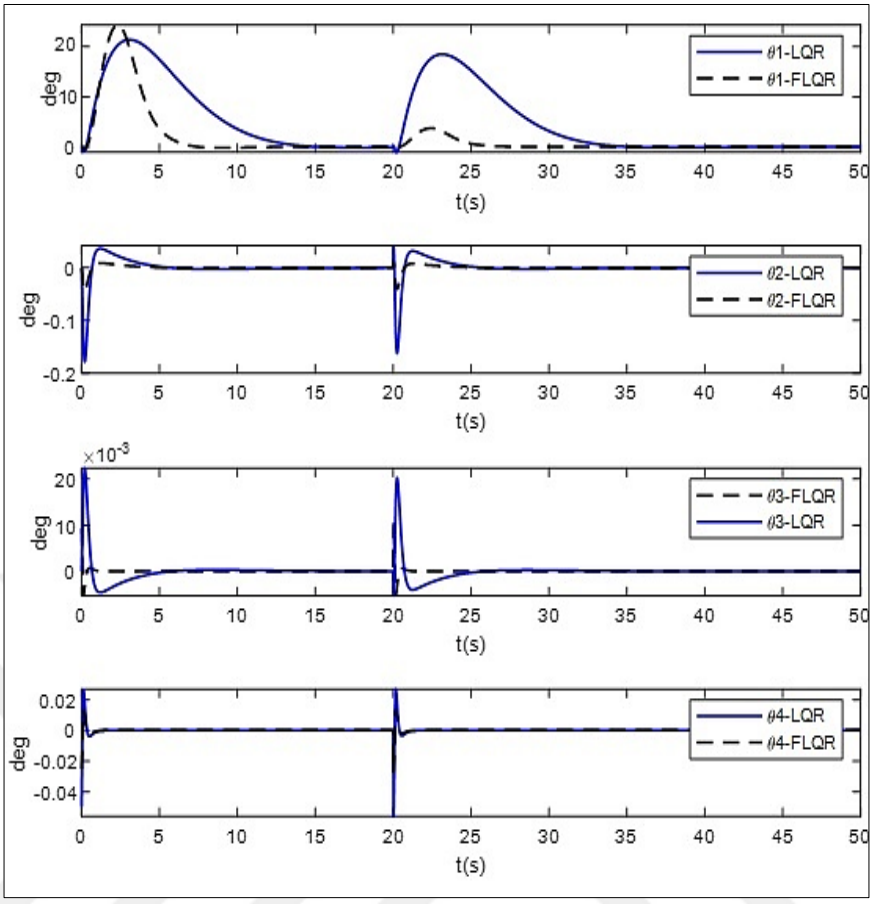

Figure 4.36. Example of the response of LQR and FLQR controller under internal disturbance with a variation of mass of the fourth link in T=20s (Initial mass + 15% of the third link)

Table 4.30. Quantitative Comparison of Performance of LQR and FLQR controllers under internal disturbance for the TLRIP

Controllers under internal disturbance	Parameters	Joints			
		First Link (θ_1)	Second Link (θ_2)	Third link (θ_3)	Fourth link (θ_4)
LQR	T_s(s)	13.67	5.31	5.22	1.35
	PO (%)	19.54	18.87	2.1	5.23
	E_{ss} (°)	1.9e-03	1.5e-03	2.0e-04	9.0e-07
	RMSE (°)	0.0038	8.5891e-05	1.0736e-05	0.0879e-05
FLQR	T_s(s)	5.341	1.16	1	1.2
	PO (%)	5.9	5	1.18	2.14
	E_{ss} (°)	1.2e-03	0.5e-03	0.1 e-04	4.5e-07
	RMSE (°)	0.0022	2.1473e-05	2.2534e-06	1.4725e-06

c) Noise and external disturbance

The simulation results obtained by LQR and FLQR controllers are obtained in the case without noise; it is not always the same case for a real experimental system. In the other hand, in a real experimental implementation, the system can be affected by noise. However, all situations cannot be measurable. White noise with different SNR is added to the system in the simulation to approach to a real experimental system. The level of added noise to the system is a critical point in the design of the controller. The LQR and FLQR controllers' performance is tested by adding white noise to the TLRIP. In the LQG and FLQG controllers, the KF has succeeded to estimate the states in the noise cases applied to the system. The reference trajectory signal ($50°$ each $25s$) shown in Figures 4.37 and 4.38 is applied to a horizontal arm when the pendulums are stabilized in the equilibrium point. The initial condition vector is $x^T = [0\ 0\ 0 - 0.05\ 0\ 0\ 0\ 0]$. The LQG and FLQG controllers are capable of eliminating noise, and the system remains stable for the determined time. The most important difference point between the LQR, FLQR controllers and LQG, FLQG controllers results is the effect of noise. LQR and FLQR controllers don't contain any algorithm to ignore the noise combined to the TLRIP. As can be seen from Figures 4.37 and 4.38, the added noise reflect the outputs of the system, which is eliminated by the LQG and FLQG controllers, respectively. Table 4.31 shows a comparison of LQG and FLQG controllers under noise and external disturbance in terms of T_s, PO, E_{ss} and RMSEs.

Table 4.31. Quantitative Comparison of Performance of LQG and FLQG controllers under noise and external disturbance for the TLRIP

Controllers under noise and external disturbance	Parameters	Joints			
		First Link (θ_1)	Second Link (θ_2)	Third link (θ_3)	Fourth link (θ_4)
LQG	T_s(s)	9.26	4.5	3.47	1.4
	PO (%)	1.24	47	20	3.7
	E_{ss} (°)	0.5	0.02	0.003	0.0004
	RMSE (°)	0.3895	2.5841e-04	1.2920e-04	1.1628e-04
FLQG	T_s(s)	5.56	3.2	2.9	0.9
	PO (%)	0.32	44	18.2	3
	E_{ss} (°)	0.04	0.005	0.001	0.0002
	RMSE (°)	0.3887	2.4587e-04	1.19874e-04	1.1578e-04

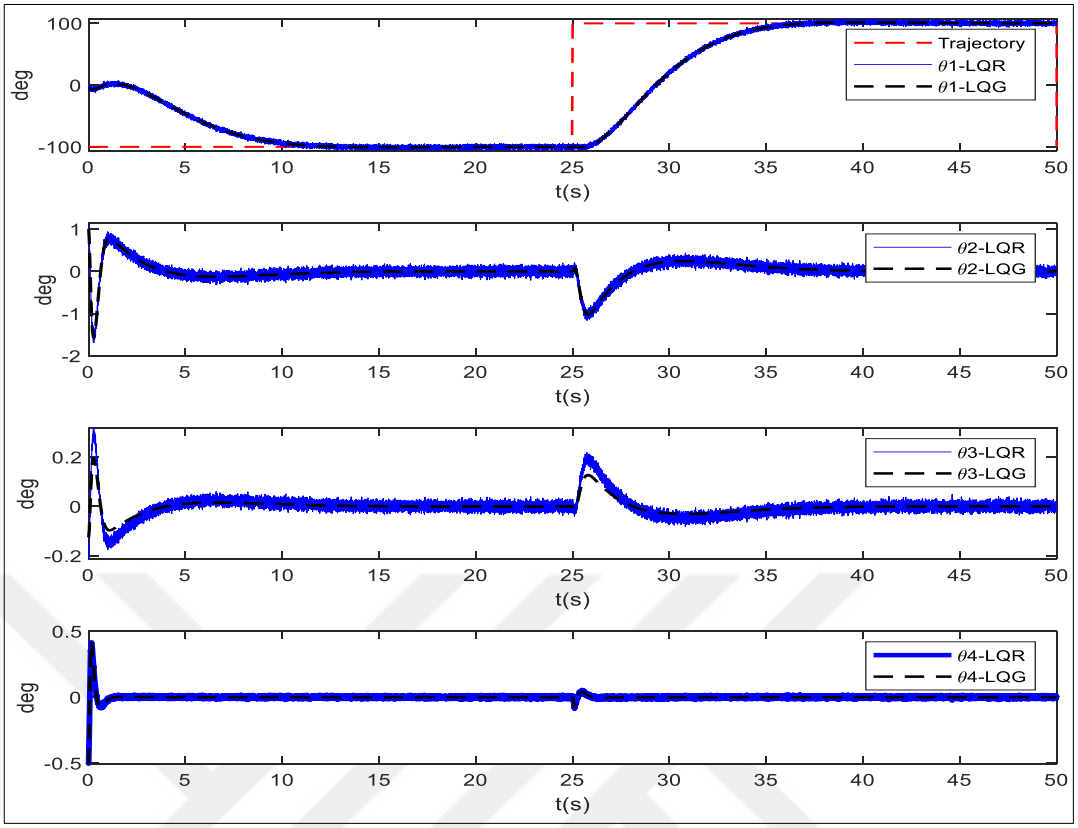

Figure 4.37. The angle signals (θ_1 , θ_2, $\theta_3$and θ_4) with noised LQR and LQG controllers for TLRIP

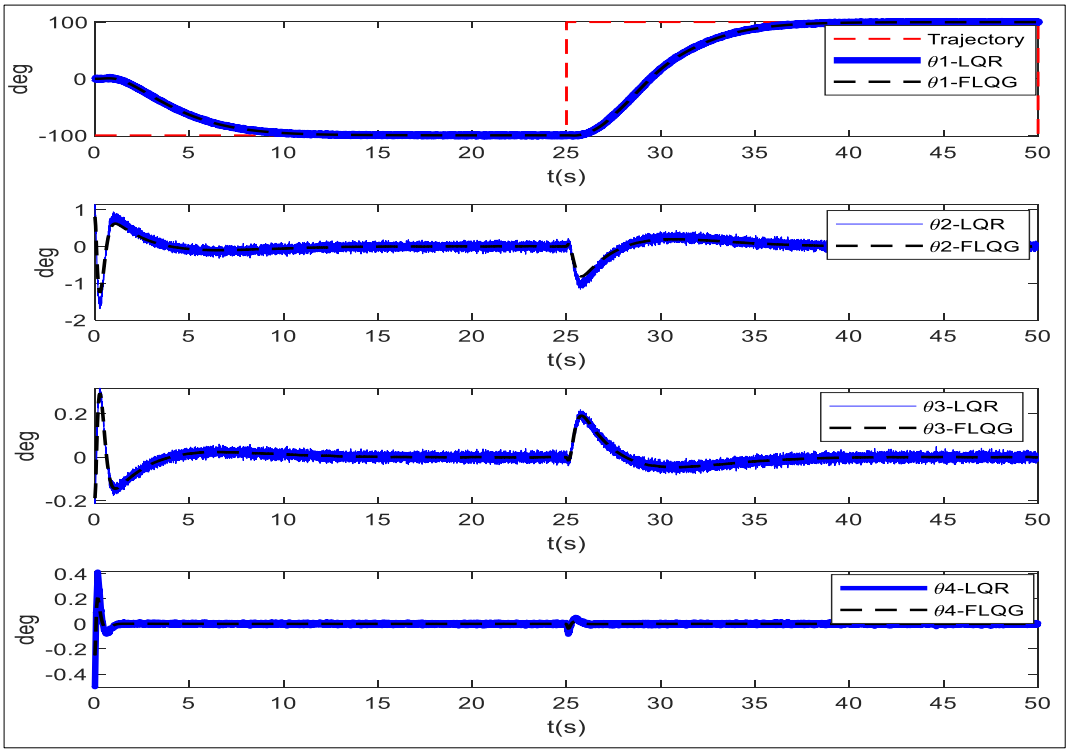

Figure 4.38. The angle signals (θ_1 , θ_2, $\theta_3$and θ_4) with FLQR and FLQG controllers for TLRIP

d) Noise and internal disturbance

The robustness of the two controllers LQG and FLQG is tested under noise and external disturbance. To test the controllers' response under noise and internal disturbance, also the mass of the fourth link is varied from [10-20%] to the initial mass of the third link in time of 20s.

The two controllers are robust under the internal disturbance. Figure 4.39. shows an example of the response of LQG and FLQG controllers under internal disturbance. Table 4.32 shows the comparison of LQG and FLQG controllers in terms of T_s, PO, E_{ss} and RMSEs under internal disturbance.

Table 4.32. Quantitative Comparison of Performance of LQG and FLQG controllers under noise and internal disturbance for the TLRIP

Controllers under noise and internal disturbance	Parameters	Joints			
		First Link (θ_1)	Second Link (θ_2)	Third link (θ_3)	Fourth link (θ_4)
LQG	T_s(s)	12.48	3.81	4.9	1.5
	PO (%)	9.21	9.1	2	4.34
	E_{ss} (°)	0.01	0.0005	0.95 e-05	3.1 e-05
	RMSE (°)	0.0019	4.2945e-05	1.0736e-05	9.614e-06
FLQG	T_s(s)	5.2	2.14	2.95	0.2
	PO (%)	2.78	5.2	0.1	2.27
	E_{ss} (°)	0.001	0.0001	0.1 e-06	2.5e-05
	RMSE (°)	7.6861e-04	2.1473e-05	1.1267e-06	6.009e-06

The performance of the two controllers' effort is determined by the RMSEs between the control signal and zero voltage. The calculated RMSEs are given in Table 4.33. According to the obtained signals results, the system controlled with FLQR and FLQG needs more effort to control the system.

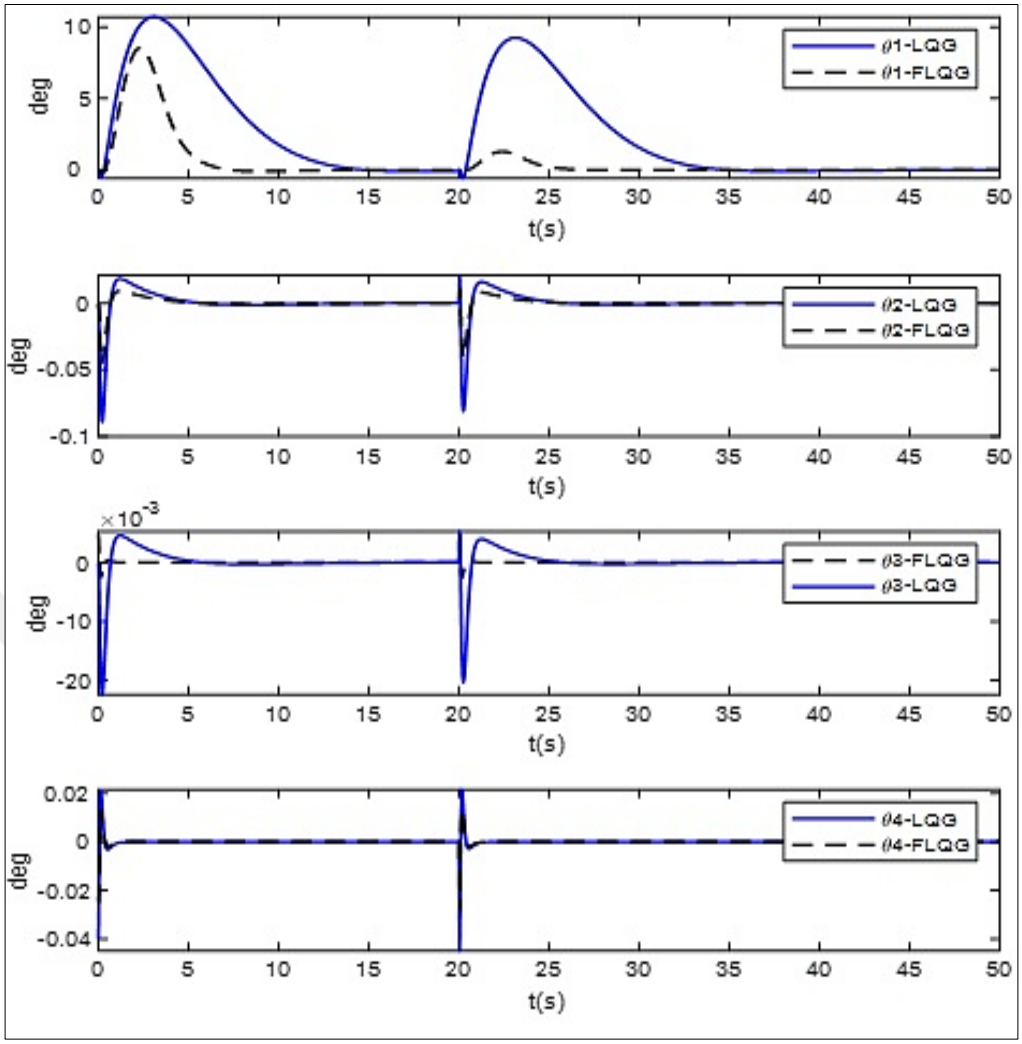

Figure 4.39. Example of the response of LQG and FLQG controller under internal disturbance with a variation of mass of the third link in T=20s (Initial mass + 15% of the Third link)

Table 4.33. RMSEs of the control signals for the controllers

Disturbances	Controller	RMSE
External disturbance	LQR	0.6369
	FLQR	1.4761
Internal disturbance	LQR	4.7102e-04
	FLQR	8.269e-04
Noise and external disturbance	LQG	6.874e-04
	FLQG	9.3946e-04
Noise and internal disturbance	LQG	5.1354e-04
	FLQG	8.9823e-04

4.7.3. Performance evaluation of controllers of the TLRIP

T_s, PO, E_{ss} and the position RMSEs of the joints of both groups of controllers (LQR-FLQR and LQG-FLQG) under external and internal disturbances are given in Tables 4.29, 4.30, 4.31 and 4.32. According to the calculated T_s, PO, E_{ss} and position RMSEs, the nonlinear controllers (FLQR and FLQG) produce more accurate results than the linear controllers (LQR and LQG). In order to see the performance of the FLQR and FLQG compared with LQR and LQG respectively; The improvement percentages of T_s, PO, E_{ss} and position RMSEs were computed for each disturbance cases, and they are given in Tables 4.34, 4.35, 4.36 and 4.37. Considering the T_s, PO, E_{ss} and position RMSEs in all joints, the percentage obtained by the FLQR and FLQG controllers yields better results.

Table 4.34. Comparison of the performance parameters in terms of percentage between LQR-FLQR under external disturbance

Controllers	Parameters	Joint			
		First Link (θ_1)	Second Link (θ_2)	Third link (θ_3)	Fourth link (θ_4)
LQR- FLQR under external disturbance	T_s	47.58%	50%	60.67%	17.29%
	PO	50%	62.5%	47.36%	21.95%
	E_{ss}	60.67%	98.77%	79.09%	59.83%
	RMSE	12.34 %	74.99%	33.33%	49.99%

According to the calculated improvement percentages in Table 4.34, the FLQR returned more accurately than LQR under external disturbance for all joints. The T_s improvement percentages are 47.58% for the first link, 50% for the second link, 60.67% for the third link and 17.29% for the fourth link. The PO improvement percentages are 50% for the first link, 62.5 % for the second link, 47.36% for the third link and 21.95% for the fourth link. The E_{ss} improvement percentages are 60.67% for the first link, 98.77% for the second link, 79.99% for the third link and 59.83% for the fourth link. The RMSEs improvement percentages are 12.34% for the first link, 74.99% for the second link,33.33% for the third link and 49.99% for the fourth link.

Table 4.35. Comparison of the performance parameters in terms of percentage between LQR-FLQR under internal disturbance

Controllers	Parameters	Joint			
		First Link (θ_1)	Second Link (θ_2)	Third link (θ_3)	Fourth link (θ_4)
LQR-FLQR under internal disturbance	T_s	60.92%	78.15%	80.84%	11.11%
	PO	69.80%	73.50%	52.38%	59.08%
	E_{ss}	36.84%	80%	95%	50%
	RMSE	42.10%	74.99%	78.99%	81.59%

According to the calculated improvement percentages in Table 4.35, the FLQR returned more accurately than LQR under external disturbance for all joints. The T_s improvement percentages are 60.92% for the first link, 78.15% for the second link, 80.84% for the third link and 11.11% for the fourth link. The PO improvement percentages are 69.80% for the first link, 73.50% for the second link, 52.38% for the third link and 59.08% for the fourth link. The E_{ss} improvement percentages are 36.84% for the first link, 80% for the second link, 95% for the third link and 50% for the fourth link. The RMSEs improvement percentages are 42.10% for the first link, 74.99% for the second link,78.99% for the third link and 81.59% for the fourth link.

Table 4.36. Comparison of the performance parameters in terms of percentage between LQG-FLQG under noise and external disturbance

Controllers	Parameters	Joint			
		First Link (θ_1)	Second Link (θ_2)	Third link (θ_3)	Fourth link (θ_4)
LQG-FLQG under noise and external disturbance	T_s	39.95%	28.88%	16.42%	35.71%
	PO	74.19%	6.38%	9%	18.91%
	E_{ss}	92%	75%	66.66%	50%
	RMSE	0.20%	4.85%	7.21%	0.42%

According to the calculated improvement percentages in Table 4.36, the FLQR returned more accurately than LQR under external disturbance for all joints. The T_s improvement percentages are 39.95% for the first link, 28.88% for the second link, 16.42% for the third link and 35.71% for the fourth link. The PO improvement percentages are 74.19% for the first link, 6.38% for the second link, 9% for the third

link and 18.91% for the fourth link. The E_{ss} improvement percentages are 92% for the first link, 75% for the second link, 60.66% for the third link and 50% for the fourth link. The RMSEs improvement percentages are 0.20% for the first link, 4.85% for the second link,7.21% for the third link and 0.42% for the fourth link.

Table 4.37. Comparison of the performance of parameters in terms of percentage between LQG-FLQG under noise and internal disturbance

Controllers	Parameters	Joint			
		First Link (θ_1)	Second Link (θ_2)	Third link (θ_3)	Fourth link (θ_4)
LQG-FLQG under noise and internal disturbance	T_s	58.33%	43.83%	39.79%	86.66%
	PO	69.81%	42.85%	95%	47.69%
	E_{ss}	90%	80%	98.94%	19.35%
	RMSE	59.54%	49.99%	98.81%	37.49%

According to the calculated improvement percentages in Table 4.37, the FLQR returned more accurately than LQR under external disturbance for all joints. The T_s improvement percentages are 58.33% for the first link, 43.83% for the second link, 39.79% for the third link and 86.66% for the fourth link. The PO improvement percentages are 69.81% for the first link, 42.85% for the second link, 95% for the third link and 47.69% for the fourth link. The E_{ss} improvement percentages are 90% for the first link, 80% for the second link, 98.94% for the third link and 19.35% for the fourth link. The RMSEs improvement percentages are 59.54% for the first link, 49.99% for the second link,98.81% for the third link and 37.49% for the fourth link. Moreover, the RMSEs of the control signals for the controllers (LQR-FLQR and LQG-FLQG) under external and internal disturbances are given in Table 4.33. According to the calculated RMSEs of the control signals, the controllers (FLQR and FLQG) produce more effort than the (LQR and LQG) to control the TLRIP. The incremental percentages of RMSEs of the control signals are computed for each disturbance cases, and they are given in Table 4.38.

Table 4.38. Comparison of the controllers based on Incremental percentages of RMSE control signal

Controllers	Rate
FLQR versus LQR	56,85% - 75,55%
FLQG versus LQG	36.65% - 74,92%

According to the incremental calculated percentages of RMSEs of the control signals in Table 4.38, the FLQR returned more effort than LQR with 56,85% under internal disturbance and with 75,55% under external disturbance. The FLQG returned more effort than LQG with 36.65% under noise and internal disturbance; Also, with 74,92% under noise and external disturbance.

In this study, both FLQR and FLQG controllers were developed for the stability control of the TLRIP, and they were compared with LQR and LQG controllers, respectively. The developed controllers were tested under internal and external disturbances to determine the robustness performance of the controllers. According to the obtained simulation results the nonlinear FLQR and FLQG controllers are robust and produce better results than the LQR and LQG controllers in terms of T_s, PO, E_{ss} and RMSEs. RMSEs improvement percentages between FLQR and LQR range from 12.34% to 74,99% and 42,10% to 81,59% under external and internal disturbances, respectively. Similarly, RMSEs improvement percentages between FLQG and LQG range from 0.20% to 7.21 % and 37,.49 % to 98,81 % under external and internal disturbances, respectively. Moreover, the increment percentages of RMSEs of the control signals for the FLQR and FLQG compared with LQR and LQG is from 36.65% to 75.55%. Accordingly, the FLQR and FLQG controllers need more control efforts than the classical LQR and LQG.

The design compromise between controller performance and efforts should be made based on which one is more important than others. Generally, the performance of the controller is a more crucial aspect of control applications.

4.8. Anti-swing Control of the TLRIP

4.8.1. Anti-swing ANFIS-LQR controller of the TLRIP

The design aspect and the procedure of the ANFIS-LQR controller are explained with details in section (4.2.6). In this section, only the ANFIS-LQR parameters used for the anti-swing control of the TLRIP will be explained. The ANFIS parameters such as the number and type of membership functions, error tolerance, epochs number and learning method applied to the TLRIP are given in Table 4.39.

Table 4.39. ANFIS parameters to the TLRIP

ANFIS parameter	Value
Number of membership functions	7
Type of membership function	Gaussian
Error tolerance	Zero
Epochs number	600
Learning method	Hybrid

e and ė are of the TLRIP calculated as follows:

$$\begin{bmatrix} e \\ \dot{e} \end{bmatrix} = Kx^T = \begin{bmatrix} K_{\theta_1}\theta_1 + K_{\theta_2}\theta_2 + K_{\theta_3}\theta_3 + K_{\theta_4}\theta_4 \\ K_{\dot{\theta_1}}\dot{\theta_1} + K_{\dot{\theta_2}}\dot{\theta_2} + K_{\dot{\theta_3}}\dot{\theta_3} + K_{\dot{\theta_4}}\dot{\theta_4} \end{bmatrix} \quad (4.44)$$

Where

$$K = \begin{bmatrix} K_{\theta_1} & K_{\theta_2} & K_{\theta_3} & K_{\theta_4} & 0 & 0 & 0 & 0 \\ 0 & 0 & 0 & 0 & K_{\dot{\theta_1}} & K_{\dot{\theta_2}} & K_{\dot{\theta_3}} & K_{\dot{\theta_4}} \end{bmatrix} \quad (4.45)$$

$$x = \begin{bmatrix} \theta_1 & \theta_2 & \theta_3 & \theta_3 & \dot{\theta}_1 & \dot{\theta}_2 & \dot{\theta}_3 & \dot{\theta}_4 \end{bmatrix} \quad (4.46)$$

The sampling rate is chosen as 1khz for the 50s. (e, ė) and (U) are the inputs and output of ANFIS, respectively. For one example, the loaded data for training, the training error, and the trained data in ANFIS editor for the TLRIP are shown in Figure 4.40. The network structure and the surface relationship of the two inputs and one output are shown in Figure 4.41.

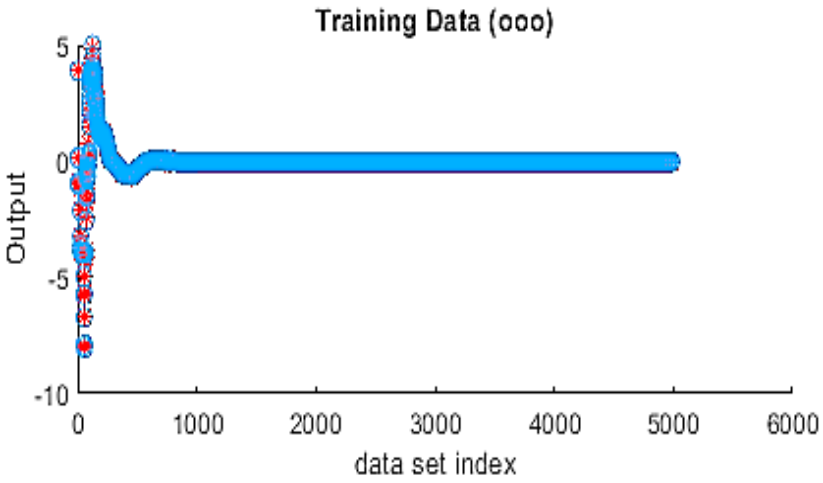

(a)

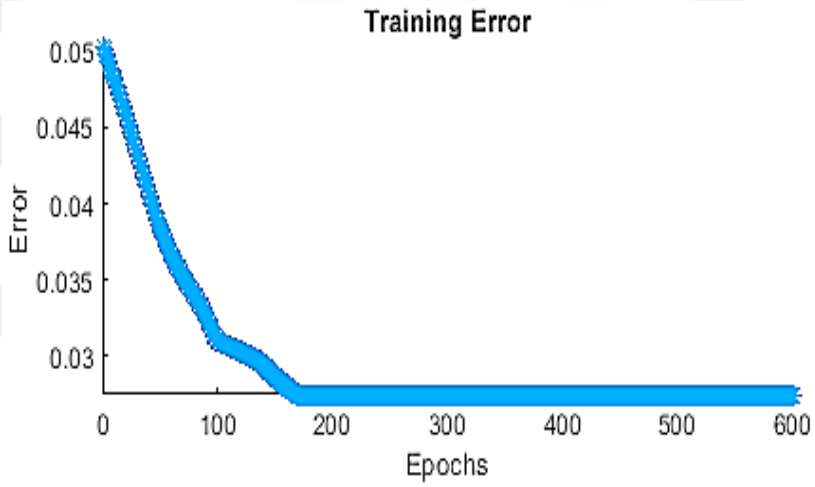

(b)

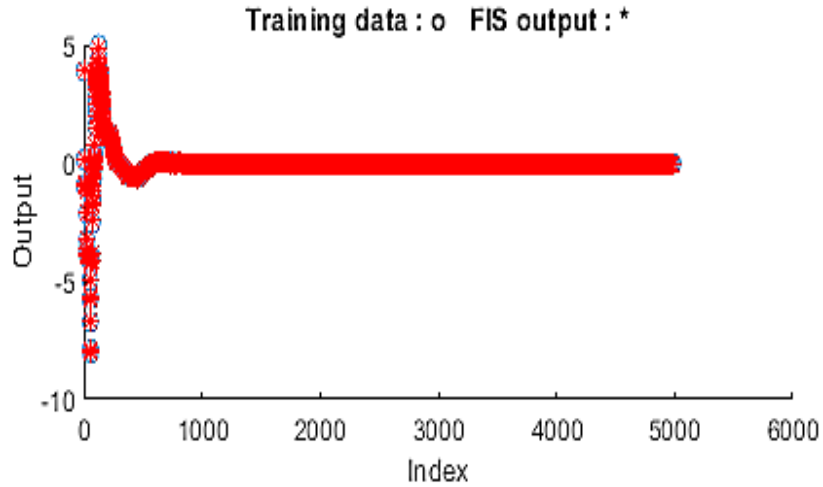

(c)

Figure 4.40. One example (a) the loaded data for training (b) the training error and (c) the trained data for the TLRIP

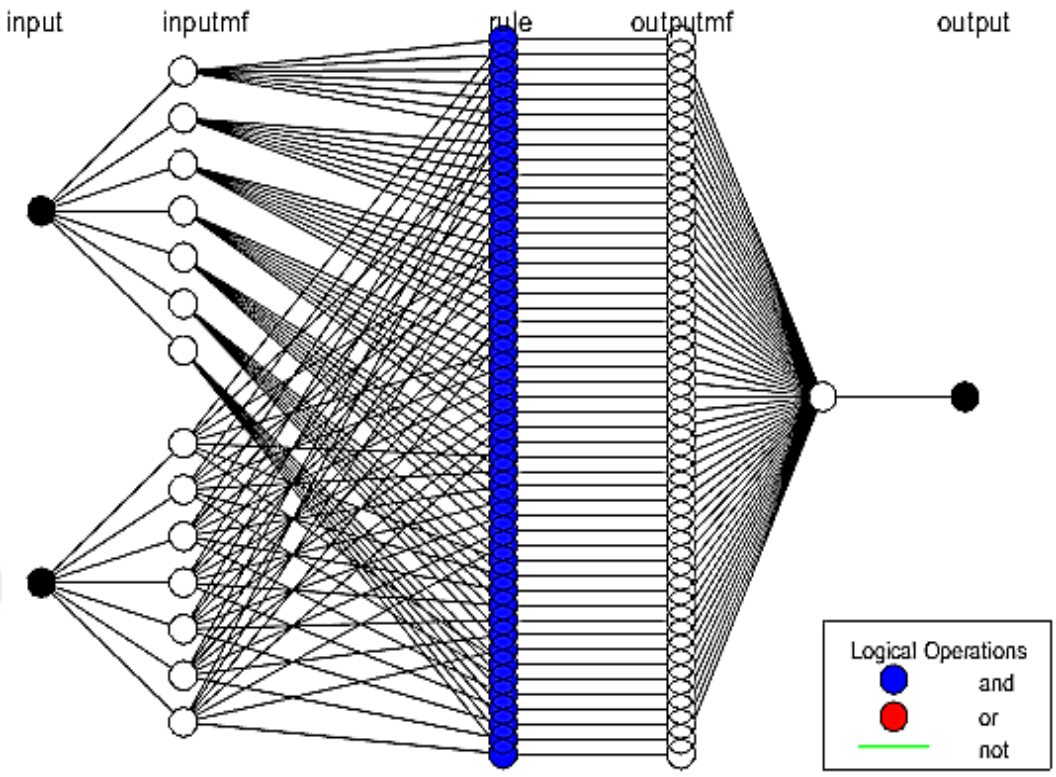

(a)

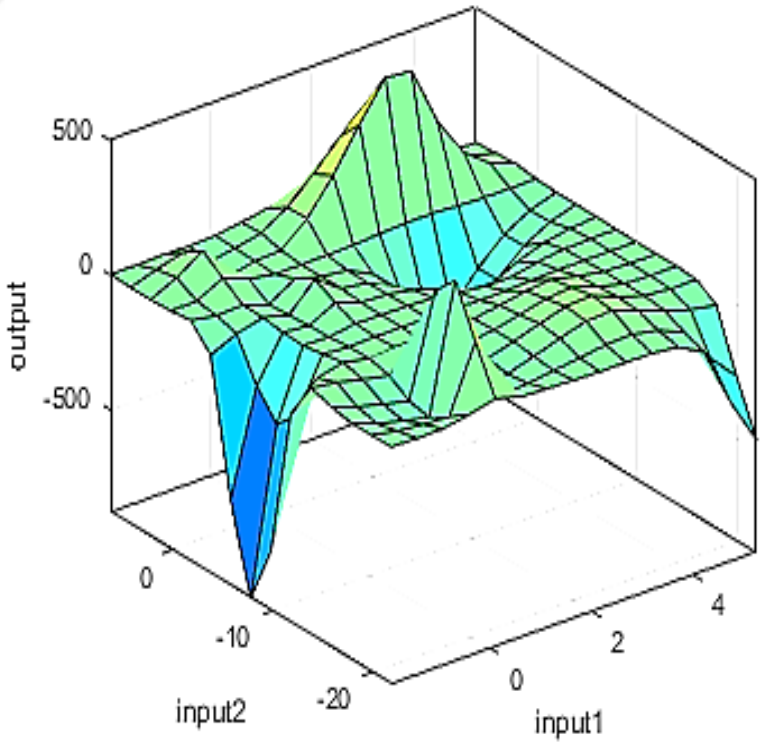

(b)

Figure 4.41. ANFIS of TLRIP: (a) network structure (b) inputs-output surface

4.8.2. Anti-swing RBNF-LQR controller of the TLRIP

The RBNF-LQR controller is explained in details in section (4.2.6). The RBNF-LQR is developed to obtain better control performance than the classical ANFIS-LQR controller. Two RBNNs are used to train the positions and velocities of state variables multiplied by their LQR gains, respectively. The inputs and output (u) data obtained from the non-linear FLQR controller are used for the training of both RBNNs. The block diagram of RBNF-LQR controller is shown as an example in Figure 4.9 in section (4.2.7). 400000 data of each input and 100000 data of output are used to train for RBNNs. For the two RBNNs, Bayesian Regularization (BR) algorithm is used to treat the inputs and the output. 70% of the data used for simulation were used for training, 15% for validation, and 15% for the testing for each RBFNN. The realized values and calculated values of all data for each RBNN of the TLRIP are shown in Figure 4.42. The regression value for all data is 0.99 for both RBNNs. As can be seen in Figure 4.43, the best validation performance value of the TLRIP is obtained at the 246-ith and 336-ith iterations for both RBNNs, respectively. The Mamdani type fuzzy model is developed and explained in section (4.2.6).

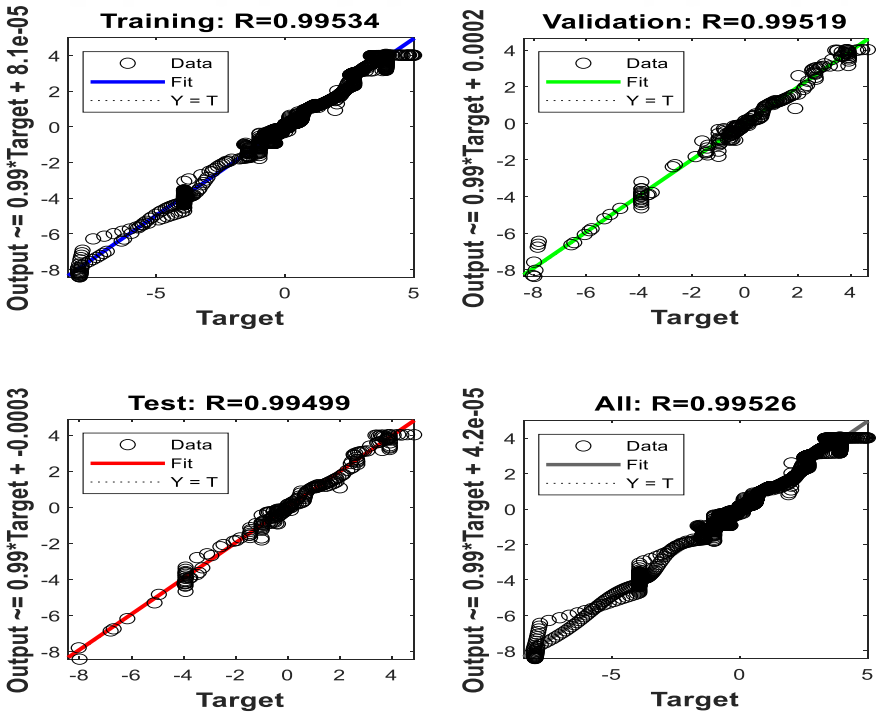

(a)

Figure 4.42. Regression graphs for : (a) positions RBNN (b) velocities RBNN

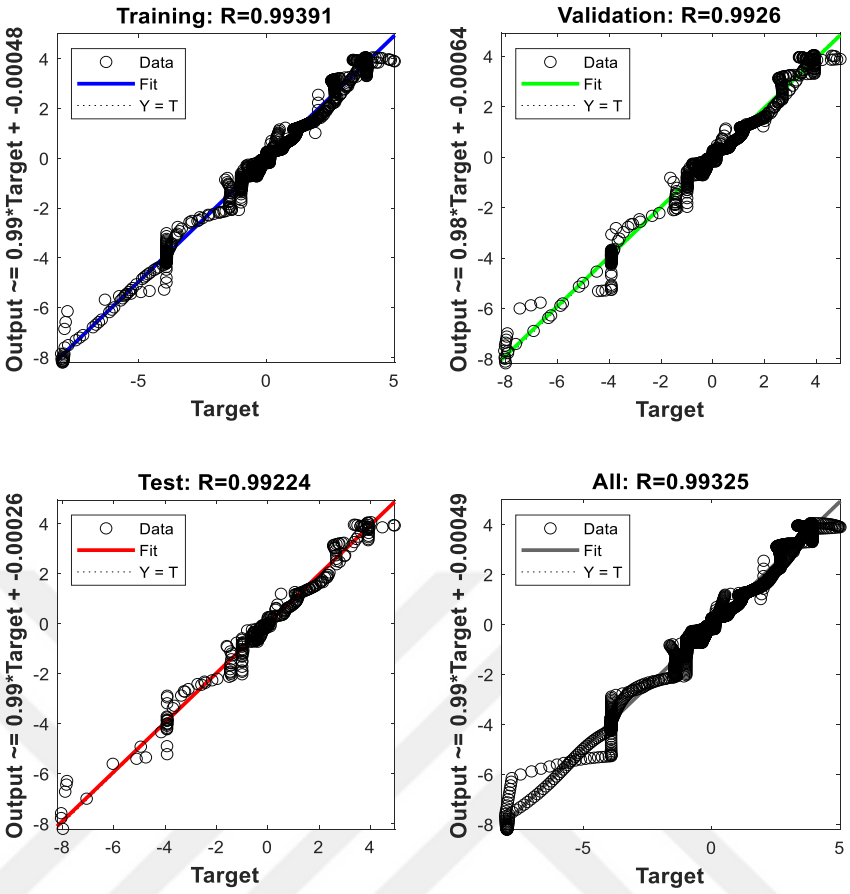

(b)

Figure 4.42.(Cont.) Regression graphs for : (a) positions RBNN (b) velocities RBNN

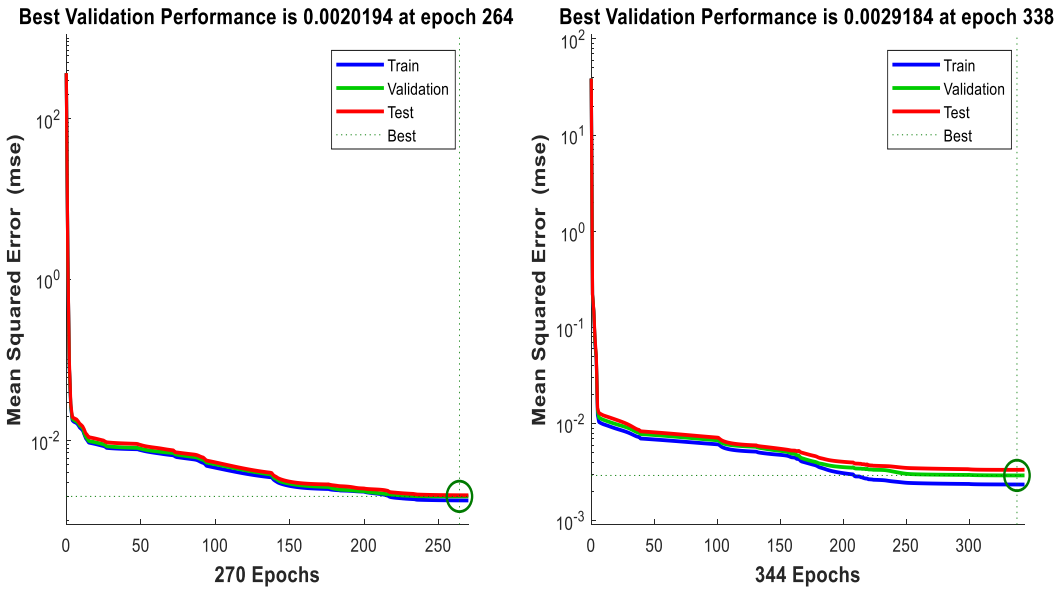

Figure 4.43. Convergence behavior of the RBNNs during training iterations: (a) positions RBNN (b) velocities RBNN

4.8.3. Comparison between the two anti-swing NF controllers of the TLRIP

In this section, both anti-swing NF controllers (ANFIS-LQR and RBNF-LQR) are compared based on the performance of the control signal obtained from the four joints of the TLRIP. According to the obtained results, the RBNF-LQR controller returned better control performance than ANFIS-LQR controller. Furthermore, the RBNF-LQR controller is chosen as our NF controller applied to the TLRIP. Figure 4.44. shown a comparison between the ANFIS-LQR and RBNF-LQR based on the performance of the control signal. In the next section, three controllers (RBNF-LQR, FLQR and LQR) are developed for the anti-swing control of the TLRIP. The three controllers are modelled and simulated in MATLAB/Simulink.

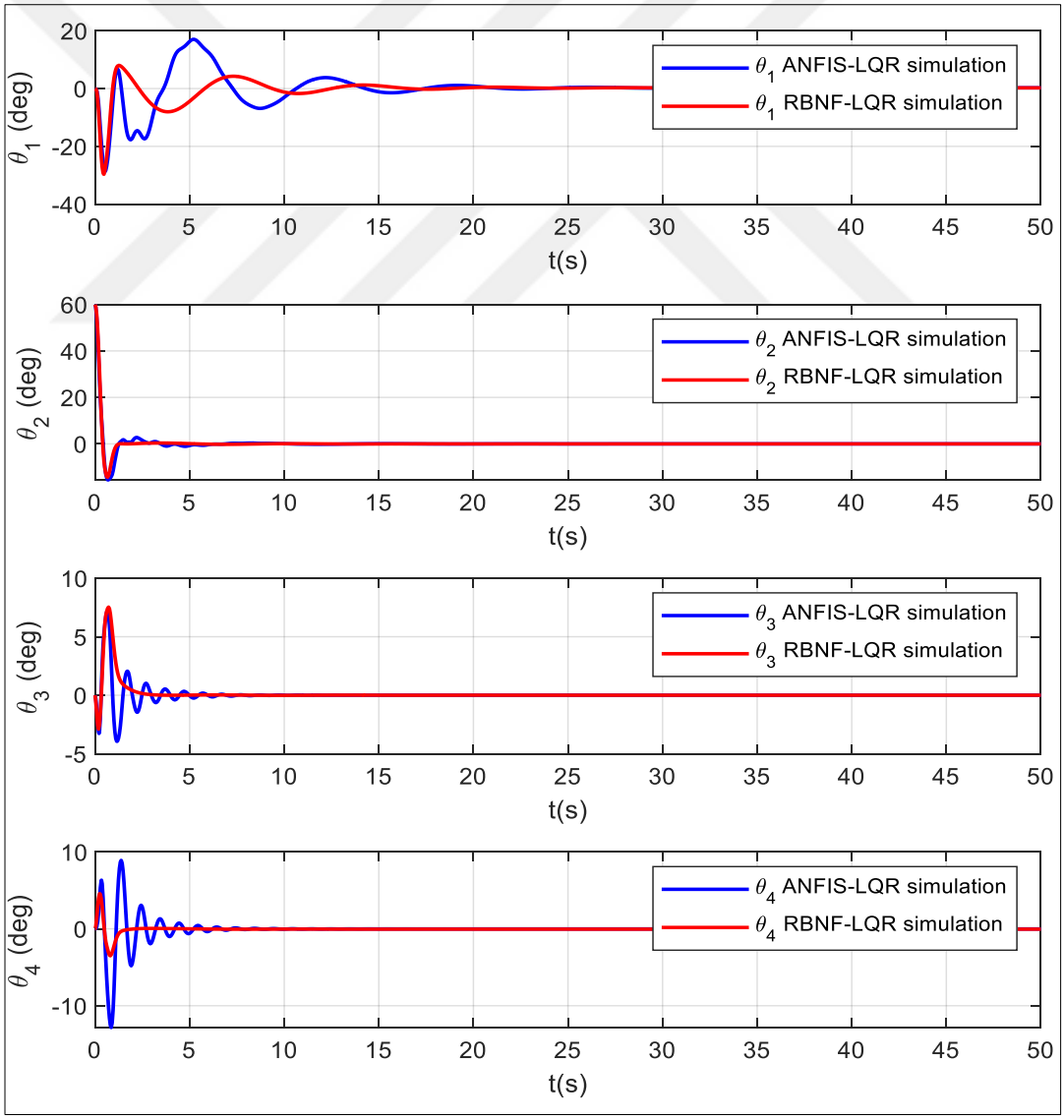

Figure 4.44. Control signal obtained by the ANFIS-LQR and RBNF-LQR

4.8.4. Anti-swing control results and robustness analysis of the TLRIP

The developed controllers (RBNF-LQR, FLQR and LQR) for the anti-swing control of the TLRIP are modeled and simulated using the SimMechanics Toolbox in MATLAB/Simulink. The anti-swing control is performed by the initial conditions of θ_1 = 0 °, θ_2 = 60°, θ_3 = 0°, θ_4 = 0°, and gain matrix K=[-0.9826 5.0197 1.5798 1.0011 -0.2527 4.9547 0.3282]. All output variables of the TLRIP need to be stabilized at the reference point by all anti-swing controllers. Moreover, a comparison between the angle signals (θ_1,θ_2, θ_3 and θ_4) with anti-swing controllers in simulation given in Figures 4.45.

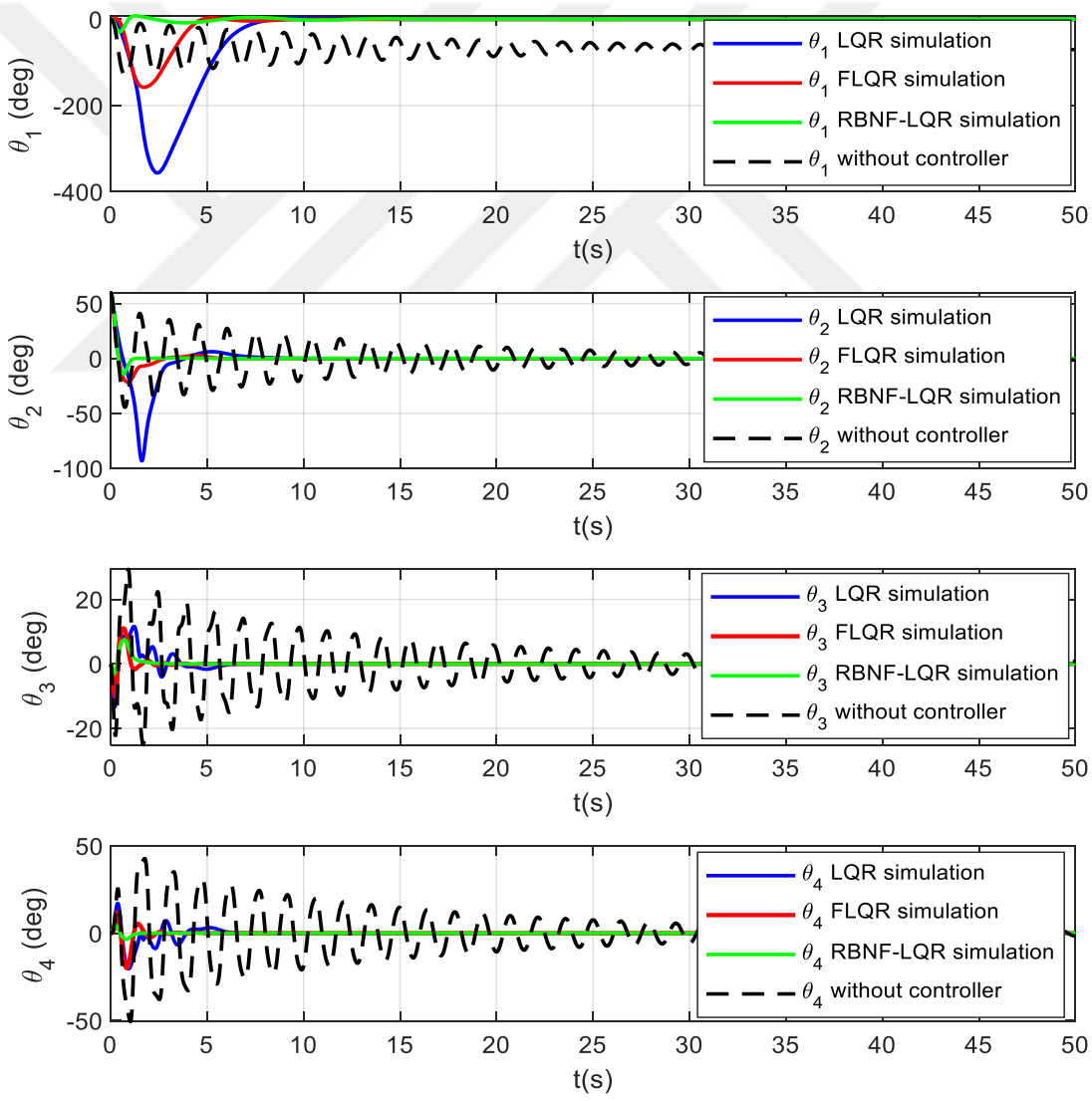

Figure 4.45. Comparison between the angle signals (θ_1,θ_2, θ_3 and θ_4) with LQR, FLQR and RBNF-LQR anti-swing controllers for TLRIP

According to the obtained results, all controllers have effectively maintained the anti-swing control of the TLRIP with minimum vibration. The RBNF-LQR controller is developed in order to give the best results in terms of T_s, MP, E_{ss} and the RMSEs than the FLQR and LQR controllers. Table 4.40 shows the comparison of LQR, FLQR and RBNF-LQR anti-swing controllers in terms of T_s, MP, E_{ss} and RMSEs.

Table 4.40. Comparison of the performance of LQR, FLQR and RBNF-LQR anti-swing controllers for the TLRIP

Controllers	Parameters	Joints			
		First Link (θ_1)	Second Link (θ_2)	Third link (θ_3)	Fourth link (θ_4)
LQR	T_s(s)	8.0366	6.9355	6.1150	6.3084
	MP (°)	356.35	93.1785	13.3801	20.3612
	E_{ss} (°)	0.28	0.00037	0.00023	0.046
	RMSE (°)	1.0593	0.1539	0.0230	0.0356
FLQR	T_s(s)	7.9398	5.1135	4.4178	4.6032
	MP (°)	157.5294	21.9637	11.0300	19.9357
	E_{ss} (°)	0.2	0.00033	0.00020	0.040
	RMSE (°)	0.4118	0.0603	0.0158	0.0257
RBNF-LQR	T_s(s)	7.6090	1.0923	2.4879	3.2473
	MP (°)	29.6568	14.3582	7.5322	4.5816
	E_{ss} (°)	0.1	0.0001	0.0001	0.020
	RMSE (°)	0.0143	0.0169	0.0033	0.0019

According to the calculated parameters, the RBNF-LQR produces better results than the FLQR and LQR. To verify the RBNF-LQR performance compared with other anti-swing controllers; the improvement percentages of all parameters are calculated and given in Table 4.41.

Table 4.41. Comparison of the performance parameters in terms of percentage between RBNF-LQR versus FLQR and RBNF-LQR versus LQR for the TLRIP

Controllers	Parameters	Joints			
		First Link (θ_1)	Second Link (θ_2)	Third link (θ_3)	Fourth link (θ_4)
RBNF-LQR versus LQR	T_s	5.32%	84.25%	59.31%	48.52%
	MP	91.67%	84.59%	43.70%	77.49%
	E_{ss}	64.28%	72.97%	56.52%	56.52%
	RMSE	98.65%	89.01%	85.65%	94.66%
RBNF-LQR versus FLQR	T_s	4.16%	78.63%	43.68%	43.68%
	MP	81.17%	34.62%	31.71%	77.01%
	E_{ss}	50.00%	69.69%	50.00%	50.00%
	RMSE	96.52%	71.97%	79.11%	92.60%

According to the calculated rate of improvement percentages in Table 4.41, the RBNF-LQR returned more accurately than LQR for the anti-swing control of the TLRIP. The T_s improvement percentages are 5.32% for the first link, 84.25% for the second link, 59.31 % for the third link and 48.52 % for the fourth link. The MP improvement percentages are 91.67% for the first link, 84.59% for the second link, 43.70% for the third link and 77.49% for the fourth link. The E_{ss} improvement percentages are 64.28% for the first link, 72.79% for the second link, 56.52% for the third link and 56.52 % for the fourth link. The RMSE improvement percentages are 98.65% for the first link, 89.01% for the second link, 85.65% for the third link and 94.66 % for the fourth link. Furthermore, the RBNF-LQR returned more accurately than FLQR for the anti-swing control of the TLRIP. The T_s improvement percentages are 4.16% for the first link, 78.63% for the second link, 43.68% for the third link and 43.68% for the fourth link. The MP improvement percentages are 81.17% for the first link, 34.62% for the second link, 31.71% for the third link and 77.01% for the fourth link. The E_{ss} improvement percentages are 50% for the first link, 69.69% for the second link, 50% for the third link and 50% for the fourth link. The RMSE improvement percentages are 96.52% for the first link, 71.97% for the second link,79.11% for the third link and 92.60% for the fourth link.

- Robustness analysis:

In this part, the developed controllers are tested for robustness under external disturbance. Figure 4.46 shows the angle signals (θ_1, θ_2, θ_3 and θ_4) with LQR, FLQR and RBNF-LQR controllers for the TLRIP under external disturbance. Based on the obtained results, all controllers are robust under external disturbance. The external disturbance is applied to the system at t=25s when the system is stable at zero position. The RBNF-LQR controller is developed to provide better control parameters than the FLQR and LQR. Table 4.42 shows a comparison of controllers in terms of Ts, MP, Ess and the RMSEs under external disturbance. According to the obtained results, the RBNF-LQR yields more perfect results than the LQR and FLQR. To analyze the performance of the RBNF-LQR compared with FLQR and LQR under external disturbance; The improvement percentages of T_s, MP, Ess and position RMSEs are calculated and given in Table 4.43.

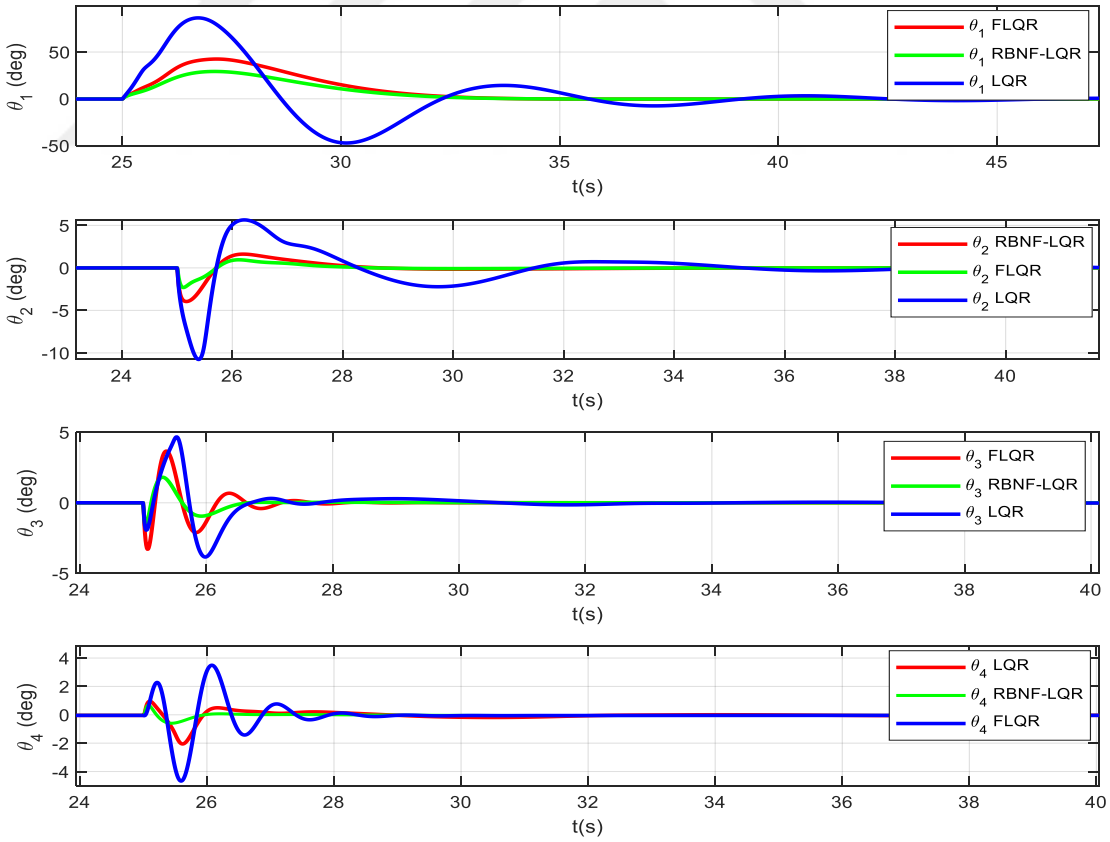

Figure 4.46. Comparison between the angle signals (θ_1,θ_2, $\theta_3$and θ_4) with LQR, FLQR and RBNF-LQR anti-swing controllers under external disturbance for TLRIP

Table 4.42. Comparison of the performance of LQR, FLQR and RBNF-LQR anti-swing controllers under external for the TLRIP

Controllers under external disturbance	Parameters	Joints			
		First Link (θ_1)	Second Link (θ_2)	Third link (θ_3)	Fourth link (θ_4)
LQR	T_s(s)	21.61	17.653	12.400	18.2952
	MP (°)	86.47	10.7703	4.6733	4.6697
	E_{ss} (°)	0.55	0.1	0.02	0.043
	RMSE (°)	0.2569	0.0179	0.0066	0.0063
FLQR	T_s(s)	13.4539	12.417	8.3664	14.6523
	MP (°)	42.4970	3.9547	3.6651	2.0547
	E_{ss} (°)	0.20	0.004	0.00022	0.041
	RMSE (°)	0.1387	0.0057	0.0045	0.0024
RBNF-LQR	T_s(s)	12.4939	12.021	8.1917	9.1151
	MP (°)	20.8681	2.3063	1.8112	0.6816
	E_{ss} (°)	0.15	0.002	0.0020	0.04
	RMSE (°)	0.0964	0.0030	0.0023	9.8547e-04

Table 4.43. Comparison of the performance parameters in terms of percentage between RBNF-LQR versus FLQR and RBNF-LQR versus LQR under external disturbance for the TLRIP

Controllers	Parameters	Joints			
		First Link (θ_1)	Second Link (θ_2)	Third link (θ_3)	Third link (θ_4)
RBNF-LQR versus LQR	T_s	41.18%	31.90%	33.93%	50.17%
	MP	75.86%	78.58%	61.24%	85.40%
	E_{ss}	72.72%	98%	90%	6.67%
	RMSE	62.47%	83.24%	65.15%	84.35%
RBNF-LQR versus FLQR	T_s	7.10%	3.189%	2.088%	37.79%
	MP	50.88%	41.68%	50.58%	66.82%
	E_{ss}	25.00%	64.91%	55.55%	2.43%
	RMSE	30.49%	47.36%	48.88%	58.93%

According to the calculated rate of improvement percentages in Table 4.43, the RBNF-LQR returned more accurately than LQR for the anti-swing control under the external disturbance of the TLRIP. The T_s improvement percentages are 41.18% for the first link, 31.90% for the second link, 33.93 % for the third link and 50.17% for the fourth link. The MP improvement percentages are 75.86% for the first link, 78.58% for the second link, 61.24% for the third link and 85.40% for the fourth link. The E_{ss} improvement percentages are 72.72% for the first link, 98% for the second link, 90% for the third link and 6.67 % for the fourth link. The RMSE improvement percentages are 62.47% for the first link, 83.24% for the second link, 65.15% for the third link and 84.35% for the fourth link. Furthermore, the RBNF-LQR returned more accurately than FLQR for the anti-swing control under the external disturbance of the TLRIP. The T_s improvement percentages are 7.10% for the first link, 3.189% for the second link, 2.88% for the third link and 37.79% for the fourth link. The MP improvement percentages are 50.88% for the first link, 41.68% for the second link, 50.58% for the third link and 66.82% for the fourth link. The E_{ss} improvement percentages are 25% for the first link, 64.91% for the second link, 55.55% for the third link and 2.43% for the fourth link. The RMSE improvement percentages are 30.49% for the first link, 47.36% for the second link, 48.88% for the third link and 58.93% for the fourth link.

In this section, a RBNF-LQR was developed and compared with FLQR and the classical LQR controller for the anti-swing control of the TLRIP. According to the obtained simulation results the RBNF-LQR controller gives better results than the FLQR and LQR controller in terms of T_s, MP, E_{ss} and RMSE. RMSEs improvement percentages between RBNF-LQR versus FLQR and RBNF-LQR versus LQR are from 71.97% to 96.52% and 85.65% to 98.65%, respectively. Furthermore, the RBNF-LQR controller produces better results than the FLQR and LQR controllers under external disturbance. RMSEs improvement percentages between RBNF-LQR versus FLQR and RBNF-LQR versus LQR are from 30.49% to 58.93% and 62.47% to 84.35% under external disturbance, respectively.

5. IMPLEMENTATION OF THE REAL SYSTEM AND EXPERIMENTAL WORK

The last chapter of this thesis deals with the real prototype of the and the experimental works. All anti-swing controllers investigate in the previous chapter for each model (SLRIP, DLRIP and TLRIP), are developed and verified experimentally. At first, the mechanical structure of the system such as the DC torque motor servo system, Motor driver, encoders, pendulums, slippings..., are described with details. Secondly, PID and LQR controllers are developed for the anti-swing control problem of the real implementation of the SLRIP. Furthermore, RBNF-LQR, FLQR and LQR are developed for the anti-swing control of the real implementations of the DLRIP and TLRIP, respectively. The dynamic responses of the anti-swing controllers were compared experimentally based on robustness analysis under external disturbances.

5.1. General Structure of the Experimental System

Our system comprises a horizontal rotary link and three pendulum links. A direct drive brushless DC torque motor servo system is mounted to provide torque to the horizontal arm to control the system. The rotary arm rotates in the horizontal plane. The first pendulum link is connected to the extremity of the rotary link, the second pendulum link is connected to the extremity of first pendulum link, and the third pendulum link is connected to the extremity of second pendulum link. The three pendulum links move like an inverted pendulum in a plane perpendicular to the rotary link. A balance mass can be attached to the other extremity of the horizontal arm to maintain the balance inertia of the system. The three pendulum links are demountable with can provide three systems SLRIP, DLRIP and TLRIP. In Figure 5.1, an original prototype design and CAD drawing of the system are depicted.

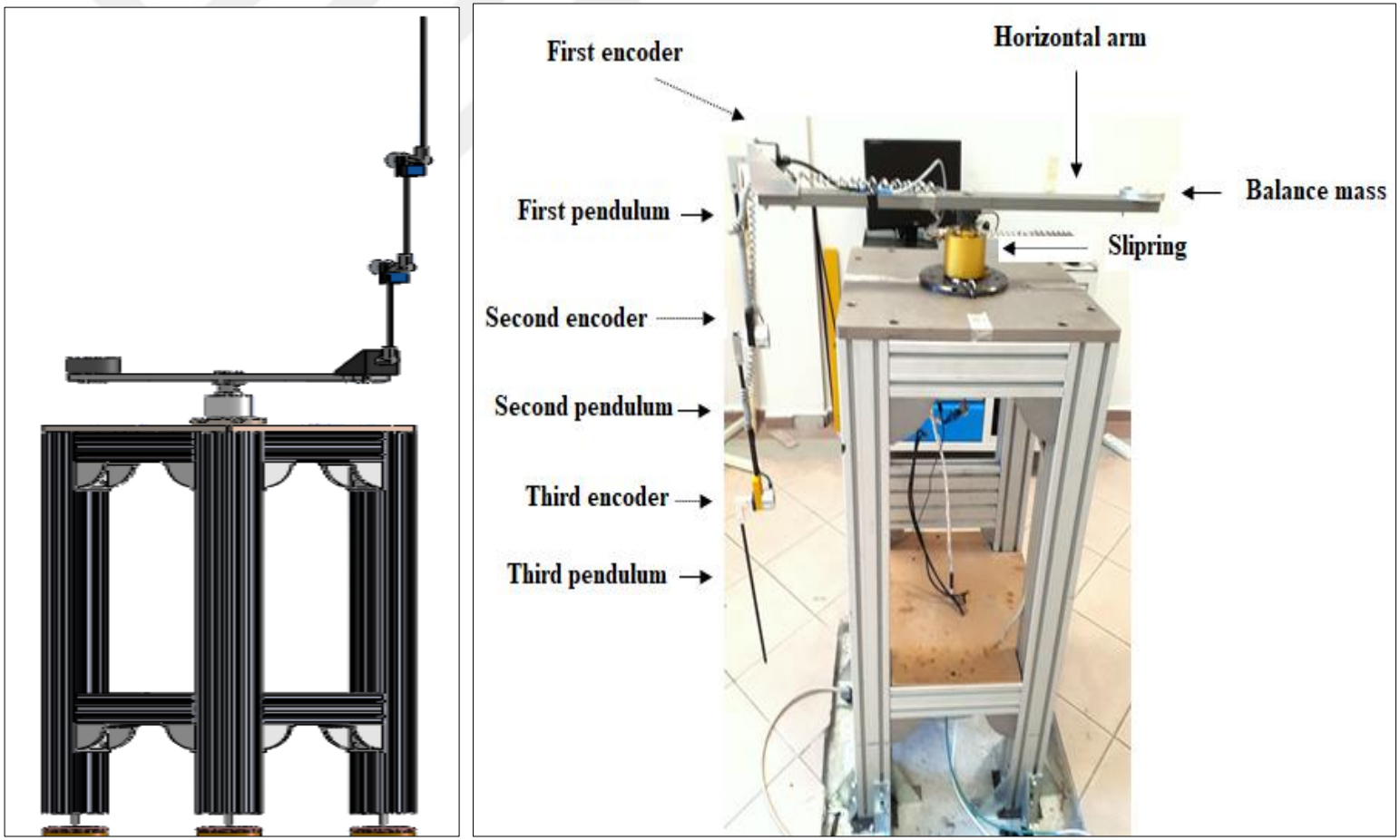

(a) (b)

Figure 5.1. (a) CAD design and (b) real prototype of the TLRIP system

The mechanical structure of the system required to achieve the following requirements:

- The base of the platform should be structurally robust and fixed to the floor to avoid the slip of the system out of the working area of the system.
- The three pendulum links must be easily demountable for different control application (SLRIP, DLRIP and TLRIP).
- The friction existing in the joint of pendulums must be seriously taken into consideration for the mechanical design of the system.
- The system must be provided for attempts to handle manual control.

Moreover, the electronic part of the system, which contains sensors, actuator and signal processing equipment needed to achieve the following requirements:

- Controller board should have a high degree of accuracy.
- Sensors must have a high rate of data acquisition.
- Actuator needed to provide the necessaire effort to control the system.
- All cables and hardware must be housed and isolated internally provide very good protection against electrical and magnetic interference.

The horizontal arm of the system is driven by a direct drive brushless DC torque motor (Type: TMH-130-050-NC, ± 10V). The motor is driven by a driver motor (Model: Lenze, Type: Inverter Drives 8400 TopLine, 2.2 Kw). The pendulums' angles are measured with three encoders having a resolution of 2048 pulses per revolution (Model: Fenac Type: 2048 PPR sin cosine accurate speed information). The signals obtained from the encoder passes through the slip ring mounted in the first joint (Model: Moflon, Type: MT10 Series). A dSPACE-DS1103 controller board treats the received signals from the encoders.

5.1.1. Brushless DC torque servo-motor

The system is driven by a direct drive brushless DC torque servo-motor (Type: TMH-130-050-NC, ± 10V) in joint of the horizontal link (θ_1). τ is the torque applied at the horizontal link produced by the torque servo-motor, it is given in the equation (5.1).

$$\tau = \frac{\eta_m K_t (V_m - K_m \dot{\theta})}{R_m} \quad (5.1)$$

Where the motor efficiency coefficient $\eta_m = 0.73$. Motor constant $K_m = 0.52$. The armature resistance $R_m = 23.4$. V_m is the input voltage. The datasheet of the servo-motor is given in Table 5.1. Figure 5.2 shows the direct drive brushless DC torque servo-motor (Type: TMH-130-050-NC, ± 10V). [145]

Table 5.1. Datasheet of the direct drive brushless DC torque servo-motor (Type: TMH-130-050-NC, ± 10V)

Motor Parameters	Symbols	Units	TMH-130-050-NC
Rated Torque	T_r	Nm	10.4
Peak Torque	T_{peak}	Nm	34.13
Rated Speed	N_r	rpm	375
No-Load Speed	$N_{no-load}$	rpm	480
Torque Constant	K_t	Nm/A	7.43
Voltage Constant	K_v	V/rpm	0.636
Max. Cogging Torque	T_{cog}	Nm	0.002
Torque Ripple	T_{ripple}	%	0.25
Number of Pole	2n	--	24
Rated Current	I_r	Arms	1.4
Peak Current	I_{peak}	Arms	5.9
Line Resistance	R_{LL}@20°	Ohm	23.4
Line Inductance	L_{LL}	mh	127.3
Stator Weight	W_s	kg	2.95
Rotor Weight	W_r	kg	0.96
Total Weight	W_{total}	kg	3.91
Meh. Time Constant	K_{mech}	ms	0.56
Thermal Resistance(2)	R_{th}	°C/W	0.61
Inertia	J	$Kg.m^2$	0.0011
Motor Constant	K_m	Nm/W	0.52
Rotor ID	mm		55
Stator OD	mm		130

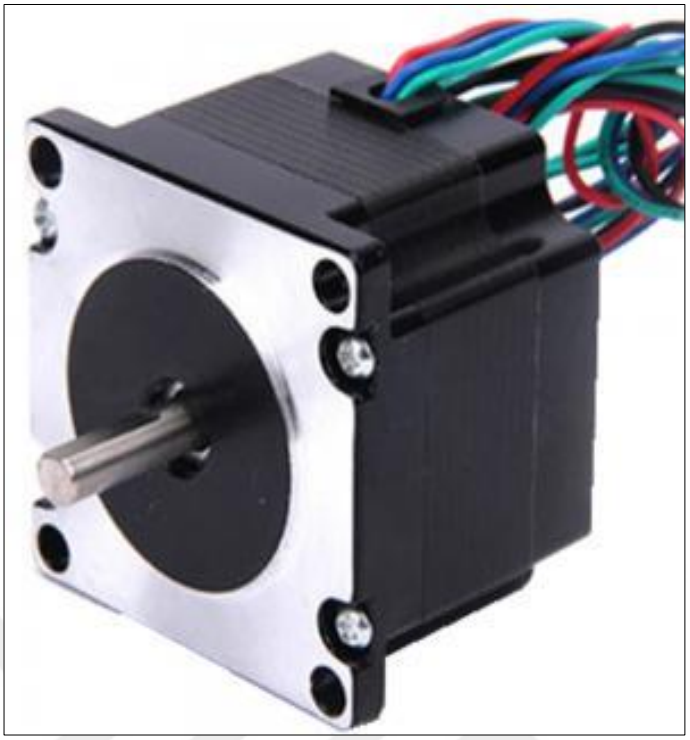

Figure 5.2. Brushless DC torque servo-motor Type: TMH-130-050-NC, ± 10V

5.1.2. Driver motor

The brushless DC torque servo-motor (Type: TMH-130-050-NC, ± 10V) is driven by a driver motor (Model: Lenze, Type: Inverter Drives 8400 TopLine) [146]. This driver is used in order to easily achieve high dynamic performance and precision in the first link of the TLRIP. The power of the driver is 2.2Kw, which supply a single phase 200/240v. This driver is particularly suitable for handling and positioning systems such as the control of the RIPS. Figure 5.3 shown the driver motor used in our system (Model: Lenze, Type: Inverter Drives 8400 TopLine).

5.1.3. Encoders

The pendulums' angles are measured with three encoders having a resolution of 2048 pulses per revolution (Model: Fenac, Type: 2048 PPR sin cosine accurate speed information) [147]. The encoder is an electro-mechanical device that converts the angular position of the shaft to digital output signals. Figure 5.4 shown an example of the encoder model used in joints for the system.

Figure 5.3. Driver motor (Model: Lenze, Type: 8400 TopLine, 2.2Kw)

Figure 5.4. Encoder (Model: Fenac, Type: 2048 PPR sin cosine accurate speed information)

5.1.4. Slip ring

The signals obtained from the encoder of each joint are passes through the slip ring mounted in the first joint. The model of the slip ring is Moflon, type: MT10 series [148]. The slip ring is an electromechanical device that allows the transmission of electrical signals from a stationary to a rotating structure. Figure 5.5 shown an example of the slip ring model mounted in the first joint of the horizontal arm.

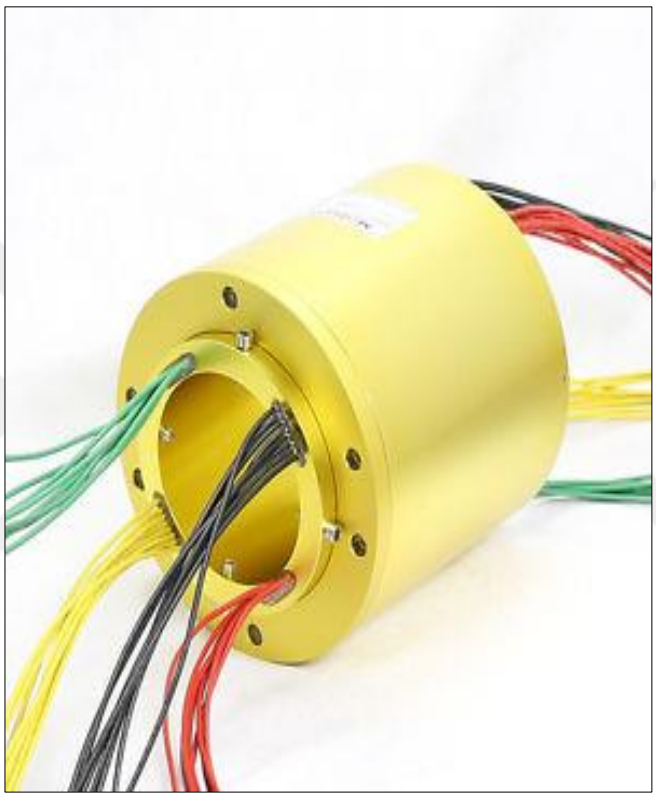

Figure 5.5. Slip ring (Model: Moflon, Type: MT10 Series)

5.1.5. Controller board

A dSPACE-DS1103 controller board is used to treat the received signals from the encoders. At present dSPACE DS1103 is the famous hardware and real-time software tools which operate through Matlab/Simulink interface programming for rapid control prototyping [149]. However, it has different various ADC and DAC ports, internal memory and a different number of input/output ports etc. Figure 5.6 shown an example of a dSPACE controller board.

Figure 5.6. An example of a dSPACE controller board

5.2. Anti-swing Control for a Real Experimental Implementation of the SLRIP

The two anti-swing controllers (PID and LQR) developed in the Simulink environment in the last chapter, will be verified experimentally in this section. The initial conditions of the links are taken with $\theta_1 = 0\,°$ and $\theta_2 = 60°$. The optimized PID controller parameters for the anti-swing controller are given in Table 4.7 in the last chapter. The anti-swing LQR controller is performed with K= [-0.2586 46.3074 1.136 -1.9724]. All output variables of the real experimental implementation of the SLRIP must be stabilized at the reference zero position by the both PID and LQR anti-swing controllers. The real experimental implementation of the SLRIP is shown in Figure 5.7. The dSPACE models of the anti-swing controllers (PID and LQR) in Matlab/Simulink are depicted in Figure 5.8. As can be seen from Figure 5.9, the horizontal arm and the pendulum link were stabilized at the reference position with minimum vibrations.

Figure 5.7. Real experimental implementation of the SLRIP

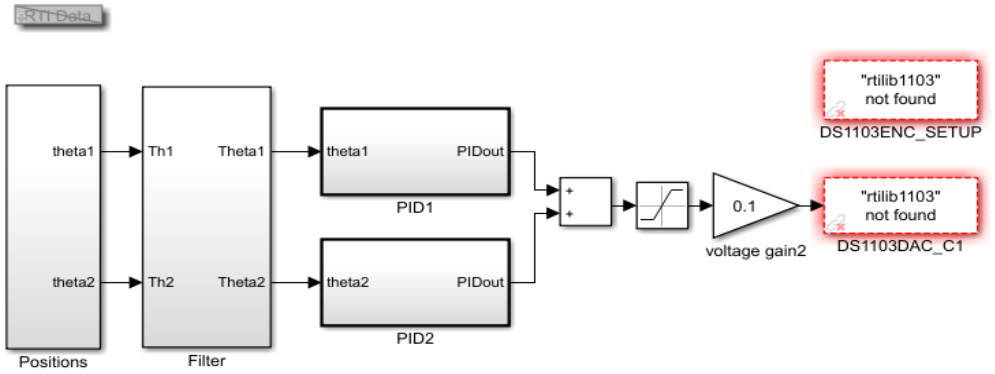

(a)

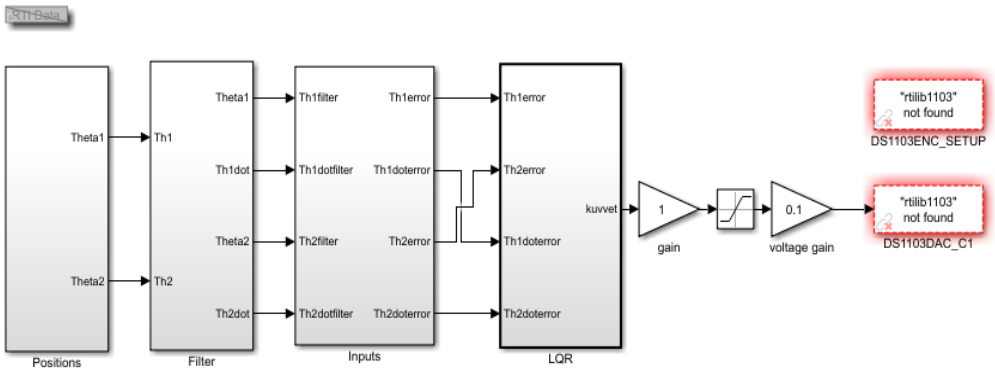

(b)

Figure 5.8. dSPACE models of the anti-swing controllers in Matlab/Simulink: (a) PID and (b) LQR

5.2.1. Performance evaluation of the anti-swing PID and LQR controllers

Figure 5.9 presents a comparison between the angle signals (θ_1 and θ_2) with PID and LQR anti-swing controllers of the real experimental implementation of the SLRIP. According to the obtained results, the PID has successfully maintained the control of the SLRIP with minimum vibrations. Furthermore, the LQR controller is developed to give better T_s, MP, E_{ss} and the RMSEs than the PID controller. Table 5.2 shown the comparison of PID and LQR controllers in terms of T_s, MP, E_{ss} and RMSEs in the experiment. According to the calculated T_s, MP, E_{ss} and position RMSEs, the LQR produces more perfect results than the PID. To understand the LQR performance compared with PID; The improvement percentages of all parameters were calculated for each case and given in Table 5.3.

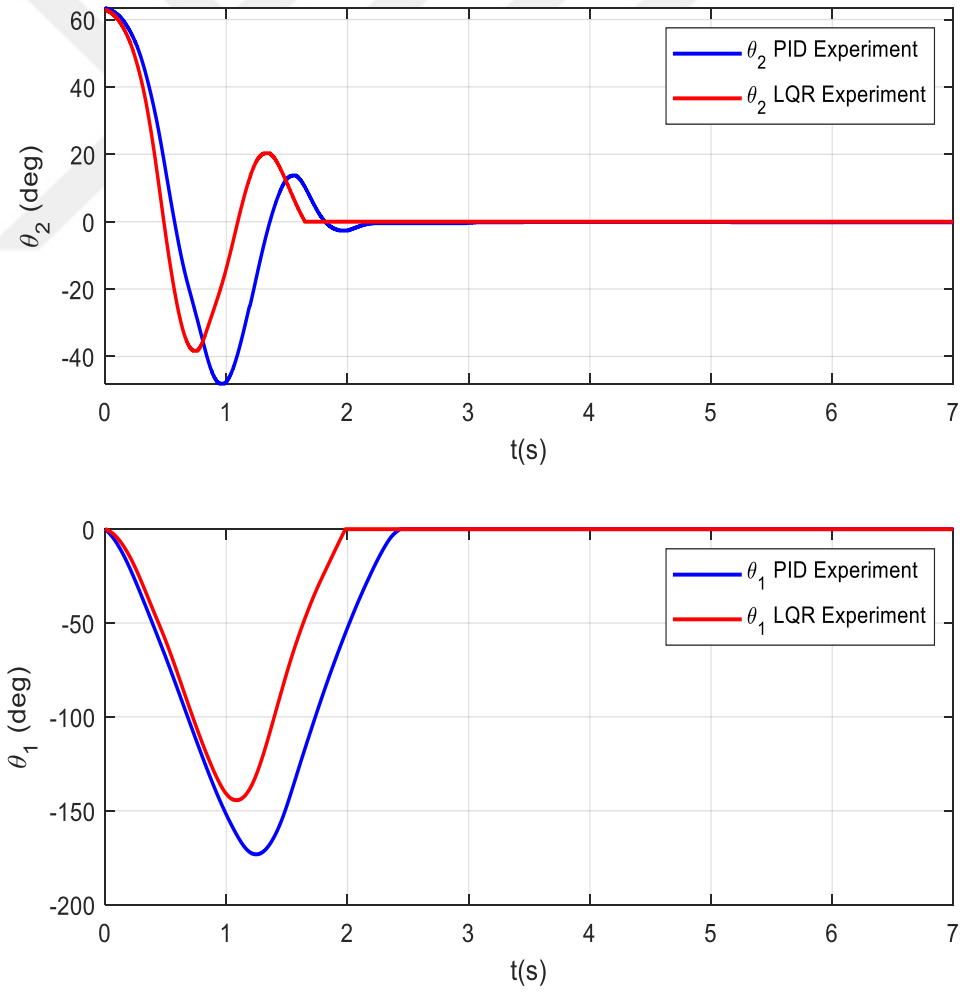

Figure 5.9. Angle signals (θ_1 and θ_2) with PID and LQR anti-swing controllers of the SLRIP in the experiment

Table 5.2. Quantitative comparison of the performance of PID and LQR anti-swing controllers in the experiment

Anti-swing controllers	Parameters	Joints	
		First Link (θ_1)	Second Link (θ_2)
PID	T_s (s)	2.3701	2.0935
	MP (°)	173.18	48.07
	E_{ss} (°)	0.1	0.01
	RMSE (°)	0.7325	0.2087
LQR	T_s (s)	1.9601	1.6307
	MP %	144.36	38.3203
	E_{ss} (°)	0.09	0.002
	RMSE (°)	0.5468	0.1808

Table 5.3. Quantitative comparison of the performance parameters in terms of percentage between PID-LQR anti-swing controllers in the experiment

Anti-swing controllers	Parameters	Joints	
		First Link (θ_1)	Second Link (θ_2)
LQR versus PID	T_s	17.21 %	22.10 %
	MP	16.64 %	20.28 %
	E_{ss}	91 %	80 %
	RMSE	25.37 %	13.36 %

According to the calculated improvement percentages in Table 5.3, the LQR returned more accurately than PID for all joints. The T_s improvement percentages are 17.21% for the first link and 22.10% for the second link. The MP improvement percentages are 16.64% for the first link and 20.28% for the second link. The E_{ss} improvement percentages are 91% for the first link, and 80% for the second link. The RMSEs improvement percentages are 25.37% for the first link and 13.36% for the second link.

The developed anti-swing controllers are tested for robustness under external disturbances in the experiment. The pendulum angles (θ_2) and the link angle (θ_1) are stabilized at zero positions. Figure 5.10 shows the angle signals (θ_1 and θ_2) with PID and LQR anti-swing controllers for the SLRIP under external disturbance in zero position at T=1s. Both anti-swing controllers are robust, and it has successfully maintained the control of the SLRIP under external disturbance. Table 5.4 shows the

comparison of PID and LQR controllers in terms of Ts, MP, Ess and the RMSEs under external disturbance in the experiment. According to the calculated parameters, the LQR yields more perfect results than the PID under external disturbance. To see the performance of the PID compared with LQR; The improvement percentages of all parameters were calculated and given in Table 5.5.

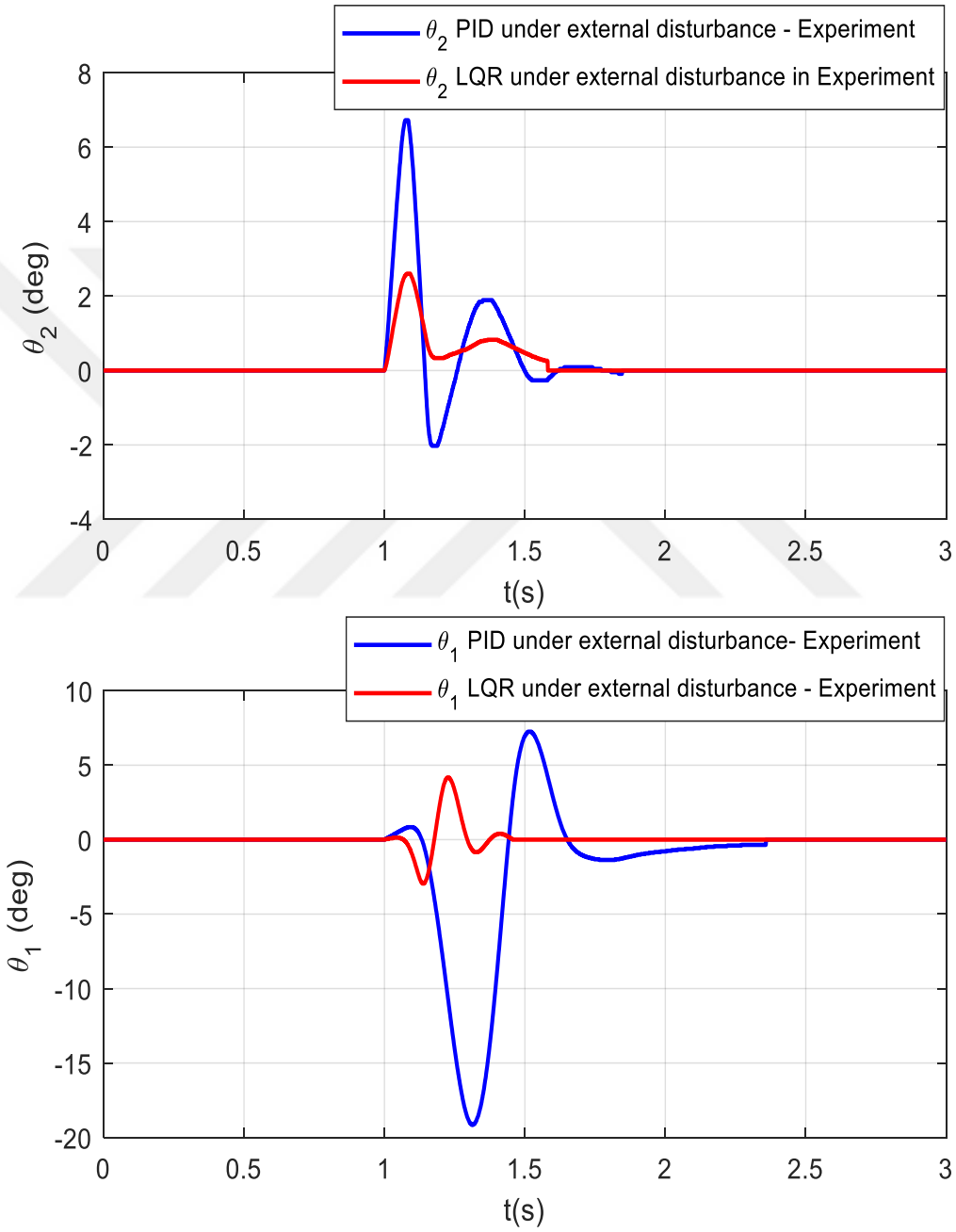

Figure 5.10. Comparison between the angle signals (θ_1 and θ_2) under external disturbance with PID and LQR anti-swing controllers of the SLRIP in the experiment

Table 5.4. Quantitative comparison of the performance of the PID and LQR anti-swing controllers under external disturbance in the experiment

Anti-swing controllers under external disturbance	Parameters	Joints	
		First Link (θ_1)	Second Link (θ_2)
PID	T_s (s)	1.2703	0.5939
	MP (°)	19.1602	6.7336
	E_{ss} (°)	0.05	0.007
	RMSE (°)	0.0778	0.0198
LQR	T_s (s)	0.4521	0.5818
	MP %	4.1748	2.6016
	E_{ss} (°)	0.03	0.005
	RMSE (°)	0.0122	0.0085

Table 5.5. Quantitative comparison of the performance parameters in terms of percentage between PID-LQR anti-swing controllers in the experiment

Anti-swing controllers under external disturbance	Parameters	Joints	
		First Link (θ_1)	Second Link (θ_2)
LQR versus PID	T_s	64.40%	2.037%
	MP	78.211 %	61.36%
	E_{ss}	40%	28.57%
	RMSE	84.31%	57.07%

According to the calculated improvement percentages in Table 5.5, the LQR returned more accurately than PID for all joints. The T_s improvement percentages are 64.40% for the first link and 2.037% for the second link. The PO improvement percentages are 78.211% for the first link and 61.36% for the second link. The E_{ss} improvement percentages are 40% for the first link, and 28.57% for the second link. The RMSEs improvement percentages are 84.31% for the first link and 57.07% for the second link.

5.3. Anti-swing Control for a Real Experimental Implementation of the DLRIP

Three controllers RBNF-LQR, FLQR and LQR developed in the Simulink environment will be verified experimentally in this section. The anti-swing control is performed by the initial conditions of $\theta_1 = 0$ °, $\theta_2 = 60°$, $\theta_3 = 0°$, and gain matrix K=[-0.1826 56.1059 1.3411 -0.8416 8.8488 0.4982]. All output variables of

the DLRIP need to be stabilized at the reference point by all anti-swing controllers. The real experimental implementation of the DLRIP is shown in Figure 5.11. The dSPACE models of the anti-swing controllers (RBNF-LQR, FLQR and LQR) in Matlab/Simulink are depicted in Figure 5.12. As can be seen from Figure 5.13, the horizontal arm and the two pendulum links were stabilized at the reference position with minimum vibrations.

Figure 5.11. Real experimental implementation of the DLRIP

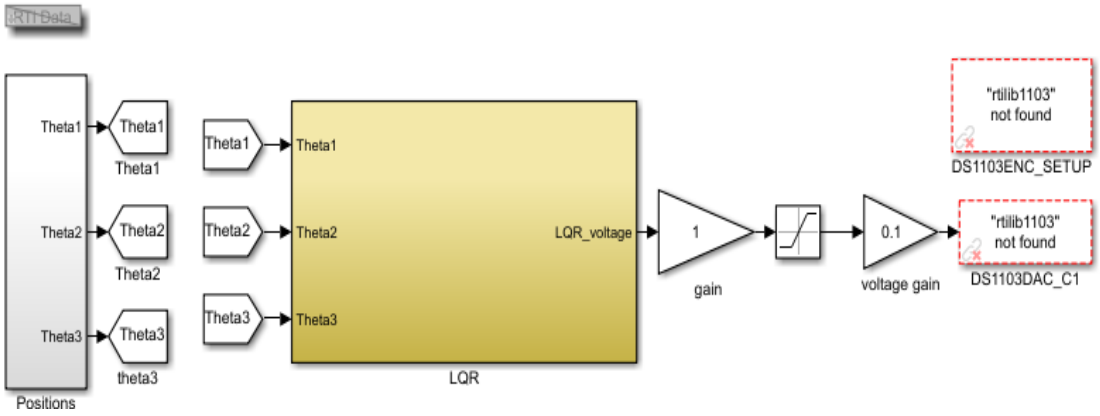

(a)

Figure 5.12. dSPACE models of the anti-swing controllers in Matlab/Simulink: (a) LQR, (b) FLQR and (c) RBNF-LQR

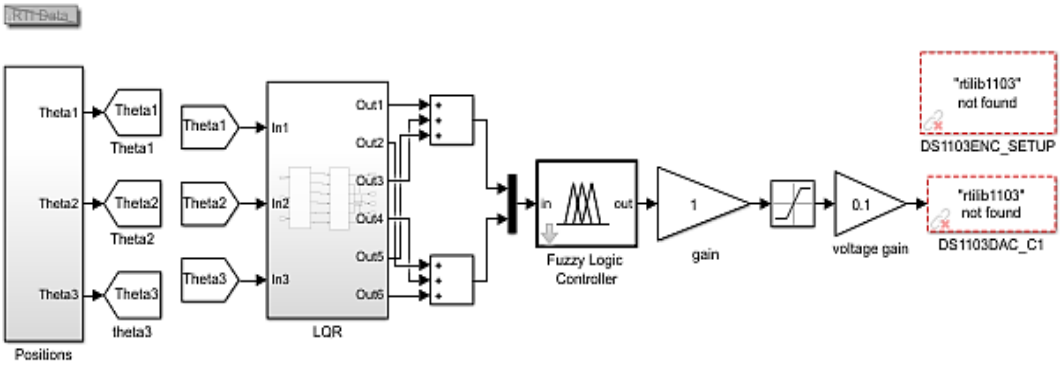

(b)

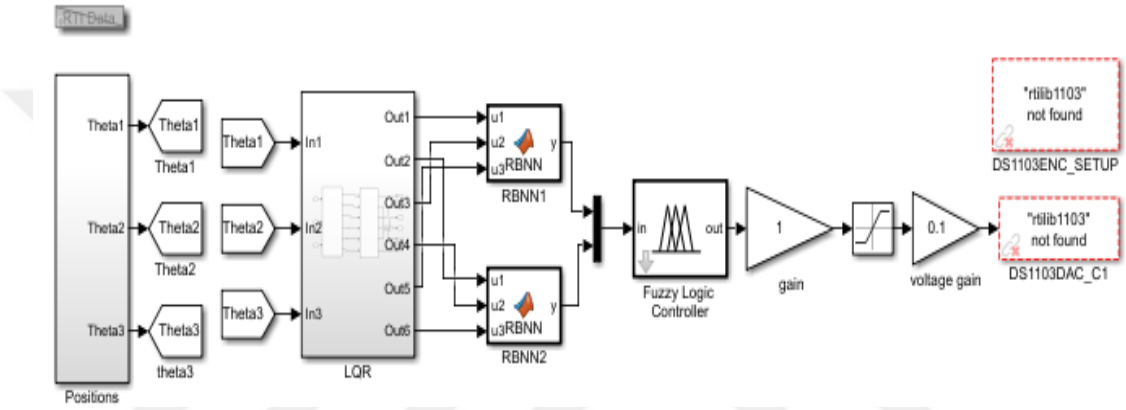

(c)

Figure 5.12.(Cont.) dSPACE models of the anti-swing controllers in Matlab/Simulink: (a) LQR, (b) FLQR and (c) RBNF-LQR

5.3.1. Performance evaluation of the anti-swing LQR, FLQR and RBNF-LQR controllers

Figure 5.13 shows a comparison between the angle signals (θ_1,θ_2 and θ_3) with anti-swing controllers of the DLRIP in experiment case. According to the obtained results, all controllers have effectively maintained the anti-swing control of the DLRP with minimum vibration. The RBNF-LQR controller is developed in order to give the best results in terms of T_s, MP, E_{ss} and the RMSEs than the FLQR and LQR controllers. Table 5.6 shows the comparison of LQR, FLQR and RBNF-LQR anti-swing controllers in terms of T_s, MP, E_{ss} and the RMSEs in the experiment. To verify the RBNF-LQR performance compared with other anti-swing controllers; the improvement percentages of all parameters are calculated and given in Table 5.7.

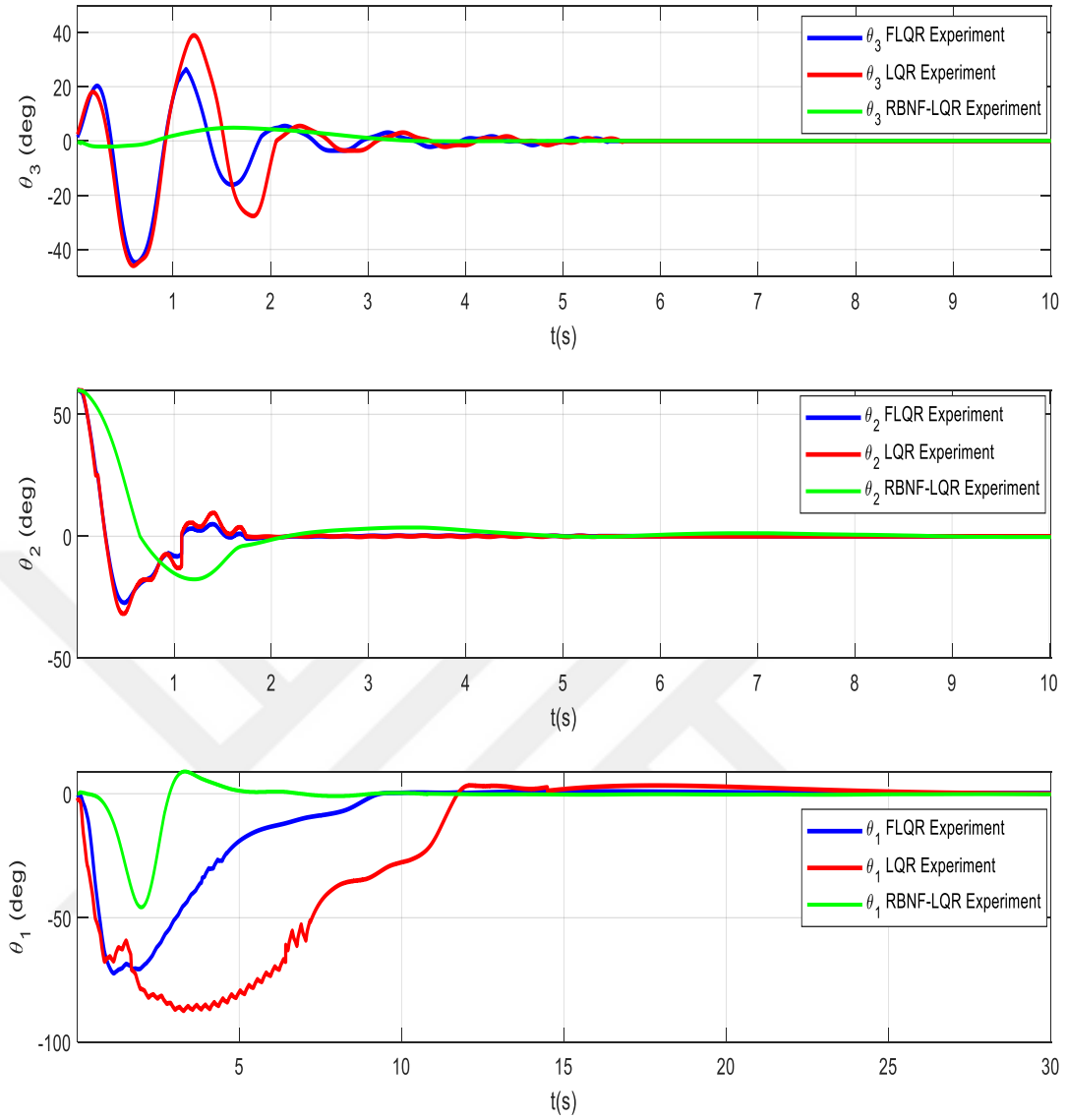

Figure 5.13. Comparison between the angle signals (θ_1,θ_2 and θ_3) with LQR, FLQR and RBNF-LQR anti-swing controllers for DLRIP in the experiment

Table 5.6. Comparison of the performance of the LQR, FLQR and RBNF-LQR anti-swing controllers in the experiment

Anti-swing controllers	Parameters	Joints		
		First Link (θ_1)	Second Link (θ_2)	Third link (θ_3)
LQR	T_s(s)	22.13	1.7292	5.2754
	MP (°)	87.56	27.7	24.3
	E_{ss} (°)	0.27	0.5	0.1
	RMSE (°)	0.1634	0.0605	0.0792

Table 5.6.(Cont.) Comparison of the performance of the LQR, FLQR and RBNF-LQR anti-swing controllers in the experiment

FLQR	T_s(s)	9.0763	1.4984	5.1250
	MP (°)	72.39	26.1	25.1
	E_{ss} (°)	0.025	0.08	0.05
	RMSE (°)	0.0908	0.0562	0.0628
RBNF-LQR	T_s(s)	6.3799	7.3946	4.1944
	MP (°)	45.77	17.65	4.8959
	E_{ss} (°)	0.01	0.02	0.001
	RMSE (°)	0.0829	0.1354	0.0256

Table 5.7. Comparison of the performance parameters in terms of percentage between RBNF-LQR versus FLQR and RBNF-LQR versus LQR in the experiment

Anti-swing controllers	Parameters	Joints		
		First Link (θ_1)	Second Link (θ_2)	Third link (θ_3)
RBNF-LQR versus LQR	T_s	71.17%	76.61%	20.49%
	MP	47.72%	36.28%	79.85%
	E_{ss}	96.29%	96 %	99%
	RMSE	49.26%	55.31%	67.67%
RBNF-LQR versus FLQR	T_s	29.70%	79.73%	18.15%
	MP	36.77%	32.37%	4.47%
	E_{ss}	60%	75%	98%
	RMSE	8.70%	58.49%	59.23%

- Robustness analysis:

In this part, the developed controllers are tested for robustness under external disturbance in the experiment. Figure 5.14 shows the angle signals (θ_1, θ_2 and θ_3) with LQR, FLQR and NLFLQR controllers for the DLRIP under external disturbance. Based on the obtained results, all controllers are robust under disturbance. The RBNF-LQR controller is developed to give better control parameters than the FLQR and LQR. Table 5.8 shows a comparison of controllers in terms of T_s, MP, E_{ss} and the RMSEs under external disturbance in the experiment. According to the obtained results, the RBNF-LQR yields perfect results than the LQR and FLQR. To see the

performance of the RBNF-LQR compared with FLQR and LQR under external disturbance; The improvement percentages of T_s, MP, E_{ss} and position RMSEs were calculated and given in Table 5.9.

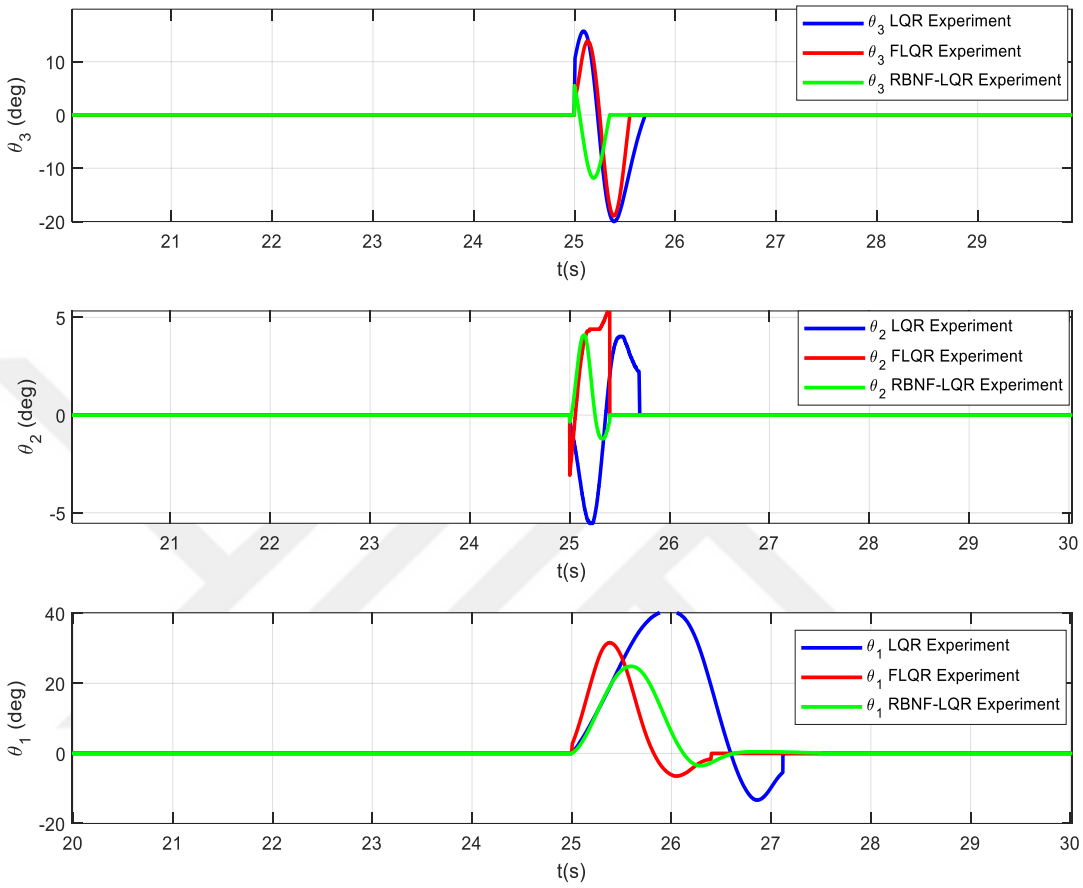

Figure 5.14. Comparison of the performance LQR, FLQR and RBNF-LQR anti-swing controllers under external disturbance in the experiment

Table 5.8. Comparison of the performance of the LQR, FLQR and RBNF-LQR anti-swing controllers

Anti-swing controllers under external disturbance	Parameters	Joints		
		First Link (θ_1)	Second Link (θ_2)	Third link (θ_3)
LQR	T_s(s)	2.0	2.1	1.1
	MP (°)	45	10	16
	E_{ss} (°)	0.21	0.040	0.01
	RMSE (°)	0.0254	0.0051	0.0038
FLQR	T_s(s)	1.0	1.1	0.9
	MP (°)	42	8	14

Table 5.8.(Cont.) Comparison of the performance of the LQR, FLQR and RBNF-LQR anti-swing controllers

	E_{ss} (°)	0.19	0.035	0.002
	RMSE (°)	0.0160	0.0024	0.0031
RBNF-LQR	T_s(s)	0.9s	0.5	0.2
	MP (°)	31	6	11
	E_{ss} (°)	0.010	0.010	0.001
	RMSE (°)	0.0111	0.0017	9.4636e-04

Table 5.9. Comparison of the performance parameters in terms of percentage between RBNF-LQR versus FLQR and RBNF-LQR versus LQR under external disturbance in the experiment

Controllers	Parameters	Joints		
		First Link (θ_1)	Second Link (θ_2)	Third link (θ_3)
RBNF-LQR versus LQR	T_s(s)	55.00%	76.19%	81.81%
	MP (°)	31.11%	40%	31.25%
	E_{ss} (°)	95.23%	75%	90%
	RMSE (°)	56.29%	66.66%	75.09%
RBNF-LQR versus FLQR	T_s(s)	9.99%	54.54%	77.77%
	MP (°)	26.19%	25%	21.42%
	E_{ss} (°)	94.73%	71.42%	50%
	RMSE (°)	30.62%	29.16%	69.47%

In this section, the RBNF-LQR was developed and compared experimentally with FLQR and the classical LQR controller for the anti-swing control of the real experimental implementation of the DLRIP. According to the obtained simulation results the RBNF-LQR controller gives better results than the FLQR and LQR controller in terms of T_s, MP, E_{ss} and RMSE. RMSEs improvement percentages between RBNF-LQR versus FLQR and RBNF-LQR versus LQR are from 8.70% to 73.40% and 49.26% to 67.67% in the experiment, respectively. Furthermore, the RBNF-LQR controller produces better results than the FLQR and LQR controllers under external disturbance. RMSEs improvement percentages between RBNF-LQR versus FLQR and RBNF-LQR versus LQR are from 29.18% to 69.47% and 59.29% to 75.09% under external disturbance in the experiment, respectively. Furthermore,

non-linear controllers may be developed and compared experimentally witch the RBNF-LQR.

5.4. Anti-swing Control for a Real Experimental Implementation of the TLRIP

Three controllers (RBNF-LQR, FLQR and LQR) are developed for the anti-swing control of the TLRIP in the Simulink environment in the last chapter, will be verified experimentally in this section. The anti-swing control is performed by the initial conditions of $\theta_1 = 0\ °$, $\theta_2 = 60°$, $\theta_3 = 0°$, $\theta_4 = 0°$, and gain matrix K=[-0.9826 5.0197 1.5798 1.0011 -0.2527 4.9547 0.3282]. All output variables of the TLRIP need to be stabilized at the reference point by all anti-swing controllers. The real experimental implementation of the TLRIP is shown in Figure 5.15. The dSPACE models of the anti-swing controllers (RBNF-LQR, FLQR and LQR) in Matlab/Simulink are depicted in Figure 5.16. As can be seen from Figure 5.17, the horizontal arm and the three pendulum links were stabilized at the reference position with minimum vibrations.

Figure 5.15. Real experimental implementation of the TLRIP

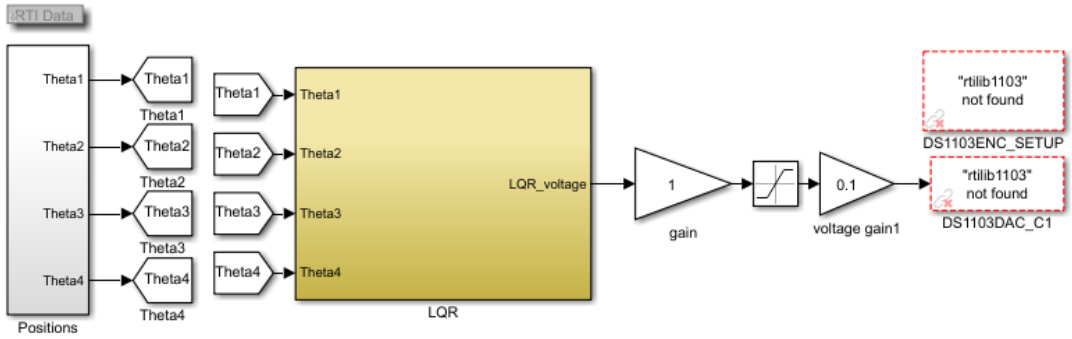

(a)

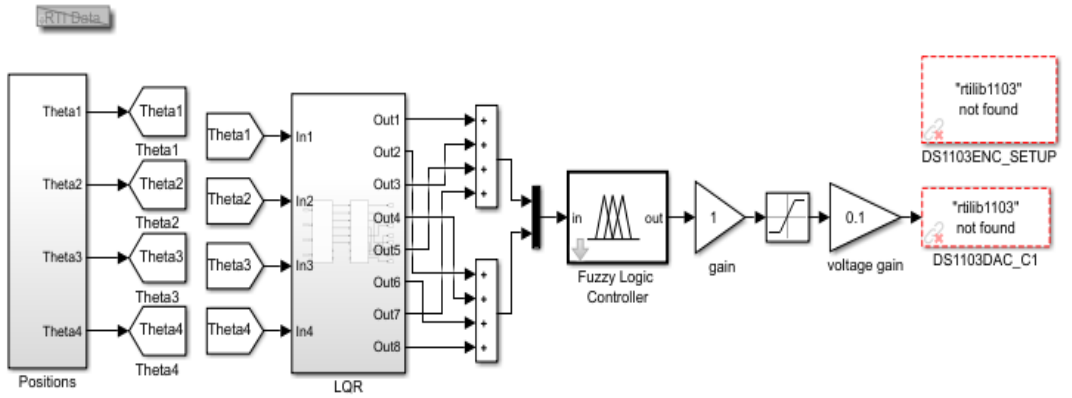

(b)

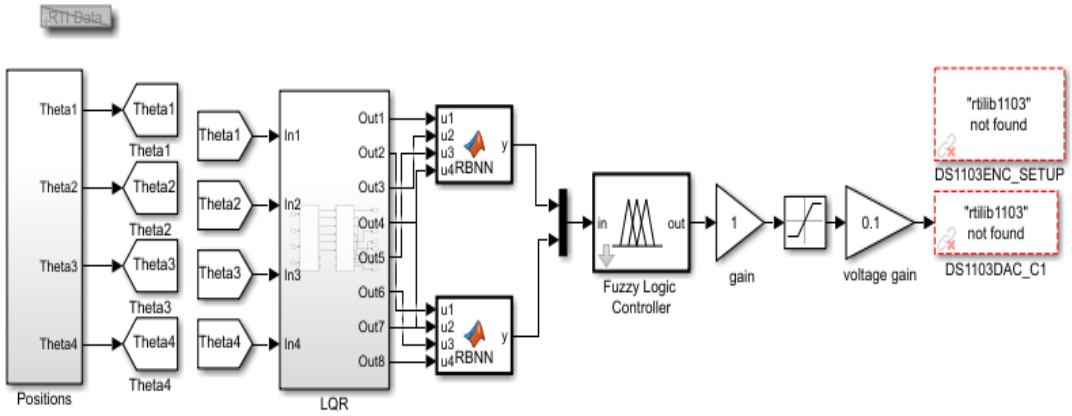

(c)

Figure 5.16. dSPACE models of the anti-swing controllers in Matlab/Simulink: (a) LQR, (b) FLQR and (c) RBNF-LQR

5.4.1. Performance evaluation of the anti-swing LQR, FLQR and RBNF-LQR controllers

Figure 5.17 shows a comparison between the angle signals (θ_1,θ_2,θ_3 and θ_4) with anti-swing controllers of the TLRIP in the experiment. According to the obtained results, all controllers have effectively maintained the anti-swing control of the TLRIP

with minimum vibration. The RBNF-LQR controller is developed in order to give the best results in terms of T_s, MP, E_{ss} and the RMSEs than the FLQR and LQR controllers. Table 5.10 shows the comparison of LQR, FLQR and RBNF-LQR anti-swing controllers in terms of T_s, MP, E_{ss} and the RMSEs in the experiment. To verify the RBNF-LQR performance compared with other anti-swing controllers; the improvement percentages of all parameters are calculated and given in Table 5.11.

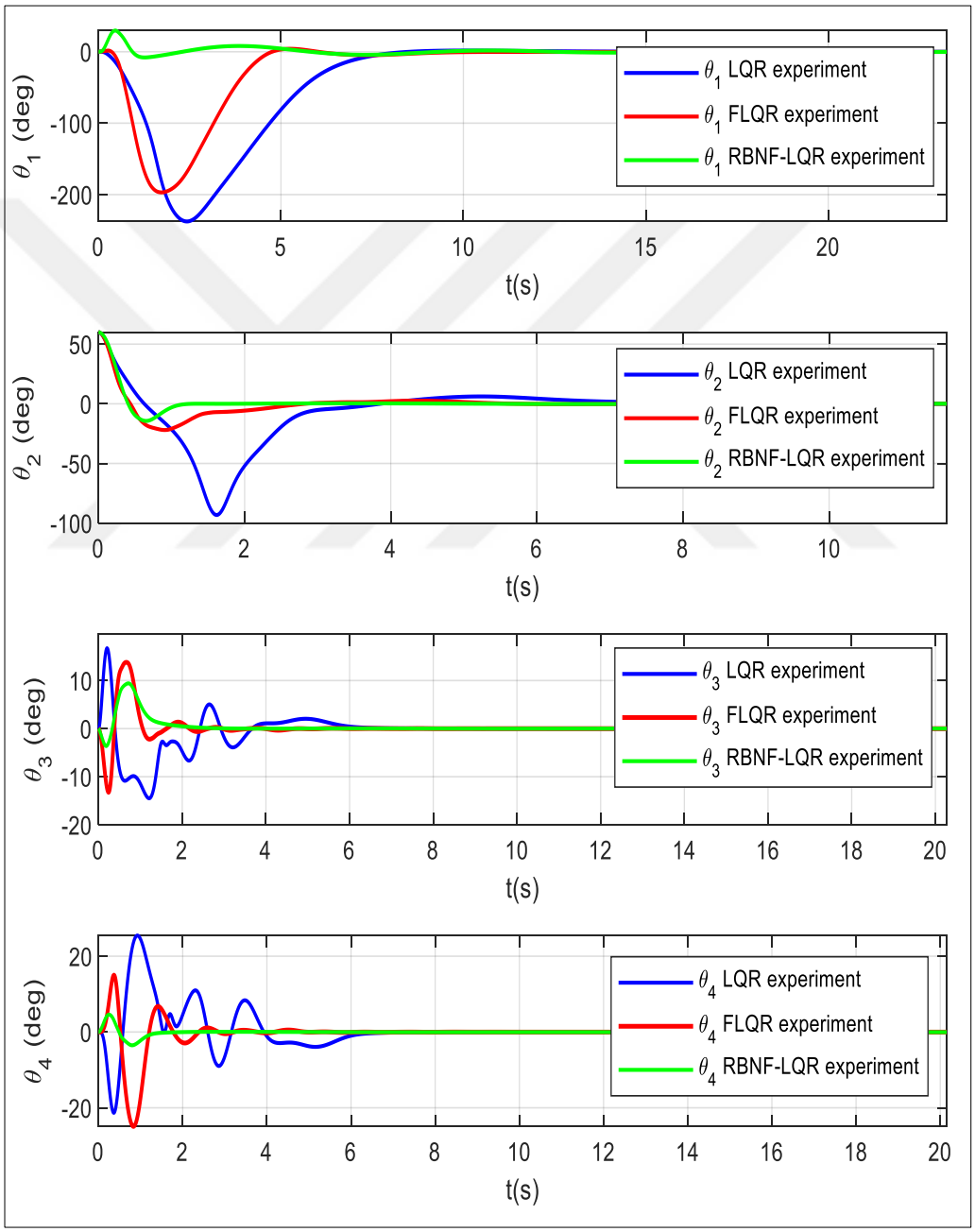

Figure 5.17. Comparison between the angle signals (θ_1,θ_2, θ_3 and θ_4) with LQR, FLQR and RBNF-LQR anti-swing controllers for TLRIP in the experiment

Table 5.10. Comparison of the performance of LQR, FLQR and RBNF-LQR anti-swing controllers for the TLRIP in the experiment

Anti-swing controllers Controllers	Parameters	Joints			
		First Link (θ_1)	Second Link (θ_2)	Third link (θ_3)	Fourth link (θ_4)
LQR	T_s(s)	7.91	3.48	4.98	5.41
	MP (°)	226.40	95.19	18.87	24.61
	E_{ss} (°)	0.35	0.02	0.055	0.1
	RMSE (°)	0.7062	0.1539	0.0248	0.0441
FLQR	T_s(s)	5.324	1.59	2.61	2.59
	MP (°)	200.64	25.05	15.03	22.39
	E_{ss} (°)	0.25	0.015	0.023	0.045
	RMSE (°)	0.5147	0.0603	0.01698	0.0321
RBNF-LQR	T_s(s)	2.1	1.27	2.197	1.21
	MP (°)	15.78	10.98	10.031	5.69
	E_{ss} (°)	0.01	0.0018	0.01	0.0020
	RMSE (°)	0.1428	0.0169	0.0041	0.0019

Table 5.11. Comparison of the performance parameters in terms of percentage between RBNF-LQR versus FLQR and RBNF-LQR versus LQR for the TLRIP in the experiment

Controllers	Parameters	Joints			
		First Link (θ_1)	Second Link (θ_2)	Third link (θ_3)	Fourth link (θ_4)
RBNF-LQR versus LQR	T_s	73.45%	63.50%	55.88%	77.63%
	MP	93.03%	56.16%	45.36%	76.87%
	E_{ss}	97.14%	91%	81.81%	98%
	RMSE	79.04%	89.01%	83.46%	95.69%
RBNF-LQR versus FLQR	T_s	60.55%	20.12%	15.82%	53.28%
	MP	92.84%	88.46%	33.26%	74.58%
	E_{ss}	96.00%	88 %	56.52%	95.55%
	RMSE	71.24%	71.97%	75.85%	94.08%

According to the calculated rate of improvement percentages in Table 5.11, the RBNF-LQR returned more accurately than LQR for the anti-swing control of the TLRIP. The T_s improvement percentages are 73.45% for the first link, 63.50% for the second link, 55.88% for the third link and 77.63% for the fourth link. The MP improvement percentages are 93.03% for the first link, 56.36% for the second link, 45.36% for the third link and 76.87% for the fourth link. The E_{ss} improvement percentages are 97.14% for the first link, 91% for the second link, 81.81% for the third link and 98% for the fourth link. The RMSE improvement percentages are 79.04% for the first link, 89.01% for the second link, 83.46% for the third link and 95.69% for the fourth link. Furthermore, the RBNF-LQR returned more accurately than FLQR for the anti-swing control of the TLRIP. The T_s improvement percentages are 60.55% for the first link, 20.12% for the second link, 15.82% for the third link and 53.28% for the fourth link. The MP improvement percentages are 92.84% for the first link, 88.46% for the second link, 33.26% for the third link and 74.58% for the fourth link. The E_{ss} improvement percentages are 96% for the first link, 88% for the second link, 56.52% for the third link and 95.55% for the fourth link. The RMSE improvement percentages are 71.24% for the first link, 71.97% for the second link, 75.85% for the third link and 94.08% for the fourth link.

- Robustness analysis:

In this part, the developed controllers are tested for robustness under external disturbance in the experiment. Figure 5.18 shows the angle signals (θ_1, θ_2, θ_3 and θ_4) with LQR, FLQR and RBNF-LQR controllers for the TLRIP under external disturbance. Based on the obtained results, all controllers are robust under external disturbance. The external disturbance is applied to the system at t=25s when the system is stable at zero position. The RBNF-LQR controller is developed to provide better control parameters than the FLQR and LQR. Table 5.12 shows a comparison of controllers in terms of Ts, MP, Ess and the RMSEs under external disturbance. According to the obtained results, the RBNF-LQR yields more perfect results than the LQR and FLQR. To analyze the performance of the RBNF-LQR compared with FLQR and LQR under external disturbance; The improvement percentages of T_s, MP, Ess and position RMSEs are calculated and given in Table 5.13.

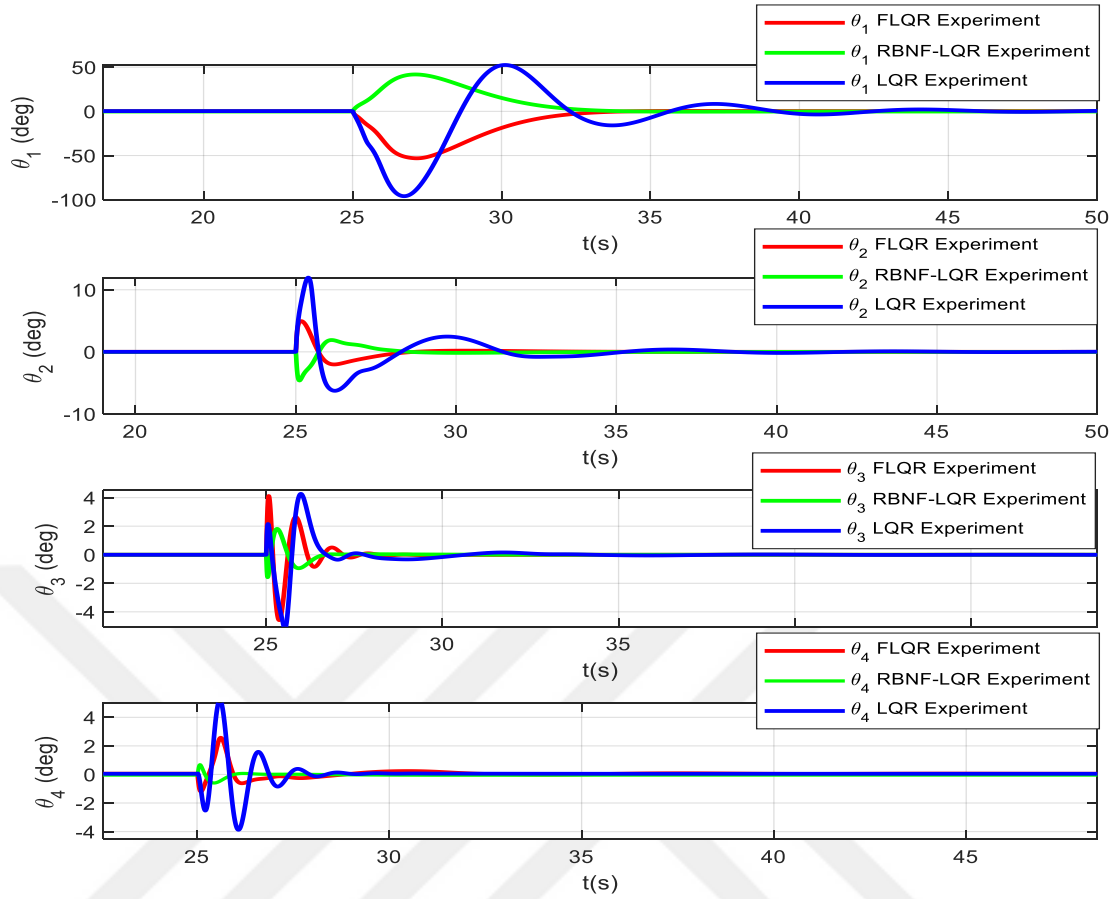

Figure 5.18. Comparison between the angle signals (θ_1,θ_2, $\theta_3$and θ_4) with LQR, FLQR and RBNF-LQR anti-swing controllers under external disturbance for TLRIP in the experiment

Table 5.12. Comparison of the performance of LQR, FLQR and RBNF-LQR anti-swing controllers under external for the TLRIP in the experiment

Controllers under external disturbance	Parameters	Joints			
		First Link (θ_1)	Second Link (θ_2)	Third link (θ_3)	Fourth link (θ_4)
LQR	T_s(s)	12.89	7.872	3.55	3.2952
	MP (°)	99.89	13.98	6.478	5.89
	E_{ss} (°)	0.5	0.65	0.1	0.05
	RMSE (°)	0.2851	0.0199	0.0074	0.0070
FLQR	T_s(s)	7.9	2.5	1.37	1.65
	MP (°)	52.13	4.78	4.71	2.2
	E_{ss} (°)	0.2	0.01	0.03	0.045

Table 5.12.(Cont) Comparison of the performance of LQR, FLQR and RBNF-LQR anti-swing controllers under external for the TLRIP in the experiment

	RMSE (°)	0.1734	0.0072	0.0057	0.0030
RBNF-LQR	T_s(s)	7.5	2.35	1.19	1.12
	MP (°)	30.91	2.11	2.01	0.71
	E_{ss} (°)	0.1	0.002	0.01	0.001
	RMSE (°)	0.1377	0.0061	0.0025	9.92628e-04

Table 5.13. Comparison of the performance parameters in terms of percentage between RBNF-LQR versus FLQR and RBNF-LQR versus LQR under external disturbance for the TLRIP in the experiment

Controllers	Parameters	Joints			
		First Link (θ_1)	Second Link (θ_2)	Third link (θ_3)	Third link (θ_4)
RBNF-LQR versus LQR	T_s	41.81%	70.14%	60.47%	66.01%
	MP	69.05%	84.90%	68.97%	87.94%
	E_{ss}	80%	99.69%	90%	98%
	RMSE	51.70%	69.34%	66.21%	85.81%
RBNF-LQR versus FLQR	T_s	5.06%	5.99%	13.13%	32.12%
	MP	40.70%	55.85%	57.32%	69.72%
	E_{ss}	50%	80.0%	66.66%	97.77%
	RMSE	20.58%	15.27%	56.14%	66.91%

According to the calculated rate of improvement percentages in Table 5.13, the RBNF-LQR returned more accurately than LQR for the anti-swing control under the external disturbance of the TLRIP. The T_s improvement percentages are 41.18% for the first link, 70.14% for the second link, 60.47% for the third link and 66.01% for the fourth link. The MP improvement percentages are 69.05% for the first link, 84.90% for the second link, 68.97% for the third link and 87.94% for the fourth link. The E_{ss} improvement percentages are 80% for the first link, 99.69% for the second link, 90% for the third link and 98 % for the fourth link. The RMSE improvement percentages are 51.70% for the first link, 69.34% for the second link, 66.21% for the third link and 85.81% for the fourth link. Furthermore, the RBNF-LQR returned more accurately than FLQR for the anti-swing control under the external disturbance of the TLRIP. The T_s improvement percentages are 5.06% for the first link, 5.99% for the second

link, 13.13% for the third link and 32.12% for the fourth link. The MP improvement percentages are 40.70% for the first link, 55.85% for the second link, 57.32% for the third link and 69.72% for the fourth link. The E_{ss} improvement percentages are 50% for the first link, 80% for the second link, 66.66% for the third link and 97.77% for the fourth link. The RMSE improvement percentages are 20.58% for the first link, 15.27% for the second link, 56.14% for the third link and 66.91% for the fourth link.

In this section, a RBNF-LQR was developed and compared with FLQR and the classical LQR controller for the anti-swing control of the TLRIP. According to the obtained experimental results the RBNF-LQR controller gives better results than the FLQR and LQR controller in terms of T_s, MP, E_{ss} and RMSE. RMSEs improvement percentages between RBNF-LQR versus FLQR and RBNF-LQR versus LQR are from 71.24% to 94.08% and 79.04% to 95.69%, respectively. Furthermore, the RBNF-LQR controller produces better results than the FLQR and LQR controllers under external disturbance. RMSEs improvement percentages between RBNF-LQR versus FLQR and RBNF-LQR versus LQR are from 15.27% to 66.91% and 51.70% to 85.81% under external disturbance, respectively

6. CONCLUSIONS AND RECOMMENDATIONS

In this thesis, a novel design of a single, double and triple link rotary inverted system is developed to be controlled. This system presents an important challenging problem in the area of linear and nonlinear control engineering applications. The contribution of this thesis consisted of the development of novel friction estimation models which take into consideration positions, velocities and accelerations of the joints of three serial pendulum links. Furthermore, more sophisticated nonlinear controllers such as FLQR, FLQG, RBNF-LQR are developed for the stabilization and anti-swing control problems. The novel nonlinear controllers take into consideration the complex inputs-outputs and nonlinear function approximation of the system.

In this research, joint frictions of the TLRIP are examined based on its experimental and simulation dynamic responses. Three different friction estimation models such as NCFM, LFM and NLFM are compared to estimate the joint frictions of the TLRIP developed in our laboratory. In order to determine the estimation performance of the friction models, RMSEs between position simulation results obtained from each joint friction model and encoders in the experimental setup are computed. According to the comparative experimental friction analysis, the joint frictions of the TLRIP are estimated more effectively using an NLFM which yields better improvement percentage from 11.56% to 94.55%. Moreover, AFEMs were developed to estimate the frictions in three pendulums' joints of the TLRIP and compared with existing friction estimation models NCFM, LFM, and NLFM. Based on the position RMSEs obtained from each joint friction model, the AFEMs were better than the existing friction estimation models (NCFM, LFM, and NLFM). Among the friction estimation models and considering the RMSEs of position in all joints, the best results were produced by the ANLFM, which provide the best improvement percentage from 1.99 % to 93.84%. At last, NFFEMs are developed to estimate the joint friction coefficients in a TLRIP system and compared with an AFEMs. The different versions of the AFEMs and NFFEMs are generated based on each of the following friction estimation models: NCFM, LFM, and NLFM. The aim of this study is to obtain joint

friction models which depend on both velocity and acceleration in a large range of motion trajectory that involves difficult and sudden large changes. In order to determine the estimation performance of the friction models, the RMSEs of position in all joints are computed. The NFFEMs produce better estimation results than the AFEMs. Among NFFEMs, the NFNLM gives the best results which provide the best improvement percentage from 11.56% and 94.55%. In this research, the friction study has three important contributions to the literature: Firstly, all friction models in the literature depend only on velocity; however, the friction model developed here depends on both velocity and acceleration. This approach has enabled us to obtain a two-dimensional friction model. Secondly, the coefficients of all friction models in the literature were constant when the physical quantities change. On the other hand, the coefficients of the friction models in this work vary depending on the state of the velocity and acceleration. Hence, this friction model allows for better estimation of the effects of friction in different velocity and acceleration conditions. Thirdly, much of existing researches in the literature have studied only the frictions of the linear motion which depends on linear velocity and force. This work examines frictions on the joints which have hard rotational motions.

The stabilization and anti-swing control problems of the system are studied for the SLRIP, DLRIP and TLRIP, respectively. To determine the control performance of all controllers, different control parameters are computed such as T_s, PO, E_{ss}, MP and the RMSEs of the joint positions. PID, LQR and swing-up based LQR controllers are developed for the stability control problem of the SLRIP. The controllers are compared under external disturbance. The robustness results indicate that the LQR controller under external disturbances was effective. The RMSEs improvement percentages between LQR versus PID are from 24.28% to 75,28%. Moreover, according to the incremental calculated percentages of RMSEs of the control signals, the LQR returned more effort than PID with 42.95 % under external disturbance. Furthermore, nonlinear FLQR and FLQG controllers are developed for the stability control of the DLRIP and TLRIP systems. The aim of this work is to study dynamic performance analysis of both FLQR and FLQG controllers and to compare them with the classical LQR and LQG controllers, respectively. The developed controllers were tested under internal and external disturbances to determine the robustness performance of the controllers.

According to the obtained simulation results, the nonlinear FLQR and FLQG controllers are robust and produce better results than the LQR and LQG controllers. Based on to the obtained results of the stability control of the DLRIP, the RMSEs improvement percentages between FLQR and LQR are from 6.69% to 75% and 25.23% to 65.26% under external and internal disturbances, respectively. Similarly, RMSEs improvement percentages between FLQG and LQG are from 14.64% to 74.99% and 25.23% to 49.41% under external and internal disturbances, respectively. Moreover, the LQG and FLQG controllers in the DLRIP were tested in the presence of white noise with different SNRs. The LQG and FLQG controllers show very good noise rejection feature. The increment percentages of RMSEs of the control signals for the FLQR and FLQG compared with LQR and LQG are from 34.53% to 66.62%. Accordingly, the FLQR and FLQG controllers need more control efforts than the classical LQR and LQG. On the other hand, based on the obtained results of the stability control of the TLRIP, the RMSEs improvement percentages between FLQR and LQR range from 12.34% to 74.99% and 42.10% to 81.59% under external and internal disturbances, respectively. Similarly, RMSEs improvement percentages between FLQG and LQG are from 0.20% to 7.21% and 37.49% to 98.81% under external and internal disturbances, respectively. Moreover, the increment percentages of RMSEs of the control signals for the FLQR and FLQG compared with LQR and LQG are from 36.65% to 75.55%. Accordingly, the FLQR and FLQG controllers need more control efforts than the classical LQR and LQG. The design compromise between controller performance and efforts should be made based on which one is more important than others. Generally, the performance of the controller is a more crucial aspect of control applications.

In this research, PID and LQR are developed for the anti-swing control problem of the SLRIP. Both controllers are compared under external disturbance. The results indicate that the LQR controller returned best results than the PID. The RMSEs improvement percentages between LQR versus PID are from 6.091% to 31.82% and 13.36% to 25.37% in simulation and experiment, respectively. Also, the LQR controller produces better results than the PID controller under external disturbance. The RMSEs improvement percentages between LQR versus PID are from 50.09% to 51.28% and 57.07% to 84.31% under external disturbance in simulation and experiment,

respectively. Furthermore, nonlinear RBNF-LQR controller is developed for the anti-swing control problem of the DLRIP and TLRIP systems in order to obtain better results than the FLQR and LQR controllers. Based on the obtained results of the anti-swing control of the DLRIP. The RMSEs improvement percentages between RBNF-LQR versus FLQR and RBNF-LQR versus LQR are from 8.79% to 73.40% and 2.82% to 93.36% in simulation, respectively. The RMSEs improvement percentages between RBNF-LQR versus FLQR and RBNF-LQR versus LQR are from 8.70% to 73.40% and 49.26% to 67.67% in the experiment, respectively. Furthermore, the RBNF-LQR controller produces better results than the FLQR and LQR controllers under external disturbance. The RMSEs improvement percentages between RBNF-LQR versus FLQR and RBNF-LQR versus LQR are from 4.042% to 47.36% and 9.090% to 36.02% under external disturbance in simulation, respectively. The RMSEs improvement percentages between RBNF-LQR versus FLQR and RBNF-LQR versus LQR are from 29.18% to 69.47% and 59.29% to 75.09% under external disturbance in the experiment, respectively. On the other hand, based on the obtained results of the anti-swing control of the TLRIP. The RMSEs improvement percentages between RBNF-LQR versus FLQR and RBNF-LQR versus LQR are from 71.97% to 96.52% and 85.65% to 98.65% in simulation, respectively. RMSEs improvement percentages between RBNF-LQR versus FLQR and RBNF-LQR versus LQR are from 71.24% to 94.08% and 79.04% to 95.69% in the experiment, respectively. Furthermore, the RBNF-LQR controller produces better results than the FLQR and LQR controllers under external disturbance. RMSEs improvement percentages between RBNF-LQR versus FLQR and RBNF-LQR versus LQR are from 30.49% to 58.93% and 62.47% to 84.35% under external disturbance in simulation, respectively. RMSEs improvement percentages between RBNF-LQR versus FLQR and RBNF-LQR versus LQR are from 15.27% to 66.91% and 51.70% to 85.81% under external disturbance in the experiment, respectively.

Some future works recommendation be given as follows:

- The fuzzification ranges and rules of the NF system can be tuned with evolutionary algorithms to enhance the estimation performance of the NFFEMs.
- More inputs such as jerks and snaps of the joints can be applied to the NF system, and the TLRIP system can be controlled using the proposed friction models.

- Swing-up controllers can be conducted to prove the experimental performance of the non-linear controllers such as (FLQR, FLQG, RBNF-LQR).
- The proposed controller method can be compared with other non-linear controllers existing in the literature.

REFERENCES

[1] Richard Dorf C., Bishop R.H., Modern Control Systems, 1998.

[2] Ness D.J., Small Oscillations of a Stabilized, Inverted Pendulum, *American Journal of Physics 35*, 1967, no. **10**, 964-967.

[3] Blitzer L., Inverted Pendulum, *American Journal of Physics*, 1965, **33**(12), 1076-8.

[4] Bogdanoff J.L., Citron S.J., Experiments with an Inverted Pendulum Subject to Random Parametric Excitation, *Journal of the Acoustical Society of America*, 1965, **38**(3), 447-52.

[5] Kalmus H.P., The Inverted Pendulum, *American Journal of Physics*, 1970, **38**(7), 874-8.

[6] Lundberg K.H., Barton TW., History of Inverted-Pendulum Systems, *IFAC Proceedings Volumes*, 2010, **42**(24), 131-5.

[7] Wang H., Chamroo A., Vasseur C., Koncar V., Stabilization of a 2-DOF Inverted Pendulum by a Low Cost Visual Feedback, *American Control Conference*, *IEEE*, 3851-3856, 11 Jun 2008.

[8] Bettayeb M., Boussalem C., Mansouri R., Al-Saggaf UM. Stabilization of an Inverted Pendulum-Cart System by Fractional PI-State Feedback, *ISA transactions*, 2014, **53**(2), 508-16.

[9] Stimac A.K., Standup and Stabilization of the Inverted Pendulum, *Doctoral dissertation, Massachusetts Institute of Technology, Dept. of Mechanical Engineering*, 1999.

[10] Krafes S., Chalh Z., Saka A., A Review on the Control of Second Order Underactuated Mechanical Systems, *Complexity*, Sep 2018.

[11] https://www.quanser.com/products/linear-servo-base-unit-inverted-pendulum/ (Last Visited: 06 Dec 2020).

[12] Chen X., Yu R., Huang K., Zhen S., Sun H., Shao K., Linear Motor Driven Double Inverted Pendulum: A Novel Mechanical Design as a Testbed for Control Algorithms, *Simulation Modelling Practice and Theory*, 2018, **81**, 31-50.

[13] Niemann H., Poulsen J.K., Design and Analysis of Controllers for a Double Inverted Pendulum, *ISA transactions*, 2005, **44**(1), 145-63.

[14] Naghmehm B., Hooshiar A., Masoudrazban J., chun-Yi Su., Stabilization of Double Inverted Pendulum On Cart: LQR Approach, *International Journal of Mechanical and Production Engineering*, 2017, **2**, Vol.5.

[15] https://www.quanser.com/products/linear-double-inverted-pendulum/ (Last Visited: 06. December.2020).

[16] Eltohamy K.G., Kuo C.Y., Nonlinear Optimal Control of a Triple Link Inverted Pendulum with Single Control Input, *International Journal of Control*, 1998, **69**(2), 239-56.

[17] Eltohamy K.G., Kuo C.Y., Real Time Stabilisation of a Triple Link Inverted Pendulum Using Single Control Input, *IEE Proceedings-Control Theory and Applications*, 1997, **144**(5), 498-504.

[18] Sehgal S, Tiwari S., LQR Control for Stabilizing Triple Link Inverted Pendulum System, *International Conference on Power, Control and Embedded Systems, IEEE*, pp. 1-5, 17 Dec 2012.

[19] Šetka V., Čečil R., Schlegel M., Triple Inverted Pendulum System Implementation Using a New ARM/FPGA Control Platform, *18th International Carpathian Control Conference (ICCC), IEEE*, pp.321-326, 28 May 2017.

[20] Glück T., Eder A., Kugi A., Swing-Up Control of a Triple Pendulum on a Cart with Experimental Validation, *Automatica*, 2013, **49**(3), 801-8.

[21] Franco E., Astolfi A., Baena FR y., Robust Balancing Control of Flexible Inverted-Pendulum Systems, *Mechanism and Machine Theory*, 2018, 130, 539-51.

[22] Gandhi P.S., Borja P., Ortega R., Energy Shaping Control of an Inverted Flexible Pendulum Fixed to a Cart, *Control Engineering Practice*, 2016, **56**, 27-36.

[23] Walker K., Hauser H., Evolving Optimal Learning Strategies for Robust Locomotion in the Spring-Loaded Inverted Pendulum Model, *International Journal of Advanced Robotic Systems*, 2019, **16**(6), 1729881419885701.

[24] Saranlı U., Arslan Ö., Ankaralı MM, Morgül Ö., Approximate Analytic Solutions To Non-Symmetric Stance Trajectories of the Passive Spring-Loaded Inverted Pendulum With Damping, *Nonlinear Dynamics*, 2010, **62**(4), 729-42.

[25] Blickhan R., The Spring-Mass Model for Running and Hopping, *Journal of biomechanics*,1989, **22**(11-12), 1217-27.

[26] Luo Q, Chevallereau C, Aoustin Y., Walking Stability of a Variable Length Inverted Pendulum Controlled with Virtual Constraints, *International Journal of Humanoid Robotics*, 2019, 1950040.

[27] Stilling D.S., Szyszkowski W., Controlling Angular Oscillations Through Mass Reconfiguration: A Variable Length Pendulum Case, *International Journal of Non-Linear Mechanics*, 2002, **37**(1), 89-99.

[28] Navarro-López E.M., Fossas-Colet E., Stabilization of the Variable-Length Pendulum, *European Control Conference (ECC), IEEE*, pp. 675-680, 4 Sep 2001.

[29] Xing L., Chen Y., Wu X., A Novel Parallel-Type Double Inverted Pendulum Control Method, *International Conference on Intelligent Computing and Intelligent Systems, IEEE*, Vol. 1, pp. 880-887, 29 Oct 2010.

[30] Xin X., Kaneda M., Analysis of The Energy-Based Control for Swinging Up Two Pendulums, *IEEE Transactions on Automatic Control*, 2005, **50**(5), 679-84.

[31] Deng M., Inoue A., Henmi T., Ueki N., Analysis and Experiment on Simultaneous Swing‐Up of a Parallel Cart Type Double Inverted Pendulum, *Asian Journal of Control*, 2008, **10**(1), 121-8.

[32] https://www.mathworks.com/products/connections/product_detail/feedback-instruments-digital-pendulum.html (Last Visited: 06. December.2020).

[33] Akhtaruzzaman M., Shafie A.A., Modeling and Control of a Rotary Inverted Pendulum Using Various Methods, Comparative Assessment and Result Analysis, *International Conference on Mechatronics and Automation*, *IEEE*, pp. 1342-1347, 4 aug 2010.

[34] Dwivedi, P., Pandey, S., Junghare, A. S., Stabilization of Unstable Equilibrium Point of Rotary Inverted Pendulum Using Fractional Controller, *Journal of the Franklin Institute*, 2017, **354**(17), 7732-7766.

[35] Ramírez-Neria M., Sira-Ramírez H., Garrido-Moctezuma R., Luviano-Juarez A., Linear Active Disturbance Rejection Control of Underactuated Systems: The Case of the Furuta Pendulum, *ISA transactions*, 2014, **53**(4), 920-8.

[36] https://www.quanser.com/products/rotary-inverted-pendulum/ (Last Visited: 06 Dec 2020).

[37] Jabbar A., Malik F.M., Sheikh S.A., Nonlinear Stabilizing Control of a Rotary Double Inverted Pendulum: A Modified Backstepping Approach, *Transactions of the Institute of Measurement and Control*, 2017, **39**(11), 1721-34.

[38] Awtar S., King N., Allen T., Bang I., Hagan M., Skidmore D., Craig K., Inverted Pendulum Systems: Rotary and Arm-Driven-a Mechatronic System Design Case Study, *Mechatronics*, 2002, **12**(2), 357-70.

[39] Jadlovska S., Sarnovsky J., Modelling of Classical and Rotary Inverted Pendulum Systems a Generalized Approach, *Journal of Electrical Engineering*, 2013, **64**(1), 12–19.

[40] https://www.quanser.com/products/rotary-double-inverted-pendulum/ (Last Visited: 06 Dec 2020).

[41] Fantoni I., Lozano R., Spong MW., Energy Based Control of the Pendubot, *IEEE Transactions on Automatic Control*, 2000, **45**(4), 725-9.

[42] Zhang M., Tarn T.J., Hybrid Control of the Pendubot, *IEEE/ASME Transactions on Mechatronics*, 2002, **7**(1), 79-86.

[43] https://www.quanser.com/blog/common-and-not-so-common-pendulum-configurations/attachment/pendubot/ (Last Visited: 06. December.2020).

[44] http://coecsl.ece.illinois.edu/pages/pendubot.html (Last Visited: 06. December.2020).

[45] Tedrake R., Underactuated Robotics: Learning, Planning, And Control for Efficient and Agile Machines Course Notes for MIT 6.832, *Working Draft Edition*, **3**, 2009.

[46] Spong M.W., The Swing Up Control Problem for The Acrobot, *IEEE Control Systems Magazine*, 1995, **15**(1), 49-55.

[47] Bortoff S.A., Spong M.W., Pseudolinearization of the Acrobot Using Spline Functions, *Proceedings of the 31st Conference on Decision and Control, IEEE*, pp. 593-598, 16 Dec1992.

[48] Spong M.W., Corke P., Lozano R., Nonlinear Control of the Reaction Wheel Pendulum, *Automatica*, 2001, **37**(11), 1845-51.

[49] Montoya O.D., Gil-González W., Nonlinear Analysis and Control of a Reaction Wheel Pendulum: Lyapunov-Based Approach, *International Journal of Engineering Science and Technology*, 2020, **23**(1), 21-9.

[50] Krishna B., Chandran D., George VI., Thirunavukkarasu I., Modeling and Performance Comparison of Triple PID and LQR Controllers for Parallel Rotary Double Inverted Pendulum, *Int. J. Emerg. Trends Electr. Electron*, 2015, **11**(2), 145-50.

[51] Hamza M.F., Yap H.J., Choudhury I.A., Isa A.I., Zimit A.Y., Kumbasar T., Current Development on Using Rotary Inverted Pendulum as a Benchmark for Testing Linear and Nonlinear Control Algorithms, *Mechanical Systems and Signal Processing*, 2019, **116**, 347-69.

[52] https://jglobal.jst.go.jp/detail?JGLOBAL_ID=201402212594922165 (Last Visited: 06 Dec 2020) .

[53] Horvath, R., Flowers, G.T., and Overfelt, R.A., Stability Investigation of a Two-Link 3DOF Rotational Pendulum, *International Design Engineering Technical Conferences and Computers and Information in Engineering Conference*, vol.37033, pp.903-912, 1 Jan 2003.

[54] Feng L., Yongchuan T., Qian Q., Stabilize the Planar Single Inverted Pendulum Based on LQR, *International Conference on Automation and Logistics (ICAL), IEEE*, pp. 238-242, 2011.

[55] Driver J., Thorpe D., Design, Build and Control of a Single/Double Rotational Inverted Pendulum, *University of Adelaide, School of Mechanical Engineering, Australia*, 4 Oct 2004.

[56] https://www.solutions4u-asia.com/PDT/GT/LAB/R-PlanarInvPen.html (Last Visited: 06 Dec 2020)

[57] Gupta N., Dewan L., Modeling and Simulation of Rotary-Rotary Planer Inverted Pendulum, *Journal of Physics, Conference Series*, Vol. 1240, No. **1**, p. 012089, Jul 2019.

[58] Nawawi S.W., Ahmad M.N., Osman J.H., Real-Time Control Of A Two-Wheeled Inverted Pendulum Mobile Robot, *World Academy of Science, Engineering and Technology*, **39**,214-20, May 2008.

[59] Jeong S., Takahashi T., Wheeled Inverted Pendulum Type Assistant Robot: Design Concept and Mobile Control, *Intelligent Service Robotics*, 2008,**1**(4), 313-20.

[60] Chowdhary P., Gupta V., Gupta D., Jadhav A., Mishra V., Design of Two Wheel Self Balancing Robot Using PID Controller, *International Journal of Engineering Research & Technology (IJERT)*, volume 5, issue 01, 2017.

[61] Aly O., Abd-Al-Azeem M.K., Mohammed R., Aly M., Mohammed S.I., Balancing a Two Wheeled Robot, *Thesis*, July 2009, DOI: 10.13140/RG.2.2.25634.63683.

[62] Jin S., Ou Y., A Wheeled Inverted Pendulum Learning Stable and Accurate Control from Demonstrations, *Applied Sciences*, 2019, **9**(24), 5279.

[63] Zhang C., Hu H., Gu D., Wang J., Cascaded Control for Balancing an Inverted Pendulum on a Flying Quadrotor, *Robotica*, 2017, **35**(6), 1263-79.

[64] Hehn M., D'Andrea R., A flying inverted pendulum, *International Conference on Robotics and Automation, IEEE*, pp. 763-770, 9 May 2011.

[65] Spong M.W., Block D.J., The Pendubot: A Mechatronic System for Control Research and Education, *34th Conference on Decision and Control, IEEE*, Vol. 1, pp. 555-556, 13 Dec 1995.

[66] Wang L.X., Stable Adaptive Fuzzy Controllers with Application to Inverted Pendulum Tracking, *IEEE Transactions on Systems, Man, and Cybernetics, Part B (Cybernetics)*, 1996, **26**(5), 677-91.9.

[67] Cheng F., Zhong G., Li Y., Xu Z., Fuzzy Control of a Double-Inverted Pendulum, *Fuzzy Sets and Systems*, 1996, **79**(3), 315-21.

[68] Aracil J., Gordillo F., Acosta J.A., Stabilization of Oscillations in The Inverted Pendulum, *IFAC Proceedings Volumes*, 2002, **35**(1),79-84.

[69] Nasir A.N., Ismail R.M., Ahmad M.A., Performance Comparison Between Sliding Mode Control (SMC) and PD-PID Controllers for a Nonlinear Inverted Pendulum System, *World Academy of Science, Engineering and Technology*, 2010, **71**, 400-5.

[70] Kizir S., Bingül Z., Oysu C., Fuzzy Control of a Real Time Inverted Pendulum System, *Journal of Intelligent and Fuzzy Systems*, 2010, **21**(1, 2), 121-33.

[71] Zhang J.L., Zhang W., LQR Self-Adjusting Based Control for the Planar Double Inverted Pendulum, *Physics Procedia*, 2012, **24**,1669-76.

[72] Li B., Rotational Double Inverted Pendulum, *Doctoral dissertation, University of Dayton*, 2013.

[73] Furuta K., Yamakita M., Kobayashi S., Swing-Up Control of Inverted Pendulum Using Pseudo-State Feedback, *Proceedings of the Institution of Mechanical Engineers, Part I: Journal of Systems and Control Engineering*, 1992, **206**(4), 263-9.

[74] Yamakita M., Nonaka K., Furuta K., Swing Up Control of a Double Pendulum, *American Control Conference, IEEE*, pp.2229-2233, 2 Jun 1993.

[75] Yamakita M Iwashiro M. Sugahara Y., Furuta K., Robust Swing Up Control of Double Pendulum, *Proceedings of American Control Conference (ACC*), *IEEE*, vol.1, pp.290-295, 21 Jun 1995.

[76] Yasunobu S., Mori M., Swing Up Fuzzy Controller for Inverted Pendulum Based on a Human Control Strategy, *Proceedings of International Fuzzy Systems Conference, IEEE*, vol.3, pp. 1621-1625, 5 Jul 1997.

[77] Åström K.J., Furuta K., Swinging Up a Pendulum by Energy Control, *Automatica*, 2000, **36**(2), 287-95.

[78] Åström K.J., Furuta, K., Swinging Up a Pendulum by Energy Control, *IFAC Proceedings Volumes*, 1996, **29**(1), 1919-1924.

[79] Rubı J., Rubio A., Avello A., Swing-Up Control Problem for a Self-Erecting Double Inverted Pendulum, *IEE Proceedings-Control Theory and Applications*, 2002, **149**(2), 169-75.

[80] Graichen K., Treuer M., Zeitz M., Swing-Up of the Double Pendulum on a Cart by Feedforward and Feedback Control with Experimental Validation, *Automatica*, 2007, **43**(1), 63-71.

[81] Jaiwat P., Ohtsuka T., Real-Time Swing-Up of Double Inverted Pendulum by Nonlinear Model Predictive Control, *International Symposium on Advanced Control of Industrial Processes*, pp.290-295, 28 May 2014.

[82] Lee H.H., Modeling and Control of a Three-Dimensional Overhead Crane, 471-476, 1998.

[83] Vikramaditya B., Rajamani R., Nonlinear Control of a Trolley Crane System, *Proceedings of American Control Conference (ACC), IEEE*, vol. 2, pp.1032-1036, 28 Jun 2000.

[84] Chang C.Y., Adaptive Fuzzy Controller of the Overhead Cranes with Nonlinear Disturbance, *IEEE Transactions on Industrial Informatics*, 2007, **3**(2),164-72.

[85] Solihin M.I., Wahyudi, Legowo A., Fuzzy-tuned PID Anti-swing Control of Automatic Gantry Crane, *Journal of Vibration and Control*, 2010, **16**(1),127-45.

[86] Zhang Z., Wu Y., Huang J., Differential-Flatness-Based Finite-Time Anti-Swing Control of Underactuated Crane Systems, *Nonlinear Dynamics*, 2017, **87**(3), 1749-61.

[87] Küçük S., Bingül Z., Inverse Kinematics Solutions for Industrial Robot Manipulators with Offset Wrists, *Applied Mathematical Modelling*, **38**(7-8), 1983-99.

[88] Küçük S., Bingül Z., Robot Kinematics: Forward and Inverse Kinematics, *INTECH Open Access Publisher*,1 Dec 2006.

[89] Bingül Z., Küçük S., Robot Dinamiği ve Kontrolü. *Birsen Yayınevi*, 2008.

[90] Crisan A., Negrean I., The Jacobian Matrix Based on the Transfer Matrices, *ACTA Technica Napocensis-Series: Applied Mathematics, Mechanics, And Engineering*, 2019, **62**(1).

[91] Furuta K., Yamakita M., Kobayashi S., Nishimura M., A New Inverted Pendulum Apparatus for Education, *Advances in Control Education*, 1992, pp. 133-138, Pergamon.

[92] Hazem Z.B., Fotuhi M.J., Bingül Z., A Comparative Study of the Joint Neuro-Fuzzy Friction Models for a Triple Link Rotary Inverted Pendulum, *IEEE Access*, 2020, **8**, 49066-78.

[93] Park D., Chwa D., Hong S.K., An Estimation and Compensation of the Friction in an Inverted Pendulum, *SICE-ICASE International Joint Conference, IEEE*, pp.779-783, 18 Oct 2006.

[94] Fang L., Chen W.J., Cheang S.U., Friction Compensation for a Double Inverted Pendulum, *Proceedings of the International Conference on Control Applications (CCA'01), IEEE*, pp.908-913, 7 sep 2001.

[95] Gäfvert M., Svensson J., Astrom K.J., Friction and Friction Compensation in the Furuta Pendulum, *European Control Conference (ECC)*, pp.3154-3159, *IEEE*, Aug1999.

[96] Hazem Z.B., Fotuhi M.J., Bingül Z., A Comparative Study of the Friction Models with Adaptive Coefficients for a Rotary Triple Inverted Pendulum, *6th International Conference on Control Engineering and Information Technology (CEIT), IEEE*, pp.1-6, 25 Oct 2018.

[97] Dupont P.E., Friction Modeling in Dynamic Robot Simulation, *Proceedings, International Conference on Robotics and Automation*, *IEEE,* pp.1370-1376, 13 May 1990.

[98] Acosta J.A., Furuta's Pendulum: A Conservative Nonlinear Model for Theory and Practice, *Mathematical Problems in Engineering*, Mar 2010.

[99] Fotuhi M.J., Hazem Z.B., Bingül Z., Comparison of Joint Friction Estimation Models for Laboratory 2 DOF Double Dual Twin Rotor Aero-Dynamical System, *Conference of the Industrial Electronics Society* (*IECON), IEEE*, pp. 2231-2236, 21 Oct 2018.

[100] Hu C., Wan F., Parameter Identification of a Model with Coulomb Friction for a Real Inverted Pendulum System, *Chinese Control and Decision Conference*, pp.2869-2874, 17 Jun 2009.

[101] Guida D., Nilvetti F., Pappalardo C.M., Dry Friction Influence on Inverted Pendulum Control, *Proceedings of the International Conference on Applied Mathematics, Simulation, Modelling, Vouliagmeni Beach*, pp.29-31, Athens, Greece, 29 Dec 2009.

[102] Hu C., Wan F., Parameter Identification of a Model with Coulomb Friction for a Real Inverted Pendulum System, *Chinese Control and Decision Conference, IEEE*, pp.2869-2874, 17 Jun 2009.

[103] Bittencourt A.C., Wernholt E., Sander-Tavallaey S., Brogårdh T., An Extended Friction Model to Capture Load and Temperature Effects in Robot Joints, *International Conference on Intelligent Robots and Systems (RSJ), IEEE*, pp. 6161-6167, 18 Oct 2010.

[104] Ding L., Li X., Li Q., Chao Y., Nonlinear Friction and Dynamical Identification for a Robot Manipulator with Improved Cuckoo Search Algorithm, *Journal of Robotics*, 2018.

[105] Dupont P.E., The Effect of Friction on the Forward Dynamics Problem, *International Journal of Robotics Research*, 1993, **12**(2), 164-79.

[106] Al-Bender F., Symens W., Characterization of frictional hysteresis in ball-bearing guideways, *Wear*, 2005, **258**(11-12),1630-42.

[107] Lampaert V., Swevers J., Al-Bender F., Experimental Comparison of Different Friction Models for Accurate Low-Velocity Tracking, *Proceedings of the Mediterranean Conference on Control and Automation (MED'02)*, 9 Jul 2002.

[108] Fotuhi M.J., Hazem Z.B., Bingül Z., Adaptive Joint Friction Estimation Model for Laboratory 2 DOF Double Dual Twin Rotor Aerodynamical Helicopter

System, *International Conference on Control Engineering and Information Technology (CEIT), IEEE*, pp. 1-6, 25 Oct 2018.

[109] Al-Sumait J.S., Al-Othman A.K., Sykulski J.K., Application of Pattern Search Method to Power System Valve-Point Economic Load Dispatch, *International Journal of Electrical Power and Energy Systems*, 2007, **29**(10), 720-30.

[110] Yu H., Xie T., Paszczynski S., Wilamowski B.M., Advantages of Radial Basis Function Networks for Dynamic System Design, *IEEE Transactions on Industrial Electronics*, 2011, **58**(12), 5438-50.

[111] Zemouri R., Racoceanu D., Zerhouni N., Recurrent Radial Basis Function Network for Time-Series Prediction, *Engineering Applications of Artificial Intelligence*, 2003, **16**(5-6), 453-63.

[112] Gençay R., Qi M., Pricing and Hedging Derivative Securities with Neural Networks: Bayesian Regularization, Early Stopping, and Bagging, *IEEE Transactions on Neural Networks*, 2001, **12**(4), 726-34.

[113] Ekekwe N., Etienne-Cummings R., Kazanzides P., Incremental Encoder Based Position and Velocity Measurements VLSI Chip with Serial Peripheral Interface, *International Symposium on Circuits and Systems, IEEE*, pp.3558-3561, 2007.

[114] Baumann W., Rugh W., Feedback Control of Nonlinear Systems by Extended Linearization, *IEEE Transactions on Automatic Control*, 1986, **31**(1), 40-6.

[115] El-Hawwary M.I., Elshafei A.L., Emara H.M., Fattah H.A., Adaptive Fuzzy Control of the Inverted Pendulum Problem, *IEEE Transactions on Control Systems Technology*, 2006, **14**(6), 1135-44.

[116] Prasad L.B., Tyagi B., Gupta H.O., Optimal Control of Nonlinear Inverted Pendulum System Using PID Controller and LQR: Performance Analysis Without and with Disturbance Input, *International Journal of Automation and Computing*, 2014, **11**(6), 661-70.

[117] Yi J., Yubazaki N., Hirota K., Upswing and Stabilization Control of Inverted Pendulum System Based on the Sirms Dynamically Connected Fuzzy Inference Model, *Fuzzy Sets and Systems*, 2001, **122**(1), 139-52.

[118] Tao C.W., Taur J.S., Hsieh T.W., Tsai C.L., Design of A Fuzzy Controller with Fuzzy Swing-Up and Parallel Distributed Pole Assignment Schemes for an Inverted Pendulum and Cart System, *IEEE Transactions on Control Systems Technology*, 2008, **16**(6), 1277-88.

[119] Tao C.W., Taur J.S., Chen Y.C., Design of a Parallel Distributed Fuzzy LQR Controller for the Twin Rotor Multi-Input Multi-Output System, *Fuzzy Sets and Systems*, 2010, **161**(15), 2081-103.

[120] Adeli M., Zarabadipour H., Zarabadi S.H., Shoorehdeli M.A., Anti-swing Control for a Double-Pendulum-Type Overhead Crane Via Parallel Distributed

Fuzzy LQR Controller Combined with Genetic Fuzzy Rule Set Selection, *International Conference on Control System, Computing and Engineering, IEEE*, pp.306-311, 25 Nov 2011.

[121] Wang D., He H., Liu D., Intelligent Optimal Control with Critic Learning for a Nonlinear Overhead Crane System, *Transactions on Industrial Informatics, IEEE*, 2017, **14**(7), 2932-40.

[122] Harifi S., Khalilian M., Mohammadzadeh J., Ebrahimnejad S., Optimizing A Neuro-Fuzzy System Based on Nature Inspired Emperor Penguins Colony Optimization Algorithm, *IEEE Transactions on Fuzzy Systems*, 2 Apr 2020.

[123] Precup R.E., Filip H.I., Rădac M.B., Petriu E.M., Preitl S., Dragoş C.A., Online Identification of Evolving Takagi–Sugeno–Kang Fuzzy Models for Crane Systems, *Applied Soft Computing*, 2014, **24**, 1155-63.

[124] Baojiang Z., Shiyong L., Ant Colony Optimization Algorithm and Its Application to Neuro-Fuzzy Controller Design, *Journal of Systems Engineering and Electronics*, 2007, **18**(3), 603-10.

[125] Chawla I., Chopra V., Singla A., Robust LQR Based ANFIS Control of xz Inverted Pendulum, *Amity International Conference on Artificial Intelligence (AICAI), IEEE*, pp.818-823, 2019.

[126] Wang J.J., Simulation Studies of Inverted Pendulum Based on PID Controllers, *Simulation Modelling Practice and Theory*, 2011, **19**(1), 440-9.

[127] Ovalle, L., Ríos, H. and Llama, M.. Robust Output-Feedback Control for the Cart–Pole System: A Coupled Super-Twisting Sliding-Mode Approach, *IET Control Theory and Applications*, 2018, **13**(2), 269-278.

[128] Kumar E.V., Jerome J., Robust LQR Controller Design for Stabilizing and Trajectory Tracking of Inverted Pendulum, *Procedia Engineering*, 2013, 64, 169-78.

[129] Yadav S.K., Sharma S., Singh N., Optimal Control of Double Inverted Pendulum Using LQR Controller, *International Journal of Advanced Research in Computer Science and Software Engineering*, 2012, **2**(2).

[130] Xiong X., Wan Z., The Simulation of Double Inverted Pendulum Control Based on Particle Swarm Optimization LQR Algorithm, *International Conference on Software Engineering and Service Sciences, IEEE*, pp.253-256, 16 Jul 2010.

[131] Luhao W., Zhanshi S., LQR-Fuzzy Control for Double Inverted Pendulum, *International Conference on Digital Manufacturing and Automation, IEEE*, vol. 1, pp.900-903, 18 Dec 2010.

[132] Kizir S., Bingül Z., Fuzzy Impedance and Force Control of a Stewart Platform, *Turkish Journal of Electrical Engineering and Computer Sciences*, 2014, **22**(4), 924-39.

[133] Akyüz I.H., Kizir S., Bingül Z., Fuzzy Logic Control of Single-Link Flexible Joint Manipulator, *International Conference on Industrial Technology*, IEEE, pp.306-311, 14 Mar 2011.

[134] Bush L., Fuzzy Logic Controller for the Inverted Pendulum Problem, *IEEE Control System Magazine*, 2001, 238-45.

[135] Yaren T., Kizir S., Stabilization Control of Triple Pendulum on a Cart, *6th International Conference on Control Engineering and Information Technology (CEIT), IEEE*, pp.1-6, 25 Oct 2018.

[136] Eide R., Egelid P.M., Karimi H.R., LQG Control Design for Balancing an Inverted Pendulum Mobile Robot, *Intelligent Control and Automation*, 2011, **2**(02), 160.

[137] Lupian L.F., Avila R., Stabilization of a Wheeled Inverted Pendulum by a Continuous-Time Infinite-Horizon LQG Optimal Controller, *Latin American Robotic Symposium, IEEE,* pp. 65-70, 29 Oct 2008.

[138] Collins EG., Selekwa M.F., A Fuzzy Logic Approach to LQG Design with Variance Constraints, *IEEE transactions on control systems technology*, 2002, **10**(1), 32-42.

[139] Odry Á., Fodor J., Odry P., Stabilization of a Two-Wheeled Mobile Pendulum System Using LQG and Fuzzy Control Techniques, *International Journal on Advances in Intelligent Systems*, 2016, **9**(1), 2.

[140] Chawla I., Singla A., Real-Time Control of a Rotary Inverted Pendulum Using Robust LQR-Based ANFIS Controller, *International Journal of Nonlinear Sciences and Numerical Simulation*, 2018, **19**(3-4), 379-89.

[141] Song S., Zhang B., Song X., Zhang Y., Zhang Z., Li W., Fractional-Order Adaptive Neuro-Fuzzy Sliding Mode $H\infty$ Control for Fuzzy Singularly Perturbed Systems, *Journal of the Franklin Institute*, 2019, **356**(10), 5027-48.

[142] Rusu P., Petriu E.M., Whalen T.E., Cornell A., Spoelder HJ., Behavior-Based Neuro-Fuzzy Controller for Mobile Robot Navigation, *IEEE transactions on instrumentation and measurement*, 2003, **52**(4), 1335-40.

[143] Hsu C.F., Lin C.M., Yeh R.G., Supervisory Adaptive Dynamic RBF-Based Neural-Fuzzy Control System Design for Unknown Nonlinear Systems, *Applied Soft Computing*, 2013, **13**(4), 1620-6.

[144] Sahnehsaraei M.A., Mahmoodabadi M.J., Bagheri A., Pareto Optimum Control of a 2-DOF Inverted Pendulum Using Approximate Feedback Linearization and Sliding Mode Control, *Transactions of the Institute of Measurement and Control*, 2014, **36**(4), 496-505.

[145] https://www.mdsmotor.com/?lang=en&content=default (Last Visited: 06 Dec 2020).

[146] https://www.lenze.com/en-tr/products/inverters/control-cabinet-installation/8400-topline-frequency-inverters/ (Last Visited: 06 Dec 2020).

[147] https://www.fenac.com.tr/img/pdf/fnc-sc2048-series-pdf-61092.pdf (Last Visited: 06 Dec 2020).

[148] https://www.moflon.com/slip-ring/?gclid=CjwKCAiAn7L-BRBbEiwAl9UtkLZ1GOy6r5rGZZUL87-D6OaVH752H5c6dm-oq5aBGggjHqZBGhTEAhoCz-sQAvD_BwE (Last Visited: 06 Dec 2020).

[149] https://www.dspace.com/en/pub/home/support/pli/elas/elashw/elads1103.cfm (Last Visited: 06 Dec 2020)

[150] https://people.kth.se/~crro/segway_challenge/model.html (Last Visited: 06 Dec 2020)

APPENDIX

Appendix-A

The Matlab .m codes used to calculate the mathematical models of the SLRIP, DLRIP and TLRIP are given in this section. Only the variables of each model must take into consideration for the codes.

```
close all; clear; clc;
%%%--------------------------------------
syms Q1 Q2 Q3 Q4
syms dQ1 dQ2 dQ3 dQ4
syms ddQ1 ddQ2 ddQ3 ddQ4
syms L1 L2 L3 L4 L5
syms g m1 m2 m3 m4
syms I1 I2 I3 I4
%%%--------------------------------------
gv = [0 0 -g].';
%%%--------------------------------------
%%%%%%%%%%  Vars: R = 0, P = 1, Not a Joint = -1.
%%%%%%%%%%  Alpha(i-1) a(i-1)  d(i)   Q(i) Vars      i
DHstruct = [       0,     0,    0,     0,    0;  %  1
                -pi/2,    0,   L1, -pi/2,    0;  %  2
                   0,    L2,    0,     0,    0;  %  3
                   0,    L3,    0,     0,    0;  %  4
                   0,    L4,    0,     0,   -1]; %  5
T = stuff(DHstruct);
%%%--------------------------------------
Zii = [0 0 1].';
s = zeros(3,1);
dq  = [ dQ1  dQ2  dQ3  dQ4].';
ddq = [ddQ1 ddQ2 ddQ3 ddQ4].';

T01 = T(:,:,1);     R01 = T01(1:3,1:3); Z01 = R01(:,3); P01 =
T01(1:3,4);
T02 = T01*T(:,:,2); R02 = T02(1:3,1:3); Z02 = R02(:,3); P02 =
T02(1:3,4);
T03 = T02*T(:,:,3); R03 = T03(1:3,1:3); Z03 = R03(:,3); P03 =
T03(1:3,4);
T04 = T03*T(:,:,4); R04 = T04(1:3,1:3); Z04 = R04(:,3); P04 =
T04(1:3,4);

R01 = T(1:3,1:3,1);%P01 = T(1:3,4,1);
R12 = T(1:3,1:3,2); P12 = T(1:3,4,2);
R23 = T(1:3,1:3,3); P23 = T(1:3,4,3);
R34 = T(1:3,1:3,4); P34 = T(1:3,4,4);

Pc11 = [0, L1/2, 0, 1].'; h1 = T01(1:3,:)*Pc11;
Pc22 = [L2/2, 0, 0, 1].'; h2 = T02(1:3,:)*Pc22;
Pc33 = [L3/2, 0, 0, 1].'; h3 = T03(1:3,:)*Pc33;
Pc44 = [L4/2, 0, 0, 1].'; h4 = T04(1:3,:)*Pc44;

Ic1 = [ I1 , 0,  0;
         0,  0,  0;
         0,  0, I1];

Ic2 = [  0 , 0,  0;
```

```
         0, I2,  0;
         0,  0, I2];

Ic3 = [  0 , 0,  0;
         0, I3,  0;
         0,  0, I3];

Ic4 = [  0 , 0,  0;
         0, I4,  0;
         0,  0, I4];
%%%---------------------------------------
A1 = [diff(h1,Q1),          s,          s,          s];
A2 = [diff(h2,Q1),diff(h2,Q2),          s,          s];
A3 = [diff(h3,Q1),diff(h3,Q2),diff(h3,Q3),          s];
A4 = [diff(h4,Q1),diff(h4,Q2),diff(h4,Q3),diff(h4,Q4)];

B1 = [Z01,  s,  s,  s];
B2 = [Z01,Z02,  s,  s];
B3 = [Z01,Z02,Z03,  s];
B4 = [Z01,Z02,Z03,Z04];

B11 = R01.'*B1; Dm1 = A1.'*A1*m1 + B11.'*Ic1*B11;
B22 = R02.'*B2; Dm2 = A2.'*A2*m2 + B22.'*Ic2*B22;
B33 = R03.'*B3; Dm3 = A3.'*A3*m3 + B33.'*Ic3*B33;
B44 = R04.'*B4; Dm4 = A4.'*A4*m4 + B44.'*Ic4*B44;

D = Dm1 + Dm2 + Dm3 + Dm4;

dD = diff(D,Q1)*dQ1 + diff(D,Q2)*dQ2 + diff(D,Q3)*dQ3 +
diff(D,Q4)*dQ4;
pKpq = 0.5*[dq.'*diff(D, Q1)*dq;
            dq.'*diff(D, Q2)*dq;
            dq.'*diff(D, Q3)*dq;
            dq.'*diff(D, Q4)*dq];
C = dD*dq - pKpq;

G = (-m1*gv.'*A1 -m2*gv.'*A2 -m3*gv.'*A3 -m4*gv.'*A4).';

tau = D*ddq + C + G;

%%%---------------------------------------
w01 = w00 + dQ1*Z01; w11 = R01.'*w01;
w02 = w01 + dQ2*Z02; w22 = R02.'*w02;
w03 = w02 + dQ3*Z03; w33 = R03.'*w03;
w04 = w03 + dQ4*Z04; w44 = R04.'*w04;

v00 = zeros(3,1);
v01 = v00 + cross(w00,P01    ); Vc1 = v01 + cross(w01, h1-P01);
v02 = v01 + cross(w01,P02-P01); Vc2 = v02 + cross(w02, h2-P02);
v03 = v02 + cross(w02,P03-P02); Vc3 = v03 + cross(w03, h3-P03);
v04 = v03 + cross(w03,P04-P03); Vc4 = v04 + cross(w04, h4-P04);

K1 = (Vc1.'*Vc1*m1 + w11.'*Ic1*w11)/2; U1 = -m1*gv.'*h1;
K2 = (Vc2.'*Vc2*m2 + w22.'*Ic2*w22)/2; U2 = -m2*gv.'*h2;
K3 = (Vc3.'*Vc3*m3 + w33.'*Ic3*w33)/2; U3 = -m3*gv.'*h3;
K4 = (Vc4.'*Vc4*m4 + w44.'*Ic4*w44)/2; U4 = -m4*gv.'*h4;
K = K1 + K2 + K3 + K4;
U = U1 + U2 + U3 + U4;
```

```
L = K - U;

Ldq1 = diff(L,dQ1);
Ldq2 = diff(L,dQ2);
Ldq3 = diff(L,dQ3);
Ldq4 = diff(L,dQ4);

dLdq1 = diff(Ldq1, Q1)* dQ1 + diff(Ldq1, Q2)* dQ2 + diff(Ldq1, Q3)*
dQ3 + diff(Ldq1, Q4)* dQ4 +...
        diff(Ldq1,dQ1)*ddQ1 + diff(Ldq1,dQ2)*ddQ2 +
diff(Ldq1,dQ3)*ddQ3 + diff(Ldq1,dQ4)*ddQ4;

dLdq2 = diff(Ldq2, Q1)* dQ1 + diff(Ldq2, Q2)* dQ2 + diff(Ldq2, Q3)*
dQ3 + diff(Ldq2, Q4)* dQ4 +...
        diff(Ldq2,dQ1)*ddQ1 + diff(Ldq2,dQ2)*ddQ2 +
diff(Ldq2,dQ3)*ddQ3 + diff(Ldq2,dQ4)*ddQ4;

dLdq3 = diff(Ldq3, Q1)* dQ1 + diff(Ldq3, Q2)* dQ2 + diff(Ldq3, Q3)*
dQ3 + diff(Ldq3, Q4)* dQ4 +...
        diff(Ldq3,dQ1)*ddQ1 + diff(Ldq3,dQ2)*ddQ2 +
diff(Ldq3,dQ3)*ddQ3 + diff(Ldq3,dQ4)*ddQ4;

dLdq4 = diff(Ldq4, Q1)* dQ1 + diff(Ldq4, Q2)* dQ2 + diff(Ldq4, Q3)*
dQ3 + diff(Ldq4, Q4)* dQ4 +...
        diff(Ldq4,dQ1)*ddQ1 + diff(Ldq4,dQ2)*ddQ2 +
diff(Ldq4,dQ3)*ddQ3 + diff(Ldq4,dQ4)*ddQ4;

Lq1 = diff(L,Q1);
Lq2 = diff(L,Q2);
Lq3 = diff(L,Q3);
Lq4 = diff(L,Q4);

tau_LE = [dLdq1 - Lq1;
          dLdq2 - Lq2;
          dLdq3 - Lq3;
          dLdq4 - Lq4];
disp('compare torque equations with LE :')
disp(simplify(tau - tau_LE))
disp(char('-'*ones(1,60)))

%%%--------------------------------------


W00 = s;
W11 = R01.'*W00 + dQ1*Zii;
W22 = R12.'*W11 + dQ2*Zii;
W33 = R23.'*W22 + dQ3*Zii;
W44 = R34.'*W33 + dQ4*Zii;

dW00 = s;
dW11 = R01.'*dW00 + ddQ1*Zii + cross(W11, dQ1*Zii);
dW22 = R12.'*dW11 + ddQ2*Zii + cross(W22, dQ2*Zii);
dW33 = R23.'*dW22 + ddQ3*Zii + cross(W33, dQ3*Zii);
dW44 = R34.'*dW33 + ddQ4*Zii + cross(W44, dQ4*Zii);

dV00 = -gv;
dV11 = R01.'*( dV00 + cross(dW00, P01) + cross(W00, cross(W00,
P01)) );
```

```
dV22 = R12.'*( dV11 + cross(dW11, P12) + cross(W11, cross(W11,
P12)) );
dV33 = R23.'*( dV22 + cross(dW22, P23) + cross(W22, cross(W22,
P23)) );
dV44 = R34.'*( dV33 + cross(dW33, P34) + cross(W33, cross(W33,
P34)) );

Pc11(4) = []; Pc22(4) = []; Pc33(4) = []; Pc44(4) = [];
dVc1 = dV11 + cross(dW11, Pc11) + cross(W11, cross(W11, Pc11));
dVc2 = dV22 + cross(dW22, Pc22) + cross(W22, cross(W22, Pc22));
dVc3 = dV33 + cross(dW33, Pc33) + cross(W33, cross(W33, Pc33));
dVc4 = dV44 + cross(dW44, Pc44) + cross(W44, cross(W44, Pc44));

F11 = m1*dVc1;
F22 = m2*dVc2;
F33 = m3*dVc3;
F44 = m4*dVc4;

N11 = Ic1*dW11 + cross(W11, Ic1*W11);
N22 = Ic2*dW22 + cross(W22, Ic2*W22);
N33 = Ic3*dW33 + cross(W33, Ic3*W33);
N44 = Ic4*dW44 + cross(W44, Ic4*W44);

f44 =          F44;
f33 = R34*f44 + F33;
f22 = R23*f33 + F22;
f11 = R12*f22 + F11;

n44 = N44           + cross(Pc44, F44);
n33 = N33 + R34*n44 + cross(Pc33, F33) + cross(P34, R34*f44);
n22 = N22 + R23*n33 + cross(Pc22, F22) + cross(P23, R23*f33);
n11 = N11 + R12*n22 + cross(Pc11, F11) + cross(P12, R12*f22);

tau_NE = [n11.'*Zii;
          n22.'*Zii;
          n33.'*Zii;
          n44.'*Zii];
disp('compare torque equations with NE :')
disp(simplify(tau - tau_NE))
disp(char('-'*ones(1,60)))
%%%---------------------------------------

disp('compare LE equations with NE :')
disp(simplify(tau_LE - tau_NE))
%%%---------------------------------------

disp(collect(simplify(D), {'sin', 'cos'}))
disp(collect(simplify(C), {'sin', 'cos'}))
disp(collect(simplify(G), {'sin', 'cos'}))
%%%---------------------------------------
% The equations of accelerations

ddQ=(inv(D)*(-C-G))
```

```
function T = stuff( DHstruct )
T  = fun_T(fun_DH(DHstruct));


function DH = fun_DH(DHstruct,Q)
    Jnts = fun_JointTypes(DHstruct(:,5,1));
    if isa(DHstruct,'sym'), Q =
fun_JointVariables('Pos',Jnts.R,Jnts.P); end
    szQ = size(Q);
    if szQ(2)>1
        DH = DHstruct(:,1:4,ones(1,szQ(2)));
        tmpQ = permute(Q,[1,3,2]);
        if any(Jnts.P), DH(Jnts.P,3,:) = DH(Jnts.P,3,:) +
tmpQ(Jnts.P,1,:); end
        if any(Jnts.R), DH(Jnts.R,4,:) = DH(Jnts.R,4,:) +
tmpQ(Jnts.R,1,:); end
    else
        DH = DHstruct(:,1:4);
        if any(Jnts.P), DH(Jnts.P,3) = DH(Jnts.P,3) + Q(Jnts.P); end
        if any(Jnts.R), DH(Jnts.R,4) = DH(Jnts.R,4) + Q(Jnts.R); end
    end
end
function Jnts = fun_JointTypes( JointTypes )
    if ~isa(JointTypes,'double'), JointTypes = double(JointTypes);
end
    if size(JointTypes,1)>1
        JointTypes = reshape(JointTypes,[1,numel(JointTypes)]);
    end
    isJnt = JointTypes ~= -1;
    Jnts.N = numel(isJnt(isJnt));
    Jnts.P = JointTypes(isJnt) == 1;
    Jnts.R = ~Jnts.P;
end
function JntVars = fun_JointVariables( type, Rinds, Pinds)
    Jnum = sum(Rinds + Pinds);
    Jinds = 48 + (1:Jnum);
    mask1 = ones(1,Jnum);
    if strcmpi(type,'pos')
        colSzs = 2;
        Q_str = 81*mask1;
        Q_str(1,Pinds) = 68;
        Q_str(2,:) = Jinds;
    elseif strcmpi(type,'vel')
        colSzs = 3;
        Q_str = [100;81;0]*mask1;
        Q_str(2,Pinds) = 68;
        Q_str(3,:) = Jinds;
    elseif strcmpi(type,'acc')
        colSzs = 4;
        Q_str = [100;100;81;0]*mask1;
        Q_str(3,Pinds) = 68;
        Q_str(4,:) = Jinds;
    elseif strcmpi(type,'all')
        colSzs = [2 3 4];
        Q_str = 100*ones(9,Jnum);
        QDrows = [1 4 8];
        Q_str(QDrows,Rinds) = 81;
```

```
        Q_str(QDrows,Pinds) = 68;
        Q_str([2 5 9],:) = ones(1,3).'*Jinds;
    end
    JntVars = sym(mat2cell(char(Q_str.'),mask1,colSzs));
End
```

Appendix-B

The Matlab .m codes used to the Jacobian matrices of the SLRIP, DLRIP and TLRIP is given in this section.

```
% Jacobian Matrix  of the SLRIP
Px= simplify(Ad(1,4))
Py= simplify(Ad(2,4))
Pz= simplify(Ad(3,4))
% % disp('Jacobian matrix with derivative ')
%%
 Jac=[simplify(diff(Px,Q1)), simplify(diff(Px,Q2));
      simplify(diff(Py,Q1)), simplify(diff(Py,Q2));
      simplify(diff(Pz,Q1)), simplify(diff(Pz,Q2));];
  %%

% Jacobian matrices obtained from the linear and angular velocities
w00 = zeros(3,1);
v00= zeros(3,1);
w11= R01.'*w00+dQ1*Zii ;
v11= R01.'*(v00+cross(w00,P01));
w22= R12.'*w11+dQ2*Zii ;
v22= R12.'*(v11+cross(w11,P12));
w33= R23.'*w22;
v33= R23.'*(v22+cross(w22,P23));
v03= simplify(R03*v33);
W03= simplify(R03*w33);
%
M11 = simplify(diff(v03(1,1),dQ1));
M12 = simplify( diff(v03(1,1),dQ2));
M21 = simplify(diff(v03(2,1),dQ1));
M22 =  simplify(diff(v03(2,1),dQ2));
M31 = simplify(diff(v03(3,1),dQ1));
M32 = simplify(diff(v03(3,1),dQ2));
%
Jaco_LV= [ M11, M12 ; M21, M22 ; M31, M32;];
%
X11 = simplify(diff(W03(1,1),dQ1));
X12 = simplify( diff(W03(1,1),dQ2));
X21 = simplify(diff(W03(2,1),dQ1));
X22 =  simplify(diff(W03(2,1),dQ2));
X31 = simplify(diff(W03(3,1),dQ1));
X32 = simplify(diff(W03(3,1),dQ2));

Jaco_AV= [ X11, X12, ; X21, X22; X31, X32;];
Jaco_Ma =[Jaco_LV;Jaco_AV]
Deter_SLRIP= det (Jaco_Ma)


% Jacobian Matrix DLRIP
Ad=simplify(T04)
Px= simplify(Ad(1,4))
Py= simplify(Ad(2,4))
Pz= simplify(Ad(3,4))
```

```
%% % % disp('Jacobian matrix with derivative ')
Jac= [simplify(diff(Px,Q1)), simplify(diff(Px,Q2)),
simplify(diff(Px,Q2));
      simplify(diff(Py,Q1)), simplify(diff(Py,Q2)),
simplify(diff(Py,Q3));
      simplify(diff(Pz,Q1)), simplify(diff(Pz,Q2)),
simplify(diff(Pz,Q3));];

%%
% Jacobian matrices obtained from the linear and angular velocities
w00= zeros(3,1);
v00= zeros(3,1);
w11= R01.'*w00+dQ1*Zii;
v11= R01.'*(v00+cross(w00,P01));
w22= R12.'*w11+dQ2*Zii ;
v22= R12.'*(v11+cross(w11,P12));
w33= R23.'*w22+dQ3*Zii ;
v33= R23.'*(v22+cross(w22,P23));
w44= R34.'*w33;
v44= R34.'*(v33+cross(w33,P34));
v04= simplify(R04*v44);
W04= simplify(R04*w44);
M11 = simplify(diff(v04(1,1),dQ1));
M12 = simplify( diff(v04(1,1),dQ2));
M13 = simplify (diff(v04(1,1),dQ3));
M21 = simplify(diff(v04(2,1),dQ1));
M22 =  simplify(diff(v04(2,1),dQ2));
M23=  simplify(diff(v04(2,1),dQ3));
M31 = simplify(diff(v04(3,1),dQ1));
M32 = simplify(diff(v04(3,1),dQ2));
M33 = simplify(diff(v04(3,1),dQ3));
%
Jaco_LV= [ M11, M12, M13 ; M21, M22 , M23 ; M31, M32, M33;];
%
X11 = simplify(diff(W04(1,1),dQ1));
X12 = simplify( diff(W04(1,1),dQ2));
X13 = simplify (diff(W04(1,1),dQ3));
% % %
X21 = simplify(diff(W04(2,1),dQ1));
X22 =  simplify(diff(W04(2,1),dQ2));
X23=  simplify(diff(W04(2,1),dQ3));
% % %
X31 = simplify(diff(W04(3,1),dQ1));
X32 = simplify(diff(W04(3,1),dQ2));
X33 = simplify(diff(W04(3,1),dQ3));

Jaco_AV= [X11, X12, X13; X21, X22, X23; X31, X32, X33;];

Jaco_Ma =[Jaco_LV;Jaco_AV]

Deter_DLRIP= det (Jaco_Ma)

% Jacobian Matrix TLRIP
Ad=simplify(T05)
Px= simplify(Ad(1,4))
Py= simplify(Ad(2,4))
Pz= simplify(Ad(3,4))
%%
% % disp('Jacobian matrix with derivative ')
```

```
Jac= [simplify(diff(Px,Q1)), simplify(diff(Px,Q2)),
simplify(diff(Px,Q3)), simplify(diff(Px,Q4));
      simplify(diff(Py,Q1)), simplify(diff(Py,Q2)),
simplify(diff(Py,Q3)), simplify(diff(Py,Q4));
      simplify(diff(Pz,Q1)), simplify(diff(Pz,Q2)),
simplify(diff(Pz,Q3)), simplify(diff(Pz,Q4));];
%%
% Jacobian matrices obtained from the linear and angular velocities
w00= zeros(3,1);
v00= zeros(3,1);
w11= R01.'*w00+dQ1*Zii;
v11= R01.'*(v00+cross(w00,P01));
w22= R12.'*w11+dQ2*Zii ;
v22= R12.'*(v11+cross(w11,P12));
w33= R23.'*w22+dQ3*Zii ;
v33= R23.'*(v22+cross(w22,P23));
w44= R34.'*w33+dQ4*Zii ;
v44= R34.'*(v33+cross(w33,P34));
w55= R45.'*w44;
v55= R45.'*(v44+cross(w44,P45));
v05= simplify(R05*v55);
W05= simplify(R05*w55);
M11 = simplify(diff(v05(1,1),dQ1));
M12 = simplify(diff(v05(1,1),dQ2));
M13 = simplify (diff(v05(1,1),dQ3));
M14 = simplify (diff(v05(1,1),dQ4));
% %
M21 = simplify(diff(v05(2,1),dQ1));
M22 = simplify(diff(v05(2,1),dQ2));
M23 = simplify(diff(v05(2,1),dQ3));
M24 = simplify(diff(v05(2,1),dQ4));
% %
M31 = simplify(diff(v05(3,1),dQ1));
M32 = simplify(diff(v05(3,1),dQ2));
M33 = simplify(diff(v05(3,1),dQ3));
M34 = simplify(diff(v05(3,1),dQ4));
%
Jaco_LV=[ M11, M12 , M13, M14 ; M21, M22, M23, M24 ; M31, M32, M33,
M34;];
%%
X11 = simplify(diff(W05(1,1),dQ1));
X12 = simplify(diff(W05(1,1),dQ2));
X13 = simplify(diff(W05(1,1),dQ3));
X14 = simplify(diff(W05(1,1),dQ4));
% % %
X21 = simplify(diff(W05(2,1),dQ1));
X22 = simplify(diff(W05(2,1,dQ2)));
X23 = simplify(diff(W05(2,1),dQ3));
X24=  simplify(diff(W05(2,1),dQ4));
% % %
X31 = simplify(diff(W05(3,1),dQ1));
X32 = simplify(diff(W05(3,1),dQ2));
X33 = simplify(diff(W05(3,1),dQ3));
X34 = simplify(diff(W05(3,1),dQ4));
%
Jaco_AV= [ X11, X12, X13 , X14; X21, X22, X23, X24; X31, X32, X33 ,
X34;];
Jaco_Ma =[Jaco_LV;Jaco_AV]
Deter_TLRIP= det (Jaco_Ma)
```

PUBLICATIONS

[1] **Hazem Z.B.**, Fotuhi M.J., and Bingül, Z., Comparison of Friction Estimation Models for Rotary Triple Inverted Pendulum, *International Journal of Mechanical Engineering and Robotics Research*, 2019, **8**(1).

[2] **Hazem Z.B.**, Fotuhi M.J., and Bingül, Z., A Comparative Study of the Friction Models with Adaptive Coefficients for a Rotary Triple Inverted Pendulum, *6th International Conference on Control Engineering and Information Technology (CEIT)*, *IEEE*, pp.1-6, 2018.

[3] **Hazem Z.B.**, Fotuhi M.J., and Bingül, Z., A Comparative Study of the Joint Neuro-Fuzzy Friction Models for a Triple Link Rotary Inverted Pendulum, *IEEE Access*, 2020, vol.8, 49066-49078.

[4] **Hazem Z.B.**, Fotuhi M.J., and Bingül, Z., Development of a Fuzzy-LQR and Fuzzy-LQG Stability Control for a Double Link Rotary Inverted Pendulum, *Journal of the Franklin Institute*, 2020, vol.357.15, 10529-10556.

[5] Fotuhi M.J., **Hazem Z.B.**, and Bingül, Z., Adaptive Joint Friction Estimation Model for Laboratory 2 DOF Double Dual Twin Rotor Aerodynamical Helicopter System, *6th International Conference on Control Engineering and Information Technology (CEIT)*, *IEEE*, pp.1-6, 2018.

[6] Fotuhi M.J., **Hazem Z.B.**, and Bingül, Z., Comparison of Joint Friction Estimation Models for Laboratory 2 DOF Double Dual Twin Rotor Aero-Dynamical System, *Conference of the Industrial Electronics Society (IECON)*, *IEEE*, pp.2231-2236, 2018.

[7] Fotuhi M.J., **Hazem Z.B.**, and Bingül, Z., Modelling and Torque Control of an Non-Linear Friction Inverted Pendulum Driven with A Rotary Series Elastic Actuator, *International Symposium on Multidisciplinary Studies and Innovative Technologies (ISMSIT)*, *IEEE*, pp.1-6, 2019.

[8] **Hazem Z.B.,** Zouhir Y., Ouni K., A Study of Speech Recognition System Based on the Hidden Markov Model with Gaussian-Mixture, *International Conference on Electrical Sciences and Technologies in Maghreb (CISTEM)*, *IEEE*, pp.1-5, 2014.

CURRICULUM VITAE

Zied Ben Hazem received the bachelor's degree in Mechanical Engineering from the Higher Institute of Technological Studies, Rades, Tunisia, in 2011, and the master's degree in Automatic Control, Robotics and Information Processing from the National Engineering School of Carthage, Carthage University, in 2013. He is currently pursuing the Ph.D. degree in Automation and Robotics Laboratory, Department of Mechatronics Engineering, Kocaeli University, Turkey. His research interest in the control of a triple link rotary inverted pendulum.